Defects in ZnO nanoparticles obtained by gas-phase syntheses

Miao Zhang

Miao Zhang. Defects in ZnO nanoparticles obtained by gas-phase syntheses. Chemical Sciences. Sorbone Université; ED, 2017. English. NNT : . tel-03952778

HAL Id: tel-03952778
https://hal.science/tel-03952778v1

Université Pierre et Marie Curie

Laboratoire de Réactivité de Surface / Institut des NanoSciences de Paris

Ecole doctorale 397

Defects in ZnO nanoparticles obtained by gas-phase syntheses

Miao Zhang

PhD thesis of Materials Science

Directed by Guylène COSTENTIN and Slavica STANKIC

Présentée et soutenue publiquement le 16 October 2017

Devant un jury composé de:

Mme. Myrtil KAHN, Directrice de Recherche (Université de Toulouse)	Rapporteur
M. Lubomir SPANHEL, Professeur (Université de Rennes 1)	Rapporteur
Mme. Maria Cristina PAGANINI, Associate professor (Università di Torino)	Examinateur
Mme. Hélène PERNOT, Professeure (UPMC)	Examinateur
M. Frédéric AVERSENG, Maître de conférences (UPMC)	Co-encadrant (invité)
Mme. Slavica STANKIC, Chargé de Recherche (UPMC)	Co-encadrant
Mme. Guylène COSTENTIN, Directrice de Recherche (UPMC)	Directrice de thèse

Contents

Résumé

L'attribution des signatures spectrales liées aux défauts dans l'oxyde de zinc fait encore l'objet de controverses. Ceci est probablement dû à la grande variété de défauts possibles, à l'incertitude de leur niveau d'énergie ainsi que leur énergie de formation dans la bande interdite. De plus, l'imprécision concernant les conditions de mesures et la possible présence d'impuretés inhérentes à certaines méthodes de synthèse peuvent souvent mener à des interprétations erronées. Le but de ce travail de thèse est donc d'identifier les défauts intrinsèques naturellement présents dans du ZnO fraîchement préparé ou bien formés via différents types de traitements post-synthèse. Pour atteindre ce but, notre stratégie fut (i) de préparer des nanoparticules modèles de ZnO en utilisant deux types de synthèses en phase vapeur (Combustion et CVS) (ii) de combiner des mesures *in situ* de photoluminescence (PL) et de RPE, également associées à des spectroscopies complémentaires (Raman, UV visible, FTIR) de façon à révéler, attribuer les défauts et discuter leur comportement selon les conditions de synthèses et de traitements post-synthèse et (iii) de révéler la réactivité des surfaces défectueuses de nos échantillons de ZnO en étudiant leur interaction avec des molécules d'eau ou de 2-méthyl-3-butyn-2-ol (MBOH). Nous avons ainsi observé que V_O^{2+} et Zn_i^+ sont les défauts natifs prédominants dans tous les échantillons fraîchement préparés de ZnO, dans des quantités relatives dépendant de la pression partielle d'oxygène utilisée lors de la synthèse. Les lacunes neutres d'oxygène (V_O^0) ont également été détectées dans le cas des préparations effectuées dans des conditions particulièrement riches en zinc. V_O^+ peut se former dans le ZnO smoke après post-traitement (recuit sous vide ou sous vapeur de zinc), la formation d'électrons associée participant à la réduction de Zn_i^+ en Zn^0. Au contraire, calciner sous O_2 mène à des processus opposés, voire, sous excès d'O_2, à la formation de défaut de type O_i. La dissociation de l'eau sur des surfaces préalablement calcinées sous vide mène au remplissage de V_O^+ et à la réduction de Zn^{2+} en Zn^+. Des tests catalytiques de conversion du MBOH ont montré que de tels processus redox, contrôlés par les conditions de prétraitement, affectent la réactivité de surface de nos matériaux

Mots clé: ZnO, défauts, signatures spectrales, traitements post-synthèse, Photoluminescence, RPE, eau, methylbutynol

Abstract

By far, the assignment of defects-related spectroscopic features of zinc oxide is still a matter of great controversy. This is probably due to the variety of possible defects in ZnO as well as to their still uncertain formation energies and positions within the band gap. Uncontrolled measurement conditions and impurities related to some synthesis methods can additionally mislead interpretations. The aim of this work is to identify the intrinsic native defects in pure ZnO or formed upon different kind of post-synthesis treatments. To fulfill this goal our strategy was to: i) prepare model zinc oxide nanoparticles using two different vapor-phase synthesis techniques (Combustion and CVS) ii) identify, assign and discuss the occurrence of the defects in line with the synthesis and post treatments conditions by combining *in situ* PL and EPR measurements together with other complementary spectroscopies (Raman, UV vis, FTIR) and iii) reveal the surface reactivity of defective ZnO samples by studying the interaction with water or 2-methyl-3-butyn-2-ol (MBOH). We observed that in all as-synthesized ZnO samples V_O^{2+} and Zn_i^+ are the predominant native defects with relative amounts depending on the partial pressure of oxygen used during the synthesis. Neutral oxygen vacancies (V_O^0) are additionally detected in samples prepared in conditions particularly rich in zinc. The formation of Vo^+ is demonstrated in ZnO smoke upon post treatment (annealing in high vacuum or zinc vapor) while the associated electron release is shown to participate to the reduction of Zn_i^+ into Zn^0. On the contrary, annealing in oxygen leads to reverse processes while if used in an excess, to creation of O_i-related defects. Dissociation of water on vacuum annealed surface leads to the filling up of V_O^+, and reduction of Zn^{2+} into Zn^+. Such redox processes controlled by the pretreatment conditions affect the surface reactivity through the change of the acid base balance, as revealed by MBOH conversion catalytic tests.

Key words: ZnO, defects, spectroscopic features, post treatments, zinc rich, Photoluminescence, EPR, water, MBOH

List of abbreviations

B3LYP	Becke 3-parameter Lee Yang Parr
BE	Binding Energy
BET	Brunauer-Emmett-Teller
BLBZA	bi-layered basic zinc acetate
CL	Cathodoluminescence
CVS	Chemical Vapor Synthesis
CW	Continuous Wave
DAP	Donor-Acceptor Pairs
DPPH	2,2-diphenyl-1-picrylhydrazyl
DR UV-vis	Diffuse Reflectance Ultraviolet-Visible Spectroscopy
EPR	Electron Paramagnetic Resonance
FTIR	Fourier Transform Infrared
FWHM	Full Width at Half Maximum
GGA	Generalized-Gradient Approximation
HREELS	High-Resolution Electron Energy Loss Spectroscopy
HRTEM	High-Resolution Transmission Electron Microscopy
HSE	Heyd-Scuseria-Ernzerhof
HV	High Vacuum
LDA	Local-Density Approximation
MBOH	2-methyl-3-butyn-2-ol
Mbyne	3-methyl-3-butene-1-yne
MO	Methyl Orange
PL	Photoluminescence

SAED	Selected Area Electron Diffraction
SEM	Scanning Electron Microscopy
TEM	Transmission Electron Microscopy
UHV	Ultra High Vacuum
UV	Ultraviolet
VBM	Valence Band Maximum
XPS	X-Ray Photoemission Spectroscopy
XRD	X-Ray Diffraction

Chapter 1: Introduction

Along with the advent of nanotechnology, semiconducting nanoparticles have attracted much attention due to their novel optical, electrical, and mechanical properties. Among various semiconducting nanoparticles, nanosized zinc oxide (ZnO) is one of the most frequently studied as due to its large range of application aspects, such as in solar energy conversion, varistors, luminescence, catalysis, photocatalysis, electrostatic dissipative coating, transparent UV protection films, and chemical sensors [1-5]. The great application potential of ZnO nanoparticles, is related to the fact that ZnO represents one of the richest families of nanostructures, both in structures and properties [6]. ZnO nanoparticles with plenty of morphologies have been synthesized via wet chemistry-and vapor-phase based methods.

1.1 General properties and applications

ZnO is a direct semiconductor with wide band gap, 3.37eV at room temperature, which is comparable to that of wurtzite GaN (3.44 eV) [7]. Moreover, ZnO possesses a large exciton binding energy of 60 meV, particularly advantageous for making highly efficient lasers [8] which enables the excitonic emission to persist even at room temperature. Based on these electrical properties, ZnO can be used in optoelectronics for light-emitting diodes, laser diodes and photodetectors [9-10]. The high thermal conductivity property makes ZnO useful as an additive, for example, ZnO can be added to rubber in order to increase the thermal dissipation in tires [11]. The low symmetry of the wurtzite crystal structure combined with a large electromechanical coupling in ZnO gives rise to strong piezoelectric and pyroelectric properties [12-13]. Its piezo-effect is the most pronounced one of all tetrahedrally coordinated semiconductors used therefore as sensors, transducers and actuators [14-16].

Physico-chemical properties of ZnO can be influenced by the particles size, morphology, surface orientation, crystal structure, and defects located on the surface or in the bulk. Moreover, these parameters are not independent but interplaying, and they cooperatively affect its properties. For instance, photocatalytic properties of ZnO were shown to strongly depend on the surface orientation [17-19]. This, however, can be tuned by modifying ZnO morphology as differently shaped particles providing different proportions of the various crystalline facets. Jang et al. [20] synthesized nanorods, nanoplates, microrods and dumbbell-shaped microrods of ZnO with different ratios of polar to non-polar faces and studied the photocatalytic properties of a specific crystal plane with respect to the generation of H_2O_2.

Among these different morphologies, ZnO nanoplates possessed the highest population of polar Zn-(0001) faces on which more oxygen molecules were thermodynamically favorable to be adsorbed and led to the effective generation of H_2O_2. The effects of ZnO morphology on the sensitivity to acetone adsorption were studied by Alenezi et al. [21]. They have shown that ZnO with hierarchical nanodisks structure was the most sensitive with fastest response to acetone compared to other ZnO morphologies. Furthermore, photocatalytic properties were shown to strongly depend on the type and location of defects in ZnO – since, it is well accepted that the photocatalytic process is determined by the separation of electron / hole pairs [22-23]. For instance, Guo et al. [24] compared the spectroscopic features and the activity of photodegradation of methyl orange (MO) on defects free ZnO and oxygen deficient ZnO_{1-x} samples. They found the green emission at 494 nm and the EPR signal with g ~ 2.01 were present only in ZnO_{1-x} sample demonstrating the sole existence of Vo^+ in this sample. Simultaneously, they observed that the photodegradation of MO on ZnO_{1-x} was higher than that of ZnO sample. Hence, they proposed that V_O^+ acts as unoccupied states that could trap photogenerated electrons, decreasing the surface recombination of electrons and holes and resulting in such higher photocatalytic activity. Likewise, defects present in ZnO also play a significant role in heterogeneous catalysis. For example, Drouilly et al [25] demonstrated that the creation of oxygen vacancies accompanying the release of electrons could strengthen the basicity of active sites, resulting in a strongly enhanced conversion of methylbutynol by ZnO. Moreover, inducing the defects into the ZnO lattice can effectively affect the optical properties of ZnO as reported by several groups [26-29]. For instance, Anantachaisilp et al. revealed that the defect-related cathodoluminescence (CL) emissions can be tuned by the annealing atmosphere. They proposed that the yellow emission (1.90 eV / 653 nm) in as-synthesized ZnO nanorods was related to Li_{Zn} deep acceptors or oxygen interstitials. Then the red emission (1.70 eV / 730 nm) and green emission (2.44 eV / 508 nm) are generated through the subsequent annealing in O_2 and Zn vapor at 923 K, respectively. Therefore, they additionally suggested that the red and green emission were due to V_{Zn} and V_O related defects, respectively.

Nanomaterials exhibit unique structures and properties compared to bulk materials, which is mostly due to their high surface-to-volume ratio. Due to the high potential in the application of optical devices (such as sensors [21], light-emitting diodes [30] or solar cells [31]), optical properties of ZnO have been intensively studied. With the beginning trend of nanosized materials, the optical properties of nano-ZnO were extensively investigated as a function of the size [32-35]. Erdem et al. [36] studied optical properties of bulk and nano-sized ZnO, and they found that ZnO nanoparticles exhibited more intense and broader emission in visible range of PL spectrum (shown in Figure 1.1). This great difference in optical property is due to the fact that ZnO nanoparticles with larger surface-to-volume ratio possess higher concentration of surface defects.

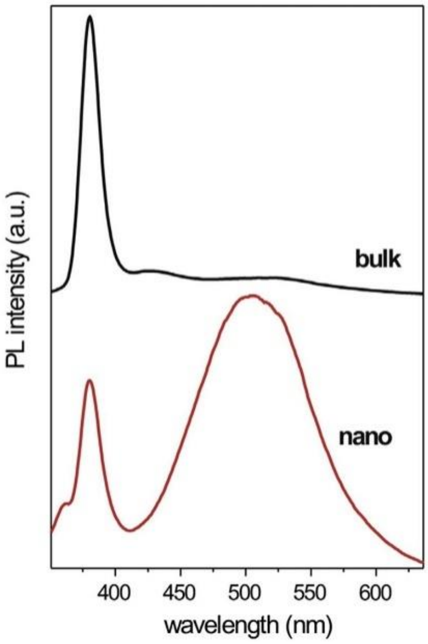

Figure 1.1 PL spectra of bulk and nano-sized ZnO paticles [36]

Finally, various crystal structures that the material may exhibit lead to its different physico-chemical properties. For example, Lazzarini et al. [37] synthesized tetrapod-shape ZnO nanoparticles with twin crystal structure - wurtzite (WZ) and zinc blende (ZB) structure. They observed that typical emissions located at 377 nm (3.29 eV) and 369 nm (3.36 eV) exhibited in PL spectrum recorded at 10 K were corresponding to the band gap of ZB and WZ structures, respectively. As a consequence, these two structures coexisting in the same tetrapod exhibit different electronic properties, which offers novel routes in the design of nanodevices made by a single nanostructure.

On the basis of the results discussed above, a variety of synthesis approaches have been developed and explored to synthesize ZnO nanoparticles with desired size, shape, surface orientation, crystal structure or type of lattice defects [17, 38-40].

1.2 ZnO nanoparticles: from syntheses to morphologies

ZnO nanoparticles synthesis can be generally classified into two categories: solution-based synthesis and vapor-phase based synthesis. In solution-based (or wet chemistry) synthesis zinc hydroxide is usually obtained by precipitating zinc salts or hydrolyzing zinc alkoxides in various solutions. Afterwards, zinc hydroxide is subjected to further calcinations to transform into zinc oxide. Solution-based synthesis includes sol-gel, solvothermal, precipitation, emulsion, template-based, and microwave-assisted methods. Here, taking precipitation method as an example, the corresponding ZnO formation can be depicted by: $Zn^{2+} + 2OH^{-} \rightarrow Zn(OH)_2 \xrightarrow{\Delta} ZnO + H_2O$. This method is commonly described by precipitating the soluble zinc salts by alkaline solution in order to generate zinc hydroxide, and then zinc hydroxide is calcined at a given temperature to obtain final ZnO products. Various morphologies of ZnO nanoparticles obtained by solution-based synthesis are presented in Figure 1.2. They include nanorods [41], nanospheres [42], hollow sphere composed of nanoparticles [43] and nanopyramids [44].

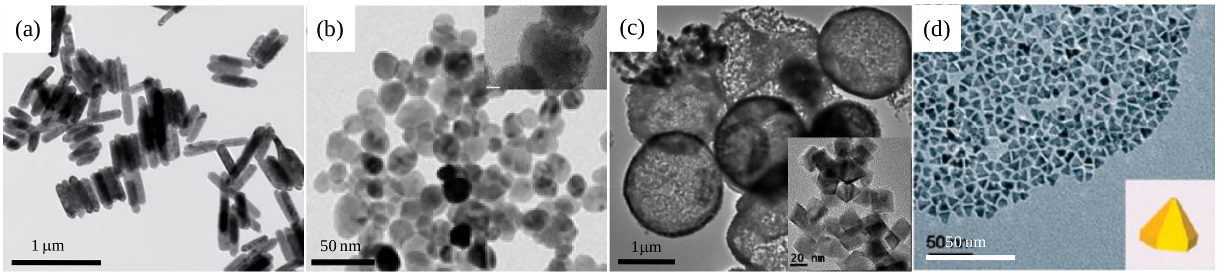

Figure 1.2 TEM images of ZnO nanostructures: (a) nanorods produced by solvothermal method [41]; (b) nanospheres obtained by solvothermal method [42]; (c) hollow spheres composed of nanoparticles and building block ZnO nanoparticles (inset) fabricated by hard template method [43]; (d) ZnO nanopyramids synthesized from metal-organic compound [45]

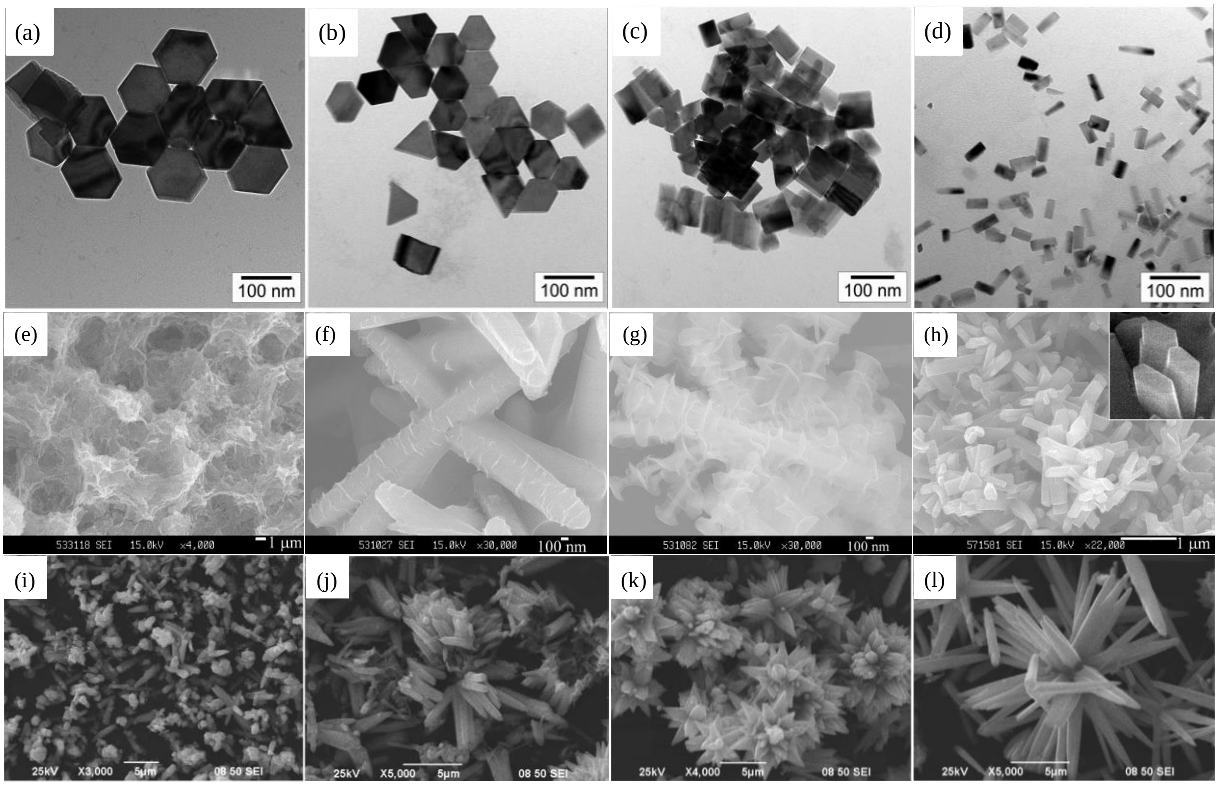

Figure 1.3 Effect of parameters on the morphologies of ZnO obtained by solution-base synthesis. TEM images of the ZnO nanoparticles synthesized in different zinc acetate concentrations: (a) 0.01 mol/L; (b) 0.025 mol/L; (c) 0.05 mol/L; (d) 0.1 mol/L [46]; ZnO particles with hierarchical nanostructures obtained from the bi-layered basic zinc acetate (BLBZA) nanobelts by refluxing at 120 °C for 1h (e), 4h (f), 12h (g), and 48 h (h) [47]; Flower-like ZnO particles assembled by nanorods obtained at different reaction temperatures: 80 ℃ (i); 100 ℃ (j); 140 ℃ (k); and 180 ℃ (l) [48].

Within the solution-based techniques, the morphology and particle size of ZnO crystals can be controlled by adapting the following synthesis parameters: solvents, precursors, reactant concentration, shape-directing agents, temperature and pH of the system. For instance, Figure 1.3 illustrates (taken from the references [46-48]) how some of these parameters affect the morphologies of ZnO nanoparticles. Via emulsion-based synthesis method, Fricke et al. [46] synthesized ZnO nanoparticles with well-defined crystal morphology by using zinc acetate as a precursor. In order to prevent the formation of zinc hydroxide, they added acetic acid during heating the solution and they found that increasing the zinc acetate concentration in the solution from 0.01 mol/L to 0.1 mol/L resulted in particle size reduction from 95 nm to 20 nm. At the same time, particles were shown to undergo also a shape transformation, from plate-like to needle-like particles, as illustrated in Figure 1.3 (a ~ d). The influence of reaction time on the morphology of ZnO nanoparticles has been investigated by Song et al. [47]. They obtained ZnO nanosheets, nanolaces, nanorods, and hexagonal nanoprisms by refluxing bi-layered basic zinc acetate (BLBZA) nanobelts at 120 °C for 1h, 4h, 12h and 48h, respectively (Figure 1.3, e ~ h). Other synthesis parameters such as temperature have been also investigated and, for instance, Feng and coworkers [48] have found that, by using hydrothermal method, the morphologies of ZnO can be easily tuned by the reaction temperatures from 80°C to 180 °C, and they observed the morphology transition from nanorods and follower-like to cube column-like ZnO (Figure 1.3, i ~ l). The effect of the solution pH on ZnO morphology was studied by Zhang et al., and they showed that, for instance, flower-like ZnO can only be obtained when the solution pH was equal to 7 [49].

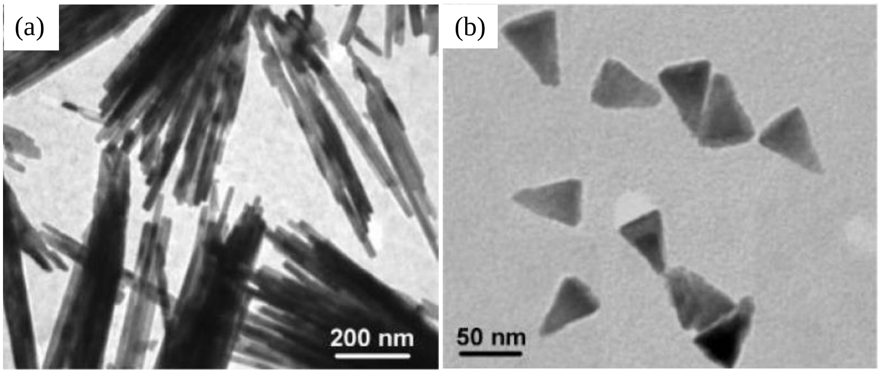

Figure 1.4 TEM images of rod-like and tetrahedral ZnO nanocrystals [50]

Generally, the changes of morphology and the particles size concurrence. Besides the examples of ZnO morphologies in Figure1.3, this coexisting behavior is also illustrated by the next example. Zhang et al. [50] produced rod-like (Figure 1.4 (a)) and tetrahedral ZnO (Figure 1.4 (b)) nanoparticles by aminolytic reaction of zinc carboxylates with oleylamine in non-coordinating (dioctyl ether) and coordinating (trioctylphosphine) solvents, respectively. In addition, the obtained ZnO nanoparticles also display different sizes, i.e. nanorods show a diameter of ~ 20nm and ~ 700 nm in length while nanotetrahedrons display a base length of ~ 35 nm and two equal side lengths of ~ 60 nm.

Although, the wet-chemistry route is an efficient way to control morphology and particle size, it may result in samples contaminated by impurities such as organic carbon compounds and / or various ions from the solvents or surfactants. This can be completely avoided by using vapor-phase based techniques which provide high-purity and high-quality ZnO crystals. In vapor-phase based synthesis, the oxidation of zinc or the decomposition of zinc organic salts takes place in the gas phase. It includes spray pyrolysis, chemical vapor deposition and metal combustion. In the present thesis, metal combustion and chemical vapor synthesis (CVS) methods are employed for the production of ZnO nanoparticles, and are, therefore, presented in more details. Both of these, fundamentally similar methods, are based on the oxidation of metallic zinc, and the general equation representing the stoichiometry of zinc-oxygen reactions is:

$$2Zn\ (s) + O_2\ (g) \xrightarrow{\Delta} 2ZnO\ (g) \rightarrow 2ZnO\ (s)$$

Metal combustion is one of the most common synthesis methods adopted to produce ZnO nanoparticles. In this synthesis, pure metallic zinc is evaporated into background gases in which oxygen is admixed. The synthesis requires a thermal activation in such a way that metallic zinc is partially heated which finally leads to the oxidation reaction to start. Thereafter, the heat required for the following metal evaporation is produced *in situ* by combustion reaction itself. The partial pressure of oxygen is the only parameter which can be tuned within this synthesis technique. Through this approach, Stankic et al. demonstrated that the particle size of cubic shaped MgO decreased with increasing the partial pressure of oxygen when burning Mg foil under different ratio of oxygen and argon gases [51]. Although metal combustion is a fast way to produce ZnO nanoparticles, the limit of such method is the difficulty to produce samples with homogeneous morphology and particle size, as well as the small yield when compared to wet-chemistry methods.

In chemical vapor synthesis, metallic zinc or metal-organic zinc compounds are evaporated or decomposed at high temperatures. Zinc atoms are then transported by carrier gas to the reaction zone where they react with oxygen (or other oxidizing gaseous agents). Finally, gas phase ZnO homogeneously nucleates and subsequently condensates in the cool gas flow resulting in ZnO powder. This method allows the control of the morphology and particle size of nanoparticles by varying the following synthesis parameters: the nature, partial pressure, and flow rate of reactant gas (as well as carrier gas), the total pressure of the system and the evaporation temperature of the precursor. For instance, Polarz et al. [52] obtained size-selected ZnO nanoparticles by changing the decomposition temperatures of the precursor (tetrameric alkyl-alkoxy zinc compound $[CH_3ZnOCH(CH_3)_2]_4$). They concluded that crystalline size tended to increase upon raising the decomposition temperature of the precursor. Qiu et al.[53] systematically studied the influence of the evaporation temperature of metallic Zn, oxidation temperature, oxygen flow rate and the total gas flow rate on the size of the arms of ZnO nanotetrapods. They found that the size of the tetrapod arms increased when increasing evaporation temperature of metallic Zn, while it decreased when increasing oxidation temperature. With increasing concentration of oxygen in the flow, more and more tetrapods were formed. Additionally, the length of ZnO tetrapods arms decreased with the increasing total transport gas flow rate with a fixed oxygen concentration of 20 %. Bacsa et al. [54] found that the morphology of ZnO can vary from spheres to tetrapods (shown in Figure 1.5) when different evaporation zinc (T_{Zn}) and oxidation temperatures ($T_{ox.}$) were applied within CVS. They also showed that the presence of water could lead to a narrower diameter distribution with a lower average diameter of ZnO tetrapods.

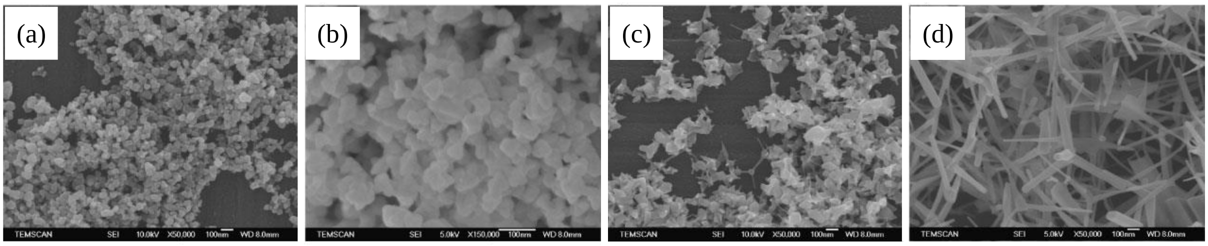

Figure 1.5 Evolution of morphologies of ZnO nanoparticles produced at different evaporation and oxidation temperatures; (a) spheres, $T_{Zn} = T_{ox.} = 923$ K; (b) defined spheres, $T_{Zn} = 1023$ K, $T_{ox} = 950$ K; (c) spheres and tetrapods, $T_{Zn} = T_{ox.} = 1073$ K; (d) tetrapods$T_{Zn} = T_{ox.} = 1173$ K [54]

1.3 Crystal structure and point defects

ZnO can be obtained in three crystal phases: rocksalt (cubic), zinc blende (cubic) and wurtzite (hexagonal), (Figure 1.6 a, b, and c, respectively). The wurtzite structure is thermodynamically the most stable one and usually obtained under normal synthesis conditions. Metastable, zinc-blende can be stabilized by growing on substrates exhibiting cubic structure [55], while rocksalt structure can only be obtained by applying elevated pressures (P > 9 GPa) [56].

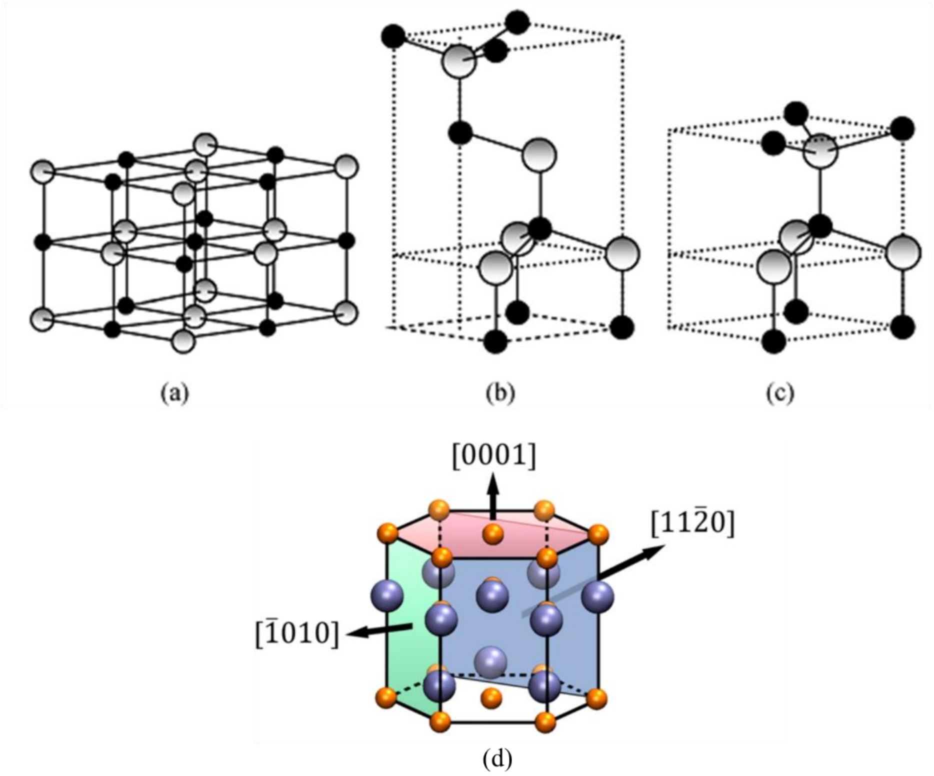

Figure 1.6 Stick and ball representation of ZnO crystal structure: (a) cubic rocksalt, (b) cubic zinc blende and (c) hexagonal wurtzite. Shade gray and black spheres denote Zn and O atoms, respectively [57]; (d) Preferential surface orientations displayed with colored planes and direction vectors for crystals in the (c) hexagonal wurtzite structure. Orange and blue spheres denote oxygen and zinc atoms, respectively[58].

The lattice parameters that correspond to ZnO wurtzite crystal structure are: $a = b = 3.2495$ Å (Angstrom) and $c = 5.2069$ Å. This phase preferentially displays four facet orientations, two non-polar, (10-10) and (11-20), and two polar, (000-1) and (0001), the former being expected to dominate [58-59] in line with cleavage energies (Figure 1.6 (d) [60])). Wurtzite structure can be represented as a number of planes composed of tetrahedrally coordinated O^{2-} and Zn^{2+} ions, alternately stacked along the *c* direction of the crystallographic axes, providing thus plenty of room for different types of defects to be accommodated [61].

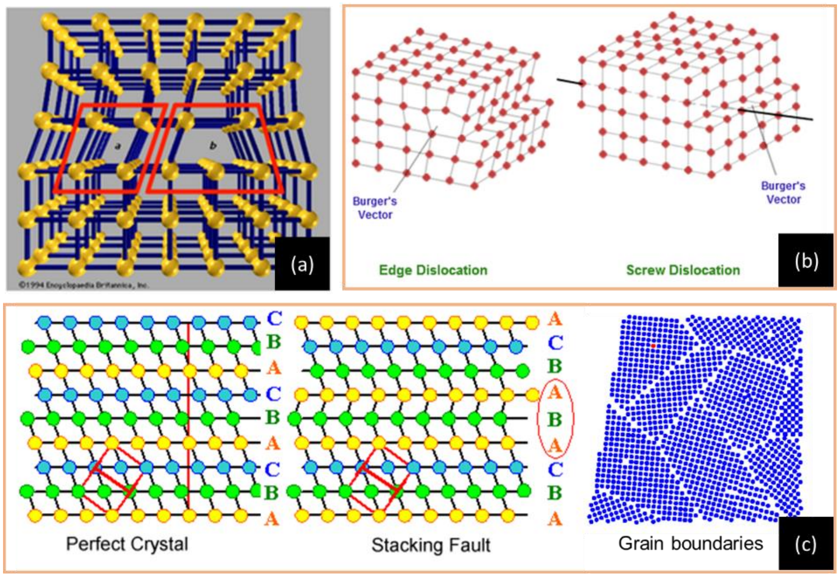

Figure 1.7 Schematic of (a) volume defects [62], (b) line defects [63] (c) planar defects [62]

In ideal crystals, the arrangement of atoms or molecules is periodic, and all unit cells line up in space of three dimensions with no distortion. On the contrary, real crystals generally possess certain number of imperfections where unit cells may have some atoms missing or replaced by other internal or external atoms. Normally, defects can be classified according to their dimensions. **Volume defects** include voids and precipitates, the scale of which is the largest among the rest of the crystal defects, and are typically deleterious to the properties of materials [64]. **Planar defects** occur at the interfaces between homogeneous regions of the material. The most typical planar defects are stacking faults and grain boundaries. **Line defects** include edge and screw dislocations and exist at the interfaces between two single crystal regions of different orientations. **Point defects** are defects where an atom is missing or in an irregular site in the lattice, and they can be divided into two categories: intrinsic and extrinsic defects. Intrinsic defects exist in pure crystals and include vacancies, interstitials and antisites, while extrinsic defects are caused by foreign atoms (present in doped crystals). Representative illustrations of volume, planar and line defects in a metal oxide are presented in Figure 1.7.The representation of point defects, to whom the attention is particularly paid in the present work, is illustrated below through ZnO example (see Figure. 1.7).

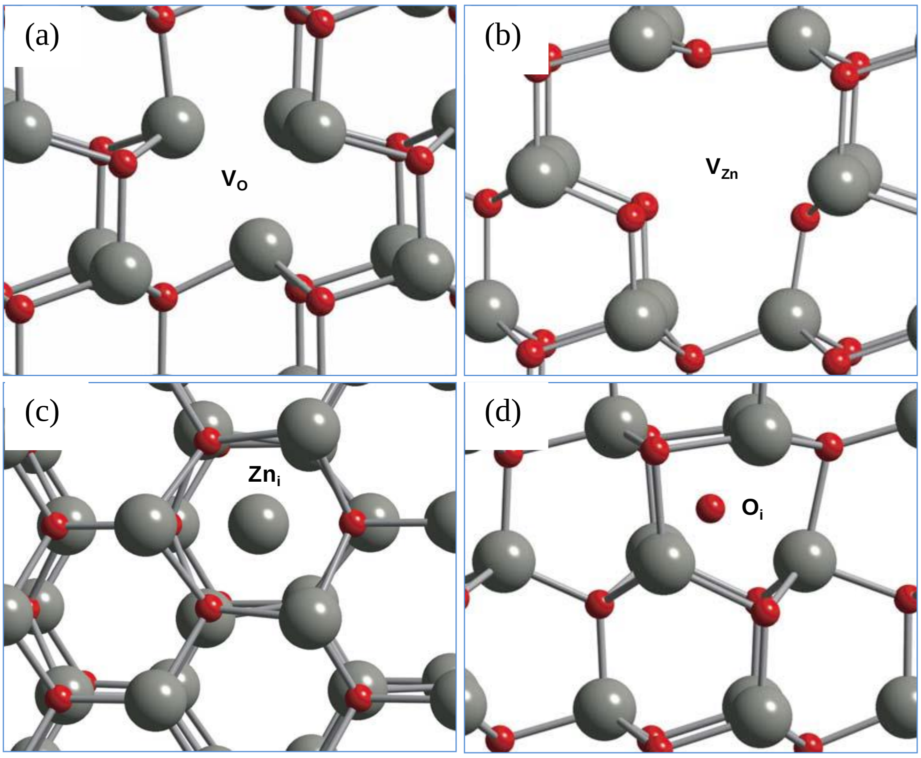

Figure 1.8 Atomic models for (a) oxygen vacancies (V_O), (b) zinc vacancies (V_{Zn}), (c) zinc interstials (Zn_i) and (d) oxygen interstitials (O_i). Gray and red spheres denote Zn and O atoms, respectively [65].

Point defects in ZnO include zinc vacancies (V_{Zn}), oxygen vacancies (V_O), zinc interstitials (Zn_i), oxygen interstitials (O_i) and antisite atoms (O_{Zn} and Zn_O). Among them, oxygen vacancies and zinc interstitials exhibit donor character i.e. their electrons can be readily promoted to the conduction band. On the contrary, oxygen interstitials and zinc vacancies behave as acceptors which, indeed, act as traps and can capture excited electrons from the valence band leaving behind holes in their place. The calculated local geometries of these four point defects in ZnO are taken from Janotti [65] and illustrated in Figure 1.8.

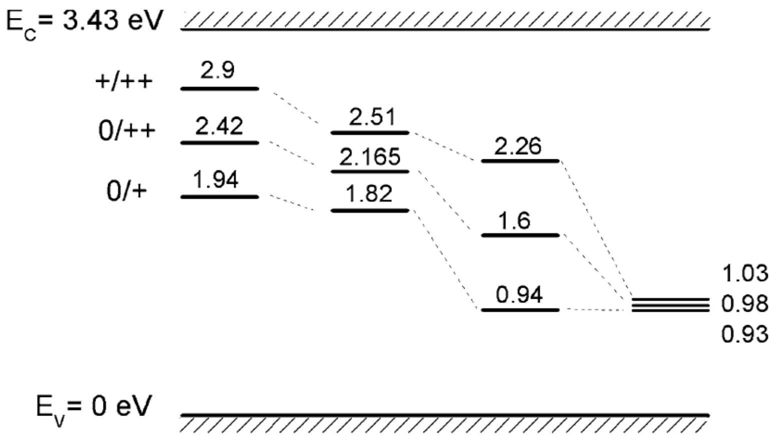

Figure 1.9 Energy levels positions for oxygen vacancy calculated by different authors[66]

Point defects exhibit different oxidation states and occupy well-defined energy levels within the band gap of ZnO. The positions of energy levels within the band gap – which are specific of each given defect, as well as of its different oxidation states – are essential for the interpretation of optical transitions. Nevertheless, no uniformity can be found in literature whether considering the position within the band gap or the donor-acceptor nature of a given point defect. This is illustrated by the example of oxygen vacancy in Figure 1.9, which compares theoretically predicted level positions for the oxygen vacancy calculated by different groups. The difference in the calculated energy level positions is caused by the fact that the band gap of ZnO is severely underestimated by the commonly used local-density approximation (LDA) or generalized-gradient approximation (GGA) functions making the interpretation of the calculations very difficult. Defects often induce occupied states in the band gap. These states have a certain ratio of conduction- versus valence-band character and, therefore, their positions with respect to the valence band maximum (VBM) can be underestimated by a significant amount. This uncertainty affects the prediction of transition levels and formation energies, leading to potentially large errors, especially in the case of wide-band-gap semiconductors such as ZnO. Different approaches to overcome the DFT–LDA or GGA deficiencies in predicting band gaps have been employed in the investigation of point defects in ZnO. These include self-interaction corrections, using the LDA+U and the Becke 3-parameter Lee Yang Parr (B3LYP) and Heyd–Scuseria–Ernzerhof (HSE) hybrid functions [67-73]. Although uncertainties still exist in the numerical values of formation energies, important qualitative conclusions can be extracted.

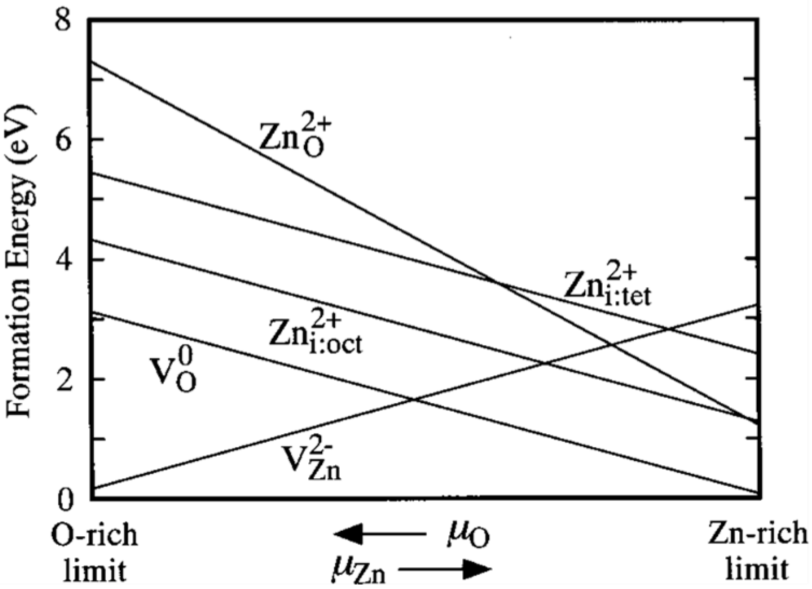

Figure 1.10 Formation energies of native defects as a function of the atomic chemical potentials under n-type condition. For each defect, only the charge state that gives the lowest formation energy is shown [74].

The formation energy (E_f) of a native defect in a solid determines its concentration through the relation [75] in Equation 1.1:

$$c = N_{\mathrm{sites}} \exp\left(\frac{-E^{\mathrm{f}}}{k_{\mathrm{B}}T}\right) \qquad \text{(Equation 1.1)}$$

Where N_{sites} is the number of sites (including different configurations) per unit volume the defect can be incorporated in, k_B is the Boltzmann constant and T the temperature. According to this equation, defects with high formation energies will occur in low concentrations. As illustrated in Figure 1.10, the E_f can be strongly affected by growth conditions. For example, the formation energy of zinc interstitials determined by the relative abundance of Zn and O atoms in the environment, as expressed by the chemical potentials μ_{Zn} and μ_O, respectively. If the defect is charged, the formation energy further depends on the Fermi level (E_F), which is the energy of the electron reservoir, i.e. the electron chemical potential. Accordingly, in Zn-rich condition, oxygen vacancies as well as zinc excess related defects like Zn_i and Zn_O are promoted. In O-rich condition, though, Zn vacancies and other defects associated with oxygen excess (O_{Zn} and O_i) may exist. Migration barrier, is another parameter that can affect the concentration of native defects, and it determines their annealing behavior [76-77]. For this reason, each type of native defects in ZnO will be described below in terms of the formation energy, migration barrier beside the definition and charge state.

Oxygen vacancy (V_O) is formed when an oxygen atom is missing from its regular position in the lattice (Figure 1.8 (a)). If no electrons remain, oxygen vacancy exhibits double positive charge state (V_O^{2+}). Oxygen vacancies capturing one electron and two electrons show single positive charge state (V_O^{+}) and neutral (V_O^{0}), respectively. According to the calculations from Oba et al. [74], the formation energy of neutral oxygen vacancy is gradually reduced with increasing zinc potential, and it tends to be zero under extreme Zn-rich conditions. In particular, the single positive charge oxygen vacancy (Vo^{+}) is thermodynamically unstable, and it tends to decay in to the 2+ or 0 charge state [68]. Therefore, the concentration of Vo^{+} is expected to be very low under equilibrium conditions. The migration of oxygen vacancy takes place when the nearest neighbor oxygen atom in the lattice jumps into the vacant site, leaving an oxygen vacancy behind. The migration barrier is dependent on the charge state of the oxygen vacancy. For instance, the calculated migration barrier for V_O^{0} is 2.4 eV, while for V_O^{2+} is 1.7 eV [65]. These energy barriers indicate that neutral oxygen vacancy (V_O^{0}) will become mobile at temperatures above 900 K whereas V_O^{2+} will become mobile at temperatures above 650 K [65].

Similarly to oxygen vacancy, **zinc vacancy (V_{Zn})** is formed when a zinc atom is missing from the lattice (Figure 1.8 (b)). A zinc vacancy can accept at most 2 electrons, so representing an acceptor with three possible charge-states, neutral, 1– and 2– (V_{Zn}^{0}, V_{Zn}^{-}, and V_{Zn}^{2-}, respectively). Among these, zinc vacancies with 2– charge states (V_{Zn}^{2-}) have the lowest formation energy, and they are expected to be easily produced in oxygen-rich conditions. The migration barrier of V_{Zn}^{2-} is 1.4 eV implying that it will be mobile above 540 K [8].

Zinc interstitial (Zn_i) is a zinc atom that occupies a place outside the normal lattice position (Figure 1.8 (c)). Regarding its electronic configuration, zinc interstitial always donates electrons to the conduction band, thus it acts as a donor and exhibits three charge states: Zn_i^0, Zn_i^+ and Zn_i^{2+}. In principal, a zinc interstitial could occupy the tetrahedral site or the octahedral site in the ZnO wurtzite structure but, according to calculations from Janotti et al. [65], if occupying the less stable tetrahedral site it will spontaneously relax to the octahedral site. As seen from the diagram in Figure 1.10, the formation energy of zinc interstitial is high even at extremely Zn-rich condition. However, it has been experimentally shown that under non-equilibrium conditions Zn_i can be introduced in ZnO [77-79]. Considering their low migration barrier, 0.57 eV according to Janottis' calculation [65], zinc interstitials are expected to be mobile below room temperature and thus unlikely to be present as isolated interstitials, but combined with other defects or impurities to form complexes [65, 80].

If an excess oxygen atom is located outside the normal lattice we speak about **oxygen interstitial (O_i)**, and it can also occupy the octahedral (Figure 1.8 (d)) or tetrahedral interstitial sites. Theoretically, interstitial oxygen can accept at most two electrons and act as an acceptor with three possible charge states – O_i^0, O_i^- and O_i^{2-}. The formation energies of oxygen interstitials are very high except under extreme O-rich conditions, so that oxygen interstitials are not expected under equilibrium conditions. The migration barrier of O_i^- is uncertain, since it is rarely discussed in the literatures. The calculated migration energy barriers for O_i^0 and O_i^{2-} are 0.9 eV and 1.1 eV, indicating that they are mobile at $T > 340$ K and $T > 440$ K, respectively [65].

Other defects such as **oxygen antisite (O_{Zn})** and **zinc antisite (Zn_O)** possess extremely high formation energy even in the most favorable conditions, therefore, antisites defects are typically created under non-equilibrium conditions, such as irradiation [81-82].

Finally, **hydrogen interstitial (H_i)** is often discussed in ZnO crystals as an extrinsic donor defect. It has been found that only positive charge state (H_i^+) is thermodynamically stable, and it presents a relatively low formation energy compared to that of oxygen vacancies, indicating that under equilibrium condition it can occur in a significant concentration – if the source of H_2 is available. It was reported that this type of defect can be stable up to 773 K in ZnO due to its high migration barrier that was calculated to be 2.5 eV [8]. Hydrogen is very often unintentionally present in the growth environment for most of the techniques used for ZnO fabrication as well as in the course of post-treatments such as wet etching, annealing in forming gas [8].

1.4 Identification of defects present in ZnO

Although a good deal of research has been carried out, the assignment of spectroscopic features to corresponding intrinsic defects in ZnO is still very controversial. Already from 1970's, researchers have used multiple techniques for the identification of lattice defects in ZnO, but the contribution of photoluminescence spectroscopy and electron paramagnetic resonance spectroscopy, turned out to be the most productive one.

1.4.1 Photoluminescence (PL)

Typically, room temperature PL spectrum of ZnO consists of two emission bands. The sharp emission centered approximately at 370-380 nm is the fundamental emission of ZnO, the so-called UV emission and results from the radiative recombination of exciton [83-85]. Some authors also suggest that it is composed of two recombination processes, in which one is related to the ZnO free exciton, and the other is related to the free-to-bound transition [86-87]. Additionally, the exact position of the UV band may differ for different forms of ZnO (films, particles or single crystals) and the sizes / morphologies. In this respect, Djurišić and coworkers have reported the UV emission of different morphologies of ZnO nanostructures varying from 397 nm in the case of nanorods to 377 nm for ZnO-shells [88].

Unlike UV emission, the origin of the broad emission band located in the visible range of the spectrum represents a great deal of controversy in ZnO-related studies. What can be said with certainty about this emission is that it results from radiative recombination occurring at defects sites. Thus this emission is usually designated as defects emission, as illustrated in Figure 1.11. It may include violet, blue, green, yellow and orange-red emissions as a separate or combination of some of them.

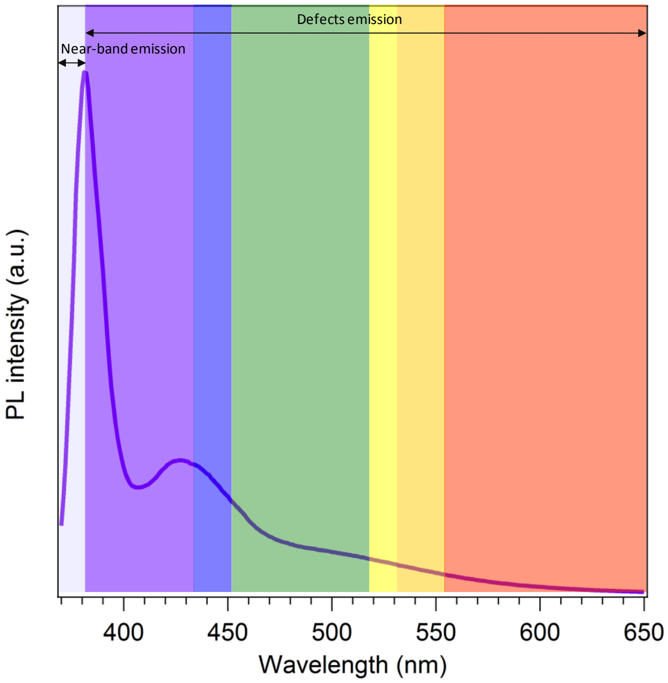

Figure 1.11 Room temperature photoluminescence spectrum of as-synthesized ZnO nanosmoke, demonstrating the UV emission and the broad emission in visible range (from this work).

Violet emission (385 - 455 nm) is not so commonly observed in PL spectrum of ZnO. For instance, PL emission with maximum at ~ 405 nm (3.09 eV) was observed in low-temperature PL spectra of ZnO films grown under oxygen-rich conditions and it was put in relation with Zn vacancy [89]. Zeng et al. [90] have studied the effect of post-annealing treatments and excitation energy on the PL properties of Zn-rich ZnO nanoparticles. They found that the intensity of the emission at ~ 440 nm first increased with increasing the excitation energy (E_{exc}), and then it reached saturation when E_{exc} is at bandgap energy. It finally decreased but still effectively emitting at E_{exc} slightly below the bandgap energy. Afterwards, they deduced that this emission was related to Zn_i located slightly below the bandgap by considering its energy level in the bandgap. The recombination mechanisms that they have proposed have been supported by many other authors [91-93]. Along with this attribution for violet-blue emission, other assignments - interstitial oxygen [94] and H-related complex defects [95] and surface OH groups[96] - have been put forward.

Another infrequently observed emission in ZnO samples is the **blue emission (455 ~ 480 nm)**. In the work by Zeng et al. [90], it was attributed to the transition from extended Zn_i

states to the valance band. However, zinc vacancies [97], oxygen vacancies [98] and shallow donor level of oxygen vacancy and zinc interstitials to the valence band have also been proposed as the origin of the blue emission [99].

Green emission (480 ~ 570 nm) is one of the most reported emissions in ZnO crystals, yet the origin of it still remains without a clear consensus in the literature. Many researchers ascribed copper impurities to green luminescence [100-101]. However, this cannot explain green emission found in all undoped ZnO crystals, especially in some cases where green emission was found to be dependent on annealing temperature or atmosphere, giving thus more consistency related to intrinsic defects rather than to Cu or any other impurity. In the case of undoped ZnO, some authors deduced the origin for green emission on the basis of the specific defects preferably formed under their particular growth condition. For example, in the paper by Ton-That et al. [102], PL emission centered at 492 nm (2.52 eV) has been detected in ZnO samples produced under oxygen-poor atmosphere. Accordingly they have assigned this PL process to be linked to oxygen vacancies since the conditions applied are in favor for the formation of this defect. Another case, in which the growth condition of ZnO is opposite to this, was reported by Repp et al. [103]. They claimed the PL emission at 549 nm (2.26 eV) that was measured for ZnO quantum dots produced in oxygen-rich condition, to be related to V_{Zn} or O_i. Nevertheless, deducing the responsibility for green emission form its tendency upon post-growth treatments seems more common. For instance, Kavitha et al. [98] have shown that after annealing the sample in air the PL emission centered at ~550 nm (2.26 eV) vanishes from the PL spectrum. Since the annealing in air can be considered as a thermal treatment in O-rich condition, these results are found to be consistent with the attribution of green emission to V_O. Such assignment is furthermore supported by other groups [96, 102, 104]. However, some authors observed completely opposite phenomenon in O-rich conditions compared to those mentioned above. For instance, Wang et al. found that the intensity of green emission increased as ZnO nanorods were either annealed in O_2 or exposed to air [105]. Likewise, the same behavior for green emission was observed by Liu et al. when ZnO tetrapods were treated by oxygen-plasma [106]. In both cases, green emission could not be linked to oxygen vacancies. The former group attributed green emission to the band bending arising from chemisorption of oxygen, while the latter one assigned it to defect complexes containing zinc vacancies and this assignment was also supported by other groups [107-108]. Some groups also proposed antisite O_{Zn} [109-110], O_i-related defects [111] and Zn_i-related defects [112] to be related to green emission – i.e. to all theoretically possible ZnO defects.

Unlike the origin of the green emission, the type of defect responsible for the **yellow-orange emission (570 ~ 620 nm)** seems less controversial. Typically, this emission is suggested to originate from oxygen interstitials [110, 113-114]. Indeed, oxygen-rich atmosphere which provides a potential source of O_i in the lattice, usually, leads to the presence of this emission in PL spectra. For instance, the PL intensity of emission peak ~595 nm (2.10 eV) of ZnO film grown in an oxygen-rich atmosphere was enhanced in comparison to that grown in zinc-rich atmosphere [115]. An another assignment for this emission was, however, proposed by Djurisic et al. [114] who fabricated ZnO by several different solution based syntheses and studied their optical properties in function of annealing atmosphere and temperature. They could detect yellow emission (maximum at 576 nm (2.15 eV)) only in as-synthesized samples produced by hydrothermal method (ZnO hollow shells). Raising the annealing temperature up to 473 K in any atmosphere, this emission was not detected anymore and they ascribed it to the desorption of hydroxyl groups rather than to interstitial oxygen, as commonly assumed.

Next ZnO specific emission in the visible range lies between **620 nm (2.00 eV) and 750 nm (1.65 eV) - red emission**. Stavale et al. [115] supposed that oxygen vacancies are responsible for this red emission, since they monitored the intensity enhancement of this emission (730 nm) in ZnO thin films after thermal treatment under vacuum and laser irradiation. Based on their assignment, the annealing in O-rich atmosphere should reduce the intensity of red emission, but Knutsen et al. [116] observed the behavior of this emission that was exactly opposite to that of Stavale's. They observed that the intensity of red emission increased after annealing in O-rich atmosphere, while it was considerably suppressed in Zn ambient annealing. Hence, in the work of Knutsen [116] this emission was assigned to zinc vacancies.

According to the reported assignments of visible emissions discussed above, it is easily seen how controversial the attribution of PL emissions to defects is. The following aspects that make this issue interestingly complicated can be listed as: (1) the broad range of positions of the emissions; (2) different calculation results of energy level of each type of defects (3) a variety of emissions or related evolution of them are made in the studied samples through the various post-growth treatments; (4) the unmentioned measurement conditions; either or any of them can make the origins of the emissions under debate. Table 1.1 summarizes some of studies that reported visible emissions of ZnO together with the corresponding assignments.

Table 1.1 Various visible emissions appearing in ZnO systems and their assignments.

Emissions		Samples	Treatments	Assignments	References
Violet 385-455 nm	405 nm	Thin film		V_{Zn}	[89]
	407 nm	Powder		Zn_i	[93]
	410 nm	Powder	773 K, O_2 or Ar	surface OH groups	[96]
	410 nm	Thin film	923 ~1173 K, air, 2 h or vacuum, 4 h	Zn_i	[91]
	416 nm	Thin film	H_2-plasma	H-related complex defects	[95]
	420 nm	Thin film		O_i	[94]
	424 nm	Thin film	Annealing Zn film in O_2 at different	Zn_i	[92]
	440 nm	Powder		Zn_i	[90]
Blue (455-480 nm)	455 nm	Powder	473 ~ 873 K, air, 6h	Ex-Zn_i^+	[90]
	446 nm	Thin film	573 K, in vacuum and oxygen	Shallow donor to the valence band	[99]

	463 nm	Powder		V_{Zn}	[97]
	468 nm	Powder	823 K, air	V_O	[98]
Green (480-570 nm)	503 nm	Powder	773 ~ 1173 K, in air, and 3% H_2+97% Ar, 24 h	Vo on the surface	[104]
	540 nm			Vo in the bulk	
	494 nm	Powder		V_O	[24]
	497 nm	Powder	O_2, 673 K, 1h	chemisoption of oxygen	[105]
	492 nm	Unclear	1573 K in zinc vapor	V_O	[102]
	539 nm		O_2, 1300 K	V_{Zn}	
	500 nm	Bulk	Cu doped, 1173 K in air for 1 h	Cu^{2+}	[100]
	500 nm	Powder	673 K in air, H_2, vacuum for 2h	V_{Zn}	[117]
	502 nm	Single crystal	1273 K in Zn vapor	V_O	[118]
	515 nm	Powder	773 K in O_2, air, and NH_3 for 1h	V_O	[119]

	520 nm	Thin film	1073 K in vacuum and in O_2	V_O	[120]
	520 nm	Powder	473, 673 and 1173 K in O_2	V_O	[121]
	520 nm	Powder	773 ~1323 K, N_2:H_2=95:5 (by volume)	V_O	[122]
	527 nm	Powder	Cu doped	Cu^{2+}	[101]
	520 nm	Thin film	1273 K in O_2	O_{Zn}	[109]
	520 nm	Powder	O_2-plasma	V_{Zn}	[106]
	520 nm	Bulk	Zn/O_2-plasma	V_{Zn}	[107]
	532 nm	Thin film	573, 673 and 773 K in air	V_O	[123]
	535 nm	Thin film	implantation of Zn-ion	V_O	[115]
	539 nm	Powder	823 K in air	V_{Zn}	[98]
	544 nm	Thin Film	1273 K in O_2	O_i	[109]
	549 nm	Powder	1073 K in O_2	O_i	[111]

	550 nm	Powder	773 K in N_2	Vo	[96]
	490 nm	Powder	1173 K in Ar, O_2 and air	Vo	[110]
	520 nm			O_{Zn}	
	490 nm	Single crystal	1323 K in O_2, Zn vapor and ZnO powder	V_O	[124]
	528 nm			V_{Zn}	
	550 nm	Thin film	473 ~ 673 K in O_2	O_i	[125]
	553 nm	Thin film	673 K in Zn vapor	V_{Zn}	[108]
Yellow-orange (570-620 nm)	570 nm	Powder		O_i	[110]
	576 nm	Powder	473 K, O_2	OH groups	[114]
	590 nm	Powder	773 K in O_2	O_i	[126]
	595 nm	Thin film	700, 800, 900 K in O_2	O_i	[115]
	605 nm	Thin film		O_i	[113]

Red (620-750 nm)	680 nm	Unclear	1023 K in O_2 and zinc vapor for 30	V_{Zn}	[116]
	730 nm	Thin film	700, 800, 900 K in vacuum	V_O^+	[115]

1.4.2 Electron paramagnetic resonance (EPR)

Electron paramagnetic resonance (EPR) spectroscopy is a useful technique for identifying paramagnetic defects and thus has been used to study defects in ZnO starting from 1960’s. Unlike PL, which can probe any oxidation state of a given defect, EPR can only detect their paramagnetic states. Among these possible defects existing in ZnO, only paramagnetic defects can be detected by EPR. For instance, Zn_i^0, Zn_i^+, Zn_i^{2+} have the electron configurations ending with $4s^2$, $4s^1$ and $4s^0$, respectively, and hence Zn_i^0 and Zn_i^{2+} are diamagnetic and EPR silent. The same applies for oxygen interstitials, oxygen vacancies and zinc vacancies for which only O_i^-, V_o^+ and V_{Zn}^- can be detected by EPR. Multifarious assignments related to paramagnetic defects in ZnO are summarized in Table 1.2.

Although the reports on EPR signals observed in ZnO are tremendous in number, the assignments of defects-related EPR signals are still under debate. For the signal with $g = 1.956$, that is rather difficult to be detected or overlapping with $g = 1.960$, some authors have suggested several plausible origins. For instance, Wang et al. [127] only detected one EPR signal with $g = 1.954$ in ZnO powders after annealing in air at 1223 K, and its intensity was enhanced with increasing the sintering temperature in a flow of reducing gas (95% N_2 + 5% H_2 in volume), a quite oxygen-poor atmosphere. Hence, they proposed that V_O^+ is responsible for $g = 1.954$ based on the fact that V_O^+ is preferably formed. However, Morazzoni et al. [128] observed two distinct EPR signals at $g = 1.958$ and $g = 1.955$ for ZnO powders recorded at 77 K. They found that the vacuum thermal treatment (still oxygen-poor atmosphere) above 573 K led to the decrease of $g = 1.955$ and dramatic increase of $g = 1.958$. Therefore, they ascribed $g = 1.955$ to Zn_i^+ and $g = 1.958$ to V_O^+. Additionally, Lv et al. [129] found that the intensity of the signal at $g \sim 1.953$ in ZnO whiskers increased significantly after H^+-

implantation. They pointed out that donor defects could be imported via H^+ irradiation, and also the position of signal g~1.960 being independent of the shallow donor identity. They suggested that the signal at g=1.954 was not solely related to Zn_i-related defects but also to Zn_i and complex defects.

Similarly to the origin of green emission, the EPR signal with g ~ 1.960 has become one of the most controversial issues when considering its attribution to a given defect in ZnO. In some cases, the intensity of this signal was shown to increase when the sample is thermally treated in reducing condition, such as thermal treatment in H_2 [130-131] or N_2 [96]. Since under such conditions oxygen vacancies are expected to be favored, many authors have attributed g=1.960 to unpaired electrons trapped in oxygen vacancies [96, 130-131]. Furthermore, it has been also assigned to electrons in the conduction band [132] or delocalized electrons [133]. In the work done by Halliburton et al. [134], where bulk ZnO was annealed in Zn-rich atmosphere at 1373 K, the double integration area of EPR signal at g = 1.96 has increased four times compared to that before annealing. Consequently, they suggested this signal to be related to shallow donors such as Zn_i^+ and / or conduction-band electrons. In the core-shell model, described by Kaftelen et al. [135], in which the type and the concentration of defects in ZnO nanoparticles were tuned through milling performed at cryogenic temperatures, the intensity of g = 1.960 decreased when increasing the milling time. Considering that surface defects should be dominated when reducing the particle size, they ascribed g = 1.960 to bulk defects (more precisely to V_{Zn}^- in bulk).

The assignment of the signal at g ~ 1.995 (or $g_{||}$ = 1.9960, $g_\perp$ = 1.9945) also is less unclear. Since some authors pointed out that the signal g~1.995 could only be observed in the course of light irradiation or illumination, they hypothetically assigned it to oxygen vacancies [136-138]. They assumed that neutral oxygen vacancies initially present in the materials are then transformed by illumination according to:

$$V_O^0 \xrightarrow{h\nu} V_O^+ + e^- \qquad \text{Equation (1.2)}$$

After illumination, the crystal comes back to equilibrium and the opposite process of Equation 1.2 transformed V_O^+ back to V_O^0, therefore, no EPR signal of V_O^+ is present any more. Soriano et al. [137] have also shown that the irradiation was necessary to observe the EPR signal at g = 1.990, and measured its decay after irradiation was turned off. They concluded, thus, that the sensitivity to the light and metastability characters should be associated to oxygen vacancies. Another experimental result which supported the assignment of g ~1.995 to V_O^+ was reported by Liu et al. [139]. They observed an intensity increase of EPR signal at g ~ 2.0, a value very close to ~ 1.995, after ZnO powder was annealed in N_2. Likewise, Choi et al. also found the same behavior of this signal but after annealing in zinc vapor [140].

The identification of defect responsible for EPR signal with g ~ 2.00**x** (**x** = 1, 2, 3...) is also very controversial. Firstly, it resonates close to the value of free electrons (g = 2.002) and some authors adopted such attribution [139, 141]. However, defects including V_{Zn}:Zn_i complex [142] or Zn_i^+ [143] were also linked to it. Besides that, the g ~ 2.003 (or ~ 2.005) represents one component of the rhombic signal specific of superoxides (g_z = 2.047, g_y = 2.009, g_x = 2.003) [144] - which, indeed, can be viewed as one electron in reduced molecular oxygen. The assignment of EPR signals to superoxides is more clear and confirmed by the majority of authors [128, 145-146]. The g_z component of the rhombic signal specific of the superoxide species is very sensitive to the environment and its value can vary from 2.060 to 2.040 – which served some authors to distinguish surface vs. bulk superoxide species. Cope and coworkers [147] have treated the as-synthesized ZnO powder with molecular O_2 and detected EPR signals specific of superoxide (g_z = 2.051, g_z' = 2.042 g_y = 2.009, g_x = 2.003). When the sample was then annealed at 573 K one of the g_z components (g_z = 2.051) was not anymore present in the EPR spectrum. The sensitivity of this signal to the thermal treatment led the authors to conclude that its location must be on the surface. On the contrary, the second g_z component (g_z = 2.042) that was still be detected after the applied annealing treatment, they claimed it should be generated by capturing electrons from donors in the bulk rather than on the surface.

In a word, the assignments of EPR signals differ from one to another depending on the evolution of signals observed under different post-growth treatments. Additionally, the accuracy of the recorded position of the signals also makes the ascription of EPR signals diverse, since some of them are very close. Definitely, combining EPR spectroscopy with other techniques is quite essential to globally understand the nature of the defects in ZnO.

Table 1.2 Typical EPR signals in ZnO systems and their assignments.

g values	**Samples**	**Treatments**	**Assignments**	**References**
g = 1.955	Powder	773 K in vacuum	Zn_i^+	[128]
g = 1.958			V_O^+	
g = 1.954	Powder	1073 and 1323 K in 95% N_2 + 5% H_2 flow	V_O^+	[127]
g = 1.956	Powder	UV illumination	H_i	[148]
g = 1.960			Conduction band electrons	
g = 1.960	Powder	773 and 1073 K, N_2:H_2 = 95:5	V_O^+	[130]
g = 1.960	Powder	773 K in N_2, O_2, N_2/O_2	V_O^+	[96]
g = 1.960	Powder	Electron irradiation	Conduction band electrons	[132]
g = 1.960	Powder	Milled by magnetic shuttling	Core defects (V_{Zn}^-)	[135]
g = 1.960	Powder	1023 K, H_2/Ar	V_O^+	*[131]*

g = 1.96	Bulk	1373 K in Zn vapor for 30 min	Shallow donors and/or conduction-band electrons	[134]
g=1.96	Quantum dots		Delocalized electrons	[133]
g = 1.960	Powder	H^+-implantion	Zn_i and complex defects	[129]
g = 1.960	Powder	Milled by balls	Core defects (V_{Zn}^-)	[135]
g = 1.960	Powder		Delocalized electrons	[149]
$g_{\parallel}$ =1.9960, $g_{\perp}$ =1.9945	Single crystal	Electron irradiation/illumination	V_O^+	[100, 136-137]
g = 2.000	Powder		Free e^-	[141]
g = 2.000	Powder	1173 K in Zn vapor	V_O^+	[140]
g = 2.000	Powder	Milled by magnetic shuttling	Shell defect (V_O^+)	[135]
g = 2.000	Powder	773 K in N_2, 2h	V_O^+	[139]
g = 2.010	Powder		V_O^+	[24]

$g = 2.019$	Powder	1473 K, 2h	$V_{Zn}:Zn_i$ complex	[142]
$g = 2.003$	Powder		Zn_i^+	[143]
$g = 2.004$	Powder	773 K in N_2, 2h	Zn_i^+ or free e^-	[139]
$g = 2.005$	Powder		O_s^-	[144]
$g_z = 2.060$, $g_y = 2.008$, $g_x = 2.003$	Au doped powder	553 K in vacuum; then 473 K in O_2 (P_{O2}= 533 mbar) for 30 min	Superoxides	[146]
$g_z = 2.051$ $g_y = 2.008$ $g_x = 2.002$	Powder	773 K in vacuum	Superoxides	[128]
$g_z = 2.050$ $g_y = 2.008$ $g_x = 2.002$	Powder	Milling	Superoxides	[145]
$g_z = 2.047 \sim 2.043$ $g_y = 2.009$ $g_x = 2.003$	Powder	773 K in vacuum, and then contacting with O_2 at RT	Superoxides	[147]

1.5 Catalytic properties

Due to the simultaneous presence of surface acid (Zn^{2+}) and basic (O^{2-}) sites, zinc oxide is often considered as an amphoteric oxide [150]. This has been revealed by adsorption of basic probe molecules (pyridine, CO) [151] and acidic ones (alcohols, CO_2) [152]. However, studies dealing with catalytic reactivity rather identify zinc oxide as a basic catalyst [153]. The reactivity of ZnO surface towards small molecules used as probe molecules (expected to simply adsorb without being transformed) or reactive ones in model reactions (methanol synthesis) is sometimes discussed in relation with the nature of the crystalline faces preferentially exposed (non-polar (10-10) or polar ones, (0001)-Zn and (000-1)-O) but also surfaces rich in defects [153].

Interaction with CO

It was shown that the interaction of the CO molecule with the polar planes (0001) and (000-1) differs from that occurring on non-polar (10-10) faces [154-155]. CO adsorbs on acidic Zn^{2+} sites, which surrounding and density are different for the three faces. From Electron Energy Loss spectra, Dorn et Lüth [156] showed that the two polar surfaces are modified upon CO adsorption, whereas the polar one is not. Moreover, previous studies indicated that the interaction of CO with the (10-10) face might be irreversible and lead to the formation of CO_2 and an oxygen vacancy. The involvement of oxygen vacancies in the interaction with CO molecules was demonstrated on ex-carbonate and kadox samples [154] and further confirmed by DFT calculations[157-158].

Interaction with CO_2

CO_2 is an acidic molecule likely to interact with basic sites. Microcalorimetry measurements performed on samples pretreated at different temperatures, have shown that CO_2 preferentially adsorbs on non-polar faces [159]. Given the basic properties of ZnO and CO_2 present in the ambient atmosphere, it favorably adsorbs at the ZnO surface and leads to a great variety of carbonates species. These are illustrated by characteristic bands in the 1700 ~1200 cm^{-1} range of infra-red spectra [160]. However, the carbonation state of native ZnO samples that are exposed to ambient atmosphere is quite questionable and may strongly impact the results reported in the literature. To investigate the interaction of CO_2 with ZnO surface, peculiar cautions should be taken: storage of the sample under inert atmosphere, thermal pretreatment to clean up the surface (with the risk of modification of the system). The same remark is still valid for the interaction of water on the surface….

Catalytic reactions

Zinc oxide is studied as heterogeneous catalyst for different types of reactions, among which alcohols conversion and methanol synthesis are very typical [161]. The catalytic activity of polar ZnO surfaces was reported to be higher than the non-polar ones for several catalytic reactions such as methanol synthesis, or decomposition of terminal alkynes[162]. In the case of methanol synthesis, even if a correlation between the conversion levels and the specific surface areas could be established for big crystallites, this correlation is no more valid for smaller particles. It was concluded that the surface reactivity was governed by the ability of the different surface facets toward hydrogen dissociation and hydrogenation of the intermediate adsorbates [162]. It is also underlined that from ethanol synthesis, the (0001) ZnO surface expose the convenient catalytic sites required the hydrogenation of CO and CO_2 [163].

Influence of defects catalytic reactivity

It was proposed that oxygen vacancies are involved in the reaction of methanol synthesis. Boccuzzi et al. described an active site that would be built up of three Zn atoms surrounded by an oxygen vacancy [164]. The oxygen vacancy would weaken the CO bond via an interaction with its oxygen, and thus, it would promote the adsorption and the activation of CO. Oxygen vacancies were also claimed to play a key role in the adsorption of formiate species [165]. Note however that all these studies deal with polycrystalline powders and an additional influence of the morphology on the performances cannot be ruled out.

In order to evaluate the influence of defects on the catalytic reactivity of zinc oxide, without any misleading effect related to its morphology, a recent study was undertaken in the Laboratoire Réactivité de Surface. In this study, the pretreatment of the catalysts was strongly controlled (i.e. the composition of the atmosphere was varied) [166]. The results unambiguously implied to an influence of the oxygen vacancies on the catalytic conversion of alcohols (2-methyl-3-butyn-2-ol (MBOH) and ethanol) since a correlation between the basic reactivity and the concentration of oxygen vacancies (measured by EPR) was obtained. However, considering that no discrimination between oxygen vacancies present in the surface and in the bulk could be achieved, oxygen vacancies were not claimed to be directly involved as active sites, but were proposed to enhance the basicity of the O^{2-}ions, via the release of electrons associated to the formation of oxygen vacancies [166].

1.6 Summary

Up to now, it has been reasonably accepted that the key properties of ZnO may depend not only on intrinsic properties such as the particular crystal structure, particle size and morphologies, but furthermore on their defect structure. Therefore, it is extraordinarily important to identify the defects present both on the surface and in the bulk. Although considerable efforts were made over the past decades, the identification of intrinsic defects by correlation to corresponding emissions in the visible region and / or EPR signals are still under debate. The unachieved consensus on the origin of almost all PL / EPR signals reported in the literature is mostly due to the variety of studied ZnO samples – including samples forms (thin films, single crystals, nanopowders), morphologies, surface orientations, synthesis methods, post-growth treatments as well as the measurement conditions such as temperature and pressure. All of these factors separately or interconnectingly lead to the uncertainty of defects identification

1.7 Motivation and goal

The aim of this Ph.D. thesis is to provide a deeper understanding of the nature and quantity of defects present both on the surface and in the bulk of ZnO nanoparticles. To overcome some difficulties encountered in the literature, in this Ph.D. thesis dealing with the investigation of ZnO defects, firstly the synthesis of ZnO nanoparticles were chosen as such to avoid extrinsic samples contaminations. Besides, ZnO nanoparticles are used as a model particle system to identify the defects through the changes introduced by synthesis methods, synthesis conditions. Secondly, all the samples, before and during the measurements, were constantly kept under high-vacuum conditions. Annealing treatments were performed with the dual aim: to clean the particles surface (to access surface defects) and to specifically create defects favored in a given post-growth treatment. The necessary path to achieve this objective was to investigate the defects at each following step:

i. As-synthesized ZnO nanoparticles of different origins (by dealing with different synthesis approaches or by controlling certain types of parameters within given synthesis technique)
ii. Under specific post-growth conditions (by annealing ZnO nanoparticles in reducing or oxidizing atmosphere, presence of zinc)
iii. In terms of the reactivity of defects toward molecular probes (by exposing as-synthesized or post-growth treated ZnO nanoparticles to controlled concentration of O_2 and H_2O).
iv. In terms of catalytic behavior of selected samples towards methylbutynol (MBOH) model reaction.

The spectroscopic techniques applied in this work to characterize ZnO nanoparticle are the following:

- Transmission Electron Microscopy (TEM): characterization of structure and morphology
- Powder X-ray diffraction: crystallinity and crystalline size
- Diffuse Reflectance UV/Vis Spectroscopy: determination of band gap energy and the selection of electronic excitation energy
- Photoluminescence (PL) Spectroscopy: characterization of optical properties
- Infrared (IR) Spectroscopy: Characterization of reactive surface sites reacting with molecular probes
- Electron Paramagnetic Resonance (EPR) Spectroscopy: Characterization of paramagnetic species

The strategy is schematically presented in the Figure 1.12. After this chapter dealing with the state of the art, the second chapter will be devoted to the experimental section. The results obtained from the synthesis of the smoke sample (combustion in air) will be reported in the third chapter whereas, influence of the synthesis parameters or method (P_{O2} partial pressure in combustion method and CVS method) on the defectiveness of ZnO samples will be discussed in the fourth chapter. Finally, we will present a general discussion and conclusion.

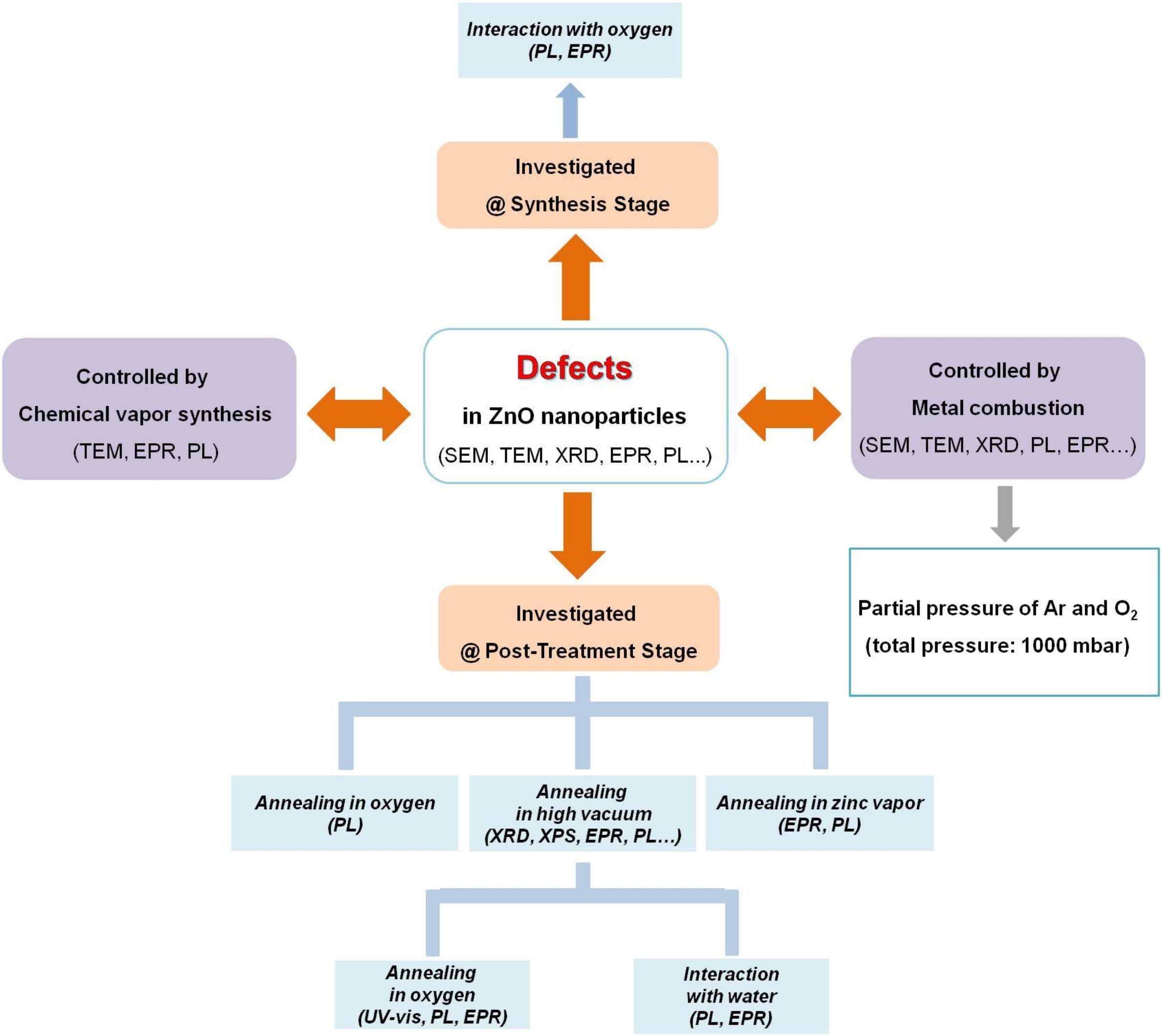

Figure 1.12 Schematic representation of this Ph.D. thesis

Chapter 2: Experimental section

This chapter is devoted to the description of the synthesis methods of ZnO, the post-growth treatments applied and the main characterization techniques. The related apparatus and setups that were used in this work are also described.

2.1 Synthesis of ZnO samples

Two synthesis methods are used within the present work for the production of ZnO samples: metal combustion and chemical vapor synthesis methods. The two fundamentally similar fabrication methods are based on the oxidation reaction of metals in the vapor phase, as illustrated by Equation 2.1. In our case, metallic Zn is first evaporated into the gas phase, where it reacts then with the surrounding oxygen molecules to form monomeric ZnO. In the next step, the critical nuclei of ZnO is generated via clustering of previously formed monomers and when the ZnO vapor supersaturation exceeds a critical value [51], the solid ZnO particles are finally obtained through the condensation.

$$\text{Zn (s)} \xrightarrow[\text{Evaporation}]{\triangle} \text{Zn (g)} \xrightarrow[\text{Oxydation}]{+\,\text{O}_2\text{ (g)}} \text{ZnO (g)} \xrightarrow[\text{Condensation}]{\text{RT}} \text{ZnO (s)} \qquad \text{(Equation 2.1)}$$

The details about these two methods are described in the following sections.

2.1.1 Metal combustion

Metal combustion is a fast way to produce ZnO nanoparticles with high purity. This synthesis requires a thermal activation to partially evaporate metallic zinc which finally leads to the oxidation reaction to start. Thereafter, the heat required for the following metal evaporation is produced *in situ* by combustion reaction itself. In other words, metal combustion is a type of self-propagating reaction.

At the INSP, a home-made stainless steel chamber is used for the combustion of metals in the air or in a controlled atmosphere (O_2 / Ar mixture). The chamber, which is connected to a primary vacuum pump and equipped with two gloves, represents a glove box which maintains a vacuum (~ 0.1 mbar) and allows for powders to be collected without their exposure to air. The oxygen and argon bottles are connected to the chamber and several gauges are fixed to control the whole pressure of the system as well as the partial pressure of oxygen. The representative photo of the chamber is given in Figure 2.1 (a). For samples produced under controlled conditions, the glove box was pumped before applying the voltage. Once the pressure was achieved to be ~ 0.1 mbar, the pump was switched off, and only argon was introduced into the chamber up to a pressure of 1 bar. Cycling inflation and deflation steps for three times were essential to efficiently purge the glove box from any traces of air. After this preparation, the chamber was again pumped to the pressure ~ 0.1 mbar and a given ratio of argon and oxygen was introduced for a total pressure of 1 bar.

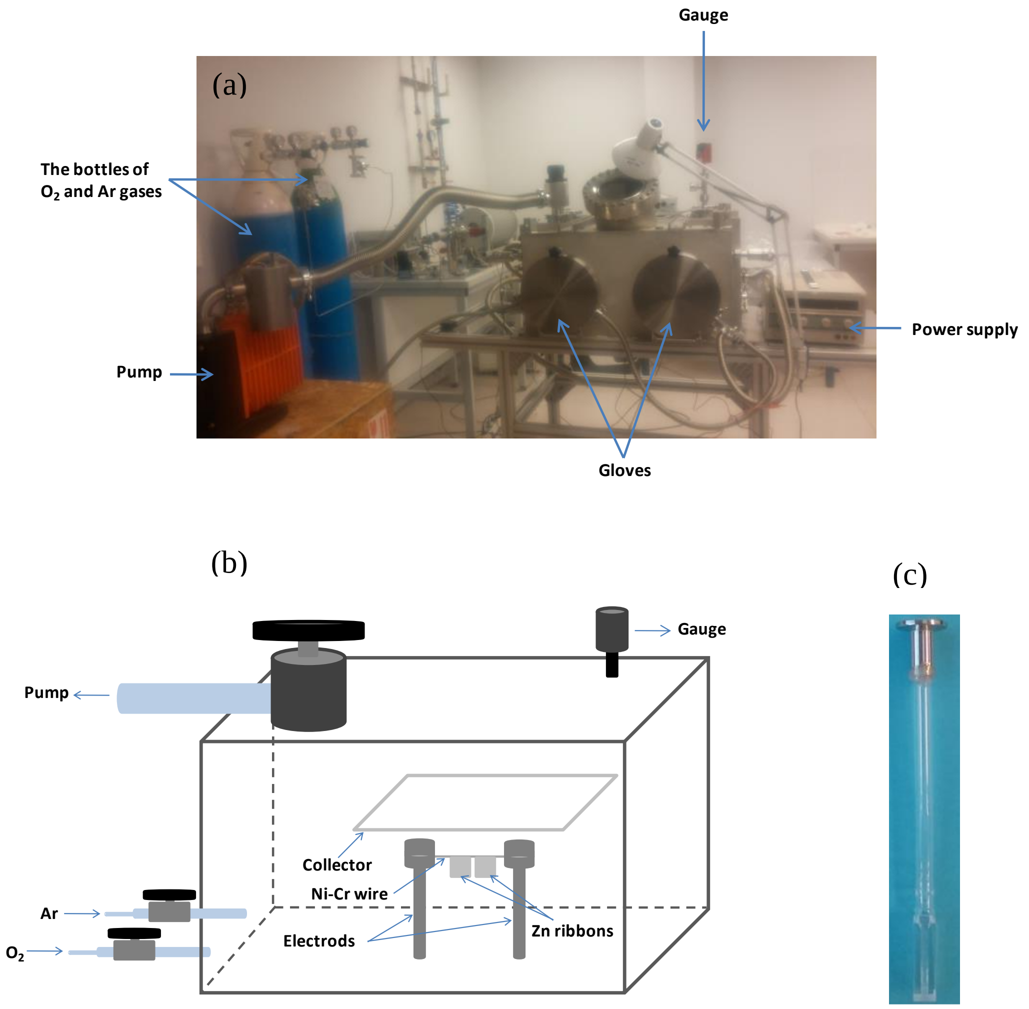

Figure 2.1 The photo (a) and schematic diagram (b) of the glove box for the synthesis of ZnO smoke by metal combustion. (c) The photo of quartz-glass cells for storage of ZnO powders.

Two electrodes are inserted inside the glove-box (Figure 2.1(b)) and connected with a thin Ni–Cr wire (20% Cr, 80% Ni, Goodfellow) which is held in contact with an extremity of the Zn ribbon (m ≈ 0.1 g). Then by increasing the electrical power, the ribbon is resistively heated in air or an O_2 / Ar atmosphere and the powder is produced and collected by a glass plate placed above the zinc ribbons, and finally transferred into quartz-glass cells (Figure 2.1 (c)). Such type of cells is used for the further optical measurements and also for the storage under dynamic ($P \leq 10^{-5}$ mbar) or static vacuum. This is essential for highly dispersed ZnO powders which, if exposed to the air, react instantly with water or other molecules (CO_2, CO, H_2, organic compounds). Such an exposure would result in a strong alteration of their native properties and may strongly affect the interpretation of results.

2.1.2 Chemical vapor synthesis

Although metal combustion is a fast way to produce ZnO nanoparticles, it has several shortcomings such as the incomplete burning (i.e. oxidation) of metal precursors, the heterogeneity of the products in terms of morphology and size as well as the difficulties in controlling the reaction parameters. Chemical vapor synthesis can strongly overcome some of the issues above, especially in terms of controlling the reaction conditions.

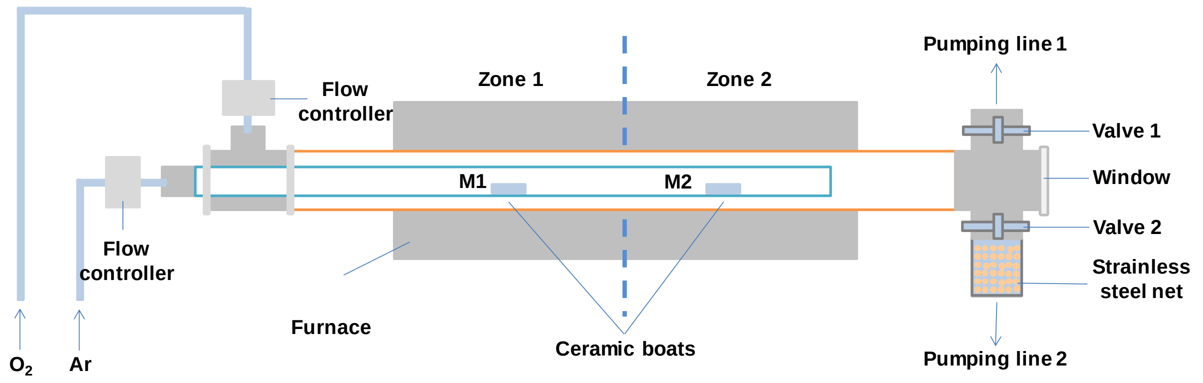

Figure 2.2 Schematic representation of the flow reactor used for chemical vapor synthesis

The chemical vapor synthesis occurs in a flow reactor (Figure 2.2) that consists of a horizontal tube furnace, a quartz glass tube (inner tube) inserted inside another quartz glass tube (outer tube) connected to argon and oxygen, respectively. The temperature distribution of the furnace (zone 1 and zone 2) was fully characterized and stable within ca. ± 5 °C. A typical synthesis of ZnO powders was performed as follows: Zn foil (m = 6g) was evenly divided and placed into ceramic boats A and B, which were positioned in the middle of zone 1 and zone 2, respectively. Then the system was pumped (pressure ~ 1 mbar) in order to remove most of the air from the system. Finally, a flow of high-purity argon (> 99.999 %, Air Liquid) was first purged into the inner tube for several minutes till a homogeneous atmosphere was reached, and then oxygen (> 99.995 %, Air Liquid) was injected into the outer tube. The pressure of the system was controlled by valve 1 at a constant value of ~ 50 mbar. Afterwards, the tube furnace was heated with a rate of 30 K· min^{-1} up to the evaporation temperature of a given Zn vapor pressure (Figure 2.3). Zinc vapor was then transported by argon flow through the inner tube into the reaction zone in which oxygen was introduced through the flow from the outer tube. ZnO powder was collected within the stainless steel net for 1 h. Then the furnace was switched off, and the system was allowed to naturally cool down to room temperature in a flow of argon. Finally, the powders were collected and transferred into the quartz-glass cells (shown in Figure 2.1 (c)) connected to dynamic vacuum ($P \leq 10^{-5}$ mbar).

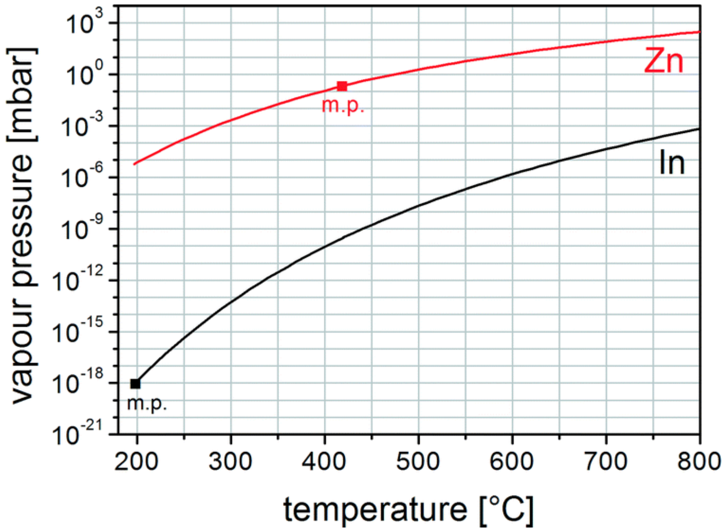

Figure 2.3 Diagram of vapor pressures for Zn and In at 200 ~ 800 °C (473 ~ 1073 K) temperature range [167]

2.2 Post-growth annealing treatments

As mentioned in Chapter 1, the experimental conditions applied during the spectroscopic measurements of ZnO are usually not well described in the reported literature. This may perfectly explain a broad spectrum of discrepancies in the identification of corresponding spectroscopic features coming from different working groups. Indeed, adsorbates that may be naturally present in the environment (CO_2, carbonates, H_2O, organic compounds) as well as additional thermal treatments may strongly impact the distribution of the native properties of the material under investigation. To avoid this, for all ZnO samples that were subject to the investigation and whose results are presented in this thesis we have adopted the following rules:

i) samples produced under controlled conditions are collected in an inert atmosphere and their exposure to air is strongly avoided

ii) samples are kept under dynamic high vacuum during all measurements

iii) annealing treatments in high-vacuum and / or O_2 were applied prior to spectroscopic measurements

The thermal treatments in vacuum and oxygen were performed following the sequence described in Figure 2.4:

i) Starting from the evacuation down to 10^{-5} mbar, the sample was annealed under vacuum up to 773 K at a rate of 2 K min^{-1}, and maintained at this temperature for 1 h then cooled down to 298 K (step 1) by removing the oven in order to remove all the species (such as hydroxyl groups and carbonates) unintentionally adsorbed on the surface. After this stage, vacuum annealed sample was obtained and ready for the next spectroscopic measurements.

ii) The annealing in O_2 was performed in the presence of 100 mbar of oxygen. Oxygen was introduced at 773 K after the sample was previously annealed under vacuum in the same manner as described in i). After 30 min of the annealing, the sample was finally cooled down to room temperature by removing the oven in presence of oxygen (step 2). After such treatment, oxygen reannealed sample was pumped to $P< 10^{-5}$ mbar and ready for further characterizations such as PL and EPR.

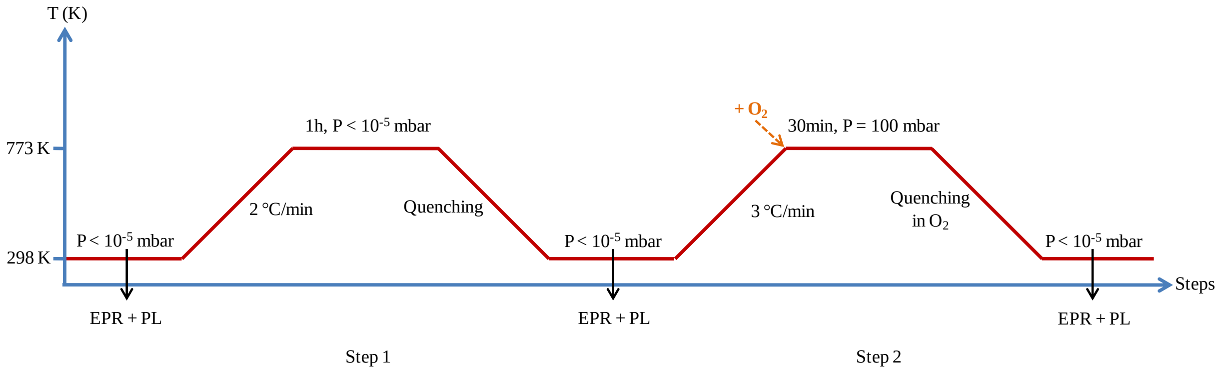

Figure 2.4 Thermal profile of successive steps indicating the nature of the atmosphere and including the steps of measurements.

Annealing in zinc as a reducing post treatment (or oxygen-poor condition) is widely performed to create specific defect. As a result, it could be a complementary experiment to indentify the type of defects in ZnO. Annealing in presence of metallic zinc was additionally performed in the following way: first, a certain amount of Zn (~ 50 mg) was admixed to ZnO powder and pumped to ~ 10^{-5} mbar. Then it was annealed up to 773 K in a static condition with the same rate as that applied in vacuum annealing. After maintaining at this temperature for 1 h, the sample was cooled down to room temperature freely. Finally, the sample was again pumped in dynamic vacuum ($P < 10^{-5}$ mbar) being then ready for the spectroscopic characterizations.

2.3 Photoluminescence (PL) spectroscopy

PL spectroscopy is one of the most important and useful techniques for the study and characterization of optical properties of the materials. It is a very sensitive and non-destructive technique for probing the electronic structure of materials and can be used to: 1) determine the band gap energy; 2) provide the understanding of the radiative recombination mechanisms; 3) identify the defect and impurity levels; 4) assess the crystalline quality of the materials; 5) investigate the surface and interface properties.

Basic principles of photoluminescence

The photoluminescence is the phenomenon of the emission of electromagnetic radiation due to the external photoexcitation of material. The light is directed onto a sample, where it is absorbed and imparts excess energy into the material within the process called photo-excitation. One way to release this excess energy by the sample is through the emission of light, or luminescence.

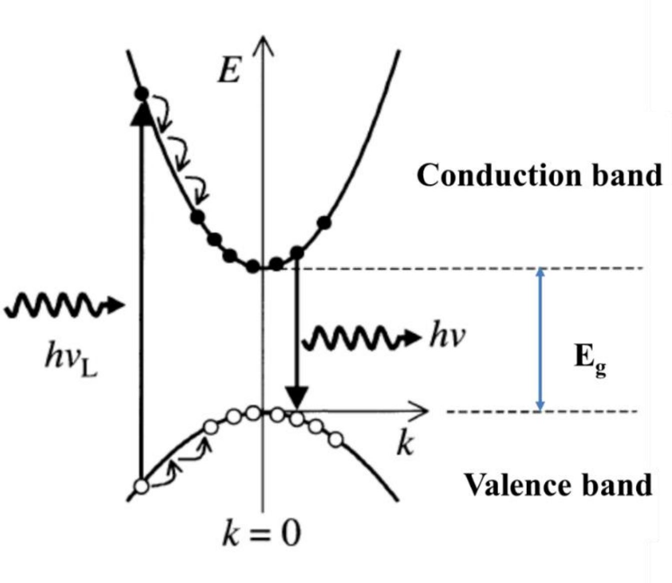

Figure 2.5 Schematic diagram of process occurring during PL in a direct band gap semiconductor after excitation with frequency ν_L.

When a direct semiconductor is excited with a light-source (Xe-lamp, laser) providing photons with energy ($h\nu_L$) that is beyond the bandgap energy (E_g), an electron is excited from the valence band into the conduction band. Consequently, a hole in the valence band is generated. This is considered as the formation of an electron-hole pair. Afterwards, the excited electron will return to the equilibrium state by emitting light (Figure 2.5). The energy of the emitted light is related to the difference in energy levels between the two electron states involved in the transition between the excited state and the equilibrium state. The return to equilibrium state is known as recombination, and may include both radiative and non-radiative recombination processes.

Radiative recombination

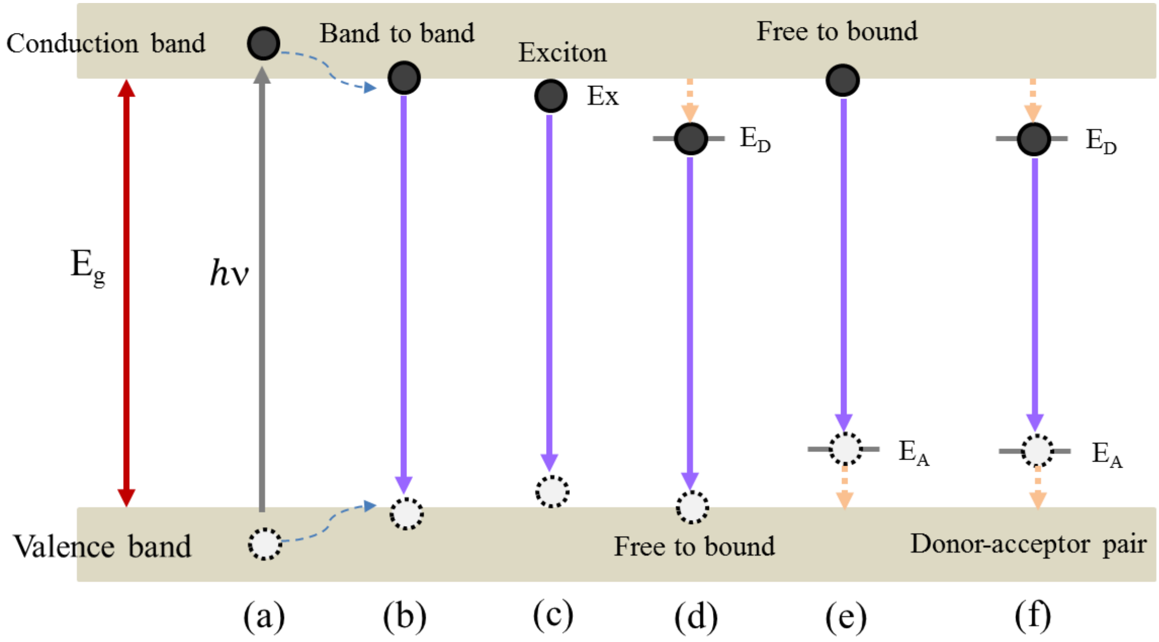

Figure 2.6 Schematic diagram of the radiative recombination in photoluminescence process. (adapted from Anantachaisilp's PhD thesis[168])

There are six principle pathways that may occur within the PL process:

(a) Excitation occurs via absorption of a photon (hν)
(b) Band to band recombination
(c) Exciton recombination
(d) Free to bound: free hole to donor bound electron
(e) Free to bound: free electron to acceptor bound hole
(f) Donor-acceptor pairs

where E_g is the bandgap of the material, E_x is the exciton binding energy, E_D is the binding energy of the donor levels as measured from the bottom of the conduction band, and E_A is the binding energy of the acceptor levels as measured from the top of the valence band.

The process of electron-hole recombination in which energy is released in the form of emitted photon, is called radiative recombination. The common channels of radiative recombination in PL process are schematically shown in Figure 2.6, and discussed below:

I. Band-to-band recombination (Figure 2.6 (b))

The electron in the conduction band directly recombining with the hole in the valence band is owing to the band-to-band recombination (Figure 2.6 (b)). This recombination yields the highest energy radiation corresponding to the bandgap of the semiconductor. It can be observed at room temperature, and can be used to estimate the bandgap energy (E_g) of semiconductors.

II. Exciton recombination (Figure 2.6 (c))

When the concentration of defects in a semiconductor is sufficiently low, in other words, the quality of the semiconductor is high, the photoexcited electrons and holes are attracted to each other by Coulomb interaction to form electron-hole pairs, so called free excitons. However, if a semiconductor contains a low concentration of donor- or acceptor-defects, the photoexcited electrons and holes are not only attracted to each other via Coulomb interaction, but also by defects via the van der Waals interaction at low temperature. The additional attraction lowers the exciton binding energy, and the defects are efficient in trapping excitons to form bound excitons. For neutral donor and acceptor bound, it is denoted by D^0X and A^0X, and for ionized donor and acceptors, by D^+X and A^-X, respectively.

When the free electron-hole pair recombines, it emits light photon energies slightly below the energy of the band-to-band recombination. The emitted photon energy can be expressed by Equation 2.2:

$$h\nu = E_g - 2\pi^2 m^* e^4 / h^2 \varepsilon^2 n^2 \qquad \text{(Equation 2.2)}$$

where m^* is the reduced effective mass of the electron-hole pair, h is the Planck constant, ε is the dielectric constant of the solid, and n is an integer indicating the various allowed states of the free excitons. The observation of free-excitons is limited for semiconductors with a small exciton binding energies (such as in GaAs) at low temperatures. However, for large exciton binding energy, recombination from free-excitons is observed even at room temperature, such as in the case of ZnO [169]. Excitons are bound to the defects and subsequently recombine within the process called bound exciton recombination. The recombination of bound excitons typically gives rise to sharp lines with a photon energy characteristic of each defect. For example, Figure 2.7 shows 10 K PL spectrum of p- and n-type of ZnO nanowires, and the emissions positioned at 3.350 and 3.360 eV were related to the recombination of excitons bound to neutral acceptors and donors, respectively [170].

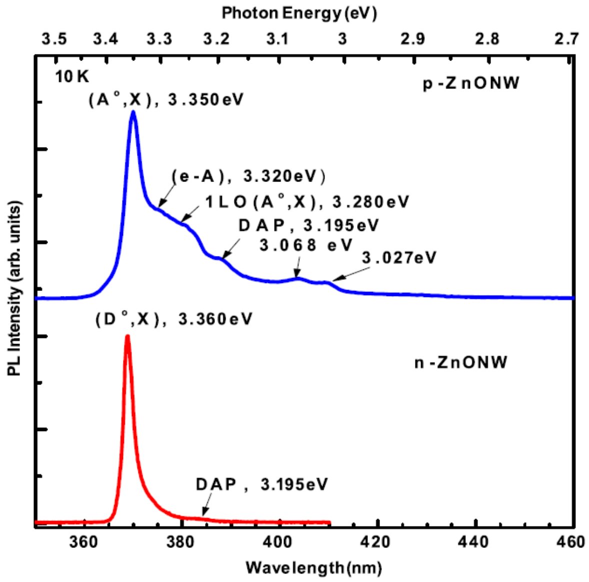

Figure 2.7 Photoluminescence spectra recorded at 10 K of the as-grown p-ZnO nanowires showing a dominant peak of a neutral donor-bound exciton (blue curve) and arsenic-doped n-ZnO nanowires showing a dominant peak of a neutral acceptor-bound exciton (red curve) [170].

III. Free-to-bound recombination (Figure 2.6 (d) and (e))

If defects are present in a crystal at sufficient low temperature, carriers (holes or electrons) can be trapped in them. For instance, in the case of p-type semiconductor containing N_A acceptors per volume unit, the number of free electrons created by photoexcitation in the conduction band is much smaller than the number of N_A, so, free electrons can recombine radiatively with the holes trapped on acceptors, which leads to photo-emission. This process is known as free-to-bound recombination (Figure 2.6 d, e). In the case of the recombination between electron and valence band, the approximate energy of emitted photon can be given by: $h\nu = E_g - E_A$, where E_A is the binding energy of acceptor. For the case that free holes recombine with electrons trapped on donors, the equation can be written as $h\nu = E_g - E_D$, where E_D is the binding energy of donor. Hence, characterization of the emission from free-to-bound is a common method of measuring the binding energy of impurities or defects.

IV. Recombination of donor-acceptor-pairs (Figure 2.6 (f))

In general, semiconductor may contain both donors and acceptors. In order to satisfy equilibrium conditions, some of the electrons from the donors will be captured (or compensated) by the acceptors giving rise to both ionized donors (D^+) and acceptors (A^-). After optical excitation, electrons and holes can be created, and then trapped at the D^+ and A^- to form neutral donors (D_0) and acceptors (A^0). When returning to equilibrium condition, some of the electrons in D_0 will recombine with holes in A^0. This process is called a donor-acceptor pairs (or DAP) recombination (Figure 2.6 f). It can be represented by the reaction below:

$$D^0 + A^0 \rightarrow D^+ + A^- + h\nu \qquad \text{(Equation2.3)}$$

The emission energy of this luminescence depends on the spatial separation between the donor and the acceptor in a pair, so the emitted photon energy can be given by:

$$h\nu = E_g - E_A - E_D \qquad \text{(Equation2.4)}$$

However, in this equation, the Coulomb interaction between the ionized donors and acceptors is neglected. Hence, the energy of the emitted photon in a DAP recombination needs to consider also the Coulomb energy that is equal to $-e^2/(\varepsilon R)$, and it is rewritten by:

$$h\nu = E_g - E_A - E_D + e^2/(\varepsilon R) \qquad \text{(Equation 2.5)}$$

where ε is the dielectric constant of the solid and R is the distance between D^+ and A^-. Figure 2.8 illustrates the PL spectra of as-grown ZnO nanorods DAP pairs (~3.324 eV) in a series of temperature-dependent PL spectra of ZnO nanorods arrays [171].

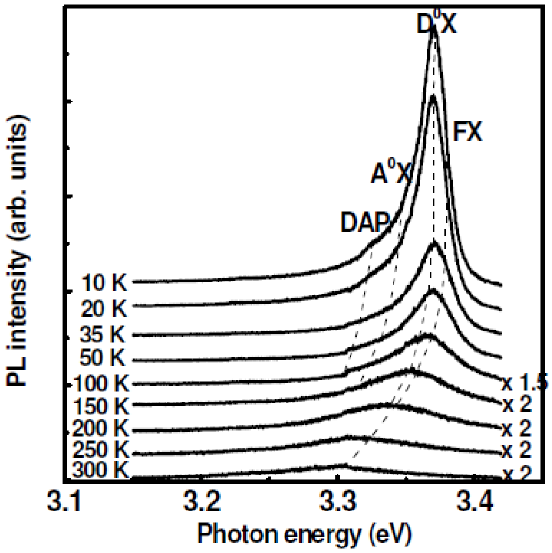

Figure 2.8 Temperature-dependent PL spectra in the near band edge region taken from as-grown ZnO nanorods [171].

Non-radiative recombination

The emission of light is the result of a radiative recombination, while non-radiative recombination involves the transformation of the absorbed electronic excitation energy into any types of energy except light. There are three basic ways to how the excitation energy can be non-radiatively dissipated: (i) transformation into heat, which comprises multiphonon non-radiative recombination, surface recombination and Auger recombination, (ii) recombination on the surface states including dislocation and stacking faults, and agglomerative boundary that can give rise to continuum of states in the band gap, through which electrons and holes non-radiatively recombine [172], (iii) transforming the excitation energy into photochemical changes of the material.

Quenching of PL intensity

Many factors can affect the PL intensity. Generally, an increase of the concentration of luminescence centers is proportional to the emitted light intensity in a semiconductor. However, a number of processes can lead to a quenching of PL intensity, such as excited state reactions, energy transfer, complex-formation and collisional quenching [173].

Two quenching processes are usually encountered:

(1) Dynamic (collisional) quenching: it occurs when the excited luminescence centers experience contact / impact with an atom or molecule that can facilitate non-radiative transitions to the ground state. One of the best-known collisional quenchers is molecular oxygen, which quenches almost all known emitters.

(2) Static (complex formation) quenching: it takes place when an adsorbed complex is formed between adsorptive sites and the emitters.

Apparatus: The schematic diagram of a classic photoluminescence spectrometer which essentially contains an optical source, two monochromators (at the excitation and emission sides), detectors and a computer for acquiring data, is shown in Figure 2.9.

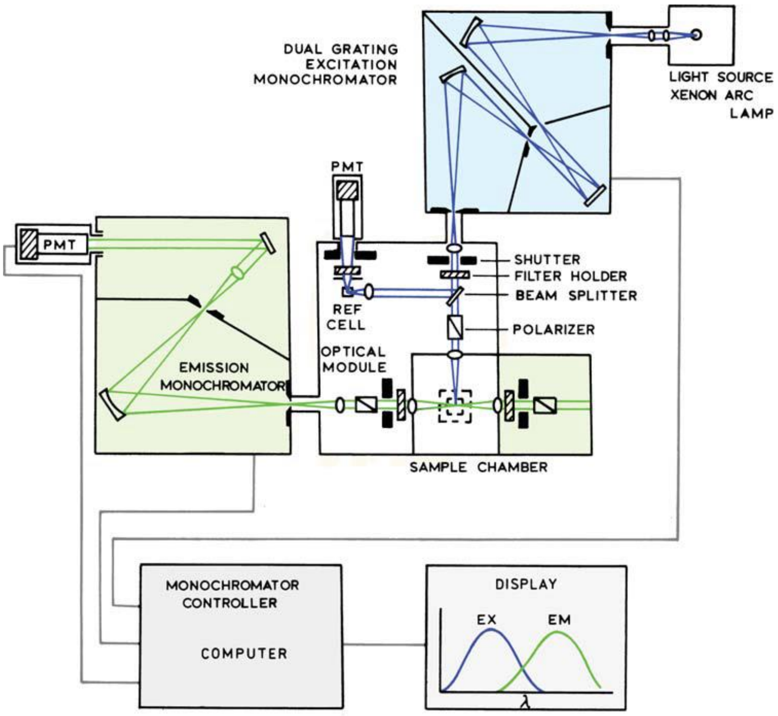

Figure 2.9 The schematic representation of a PL spectrometer [173].

PL results presented in this thesis were obtained with a Fluorolog 3 photoluminescence spectrometer (Jobin-Yvon Horiba Inc.), which is composed of:

- A Xenon lamp as an excitation source of 450 W that givesat 5.17 eV (240 nm) a sufficient quantity of photons in UV-visible.
- Two double monochromators to cut the stray light from the light source.
- A detector which is a photomultiplier Hamamatsu R928.

In addition, during PL emission measurements an optical filter is placed on the emission side in order to eliminate the contributions of the second-order of the excitation light. In this work, filter WG360 is used for the emission side. It is a long pass filter, which means more than 50% light of wavelength larger than 360 nm can pass through this filter seen from the its transmittance spectrum in Figure 2.10. The values of the excitation and emission slit widths corresponding to a good resolution were chosen to be 1.5 nm.

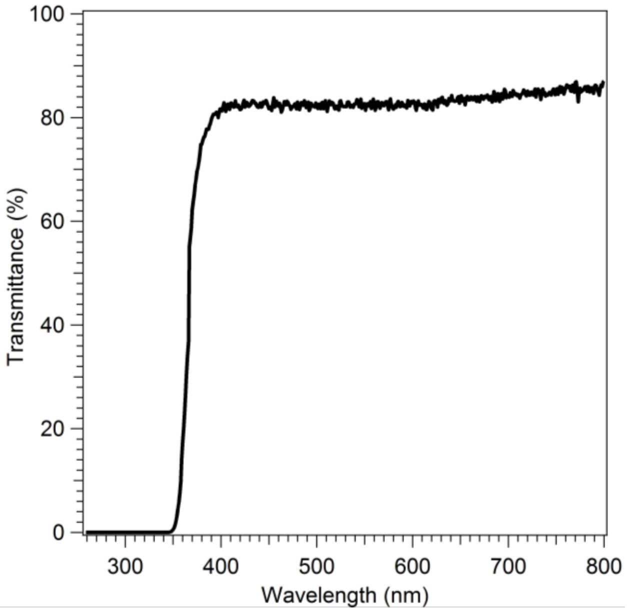

Figure 2.10 Transmittance spectrum of filter WG360 applied at the emission side

Band Fitting

Normally, PL signal data recorded from a spectrometer in intervals of wavelength are often plotted in energy units, especially in materials science. However, this noting is not sufficient in some cases. For the quantitative analysis of luminescent nanomaterials, PL spectra are often presented as a function of energy. The conversion of a value from wavelength to energy proceeds via:

$$\mathrm{E} = \frac{hc}{\lambda} \qquad \text{(Equation 2.6)}$$

If the recorded signal is considered as a function *f* (λ), then considering conservation of energy

$$f(\mathrm{E})\mathrm{dE} = f(\lambda)\mathrm{d}\lambda \qquad \text{(Equation 2.7)}$$

Combining equation (1) and (2), *f* (E) can be presented by the following

$$f(\mathrm{E}) = f(\lambda)\frac{d\lambda}{dE} = f(\lambda)\frac{d\left(\frac{hc}{E}\right)}{dE} = -f(\lambda)\frac{hc}{E^2} \qquad \text{(Equation 2.8)}$$

This presentation of raw data provides better physical insight and may facilitate better quantitative analysis of the excited state of a system, therefore, the band fitting analysis is based on the conversion of PL raw data from wavelength to energy in this work.

2.4 Electron paramagnetic resonance (EPR) spectroscopy

Electron Paramagnetic Resonance (EPR), also called electron spin resonance (ESR), is a widely used and sensitive spectroscopic technique to study paramagnetic systems containing at least one unpaired electron. These include radicals, transition metal ions, conduction electrons and defects in solids.

Basic Principles of EPR

The electron possesses an orbital angular momentum, **L,** as it moves around the nucleus, and also an intrinsic angular momentum called “spin”, denoted as **S**. As a vector, **S** contains its components along the x, y, and z axes represented by S_x, S_y and S_z, respectively. By restricting the dimension to only one component, S_z can be measured certainly, and then the component of the spin angular momentum can be assumed in $\hbar(= h/2\pi)$ units as:

$$S_z = M_s \hbar \qquad \text{(Equation 2.9)}$$

where M_S is the secondary spin quantum number. M_S can have 2S+1 different values: –S, –S+1, …, S–1, S. As the possible values of M_S differ by one and range from –S to +S, the only two possible values for M_S are +1/2 (also called α state) and –1/2 (β state) for a single unpaired electron. The magnetic moment μ_e of the electron is proportional to S. μ_e and S are vectors parallel to each other. One may be expressed as:

$$\mu_e = -g\mu_B S \qquad \text{(Equation 2.10)}$$

where g is a scalar called the Landé factor (or simply the g-factor). For a free electron, $g = g_e \approx 2.002319$. μ_B (also noted as β_e) is the atomic unit of magnetic moment called Bohr magneton, with $\mu_B = |e|\hbar/2m_e = 9.274 \cdot 10^{-24}$ J·T^{-1}

In the absence of external magnetic field, the magnetic moments (μ_e) of negatively charged electrons are oriented randomly. When an external magnetic field (B) is applied, electron magnetic moments become oriented towards the field and the energy difference is generated depending on the value of spin magnetic moment: this is called **Zeeman effect**. The Zeeman effect is represented graphically in Figure2.11. In classical terms, the energy of the interaction between the magnetic moment, μ_e, and the external magnetic field, B, is given by:

$$E = -\mu_e \cdot B = g\,\mu_B S \cdot B \qquad \text{(Equation 2.11)}$$

Combined with quantum mechanical theory, the energies of the two allowed orientations of the spin are therefore:

$$E_{\pm} = \left(\pm\frac{1}{2}\right) g\,\mu_B \cdot B \qquad \text{(Equation2.12)}$$

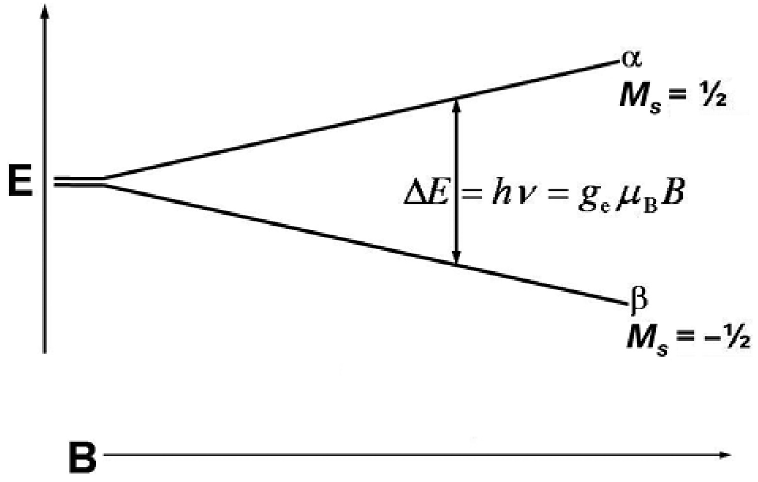

Figure 2.11 Energy levels for an electron spin (S = ± 1/2) in an applied magnetic field B.

g-factor

If a system of unpaired electrons in a magnetic field is submitted to an electromagnetic radiation, a transition from the low energy state (β state) to the high energy state (α state) will take place when the energy quantum of the radiation, hν, exactly coincides with the energy difference between the α and β states (ΔE):

$$\mathrm{h}\nu = \Delta \mathrm{E} = E_\alpha - E_\beta = \mathrm{g}\ \mu_B B \qquad \text{(Equation 2.13)}$$

where ν is the radiation frequency. Equation 2.13 is the fundamental equation of EPR spectroscopy. Since μ_B is a constant and ΔE and the magnitude of B can be known from the applied microwaves with a set frequency and the applied magnetic field, respectively, the value of g-factor can be calculated from ν and B by using,

$$g = \frac{h\nu}{\mu_B B} \qquad \text{(Equation2.14)}$$

In a real chemical system, the electron is not free but bound to one or more nuclei. Considering the simplest case of an atom with a closed electronic shell and an extra electron, the electron angular momentum has two contributions: one arises from the electron spin itself, and another one arises from the orbital motion of the electron around the nucleus. Therefore, the total magnetic moment is the sum of two terms and can be expressed by the equation:

$$\mu_e = \mu_B L + g\mu_B S \qquad \text{(Equation 2.15)}$$

where L is the orbital angular momentum.

Analogous to the spin angular momentum, the component of L along z direction may assume only (2L+1) quantized values: −L, −L+1, …, L. The equation 2.15 would be correct only if the spin angular momentum and orbit angular momentum were independent of each other. Indeed, they are coupled via the spin–orbit coupling. Hence, equation 2.15 can be rewritten by

$$\mu_e = g\mu_B S + \text{spin-orbit coupling contribution} \qquad \text{(Equation 2.16)}$$

Considering an electron in an atom with spherical symmetry, the orbital angular momentum is quenched (its average is zero), in this case, the electron angular momentum is only due to spin. However, molecules in real chemical systems are of low symmetry. The effect of spin–orbit coupling can thus restore a small amount of orbit contribution, which results in a deviation $\Delta g = g - g_e$. Since Δg depends on the spin–orbit coupling, it could give important structural information, as well as information about the radical environment.

Line shape and symmetry

The spin–orbit interaction is related to the angular momentum, therefore, it is anisotropic, which indicates that the amount of orbital character in the angular momentum is different for the different directions in a molecule. As a result, the measured g-factor will depend on the direction of the magnetic field with respect to the molecular axes. In liquids or gases, the g-factor anisotropy is averaged out due to molecular motion and a mean g value (g_{iso}) is measured. In single crystals, molecules are in fixed orientations, so the anisotropy of g can be measured by rotating the crystal in the spectrometer's magnetic field. In the case of powder samples a large number of microcrystals are oriented randomly in space, so powder EPR spectra which result from the superposition of spectra of all microcrystals orientations are often more complex than spectra of single crystal materials, liquids or gases. Idealized ESR patterns, together with their corresponding absorption profile, are given in Figure 2.12. The anisotropy in g is classified into isotropic ($g_x = g_y = g_z = g_{iso}$), axial ($g_x = g_y \neq g_z$ often referred to as $g_z = g_{||}$ (parallel to the axis) and $g_x = g_y = g_{\perp}$ (perpendicular to the axis)) and rhombic ($g_x \neq g_y \neq g_z$) depending on the symmetry of the paramagnetic centers.

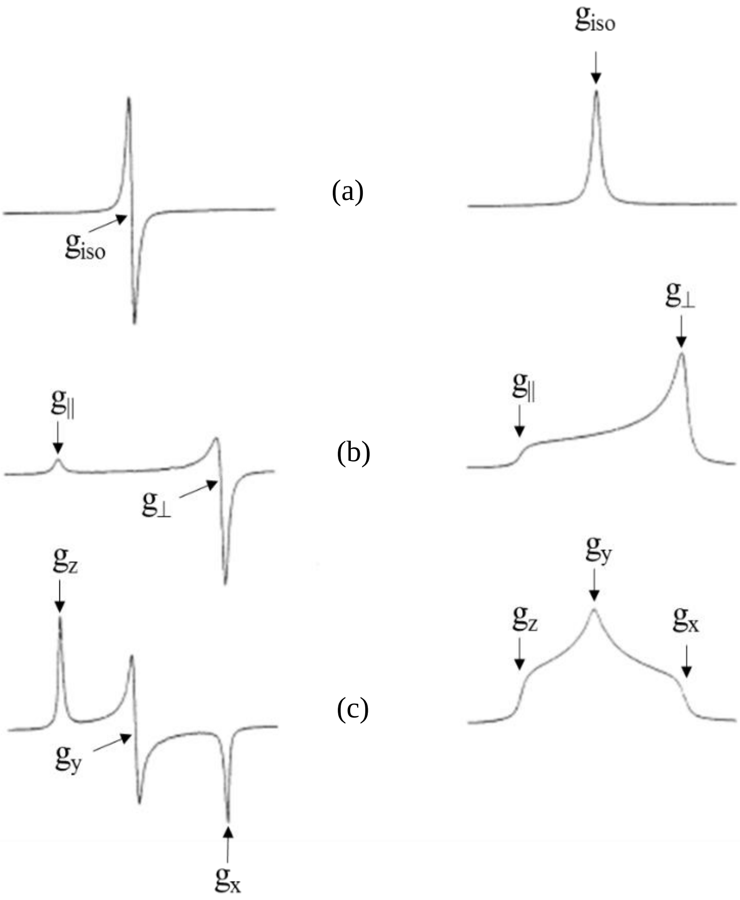

Figure 2.12 Idealized powder ESR patterns as first derivative of the absorption with respect to the magnetic field (left) together with their corresponding absorption profile (right): a) isotropic; b) axial (with $g_{||} > g_{\perp}$) and c) rhombic [174]

Line intensity

The intensity of EPR signal is, at first, proportional to the concentration of paramagnetic centres in the sample. In the language of EPR spectroscopy, the intensity of the signal is defined as the integrated area beneath the absorption curve or as the double integration of the

EPR signal as seen in Figure 2.13. Yet, EPR signal intensity does not only depend on concentrations but also on (i) the microwave power and (ii) the measurement temperature:

(i) applying a suitable microwave power, the signal intensity is proportional to the square root ofthe microwave power. Yet, when higher power level is applied, the signal may grow more slowly, or even diminish, as well as broaden. A quick means of checking the absence of saturation is to decrease the microwave power and verify that the signal intensity decreases proportional to the square root of the microwave power.

(ii) For the species that obey the Curie law (absence of saturation effect), the signal intensity is proportional to 1/T with T in K. Hence, the relative intensity of signals is obtained by multiplying the ratio of the temperatures.

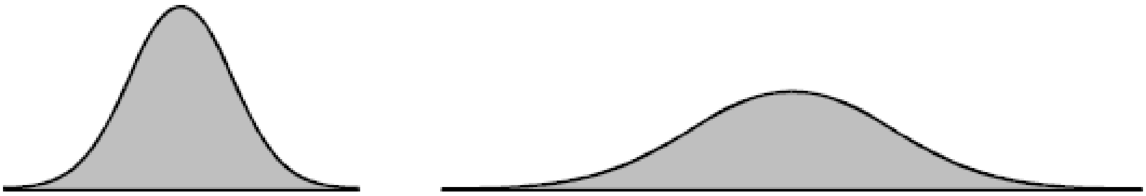

Figure 2.13 Integrated intensity of absorption signals in grey. The two signals have different linewidths yet the same integrated intensity[175].

EPR spectroscopy

The method we used to record EPR spectra is called continuous wave (cw) method, which means the sample is subjected to a continuous irradiation by the microwave. The schematic diagram of cw-EPR spectrometer is shown in Figure 2.14, and it mainly contains:

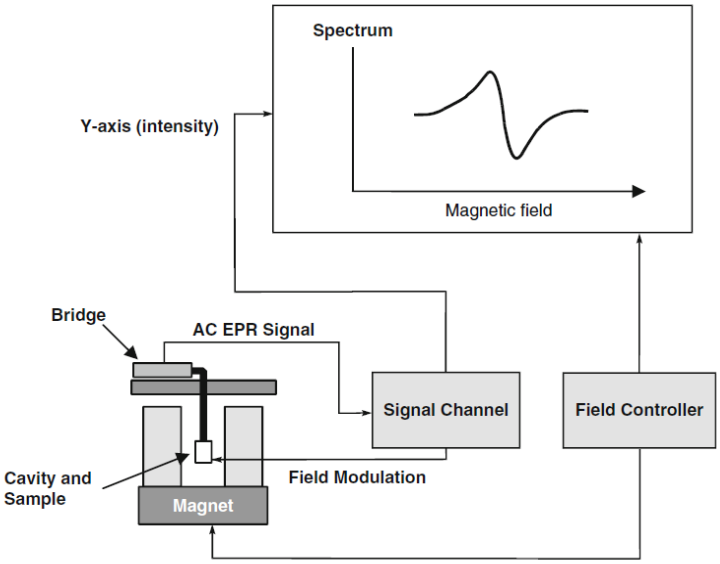

Figure 2.14 Schematic diagram for an EPR spectrometer [175].

(i) Magnetsystem: The usual source of the static magnetic field should be stable and uniform over the sample volume, and, in addtion to this, the field variations should be kept within ±1 μT to resolve very narrow lineshape and to obtain the correct lineshape. For this porpose, a highly stable regulated power supply is appled to generate stable and controlled magnet. Typical EPR spectra are obtained when the magnetic field is swept over a certain range. The spectroscopic charaterisitics of EPR spectra on the axis of magnetic field are linewidth, line position and line seperation, as seen in Figure 2.15. Since these charaterisitics are very easy to be changed by the magnetic field, caution should be taken to avoid obtaining the incorrect results. Usually, a Hall sensor is mounted to measure and regulate the magnetic field, and an electronic controlreads the Hall voltage and feeds the power supply with this information either to generate the sweep or to stabilize the field at a certain value. Although the precision of the measured microwave frequency is quite high, attention should be paid when precise determinination of the value of g factors is needed (± 0.001): a reference sample with very precisely known g factor (2,2-diphenyl-1-picrylhydrazyl (DPPH) with g = 2.0036, in this work) is placed at the same position as the sample and then subjected to the same magnetic field in order to calibrate the value of g factor of the samples.

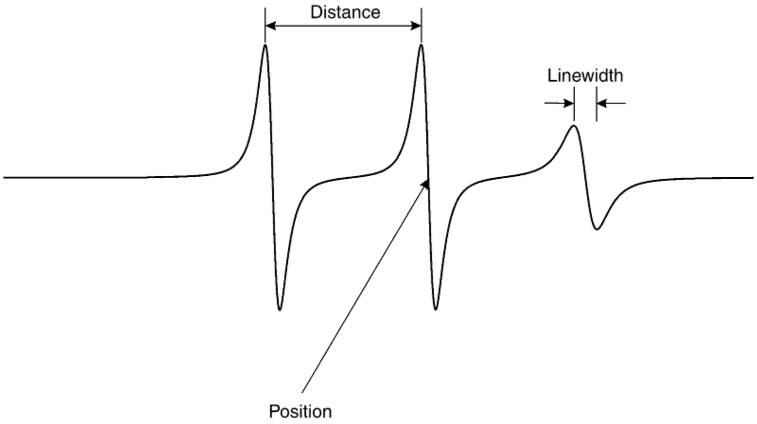

Figure 2.15 The EPR spectrum is characterized by the line positions, distances between lines, and linewidth.

(ii) Resonator system: The heart of an EPR spectroscopy is a deviced called “resonator” containing the sample. In the practice of common cw-EPR with X-band frequency, it is conventional in EPR to refer to the resonator as the cavity. The cavitiy employed for EPR spectrometer used in this work is a cylindrical one, the mode of which is TE_{011}. With this configration, this type of cavity can generate a high energy density in order to observe the EPR transitions.

The sharpness of the response of any resonant system is generally described by a Q factor which is defined as:

$$Q = \nu_{res}/\Delta\nu \qquad \text{(Equation 2.17)}$$

where ν_{res} is the resonance frequency of the resonator and $\Delta\nu$ is the width of the signal. Q value is used to indicate how efficiently the cavity stores microwave energy. As Q increases, the sensitivity of the spectrometer increases.

(iii) Radiation source: Since the output of the once commonly used klystron source is less flat than that of Gunn diodes, klystrons are largely replaced by Gunn diodes souces in modern EPR spectrometers (also including the one used in this work) to produce the frequency (ν) in the microwave domain ($1 \leq \nu \leq 100$ GHz).

(iv) The field-modulation system: A serious disadvantage of the cw-EPR spectrometer is the contribution of the noise to the output signals. The field modulation system allows: (1) the amplification of the EPR signals, (2) the elimination of most of the contribution from the noise components, and (3) enhancing the resolution of the signals. Depite of these, an unsuitable choice of field modulation willl lead to the distortion of the EPR signals and make the interpretation of the results from difficult to completely erroneous. For example, as the amplitude of the magnetic field modulation (also referred to as "modulation width" for JEOL spectrometers) increases, the height of the detected EPR signals increases. If the modulation amplitude is too large (larger than the line width of the EPR signal), the detected EPR signal broadens and becomes distorted (seen in Figure 2.16). However, the smaller the modulation is, the bigger the signal-to-noisy is. Normally, the modulation width should be about 1/3 of the linewidth of the signal in order to obtain EPR signal with an optimized best resolution / small distortion condition.

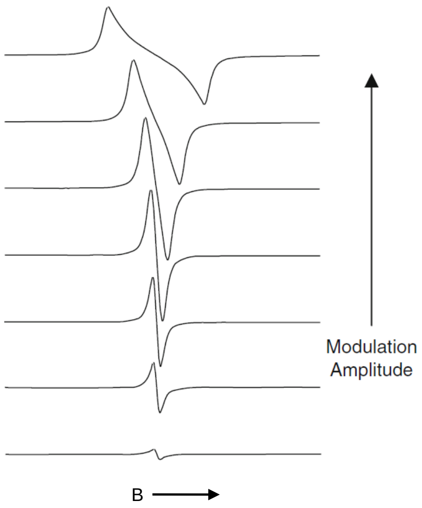

Figure 2.16 Distortion of EPR signal due to excessive field modulation.

(v) The detection system: The most commonly used detector for cw EPR is a Schottky diode crystal that acts as a rectifier of the microwave radiation. It can produce an inherent noise that is inversely proportional to the frequency (f) of the detected signal (noise, '1/f'). The widespread use of 100 kHz as the field-modulation frequency is based on the fact that at this frequency the 1/f detector noise is less than that from other causes.

Apparatus: X-band CW-EPR spectra were recorded on a JEOL FA300 spectrometer at ~ 9.3 GHz (operating at the X-band frequency) equipped with a cylindrical cavity. The presented spectra were recorded in dynamic vacuum ($P < 10^{-5}$ mbar) at 77 K using an insertion dewar containing liquid nitrogen in which the EPR tube is placed with a microwave power of 2 mW, 100 kHz field modulation and a 1.4 G standard modulation width. The g factors were calibrated by using solid α,α′ diphenyl-β-picrylhydrazyl (DPPH). Care was taken to always keep the most sensitive part of the EPR cavity (2 cm length) filled. For the purpose of subsequent annealing treatments, a homemade vacuum line was built up and adapted to the EPR spectrometer. A quartz tubular cell with a diameter of 5 mm was employed to perform EPR measurements *in situ*.

2.5 Other techniques

Scanning Electron Microscopy (SEM) and Transmission Electron Microscope (TEM)

In scanning electron microscopy (SEM), as the high energy electron beam (primary electrons) hits the specimen surface, scattered electrons such as secondary electrons, backscattered electrons and characteristic X-rays will be produced and collected by the appropriate detector to yield structural information about the material. In transmission electron microscopy (TEM), a high energy electron beam is directed toward the sample and these highly energetic incident electrons interact with the atoms in the sample producing characteristic radiation to provide information such as particle shape, crystal structure and structural features such as dislocations and grain boundaries. TEM is based on the detection of elastic and inelastic scattering electrons, backscattered and secondary electrons, and emitted photons.

Apparatus: SEM measurements were performed on a field emission Zeiss Supra 40 scanning electron microscope.The TEM analysis of the particles was achieved using a JEOL 2100 field emission transmission electron microscope operating at 200 kV with a 0.18 nm resolution.

X-ray diffraction (XRD)

X-ray diffraction (XRD) is a well-known technique in the field of crystalline materials characterization. It provides information on crystal structures, phases, preferred crystal orientations, and other structural parameters, such as average grain size, crystallinity and strain. X-rays are generated when electrons are accelerated by a high voltage and allowed to collide with a metal target. When X rays collide with atomic planes of a crystal, it can be scattered by a periodic array with long-range order, producing constructive interference at specific angles. This phenomenon is called X-ray diffraction, and it can only occur when satisfying Bragg's Law:

$$n\lambda = 2d_{hkl} sin\theta \qquad \text{(Equation 2.18)}$$

Where n (an integer) is the "order" of reflection, λ is the wavelength of the incident X-rays, d_{hkl} is a given interplanar spacing of the crystal and θ is the angle of incidence (Bragg angle).

Apparatus: Powder diffraction measurements were performed using a PANalytical X’Pert PRO MRD diffractometer operatingat 40 kV and 30 mA by means of the CoKα (λ = 1.79 Å) and CuKα(λ = 1.54 Å) radiations for the measuremnts of ZnO smoke and ZnO-5 / -50 samples, respectively.

Diffuse Reflectance UV-vis (DR UV-vis) spectroscopy

UV-vis spectroscopy is one type of absorption spectroscopy in which light required for electronic transitions is typically in the UV and visible regions of the electromagnetic radiation spectrum. UV-vis spectroscopy of diluted solutions obeys the Beer-Lambert law (equation 2.19),

$$A = \log I_0 /I = \varepsilon lc = \alpha c \qquad \text{(Equation2.19)}$$

in which absorbance A, is related to the incident light intensity (I_0) and transmitted light intensity (I), molar concentration of a solute (c), path length of the sample (l), absorption coefficient (α), and molar absorptivity (ε).

The spectrum of UV-vis spectroscopy is a plot of A as a function of wavelength λ, and it reflects the fundamental electronic properties of the sample. For solid samples, the expression in Equation 2.19 can be derived in terms of the thickness of the sample. Actually, the interaction of light of the UV visible region with solids is considered to be a complex process due to the concurrence of scattering and absorption processes. In order to separate these two phenomena (absorption vs. scattering), Diffuse Reflectance (DR) UV-vis spectroscopy is considered in the case of solids. Kubelka and Munk [176] proposed a theory for which the DR UV-Vis spectra characteristics can be described by the following equation below:

$$\frac{K}{S} = \frac{(1-R_{\infty})^2}{2R_{\infty}} = F\,(R_{\infty}) \qquad \text{(Equation 2.20)}$$

S and K are the so called K-M scattering and absorption coefficients, respectively. $F\,(R_{\infty})$ is the so-called Kubelka-Munk function, where the reflectance $R_{\infty} = R_{sample}/R_{standard}$.

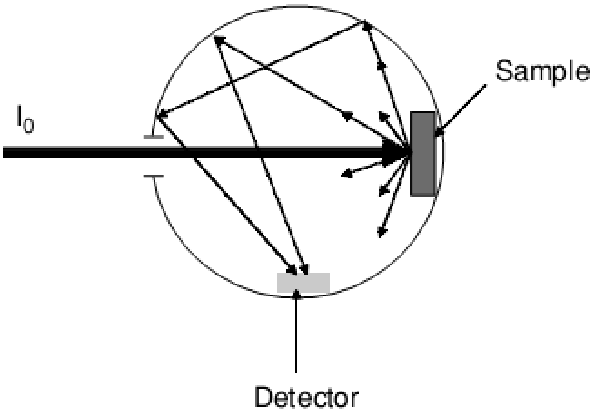

Figure 2.17 Schematic drawing of an integrating sphere for measuring diffuse reflectance spectra [177].

For diffuse reflectance measurements, an integrating sphere (a sphere with a fully reflective inner surface) is used (Figure 2.17). Such a sphere has a pinhole through which the light enters and is transmitted toward the sample. The diffusively reflected light reaches the detector after suffering multiple reflections in the inner surface of the sphere. Such an integrating sphere is incorporated as an additional instrumentation onto conventional spectrophotometers.

A Tauc-plot is used to determine the bandgap energy of a semiconductor, which is described below:

$$(\alpha h\nu)^{1/n} = A(h\nu\text{-}E_{bg}) \qquad \text{(Equation 2.21)}$$

where α is the absorption coefficient, h is Planck's constant, E_{bg} is the band gap, A is a proportionality constant, and □ is the photon's frequency. Since ZnO is direct semiconductor, n=1/2 is used.

Apparatus: UV-vis diffuse reflectance spectra reported in this work were acquired by using a Varian Cary spectrometer spectrophotometer covering a range from 200 nm to 800 nm and being equipped with an integrating sphere. The background reflectance of $BaSO_4$ (reference) was measured before each samples measurements and the reflectance was converted into absorption spectra via the Kubelka-Munk equation (Equation 2.21).

Infrared (IR) spectroscopy

IR spectroscopy is based on the absorption of infrared radiation at specific wavelengths as it passes through a sample. When infrared light directs on the sample, its photon energy absorbed by molecule is not enough to create electronic transitions but it does contain enough energy to interact with a molecule causing vibrational and rotational motions. When the frequency of the IR is the same as the vibrational frequency of a bond, the absorption occurs. Taking diatomic molecule as an example, m_1 and m_2 being the masses of two atoms, respectively, the frequency of vibrational bond can be converted into corresponding wavenumber, and then it can be given by:

$$\sigma = \frac{1}{2\pi c}\sqrt{\frac{k}{\mu}} \qquad \text{(Equation 2.22)}$$

where c ($m \cdot s^{-1}$) is the speed of light, $\sigma = \frac{\nu}{c}$ in cm^{-1}, k is a force constant in $N \cdot m^{-1}$, reduced mass is $\mu = m_1m_2 / (m_1 + m_2)$, in kg.

For solid nanoparticles, IR measurements conventionally provide the vibrating information of phonon modes. However, in this work, we perform IR measurements after absorbing water which act as surface probe to look for the newly formed bonds and its corresponding vibrations.

Apparatus: the infrared (IR) measurement was performed under ultra-high vacuum (P ~ 10^{-10} mbar) on the Fourier transform infrared spectrometer composed of Michelson interferometer and Vertex 70 provided by Bruker. The acquisition of spectrum is performed by using software OPUS with a resolution of 4 cm^{-1}, and 250 scans were accumulated in a range from 4000 to 560 cm^{-1}. The transmitted radiation was detected with a MCT 316 detector that is cooled down at 77K.

The IR system in this thesis work is schematically represented in Figure 2.18. The sample is evaporated on the silicon wafer. It is firstly introduced into the chamber 1 under nitrogen flow, and thereafter pumped until the achieved pressure is ~ 10^{-8} mbar. Then the sample is transferred into chamber 2 and subjected to the thermal treatment at 773 K for one hour. After the sample was cooled down to room temperature, it is transferred into chamber 3 to record the reference spectrum in ultra-high vacuum. After this, the sample was exposed to a certain pressure of water vapor (P=10 mbar) to investigate the surface properties of ZnO.

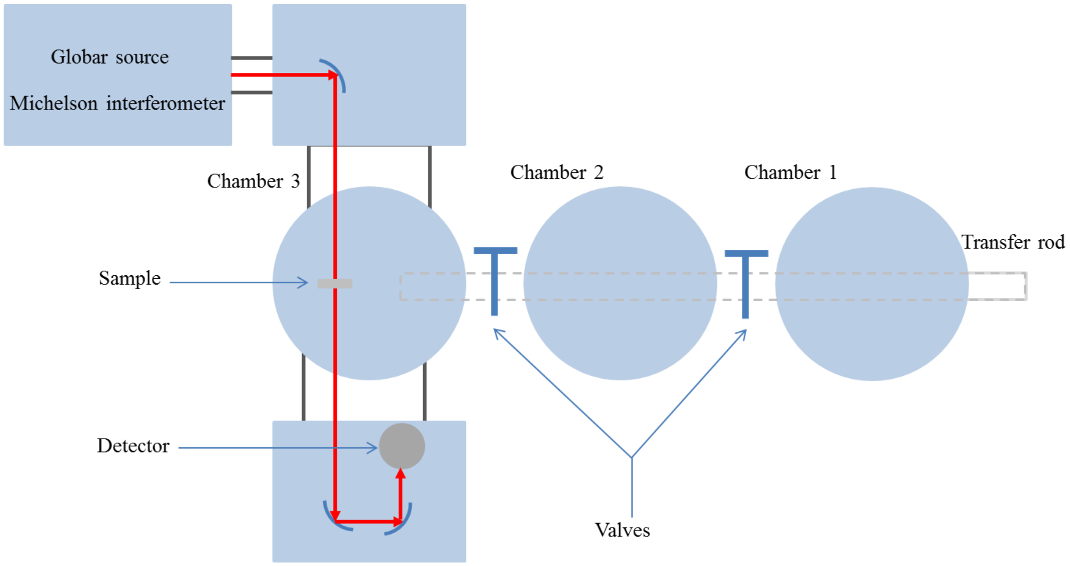

Figure 2.18 Schematic representation of the IR system (from Haque's thesis [178]).

Raman spectroscopy

Raman spectroscopy is very useful in identifying vibration modes (phonons) in solids. This means that structural changes induced by external factors (such as pressure, temperature, magnetic fields, etc.) can be explored by Raman spectroscopy. It is also a very useful technique in chemistry, as it can be used to identify molecules and radicals. Wurtzite ZnO structure with four atoms in the unit cell has a total of 12 phonon modes (one longitudinal acoustic (LA), two transverse acoustic (TA), three longitudinal optical (LO), and six transverse optical (TO) branches). The zone-center optical phonons can be classified according to the following irreducible representation: $\Gamma_{opt} = A_1 + E_1 + 2E_2 + 2B_1$, the where B1 are silent modes, A_1 and E_1 are polar modes, both Raman and infrared active, while E_2 modes are nonpolar and Raman active only.

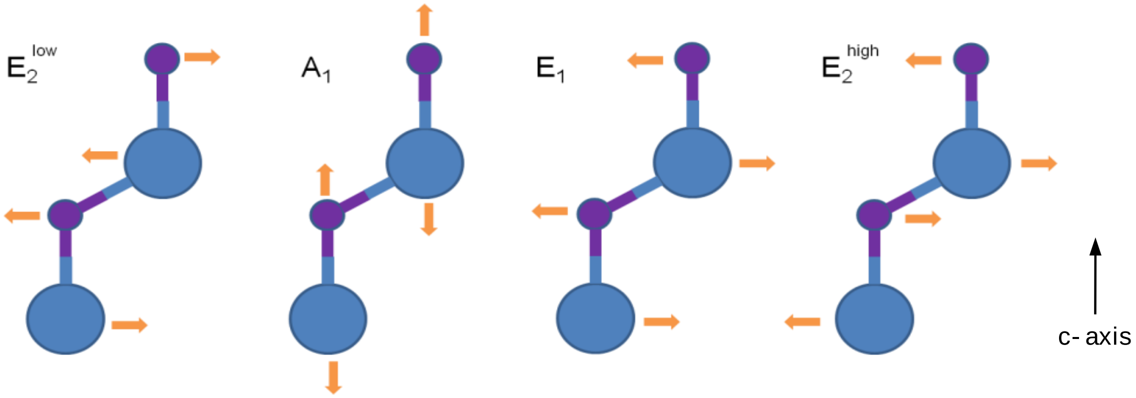

Figure 2.19 The vibrations of the active modes in wurtzite ZnO structure

The vibrations of active modes in wurtzite ZnO structure are shown in Figure 2.19, for the A_1 and E_1 mode lattice vibrations, the atoms move parallel and perpendicular to the c-axis, respectively. On the other hand, E_2 modes are mainly due to the vibration of only the Zn sublattice (E_2^{low}) or oxygen sublattice (E_2^{high}).

Apparatus: in our work, Raman spectra were recorded at room temperature in the range of 0 –3450 cm^{-1} on a commercial modular Raman spectrometer (Model RXN1 of Kaiser Optical Systems, Inc.). It displayed a high-powered near-IR laser diode working at 785 nm.

Before recording the spectra, a microscopy probe head coupled with non contact optics was used to focus the laser beam and to collect Raman diffusion.

2.6 Catalytic reaction

The set up schematically represented in Figure 2.20 allows us to carry out a gas phase reaction at atmospheric pressure monitored by a heterogeneous catalyst. When the reactant is 2-Methyl-3-butyn-2-ol (MBOH) in liquid state in usual conditions, its controlled vaporization is requested to study the gas phase reaction. The inlet and outlet gases are analyzed on line by a micro gas chromatograph.

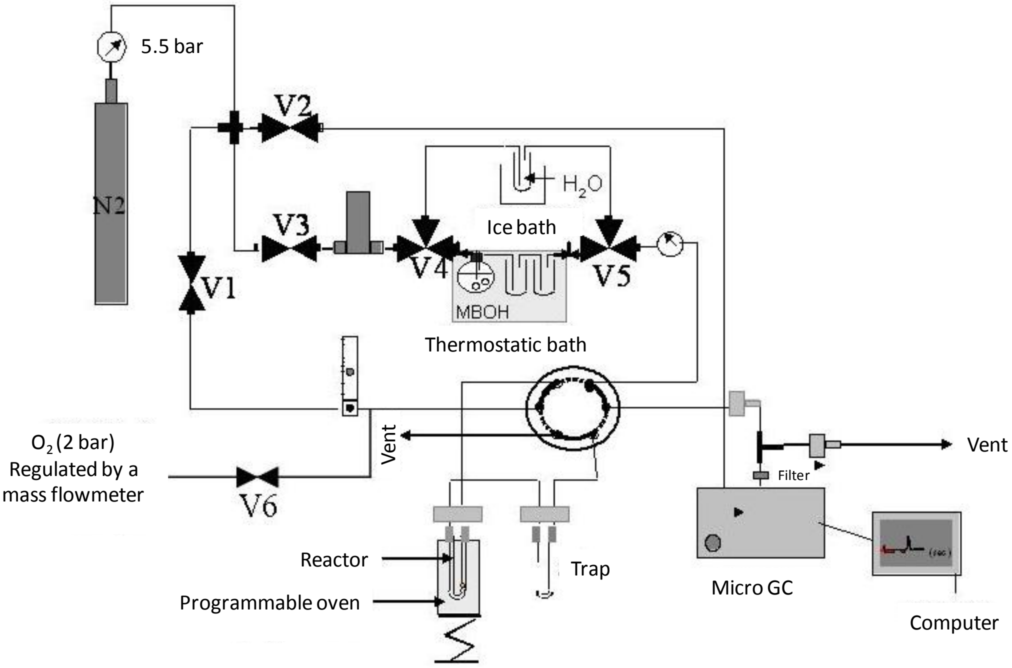

Figure 2.20 Schema of the catalytic test

The home-made set up involves two-way interconnected flow device made of 316 stainless tubes (diameter of 1/8 inch). The first one is devoted to the thermal pretreatment under controlled atmosphere (a controlled flow of O_2 or N_2) that is usually performed in order to clean the surface from any natural adsorbates (hydroxyl and carbonates) before the catalytic reaction is carried out and a second one is devoted to the reaction. Four different zones can be discriminated:

- gas supplying: dehydrated nitrogen (using 5A molecular sieves) is classically used as the pretreatment gas (possibly replaced by air or O_2), and carrier gas for the reaction and finally as the eluting and carrier gas for the chromatograph.

- distribution area: it is used to direct the gas through the pretreatment and the reaction ways using a variable flowmeter and mass-flow controller, respectively. The nitrogen provided by the mass-flow controller (reaction device) is then bubbled in a saturator filled with MBOH which temperature is controlled by a cryostat. A six-way valve allows to select which way (pretreatment or reaction) is connected to the furnace zone.

- reaction area: the classical reactor corresponds to quartz or pyrex U-shaped tube (depending on the pretreatment/reaction temperatures) containing the catalyst that is positioned in the furnace. Its temperature is monitored by a thermocouple located close to the reactor. The analytic zone allows the on-line analysis of the inlet gases (in this case the reactant gas by-passes the reactor, providing the orientation of the six-way valve is in pretreatment position) or of the outlet gas (gathering the unreacted reactant and products at the exit of the reactor when the six-way valve is in reaction position). The outlet gas is sampled first after 120 s of reaction then every 150 s and analyzed by the microGC apparatus (Varian CP-2003P) that is equipped with CP WAX 52 CB column and a thermal conductivity detector (TCD). When a gas with different conductivity compared to the carrier gas (here N_2) is detected, a signal is observed. For quantification purpose, its measured area has to be corrected from the response coefficients that depend on the nature on the gas and had been previously determined by calibration curves. The key parameter for the reaction are the conditions of the pretreatment that will impact the surface state, the temperature of the reaction, the contact time that depends on the weight on the catalyst and on the reactant flow.

Experimental conditions

MBOH conversion experiments were performed in an automated differential flowing quartz micro-reactor. ZnO powders were placed on a porous quartz disk in the centre of a U shape quartz reactor with an inner diameter of 10 mm (Figure 2.21 (a) and (b)). Three series of pretreatments before starting the catalytic reaction have been implemented:

(1) as-synthesized samples (w =100 mg) were pretreated in the reactor (Figure 2.21 (a)) under either N_2 or O_2 flow with the same flow rate of 20 mL·min^{-1} at 773 K. This pretreatment is directly implemented on the catalytic set up.

(2) in order to reproduce surface states similar to those associated to the PL and EPR characterizations, additional pretreatments conditions have been investigated: (1) as-synthesized ZnO samples(w = 50 mg) were pre-treated in vacuum or under oxygen (P_{O_2} = 100 mbar) at 773 K (Figure 2.4); (2) as-synthesized sample after annealing in vacuum was then exposed to 10 mbar of water for 15 min (Figure 2.22), and then it was evacuated (P<10^{-5} mbar) and transferred to the setup for catalytic measurements. In these cases the U-shape reactor equipped with three valves (Figure 2.21 (b)) was used, allowing to isolate the sample from any transient contamination by air between pretreatment steps and catalytic measurements. In all these cases, once the sample is cooled down to room temperature, the reactor was evacuated and then the valves were closed to isolate the sample. The reactor was then connected to the catalytic set up and rapidly heated to 403 K under static vacuum.

Figure 2.21 The reactor used for various pretreatments. (a) U-shape reactor equipped on catalytic setup, (b) U-shape reactor with three valves equipped on vacuum line.

The feed consisted of MBOH diluted by bubbling nitrogen (50 mL·min^{-1}) in liquid MBOH (Fluka, 99.9%) at 293 K leading to a MBOH partial pressure of 1.73 kPa [25]. The final temperature of 403 K corresponds to the reaction temperature.

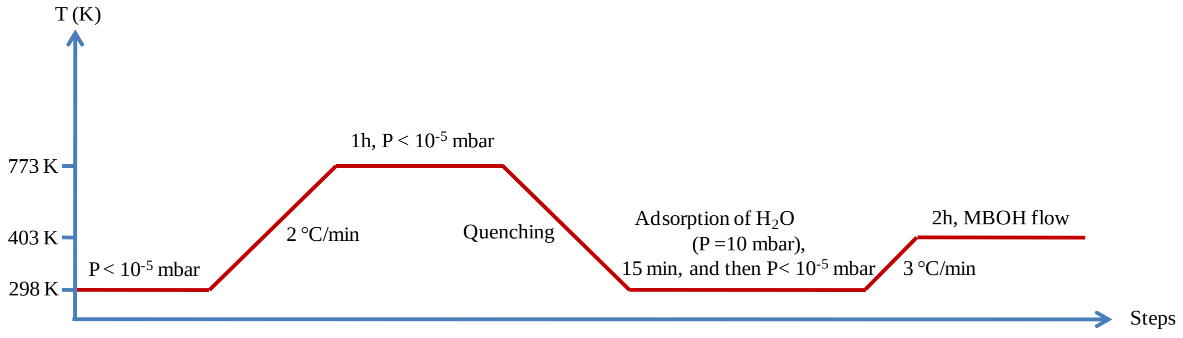

Figure 2.22 Description of the sequential pretreatment steps achieved for the adsorption of water on previously vacuum annealing samples, just before implementation of the reaction

Data processing

Analysis of the MBOH conversion level can be calculated considering either the consumption of MBOH compared to MBOH introduced in the reactor, or the concentration of products formed in the gas phase. These two methods for evaluating the conversion are hereafter referred to as Conv$_{\mathrm{MBOH}}$ and Conv$_{\mathrm{products}}$, respectively and are calculated from the following equations:

$$\mathrm{Conv}_{\mathrm{MBOH}} = \frac{A°_{\mathrm{MBOH}} - A_{\mathrm{MBOH}}}{A°_{\mathrm{MBOH}}}.100 \qquad \text{(Equation 2.23)}$$

$$\mathrm{Conv}_{\mathrm{prod}} = \frac{\sum\limits_{i \neq \mathrm{MBOH}} \alpha A_i}{A°_{\mathrm{MBOH}}} \cdot 100 \qquad \text{(Equation 2.24)}$$

where $A°_{MBOH}$ is the average area of the MBOH peak of the chromatogram measured in by pass conditions (the inlet gases are not sent to the reactor zone) and was measured from 10 analysis), A_{MBOH} is the area of the MBOH unreacted gas (reaction condition), A_i is the area on the chromatogram (after correction of the response coefficient) of the i product. α is 1/2 for acetone and acetylene due to the different amount of carbon in the MBOH molecule compared to acetone and acetylene.

The selectivity in the i product (S_i) is calculated as follows:

$$Sel_i = \frac{1/2A_i}{\sum_{i \neq MBOH} \alpha A_i}.100 \qquad \text{(Equation 2.25)}$$

Chapter 3: ZnO smoke: influence of annealing treatments on defects

As already discussed in Chapter 1, ZnO as a semiconductor material has some unique properties (wide band gap of 3.37 eV and high exciton energy of 60 meV at room temperature), which make it a potential and low cost alternative to GaN for blue to ultra-violet (UV) light emitting applications. The wurtzite crystal structure of ZnO is relatively open with Zn atoms filling only half of the tetrahedral sites, leaving eight interstitial sites that can support atom introduction or dislocation from the idealized wurtzite structure. Consequently, ZnO materials typically exhibit deviations from perfect crystalline structure and they generally contain a certain amount of extrinsic or intrinsic defects. The properties of ZnO in the above-exampled application, as well as in many others, are typically affected by impacting the electronic structure through the corresponding defects. This is particularly pronounced for the nanostructured form where plenty of surface defects act as competing centers in many physico-chemical processes. For instance, the UV luminescent efficiency in nano-ZnO is usually observed to be lower than that in the bulk form since the surface defects serve as competing sites for recombination that result in emissions in the visible range. Such defects-related emissions may, however, boost the photonic applications of ZnO in blue or other visible spectral range. When considering nano-ZnO for photocatalytic application the corresponding efficiency can also be enhanced by the presence of defects. Therefore, it is a significant challenge not only to enhance ZnO’s UV emission efficacy, important for optoelectronic applications, but also to: i) resolve in the first place the correlation between the chemical nature of the defects and observed spectroscopic features and ii) control the defects either upon fabrication routes or additional post-synthesis treatments. This is of great importance especially having in mind that the visible PL emissions observed in ZnO have been assigned to theoretically all types of defects, making their origin to become one of the most controversial issues that is still not conclusively settled up to now. Even though tremendous efforts have been made to identify these defects in terms of the corresponding crystallographic configurations, a precise assignment of defects-related optical emissions is still lacking since both the experimental studies of defect-related spectroscopic properties and the theoretical simulations of the electronic structure and formation energy of detects have not yet provided a conclusive assessment.

So far, many different methods have been explored to produce nanostructured ZnO with a large spectrum of morphologies including rods, tetrapods, discs and hollow spheres [41-43, 179]. In this work, metal combustion, which is an evaporation-based method, was adopted as a simple route to synthesize ZnO nanoparticles (ZnO smoke) of extremely high purity and crystalline quality. Hence, the introduction and therefore the presence of extrinsic defects can be excluded in our ZnO sample, offering a better platform to investigate only the intrinsic defects-related properties. For this purpose, photoluminescence (PL) and electron paramagnetic resonance spectroscopy (EPR) have been combined with the intentional manipulation of defects via changing the synthesis parameters and / or applying post-synthesis treatments (either annealing or adsorption of gaseous probe molecules). Indeed, based on the fact that different types of defects are favorably generated under different conditions, it is expected that the nature of the defects could be understood by modifying the growth or post-growth atmosphere. For instance, oxygen vacancies are expected in reductive atmospheres (vacuum, H_2, Ar, N_2, etc.) at certain temperatures whereas oxygen interstitials tend to be formed in oxidative atmospheres, such as annealing in oxygen. Therefore, in this work vacuum annealing and subsequent oxygen annealing at 773 K were applied and followed by PL / EPR measurements to correlate the observed spectroscopic features with the nature of defects generated under certain / specific stages. Before doing so, the structural and morphological properties of ZnO nano-smokes have been characterized by various techniques (XRD, SEM, TEM, Raman spectroscopy).

3.1 As-synthesized sample

3.1.1 Structural and morphological characterizations

ZnO nanoparticles with specific surface area (S_{BET}) ~ 9 $m^2 \cdot g^{-1}$ have been produced by combusting metallic zinc in air – a highly non-equilibrium synthesis process. The crystal structure of as-synthesized ZnO smoke was characterized by X-ray powder diffraction (XRD) measurements, and its XRD pattern is shown in Figure 3.1. According to the X-ray profile analysis, as-synthesized ZnO smoke exhibits wurtzite structure. No extra diffraction peaks were detected indicating that such obtained ZnO is purely monophasic with crystals free of any impurities. The diffraction peaks are sharp and narrow, confirming high crystal quality of the sample. The lattice parameters are calculated by the Rietveld refinement analysis, to be a = b = 3.250 Å, c = 5.207 Å. These values are consistent with the lattice parameters reported in the literature and database [180]. X-ray diffraction profile analysis allows furthermore evaluating the crystal size and strain. Crystallite size (D) – which is generally not the same as the particle size due to the formation of polycrystalline aggregates – is a measure of the size of coherent diffraction and can be estimated by using the Debye–Scherer equation [181]:

$$D = K\lambda / B\cos\theta \qquad \text{(Equation 3.1)}$$

where K is a shape factor (0.9), λ is the wavelength of Co kα radiation, θ is the Bragg angle, and B is the full width at half maxima on 2θ scale. According to this equation, the average crystalline size of ZnO smoke was calculated to be 88 nm. The microstrain is calculated by Williamson-Hall method [182] which is explained elsewhere [183], giving a value of 2.5%, which can be due to the presence of some crystal imperfections and distortion.

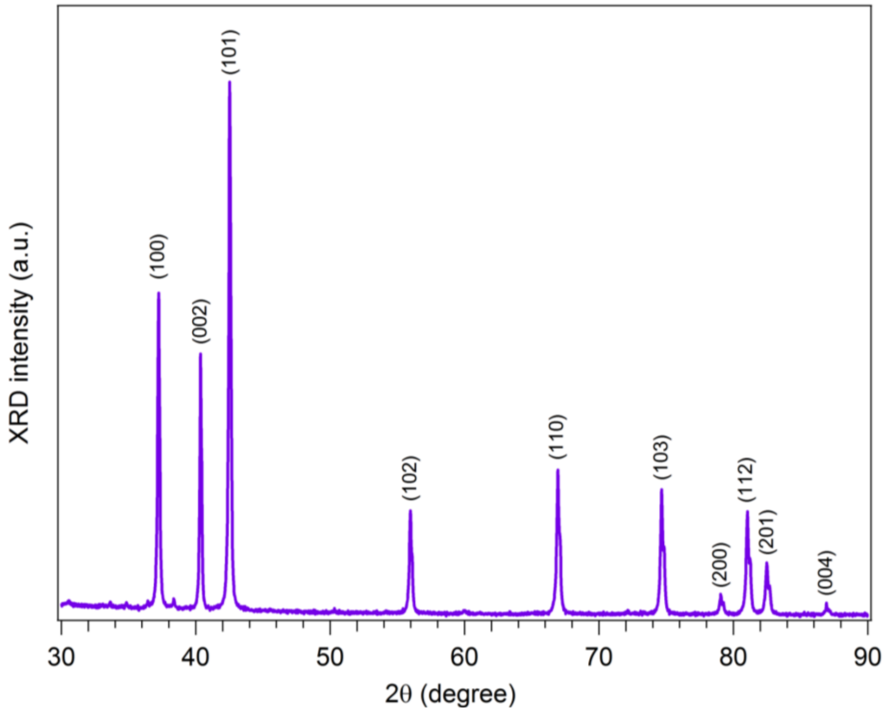

Figure 3.1 X-ray diffraction pattern of as-synthesized ZnO smoke sample.

A representative TEM image of ZnO-smoke is shown in Figure 3.2 (a). A strong tendency for agglomeration and morphological inhomogeneity is observed. Typically, tetrapod- and rod-like structures dominate among others but also irregular shapes – such as multipods wherein rod-like structures grow out of a plate-like crystal – are largely present. The tetrapod-like structure, which was systematically found in all micrographs, consists of four individual rod-like crystals (tetrapod-arms) arranged together in the form of a tetrahedron. The length of the rods can be larger than 100 nm but the diameter is principally between 10 to 30 nm (see Figure 3.2 (b, c)). Such morphological irregularity can be explained by the synthesis conditions that are far from equilibrium and in which the evaporation and oxidation of zinc are immediate and the formation of ZnO is a highly exothermic event. Consequently, the conditions during crystal growth are locally different due to the non-uniform distribution of the temperature in the combustion flame and tetrapod-like structures are typically obtained upon such synthesis technique [184]. Contrary to MgO obtained by other gas-phase techniques, MgO smoke particles produced by this method [51] were shown to exhibit a broad (and bimodal) size distribution yet exceptionally regular in shape [185]. Non-uniform size of MgO smokes has been explained by different residence times of particles in the flame [186]. Obviously, in the case of ZnO, the shape asymmetry is also due to different residence times – which is not surprising keeping in mind the huge span of shapes in which nano-ZnO can be obtained [187]. HRTEM image in Figure 3.2 (c) represents a part of a ZnO tetrapod arm viewed along the [021] zone axis. No disordered areas could be observed while the lattice spacing was measured to be 0.281 nm between adjacent lattice planes corresponding to the d-spacing of the {1011} planes. The tetrapod structure has recently gained a great attention since it shows particular electron transport properties [188]. The strain, which was obtained by XRD to be 2.5 %, produces usually a ripple-like contrast in the junction region of tetrapod arms, as shown by Rot et al. [189]. There exist a few suggestions in the literature that such junctions, and this type of synthesis in general, may result in the presence of zinc blende phase [190-191]. However, the lattice parameters calculated from both Rietveld analysis and HRTEM (Figure 3.2 (d)) match only with the pure wurtzite phase – reflecting strongly the purity of the synthesis conditions and supports our synthesis approach that avoids incorporation of extrinsic defects. Fabrication of high-quality single-crystal particles is furthermore demonstrated by selected area electron diffraction (SAED) pattern (inset, Figure 3.2 (d)).

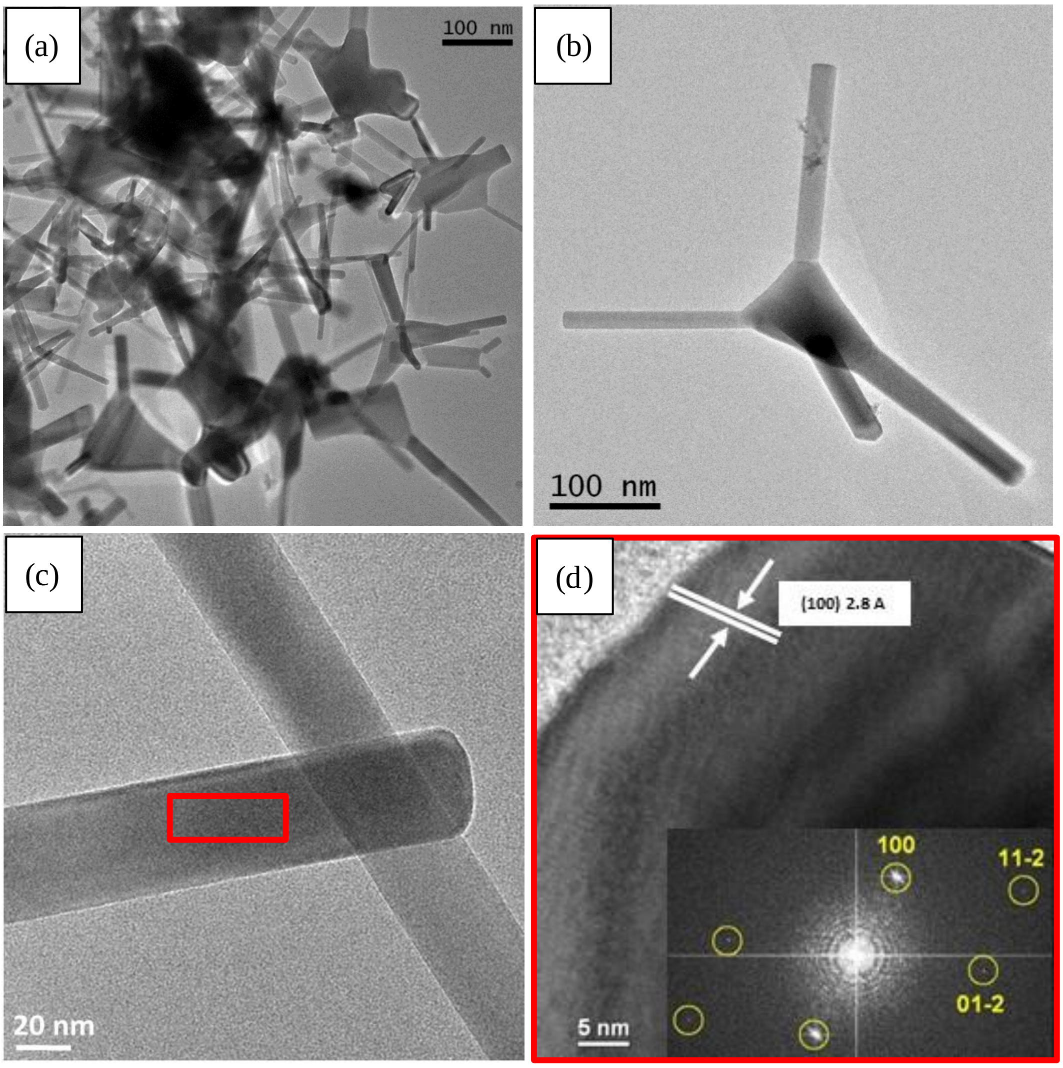

Figure 3.2 TEM (a and b) and HRTEM (c and d) images of as-synthesized ZnO smoke sample. HRTEM image (c) corresponds to ZnO tetrapod arm viewed along a [021] zone axis of wurtzite structure. The inset in (d) shows SAED of the selected HRTEM zone in red (c).

3.1.2 Optical properties

The absorption spectrum of as-synthesized ZnO smoke sample is shown in Figure 3.3, and it reveals a threshold measured at ~380 nm which corresponds to E_{bg} ~ 3.26 eV (see inset in Figure 3.3), a value similar to the one usually reported for nanostructured ZnO (3.2 ~ 3.3 eV) [192-194] and slightly lower than those measured for single crystal ZnO (3.37 eV) [195]. The determination of the bandgap energy was done by extrapolating the linear region observed in a Tauc-plot based on the equation described below:

$$(\alpha h\nu)^{1/n} = A\,(h\nu - E_{bg}) \qquad \text{(Equation 3.2)}$$

where α is the absorption coefficient, h is Planck's constant, E_{bg} is the band gap, A is a proportionality constant, and ν is the photon's frequency. Since ZnO is a direct semiconductor, n = 1/2.

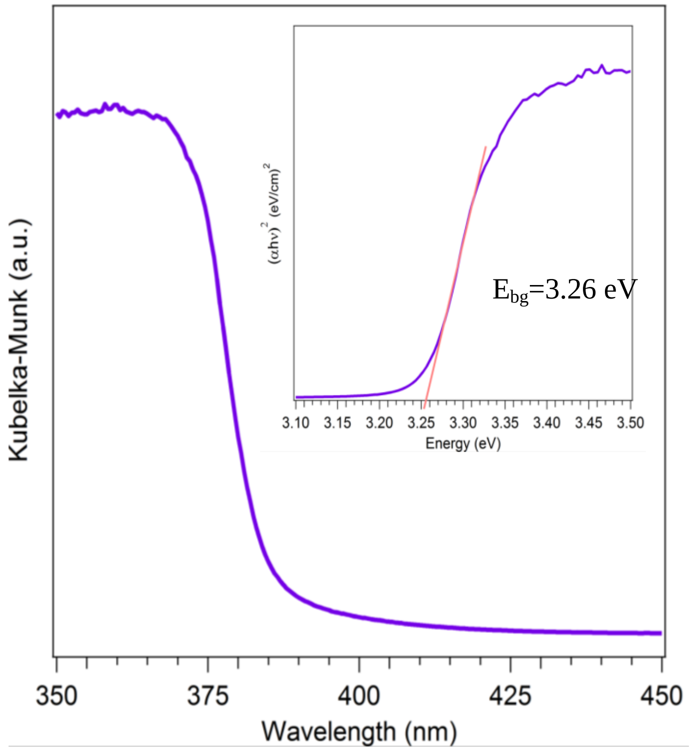

Figure 3.3 UV-Vis diffuse reflectance spectrum of as-synthesized ZnO smoke sample. The inset is the corresponding Tauc-plot for determining its band gap energy.

An excitation energy (E_{exc}) slightly exceeding the measured bandgap (E_{exc} = 4.13 eV, 300 nm) was used to obtain the room-temperature PL-emission spectrum of the as-synthesized ZnO-smoke. This spectrum is shown in Figure 3.4 (a) together with the corresponding band-fitting analysis (b). One can see that PL emission of ZnO smoke is dominated by a strong UV-emission, with a maximum (380 nm, 3.26 eV) near the absorption edge. Related to band-to-band transitions, the high intensity of the UV-emission of ZnO demonstrates the high crystal quality of the sample, which is in line with the results previously shown by structural characterization technique – i.e. XRD.

Band-fitting analysis demonstrates that the UV-emission can be decomposed into two Gaussian bands centered at 3.26 eV and 3.19 eV. The former band matches well with the E_{bg} of our sample obtained from the Tauc plot whereas the latter one was suggested to be correlated to zinc vacancies [196]. However, the presence of different shapes and particle sizes in our sample should be also considered when the band-to-band transition is considered. The existence of the second peak (3.19 eV) can be, therefore, linked also to the morphological inhomogeneity of the sample. Additionally, two different structures may also result in the two different emissions in the UV region. For instance, Lazzarini et al. [37] synthesized tetrapod-shape ZnO nanoparticles with twin crystal structure - wurtzite and zinc blende structure. They observed that typical emission peak at 377 nm (3.29 eV) and 369 nm (3.36 eV) detected in the PL spectrum recorded at 10 K were corresponding to the band gap of wurtzite and zinc blende structures, respectively.

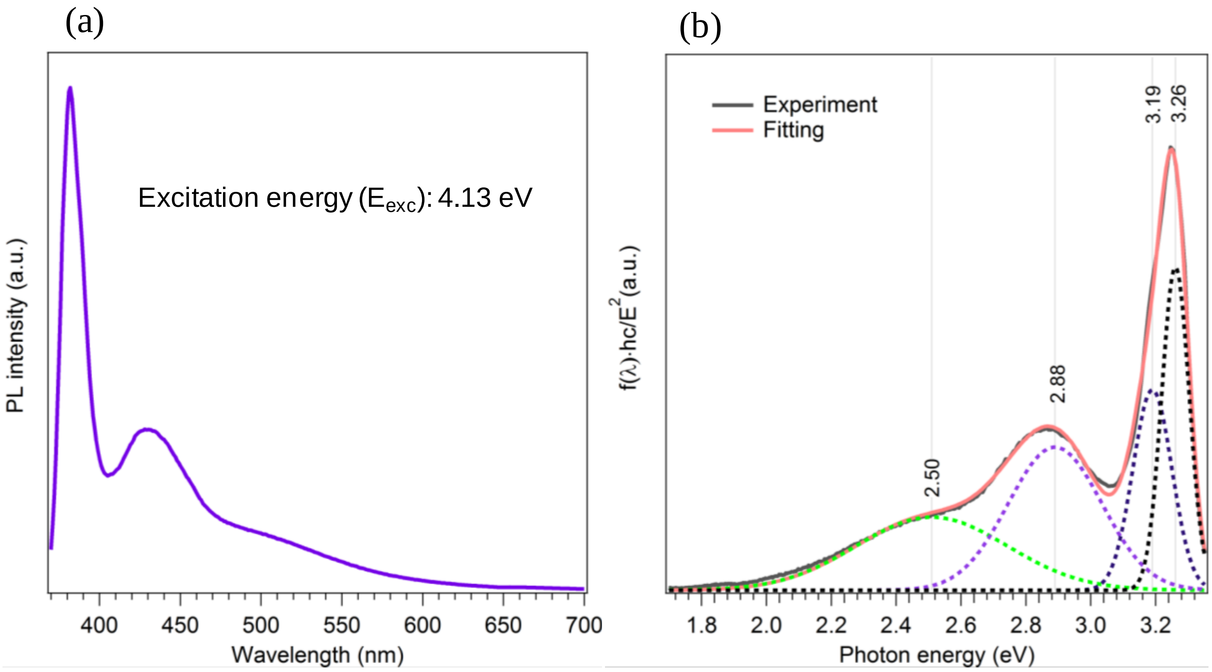

Figure 3.4 PL spectra of as-synthesized ZnO smoke sample (a) and corresponding band-fitting analysis (b). The black, pink, violet and green dotted curves in (b) show the contribution of the each emission.

As for the visible part of the spectrum, an intense emission positioned at ~ 430 nm (2.88 eV) in violet region was measured together with a tail, the maximum of which (~ 495 nm, 2.50 eV) matches well with that of usually discussed green emission, implying the presence of different types of intrinsic defects in the as-synthesized ZnO smoke sample. Infrequently measured in ZnO samples, the violet emission has never gained as equivalent attention as the bands in the green and yellow / red regions. Furthermore, its assignment is less controversial than considering other visible emissions – it is, indeed, quite consistently attributed to transitions that involve zinc interstitial related defects [91-93]. According to the theoretical calculations [197-199], many studies predict Zn_i to behave as a shallow donor with the corresponding energy level being located slightly below the conduction band. It is demonstrated also experimentally, that the energy level of Zn interstitial is ~ 0.47 eV below the conductive band [200] being perfectly in line with calculations, therefore, the emission at 2.88 eV (430 nm) observed in this work fits well to the assignment to Zn_i defects. This attribution is additionally supported by the applied synthesis conditions – that are far from equilibrium – that favor an excess of zinc in the final material. Indeed, the violet emission was usually reported for ZnO samples fabricated through non-equilibrium methods [90], and its intensity found to strongly depend on post-annealing treatments – such as ultra-rapid reactive quenching. Taking into account that smoke nanoparticles are very quickly formed via Zn-combustion in air and that the synthesis route strongly deviates from thermodynamic equilibrium, the presence of interstitial Zn in ZnO smoke, even as the dominant intrinsic defect appears to be reasonable [90].

The second band in the visible part of the spectrum (see Figure 3.4 (b)) obtained via band-fitting analysis is a broad emission with maximum at 2.50 eV (495 nm). The so-called green emission is the most commonly reported PL emission in ZnO and has been reported with the maximum at different wavelengths such as 494 nm [24], 500 nm [117], 515 nm [119], 520 nm [121], 532 nm [123], and 539 nm [98]. Furthermore, green emission has been attributed to theoretically all possible defects in ZnO [201-202] representing, thus the most controversial issue among all ZnO optical properties.

Indeed, the attribution of green emission to oxygen vacancies appears to slightly precede over the other assignments [83, 102, 203-204]. One of the arguments that strongly supports this hypothesis is given by the increase of its intensity upon thermal treatment under nitrogen / argon or under vacuum. Oxygen vacancies can be generated directly during the synthesis or introduced by the post-growth treatment – in both cases, by applying conditions that are oxygen insufficient. Vanheusden et al. [122], have found an intensity increase of PL emission at 520 nm with increasing the annealing temperature in the forming gas (a mixture of N_2 and H_2, that correspond to oxygen insufficient condition) and attributed this optical feature to oxygen vacancies. The same assignment of green emission was reported for annealing treatment in presence of Zn at 1273 K [118].

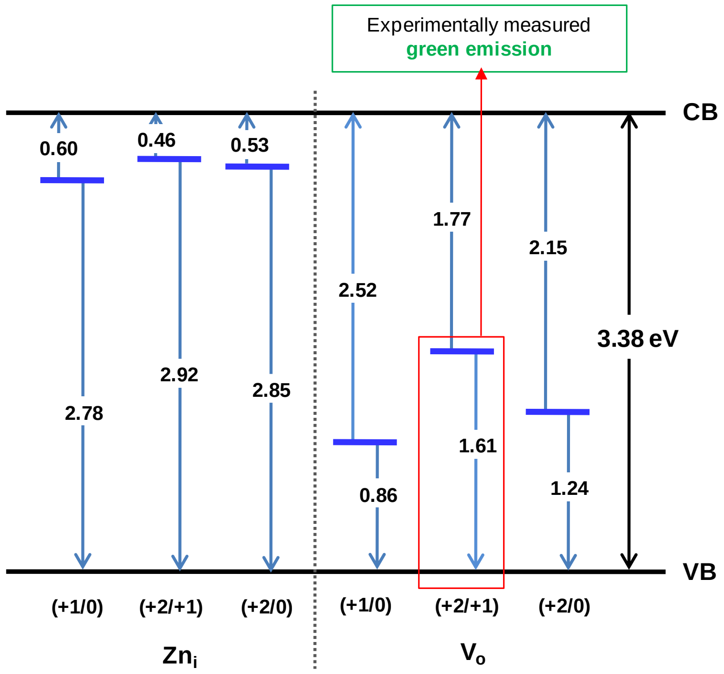

Figure 3.5 Optical transition levels in the band gap of ZnO taken from the reference [205] and adapted to only present Zn_i *and Vo related defects. The symbol of (+1/0) stands for the transition between charge state of +1 and 0.*

Green emission can be correlated with oxygen vacancies also, according to theoretical calculations that predict, indeed, this defect to act as a deep double donor. In the group of Van de Walle [65], they have calculated the (0/+2) transition at ~ Ev +2.7 eV, the (+1/+2) level close to the conduction band (Ev +3.3 eV) and the (0/+1) level at ~ Ev +2.0 eV. In another theoretical work, by Gallino et al. [205], the energy level of oxygen vacancy has also been predicted to lie deep in the band gap. For experimentally observed green emission they tentatively put the following transition $V_O^+ \rightarrow V_O^{2+} + e^-_{VB}$ into account. Nevertheless, they also consider the high formation energy (E_{form}) of V_O^+ and exclude these defects to be present as native ones in ZnO but they suggest that V_O^+ can be generated upon photoexcitation of neutral V_O – assuming this defect to possibly exist in ZnO. Still, their assignment has to be taken with precaution since for the suggested (+1/+2) transition they only obtain the value of 1.61 eV – which strongly differs from the experimentally one at 2.45 eV, the process of which is emphasized by the frame in Figure 3.5. V_O and Zn_i related optical transition levels in the band gap of ZnO that are calculated by Gallino et al. [205] are presented in Figure 3.5.

3.1.3. PL-excitation dependence

The influence of excitation energy on the previously described emission bands was furthermore investigated. The selection of excitation energies was based on the band gap energy obtained from ZnO smoke absorption spectrum. Three ranges were used: i) $E_{exc} > E_{bg}$ (4.13 eV), ii) $E_{exc} = E_{bg}$ (3.26 eV) and iii) $E_{exc} < E_{bg}$ (3.10 eV). The corresponding PL emission spectra are presented in Figure 3.6. One can see that the emission band at ~ 440 nm (2.80 eV) is present in PL spectrum regardless of the excitation energy. This, however, does not apply for the green emission which cannot be excited with energy lower than the band gap i.e. < 3.26 eV. In similar studies by Zeng and coworkers [90] the same trend has been observed for the violet emission upon excitation with different E_{exc}. However, they found green emissions to be preferentially excited by energies larger than the bandgap whereas in our case the intensity of this band was found to be the strongest when applying the excitation energy close to E_{bg}.

The position of the maximum of violet emission implies that its initial energy level should be below the conduction band edge. This ensures that it can effectively emit when the excitation energy is below the bandgap energy. Among the six types of point defects in ZnO lattice and according to the defect energy level, only Zn_i is located slightly below the conduction band-edge. This has been shown by both experimental results and theoretical calculations by many groups [70, 206-207]. Such observations together with the highly non-equilibrium synthesis used in this work, enable the PL emission observed at 440 nm in our sample to be attributed to Zn_i-related defects. As for the green emission, being undetectable for $E_{exc} < 3.26$ eV (that is a measured E_{bg}) we may assume its initial state to be deeper in the band gap.

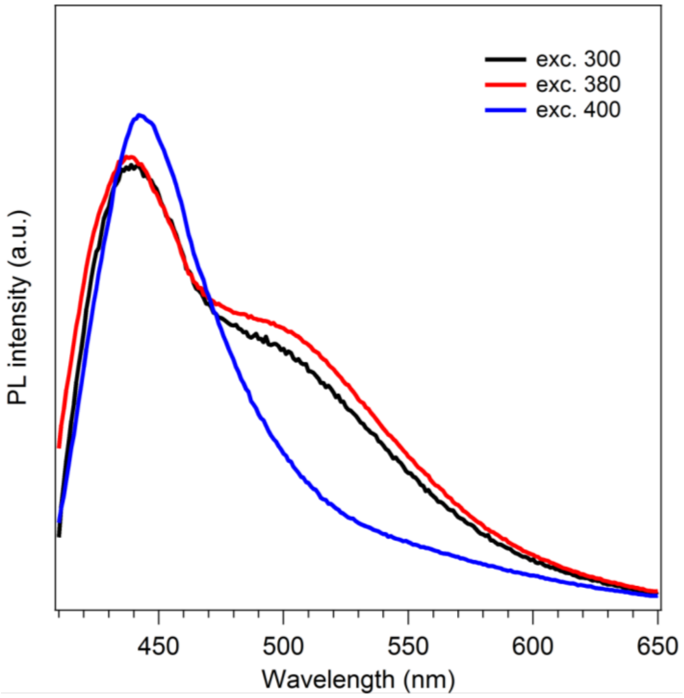

Figure 3.6 PL spectra of as-synthesized ZnO smoke sample recorded under different excitation energies (red, blue, black curves indicating the excitation energy at 4.13 eV / 300 nm, 3.26 eV / 380 nm and 3.10 eV / 400 nm).

3.1.4. Electron paramagnetic resonance spectra

Since many types of point defects present in solids, and, in particular, in oxides are paramagnetic, electron paramagnetic resonance (EPR) spectroscopy is one of the most suitable techniques to investigate defective materials. The EPR spectrum of bare ZnO smoke, recorded at 77 K, is not a flat line (as one should expect in the case of the perfect stoichiometry) and shows two distinct signals, indicating the presence of some intrinsic paramagnetic defects in the as-prepared material. The signals monitored in this experiment are reported in Figure 3.7 (a) together with the results of the corresponding simulation in Figure 3.7 (b). The EPR spectrum of ZnO smoke consists of an intense and very slightly axial signal ($g_{||}$ = 1.957 and $g_{\perp}$ = 1.956, species A in Figure 3.7 (b)) and a weak and isotropic signal with g_{iso} = 1.960 (Species B in Figure 3.7(b)) – the intensity of which is sometimes at the limit of detectability due to the overlapping with the signal of species A.

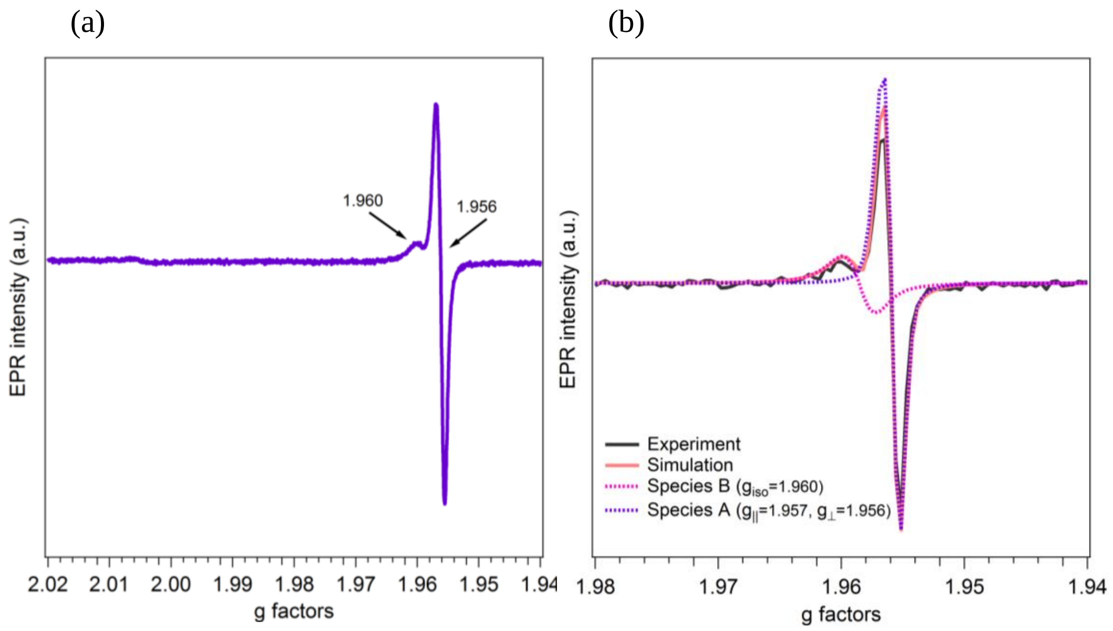

Figure 3.7 EPR spectra (recorded at 77K) of as-synthesized ZnO smoke sample (a) and its corresponding simulated spectra (b). The violet and magenta dotted curves in (b) show the contribution of each paramagnetic species.

In general, an EPR signal with values in the range 1.960 – 1.955 has been widely reported in the ZnO literature but, until present, no clear origin was concluded for such signal. Interestingly, in most of the reported EPR data on ZnO, either the signal with g ~ 1.960 or the one ~ 1.955 were observed but very rarely both signals, being so close, were reported at the same time. In one of such rare reports, Morazzoni and coworkers [128] identified two similar EPR signals (g ~ 1.959 and g ~ 1.955) on commercial ZnO nanopowder. They followed the evolution of the two signals upon vacuum annealing and assigned the one with g ~ 1.959 to V_o^+ and the one with g ~ 1.955 to Zn_i^+. They made such attribution on the basis of vacuum annealing treatment upon which the intensity of g ~ 1.959 increased whereas a strong reduction of the signal with g ~ 1.955 was observed. The assignment obtained out of that annealing trend can be illustrated according to Morazzoni's study [128] as follows:

(1) The increase of the g = 1.959 signal would be related to the formation of oxygen vacancies (V_O) through desorption of O_{latt}^{2-}:

$$O_{latt}^{\,2-} \rightarrow \tfrac{1}{2} O_2 + (V_O^0)_s \qquad \text{(Equation 3.3)}$$

$(V_O^0)_s \rightarrow (V_O^+)_s + e^-$ (Equation 3.4)

(2) The decrease of the 1.955 signal is related to the suppression of Zn_i^+ by the electron formed in Equation 3.3, and this process is described below:

$Zn_i^+ + e^- \rightarrow Zn_i^0$ (Equation 3.5)

However, since the g-tensor of these two signals is so close we may also hypothesize that they originate from the same type of paramagnetic defect which only experiences different crystallographic environments. For instance, Zn_i^+ at the surface versus Zn_i^+ in the bulk. Indeed, in the framework of the core-shell model, by Kaftelen et al. [135], the signal at g = 1.960 was assigned to a core signal (V_{Zn}^-).

The assignment of the signal at g = 1.96 to oxygen vacancies – not only in Morazzoni's work but also in many others [96, 130-131] – was questioned. Usually, it is attributed to some shallow donor, such as ionized impurity atoms in the crystal lattice of ZnO [208], but sometimes also to unpaired electrons trapped at oxygen vacancies [209] or even free carriers in the conduction band [133-134, 149]. Indeed, experiments have suggested that the signal at ~ 1.96 is typical of a conduction band electron, coulombically attracted by the ionized donor center in a "hydrogenic effective mass state" [210-211] and also observed the increase of its intensity for H-, Al-, Ga-, and In-doped ZnO [212-213]. Djurisic et al. [201] in a series of differently prepared nano-ZnO samples observed this signal only if the fabrication implied humid conditions – implying connection with H-related defects. Theoretical studies have predicted that hydrogen may behave as a shallow donor and experimental data have provided supporting evidence [214-215]. The synthesis applied in our work excludes any external impurity in terms of other chemical composition. However, considering that some authors claimed that "hydrogen related" defects may exist in ZnO [8, 205]. Hence, keeping in mind that our synthesis is carried out in air and locally leads to very high temperature, it is questionable if water vapor may act as a source of hydrogen and be responsible for EPR signals observed around 1.96. On the other hand, having in mind the PL emission at 430 nm (2.88 eV) to appear as the dominant one in the PL spectrum of our sample, we tentatively correlate the 1.956 signal to this optical feature and, correspondingly to Zn_i^+-related defects.

3.1.5. PL and EPR in function of surface adsorbates

When studying ZnO it is often neglected that the samples are usually exposed to the air. This may take place during the synthesis or the storage, either intentionally or not. Surface defects, if present, are very reactive towards adsorbates (O_2, H_2, H_2O, CO, CO_2, etc.) and several phenomena may occur, strongly affecting the spectroscopic results. Besides the dissociation in which new chemical bonds are created ($ZnO + H_2O \rightarrow Zn(OH)_2$), an electron transfer may also proceed between semiconductor surface and gas molecules (i.e. adsorbates). For instance, when oxygen molecules are adsorbed on the surface, they can trap free electrons from ZnO [216], i.e. defects that will later act as donors (Zn_i^+, Vo^+). As a result, chemisorbed O_2-species are created, the accumulation of which induces an electric field (depletion layer). This results in a slight upward band bending. Consequently, changes in optical properties must be detected with respect to both: changes in the band gap and changes of the charge state of the involved defect.

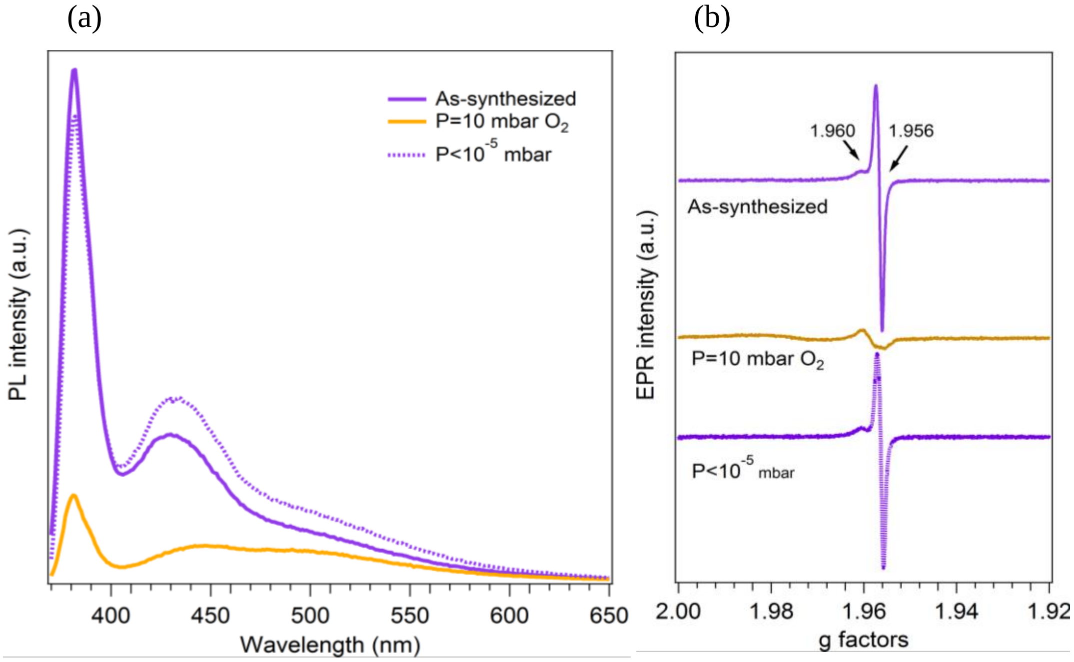

Figure 3.8 PL (a) and EPR (b) spectra of as-synthesized ZnO smoke (solid violet curve), then exposed to O_2 ($P = 10$ mbar) (solid orange curve) and after removing O_2 (dotted violet curve, $P < 10^{-5}$ mbar).

Figure 3.8 compares the PL (a) and EPR (b) spectra of the as-synthesized ZnO before and after admission of oxygen. A decrease of all the PL emissions is observable after the O_2-admission (orange curve, Figure 3.8 (a)). Such PL intensity reduction indicates that the intense photoluminescence features, observed in as-synthesized ZnO smoke mostly originate from surface species since their radiative recombination can be partially deactivated by collisional quenching in an O_2 atmosphere. On the other hand, the adsorption of an e^--acceptor or e^--donor on the semiconductors' surface alters its surface potential. This affects the interfacial depletion layer and, consequently, determines the depth of the active PL region. Accordingly, PL emission intensity may vary on semiconductors and can be related to the adsorption of charge-donating and –accepting molecules and concomitant changes in the band bending. In our case, upon admixture of molecular oxygen a dramatic decrease of the UV-band intensity is observed together with a strong reduction of the emission at 430 nm (2.88 eV), while the intensity of the emission at 495 nm (2.50 eV) suffered the least (see Figure 3.8 (a), orange curve). A partial quenching of emission at 2.88 eV (430 nm) that results in the red-shift (440 nm / 2.80 eV) of the maximum implies its correlation to more than one Zn_i-related defects – and that only some of them are subject to the interaction with molecular oxygen, i.e. those that are located on the surface. The adsorption phenomena and eventual interaction with defects were further investigated by EPR studies. EPR spectrum of ZnO smoke exposed to P = 10 mbar O_2 (Figure 3.8 (b), orange curve) shows strong reduction of the signal with g = 1.956 while the signal at g = 1.960 is not affected. Once the oxygen was removed, both the emission at 430 nm (2.88 eV) and EPR signal with g = 1.956 almost recovered to their initial state. This is represented by the dotted violet curves in Figure 3.8 (a) and (b). Such tendency supports the hypothesis of the 1.956 signal to be associated with electrons in Zni^+ defect located on the surface. Such a phenomenon can be understood following two hypotheses: (i) Once the O_2 is adsorbed, these e^- (from Zn_i) is consumed by creating O_2^- inducing the decrease of 1.956 signal. Yet, at the same time, the high P_{O2} induces strong dipolar interactions between the O_2^- formed and surrounding O_2 molecules, resulting in such a strong broadening that it leads to undetectable EPR signal of superoxides. (ii) The added O_2 can in a same manner induces dipolar broadening of the 1.956 signal leading to its decrease. In both of these cases, Zn_i must be on the surface to be accessible to O_2. The recovery of the 1.956 signal after the pumping points out more strongly towards the dipolar broadening as a reason of its absence in O_2 rather than e^- transfer i.e. creation of O_2^-. Being unaffected in the presence of O_2, the signal with g = 1.960 may be related to the defect similar to that of 1.956

but being located in the bulk. A similar trend that is observed for emission centered at 440 nm (2.80 eV), which only partially becomes reduced under O_2-atmosphere suggests that PL emission at 430 nm (2.88 eV) and EPR signal with g ~ 1.956 are related to the species on the surface, while PL emission at 440 nm (2.80 eV) and EPR signal with g ~1.960 are related to the species in the bulk.

In short, the most pronounced features of PL emission at 430 nm (2.88 eV) and EPR signal with g~1.956 are observed in as-synthesized ZnO smoke. This indicates ZnO smoke produced by metal combustion method is non-stoichiometric. Both signals are proposed to be caused by the same species, i.e. Zn_i^+ located on the surface, since they are strongly affected by the admission of oxygen at room temperature. At the same time, we suggest the unaffected PL emission at 440 nm (2.80 eV) and EPR signal at g~1.960 to be related to Zn_i^+ located in the bulk.

3.2 Annealing in high vacuum

3.2.1 Structural and morphological changes induced by vacuum annealing

The presence of contamination from air or the residuals from the synthesis, especially if the synthesis takes place via wet chemistry routes, can strongly affect the nanoparticles surface and the related physical-chemical properties. This is particularly true for the nano-sized particles in which the contribution of surface related optical processes becomes significant. The adsorbates may act as novel, i.e. fake active sites, and / or react with some native active sites on the surface (for instance defects) transforming them into non-active centers. For instance, water can passivate oxygen vacancies and, so, quench the related PL emission – as reported by many groups [217-219]. Therefore, the additional processing treatments are essential to be applied after the synthesis in order to obtain at first a clean surface before studying the surface properties of ZnO [220]. Annealing in (ultra) high vacuum at a given temperature is considered as an efficient way to remove contaminations – a treatment that is commonly applied in surface science. In this work, annealing at $T = 773$ K in high vacuum ($P < 10^{-5}$ mbar) was adopted from previous studies and has shown to be sufficient for obtaining surfaces free of adsorbates [221]. Moreover, the same annealing treatment was employed with the intention to also provide reducing, i.e. oxygen-poor, atmosphere where corresponding type of defects are expected to be formed [222-223].

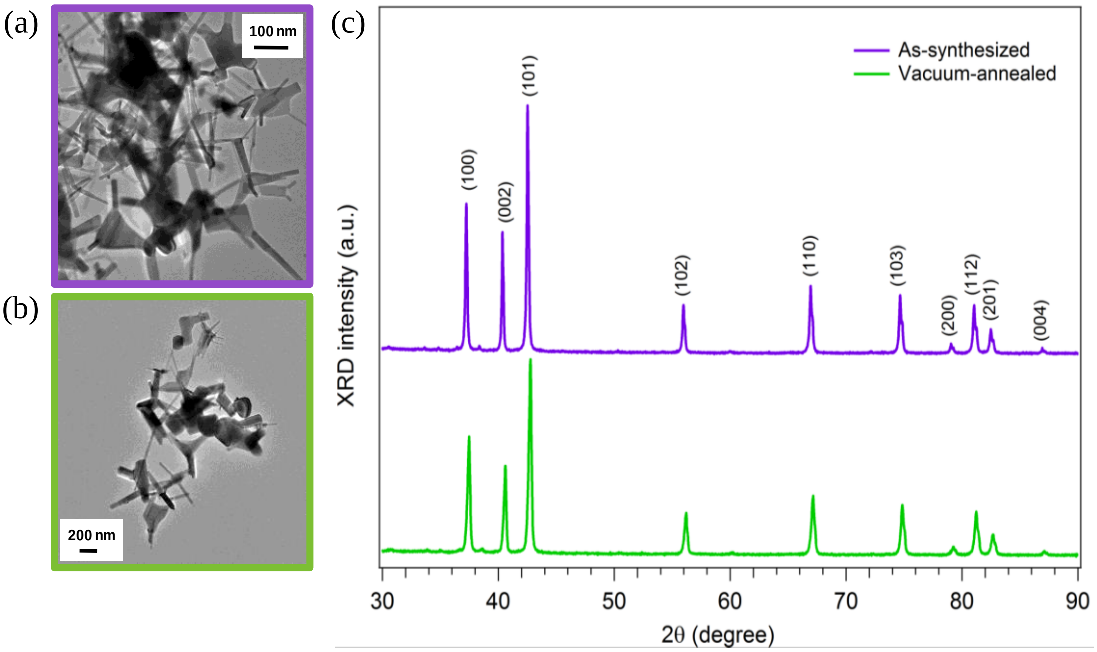

Figure 3.9 X-ray diffraction patterns of as-synthesized ZnO-air sample (violet curve) and sample annealed under vacuum at 773 K (green curve), and their corresponding TEM images (b) and (c), respectively.

Figure 3.9 (a) and (b) compare TEM images of the sample as-synthesized then subjected to vacuum-annealing treatment, respectively. TEM images show that the morphology of the vacuum-annealed sample has slightly changed when compared to the as-synthesized one. Indeed, the major difference being the disconnection of the legs from some tetrapods. The annealing treatment caused no change in terms of crystal phase and, as expected, as only one set of the same diffraction peaks (wurtzite) is seen in both XRD patterns – as shown in figure 3.9 (c). However, peak broadening and the reduction of the intensity is observed for all peaks in the XRD-pattern of the annealed sample implying that the high-vacuum annealing induces some loss of crystallinity in ZnO. Indeed, the crystalline size is found to decrease from the initial value of 88 nm to 62 nm after the annealing treatment, which is evident from Table 3.1 that summarizes lattice parameters of the two samples obtained via Rietveld analysis.

Additionally, the microstrain increased from 2.5 to 12 % i.e. almost five times upon annealing. The reduction of the crystalline size is followed by an increase of lattice strain, which reflects the situation of additional new defects introduced through vacuum annealing. A similar phenomenon has been observed by other groups when commercial ZnO nano-powders were milled with increasing milling time, and they concluded that the milling generated some defects, resulting in the broadening of the diffraction [135, 224]. This is consistent with what we observed after vacuum annealing.

Table 3.1 Comparison of lattice parameters, crystalline size and microstrain of as-synthesized then vacuum-annealed samples.

	As-synthesized	Vacuum-annealed
Lattice parameters		
a (Å)	3.250	3.250
b (Å)	3.250	3.250
c (Å)	5.207	5.207
Microstrain (%)	2.5	12.0
Crystalline size (nm)	88	62

3.2.2 XPS measurements

The X-ray photoelectron spectroscopy (XPS) was used to study the effect of vacuum-annealing on the chemical bonding and state of ZnO smoke sample. Figures 3.10 (a) and (b) show the Zn 3s and O 1s XPS spectra of the as-synthesized ZnO powders (violet) and after vacuum-annealing at T = 773 K for 1 hour (green). These spectra were obtained with a non-monochromatic Al Kα source (photon energy of hν = 1486.7 eV) and a hemispherical analyzer Phoibos 100 with a pass energy of 20 eV at normal emission. The binding energy (BE) of the Zn 3s and O 1s spectra is calibrated taking the Fermi level of metal substrate as an absolute reference, while their intensity is normalized to the same background in the low binding energy range (∼ 130 eV and ~ 523 eV for Zn 3s and O 1s, respectively). Both Zn 3s spectra are composed by only one component located at BE = 140.1 eV which is comparable to the value reported in the literature for ZnO [225]. No changes in terms of shape, intensity and BE position of the Zn 3s peak are observed upon vacuum annealing. On the other hand, the O 1s spectra – shown in Figure 3.10 (b) – consist clearly of more than one component.

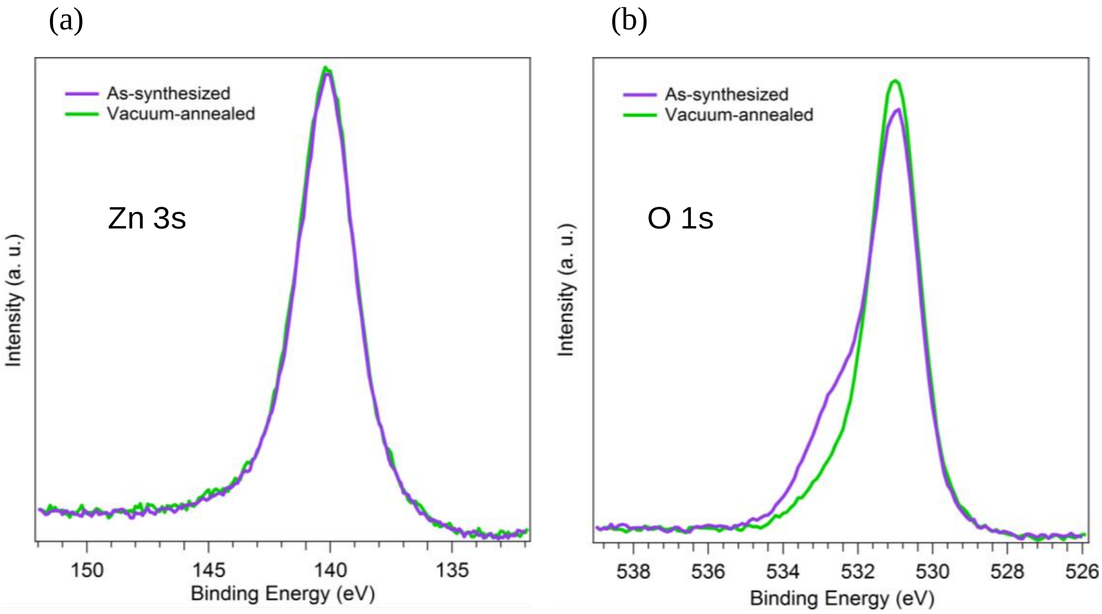

Figure 3.10 XPS spectra of as-synthesized (violet curves) and vacuum-annealed (green curves) ZnO smoke (T_{ann} = 773 K): (a) Zn 3s, (b) O1s.

Accordingly, the fitting analysis of O 1s spectra was performed by using a Shirley background and a set of Gaussian functions (see in Figure 3.11). The results of this fitting analysis showed that the most intense component is centered at 531.0 eV, while the less intense shoulder is centered at 532.5 eV. The former one corresponds to O^{2-} ions in the wurtzite structure of hexagonal ZnO [193], while the latter one is attributed to the oxygen originating from contaminations such as –OH, –CO, adsorbed H_2O and/or O_2 [226-229]. Comparing the spectra of the as-synthesized sample with the vacuum annealed sample (Figure 3.11), the ratio of integration area of peak at 532.5 eV to the one at 531.0 eV ($I_{532.5}$ / $I_{531.0}$) decreases from 0.46 to 0.15 after vacuum annealing. That indicates that the majority of contaminations previously present in the as-synthesized sample is removed upon vacuum annealing treatment.

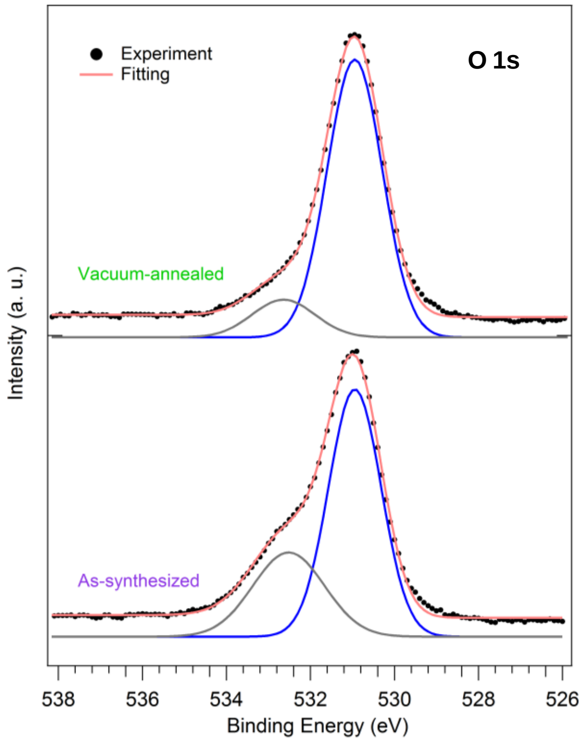

Figure 3.11 Experimental and fitted curves for normalized O 1s XPS spectra of as-synthesized ZnO smoke (bottom spectrum) and the one after annealing in vacuum at 773 K (top spectrum). The components, resulting from the fitting analysis, that correspond to O^{2-} *ions in wurtzite structure of ZnO and contaminants are indicated by the solid blue and grey curves, respectively.*

Since XPS allows to perform a semi-quantitative analysis of the elements present in the sample, the atomic ratio of Zn/O was also calculated. This ratio can be estimated by taking into account that, for a homogeneous solid, the photoelectron intensity (integration area) detected for a peak can be written as:

$$I = C \cdot \sigma \cdot F \cdot \lambda \cdot T \cdot n \qquad \text{(Equation 3.6)}$$

where C is a factor of proportionality, σ the photoelectron cross section for the specific core level, F is the incident photon flux, λ is the IMFP (inelastic mean free path, for the electrons in the sample), T is the transmission function of the analyzer, and n is the number of atoms in the analyzed volume. In practice, if we consider the stoichiometric ratio n_1/n_2 between two species distributed homogeneously in the sample, F and C cancel out and the following equation is obtained:

$$n_1 / n_2 = I_1 \cdot (\sigma_2 \cdot \lambda_2 \cdot T_2) / I_2 \cdot (\sigma_1 \cdot \lambda_1 \cdot T_1) \qquad \text{(Equation 3.7)}$$

In the present analysis, the Zn/O ratio is obtained by considering the integration areas of the peak Zn 3s and that of the main component of O 1s (BE =531.0 eV). In addition, the values for T are those tabulated for the analyzer Phoibos 100, λ_{Zn} and λ_O are provided by the NIST standard reference database for the ZnO material [230-231], while σ_{Zn} and σ_O are taken from [232-233]. According to the Equation 3.7, the Zn/O values of 1.26 ± 0.15 and 1.10 ± 0.15 are obtained for as-synthesized sample and for the one annealed in vacuum, respectively. In the first place, these values indicate that the surfaces of the samples are non-stoichiometric and that an excess of Zn is present in both. This supports well our assumption of PL / EPR couple (λ_{emiss} = 430 nm / g = 1.956) to result from Zn_i^+ in the as-synthesized sample – as reported in Section 3.1.2 and 3.1.4. Upon vacuum-annealing treatment, the decrease observed in the Zn/O ratio is a result of the Zn-excess being evaporated out of the sample surface. As discussed in Section 3.2.3, when sample is subjected to the same annealing treatment (vacuum, T_{ann} = 773 K) for PL and / or EPR measurements a greyish layer on the wall of the corresponding tube for measurements is seen – that explains the out-evaporation of excess of Zn present in as-synthesized sample.

3.2.3 Changes in optical properties induced by vacuum annealing

The influence of vacuum annealing treatment on optical properties of ZnO-smoke sample was firstly investigated by UV-Vis spectroscopy. Kubelka-Munk transformed from DR UV-vis spectra of the sample progressively annealed in vacuum ($P < 10^{-5}$ mbar) from 373 to 773 K while maintained at the given temperature for 1h are presented in Figure 3.12. By an increase of the annealing temperature up to 773 K, only a slight modification in the absorption band edge is observable. However, the alteration of the electronic structure appears in the form of tail states in the sub-band-gap region – the density of which becomes higher for the samples annealed at 773 K (inset of Figure 3.12). At the same time sample undergoes a grey coloration. This implies that excess Zn (such as Zn_i^+) previously present in the as-prepared sample is partially reduced and transformed into neutral Zn (metallic) upon vacuum-annealing treatment [103, 234], since an excess of Zn (ration of Zn/O is 1.10) was still found even in the vacuum annealed sample.

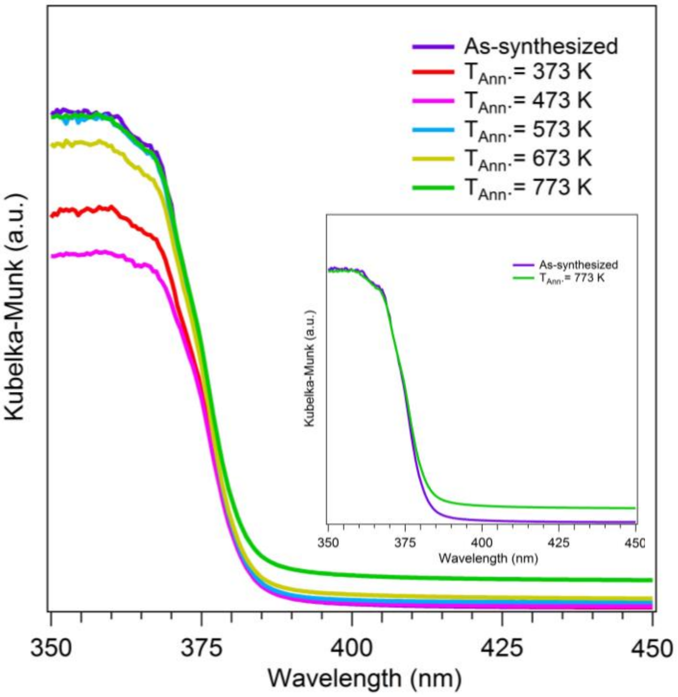

Figure 3.12 Diffuse reflectance UV-Vis spectra of the as-synthesized ZnO smoke sample in function of vacuum annealing at different temperatures. Inset focusses on the UV-vis DR spectra of as-synthesized and the one after annealing in vacuum at 773K.

PL measurements were performed in the next step to investigate how annealing in vacuum affects PL properties i.e. the related defects that were previously identified in the as-synthesized ZnO. The corresponding spectra obtained on samples annealed at different temperatures in high vacuum ($P < 10^{-5}$ mbar) are presented in Figure 3.13 (a). Overall, the PL emission was found to become strongly suppressed when the annealing temperature was progressively increased from 373 K to 773 K. The loss of the crystal quality upon vacuum annealing – that was previously shown also by XRD – is manifested in the PL properties. Indeed, the intensity of the UV-emission, which dominates in the as-synthesized sample, is strongly reduced upon annealing. This becomes most visible above 573K – the $T_{ann.}$ after which the intensity ratio between UV- and visible emissions strongly changes. Applying temperatures up to 473 K is most probably sufficient to remove the molecular water adsorbed on the surface [235] and up to that annealing temperature the shape of the spectra remain similar to the one of the as-synthesized sample. However, passing to higher $T_{ann.}$ (> 573 K) has a two-fold effect on PL properties: while some PL emissions in the visible part of the spectrum disappear (emission at ~ 440 nm / 2.80 eV), a new one is generated (emission at ~ 515 nm / 2.41 eV). Interestingly, Kang et al. [120] also observed a green emission (at 490 ~ 530 nm) after an annealing treatment similar to ours.

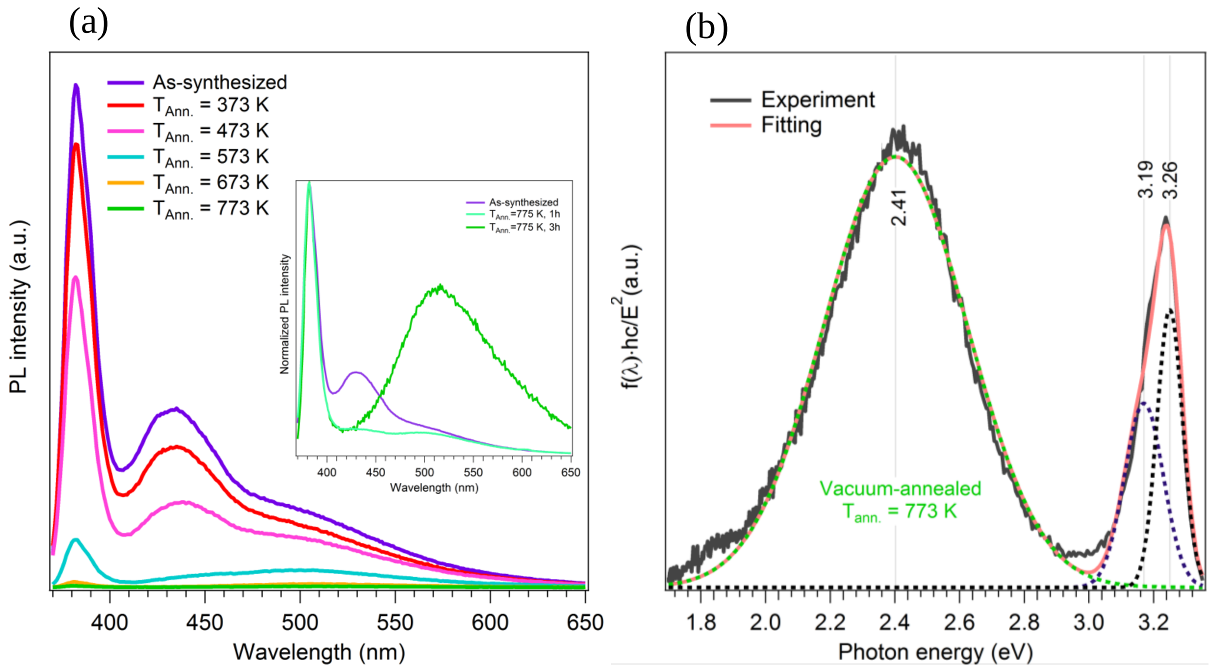

Figure 3.13(a) PL spectra of ZnO smoke sample in function of annealing temperature (1h) under high vacuum condition (P < 10^{-5} mbar). The Inset presents the normalized PL spectra corresponding to as-synthesized and the ones after annealing in vacuum for 1 h and 3h. The intensity of UV emissions has been normalized to 1. (b) Band fitting analysis performed on PL spectrum of the sample annealed 3h in high vacuum at 773 K.

Additionally, the annealing treatment duration strongly affects the PL properties of the sample as can be better seen from the inset in the Figure 3.13 (a) in which the PL spectrum of the as-synthesized sample is compared to those of sample annealed at 773 K for different annealing times. Annealing in vacuum in the first step leads to the strong reduction of the emission at 430 nm (2.88 eV), while the peak in green region seems unchanged in terms of intensity. However, the continued annealing in vacuum at such high T_{ann} induces a clear new PL emission with a maximum around 515 nm (2.41 eV). The peak intensities were normalized to the UV-band for the sake of qualitative comparison.

Table 3.2 Peak position, FWHM and integrated area obtained from fitting results.

	As-synthesized		Vacuum-annealed	
Peak position	FWHM (eV)	Integration area	FWHM (eV)	Integration area
3.26 eV (380 nm)	0.10	4.64×10^7	0.10	1.55×10^6
3.19 eV (389 nm)	0.14	4.09×10^7	0.14	1.57×10^6
2.88 eV (431 nm)	0.34	7.01×10^7	---	---
2.50 eV (495 nm)	0.55	5.78×10^7	---	---
2.41 eV (515 nm)	---	---	0.52	1.36×10^7

In order to, quantitatively, get more into what happened after the annealing 3h in vacuum at 773 K, a band-fitting analysis was performed on the corresponding spectrum and presented in Figure 3.13 (b). The UV emission can be fitted with two Gaussian bands – which exhibit the same maximum (3.26 and 3.19 eV) and comparable FWHM (~ 0.1 eV) to those previously shown in the band-fitting analysis of as-synthesized sample (Figure 3.5). Finally, the emission in visible range that develops upon vacuum annealing can be reproduced by a

Gaussian curve of similar FWHM (~ 0.5 eV) that is centered at 2.41 eV (515 nm). PL emission peaking at 2.50 eV (495 nm), initially observed in as-synthesizes sample is either absent or red-shifted to 2.41 eV (515 nm) in the spectrum of vacuum annealed sample. In conclusion, the vacuum annealing treatment at 773 K reduces the emission at 2.88 eV (430 nm) and the emission at 2.50 eV (495 nm), while the new emission is observed at 2.41 eV (515 nm). All fitting parameters are summarized in Table 3.2. The integration area of the UV emission contributing in the spectrum of annealed sample is ~ 30 times smaller when compared to its initial value in the as-synthesized sample. Again, this implies a significant loss of crystal quality and matches well with the XRD results. The emission at 2.88 eV (430 nm) is hardly detected in annealed sample demonstrating the strong reduction of this emission upon vacuum annealing. The emission with maximum at 2.50 eV (495 nm), contributes in the as synthesized sample with $I_{2.50}$ / $I_{3.26}$ = 1.25 (integration area of emission at 2.50 eV divided by that of UV-emission). The contributions of the new emissions at 2.41 (515 nm), when taking the integration area of the UV-emission as a reference, is $I_{2.41}$ / $I_{3.26}$ = 8.77.

The intensity reduction of the emission at 2.88 eV (430 nm) upon vacuum annealing is in good agreement with our hypothesis (based on UV-Vis absorption) of neutral zinc being generated upon vacuum annealing treatment. This is moreover supported by high mobility of Zn_i that exhibits migration barrier of only ~ 0.54 eV and can diffuse onto the surface [65]. On the other hand, vacuum annealing corresponds to reducing condition under which, Zn_i^+ can easily be reduced into Zn^0. The similar phenomenon was also shown by Repp et al. [103] who found the similar color change to grayish after annealing the zinc-rich ZnO quantum dots. We have also noticed a grayish layer on the walls of the PL-tube after annealing, which further proves desorption of neutral i.e. metallic zinc from our sample. Green emission is measured in both, as-synthesized sample and the one after annealing at 773 K in vacuum, but with different maximum positions, 2.50 eV (495 nm) and 2.41 eV (515 nm) – most probably indicating that different type of defects are behind their origin in the two samples.

3.2.4 EPR spectra of vacuum annealed samples

Sample subjected to the same vacuum annealing steps as in section 3.2.1, was also investigated by EPR spectroscopy. The corresponding spectra are presented in Figure 3.14 (a) together with the EPR spectra ranging from g = 1.98 ~ 1.94 (b). Compared to EPR spectrum of the as-synthesized ZnO smoke, the axial signal with $g_{||} = 1.956$ and $g_{\perp} = 1.957$ completely disappears upon vacuum-annealing whereas almost no changes were observed in terms of shape and intensity for the peak resonating at g = 1.96. Simultaneously, new features at g > 2.00 (species C in Figure 3.15) appear.

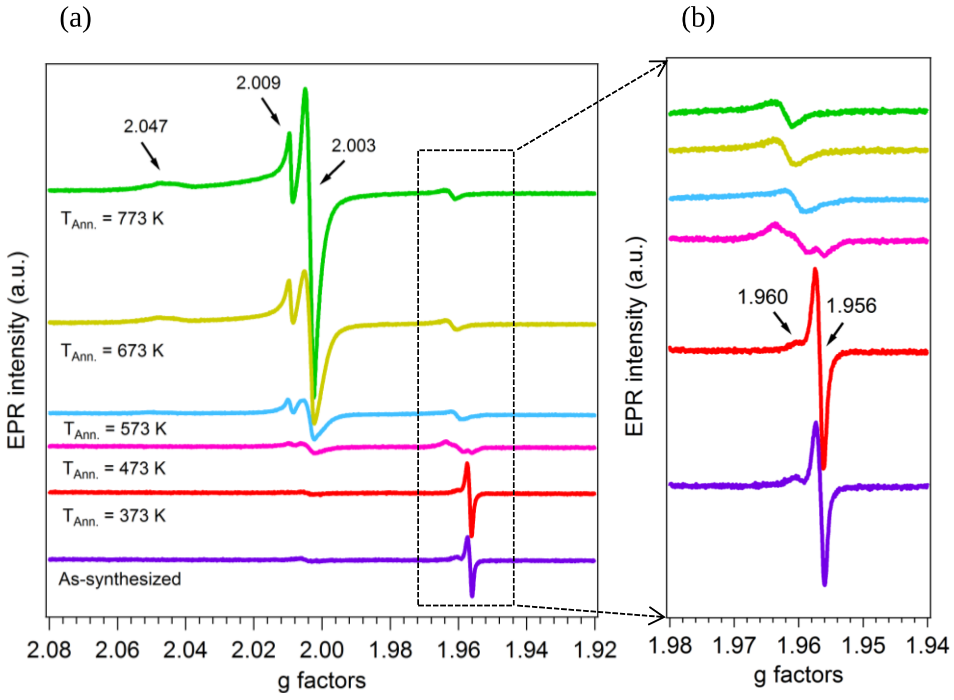

Figure 3.14 (a) EPR spectra of ZnO smoke sample in function of annealing temperature under high vacuum condition (P < 10^{-5} mbar); (b) zoomed region of EPR spectra from g = 1.98 to 1.94.

Annealing under strongly reducing, i.e. vacuum conditions, on one hand, induces an evaporation of Zn^0 driven onto the surface (the decrease of ration of Zn/O after such treatment), on the other hand, it also leads to a loss of oxygen and generates, beside oxygen vacancies, various types of reduced species or even conduction electrons. This is mostly pronounced in the case of reducible oxides such as ZrO_2, as shown by Gionco et al. [236]. The generation of oxygen vacancies can be depicted by the Equation 3.8:

$$ZnO \rightarrow ZnO_{1-x} + x\, V_O^{+} + x/2\, O_2 + x\, e^{-} \qquad \text{(Equation 3.8)}$$

In order to fully understand the EPR signal at $g > 2.00$ that we have detected after vacuum-annealing, a simulation of the spectrum recorded after annealing at 773K (green curve in Figure 3.14 (a) and (b)) has been undertaken (Figure 3.15). The corresponding parameters of each species obtained by simulation are summarized in Table 3.3, in which as-synthesized ZnO (previously shown in Figure 3.7 (b)) and sample annealed at 573 K are also compared. The complex signal at $g > 2.00$ consists of three overlapping contributions with the following g-components:

I. $g_{iso} = 2.003$ (species C in Figure 3.15, green doted signal).
II. $g_x=2.002$, $g_y=2.009$ and $g_z = 2.043$ (species D in Figure 3.15, yellow dotted signal)
III. $g_x=2.002$, $g_y=2.009$ and $g_z = 2.047$ (species E in Figure 3.15, brown dotted signal)

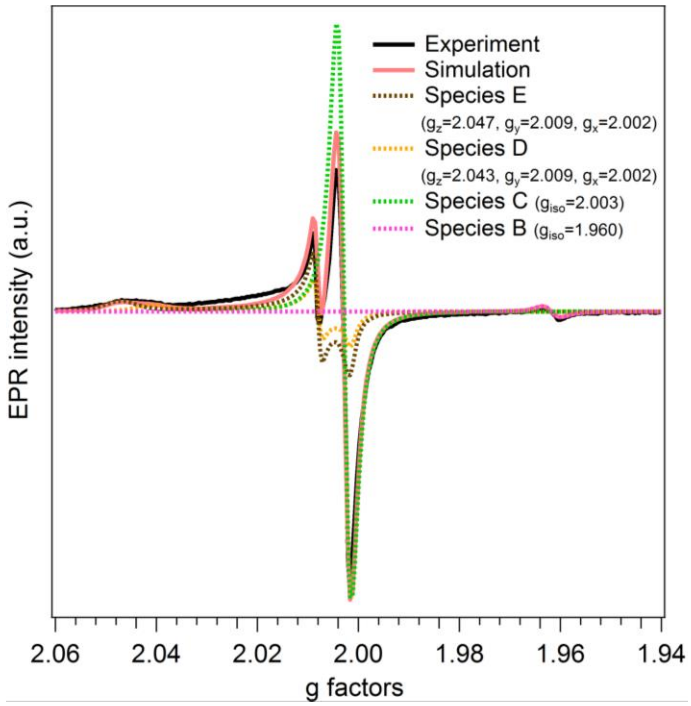

IV.

Figure 3.15 Simulated EPR spectrum of sample annealed in vacuum at 773 K with all species that contribute.

Table 3.3 Parameters of as-synthesized, 573 K and 773 K vacuum-annealed ZnO obtained by EPR simulation.

Samples	g-factor	Contribution of each center	Double integrated area (a.u.)	Double integrated area of each center
As-synthesized	$g_{\parallel}$= 1.957 $g_{\perp}$= 1.956	9%	4	0.36
	g_{iso}=1.960	91%		3.64
Vacuum-annealed @573 K	g_z=2.047 g_y=2.009 g_x=2.002	21%	65	14
	g_z=2.043 g_y=2.009 g_x=2.002	11%		7
	g_{iso}=2.003	68%		44
	g_{iso}=1.960	100%	3	3
Vacuum-annealed @773 K	g_z=2.047 g_y=2.009 g_x=2.002	17%	400	68
	g_z=2.043 g_y=2.009 g_x=2.002	9%		36
	g_{iso}=2.003	74%		296
	g_{iso}=1.960	100%	2	2

One should note, before assigning these components, that the intensity of all three C, D and E species becomes stronger with the increase of annealing temperature – the double integrated area increased five times when the annealing temperature raised from 573 K to 773 K (see Table 3.3). Since all of three species follow in parallel the same trend within the annealing, it illustrates their origin might have something in common.

Among the three components, two of them (D and E) are rhombic signals that differ only in their g_z-component. They can be correlated to superoxide anion (O_2^-) at the surface of ZnO [128, 145-146, 237]. At metal oxide surfaces, superoxide anions are usually detected in the following sequence: the oxide is annealed under vacuum and a small amount of gaseous oxygen is added to the sample. This was shown to induce electron transfer from the solid to surface O_2 and to form surface-adsorbed superoxide ions, which result finally in an EPR signal of specific g-tensor. Yet, in our case, no oxygen was added after the annealing treatment and despite this an EPR signal with g-tensor of superoxide anion is measured. This unambiguously demonstrates that an effective loss of oxygen occurred during the annealing which served then for the interaction with electrons from ZnO smoke sample, resulting in the formation of superoxide radical anions. The different g_z values of species D and E, which are known to be the most sensitive, point out O_2^- species experiencing different surroundings.

Considering that lattice oxygen was desorbed upon annealing, this strongly implies that V_O must have been consequently created. Therefore, the third signal with $g_{iso} = 2.003$ was tentatively assigned to this type of defects, i.e. the paramagnetic V_O^+. This value fits well with that of an electron trapped in an oxygen vacancy ($\sim g_e = 2.002$ for a free electron). Going back to the PL results obtained after vacuum annealing, the appearance of a green luminescence with maximum at 2.41 eV (515 nm) can be brought into correlation with $g = 2.003$, and hence to V_O^+. The assignment of EPR at $g \sim 2$ to V_O^+ is in line with results obtained in oxygen-deficient ZnO samples by many groups [24, 135, 139-140].

The creation of V_O^+ in ZnO is not supported by many theoretical studies on the basis of thermodynamically equilibrium condition [65, 68], however, our ZnO sample was produced in a highly non-equilibrium process, under which V_O^+ may be formed. In addition to this, we should keep in mind that our ZnO sample is in the nanoscale range – which may dramatically influence the formation energy. This was recently shown on the example of ZrO_2 by Puigdollers and coworkers [238]. They have calculated the energy formation of oxygen vacancies in small ZrO_2 clusters to be much smaller than in those of larger size. For example, for a periodic (101) zirconia surface, the calculated formation energies of three- and four-coordinated oxygen vacancies are +5.97 and +5.67 eV, respectively, while in nanoparticles, the formation energy is lowered down to only ~2.62 eV for two- coordinated oxygen vacancies.

From this section, we can conclude that new emission at 515 nm (2.41 eV) and EPR signal at g = 2.003 are formed upon vacuum annealing – indicating both of them are due to V_O^+. This proposition is strengthened by the detection of EPR signal related to superoxide ions under such thermal treatment without any admission of oxygen. Simultaneously, upon such treatment, the emission at 430 nm (2.88 eV) and g = 1.956 are strongly reduced implying the transforming of Zn_i^+ to Zn^0. This is supported by the decrease of the Zn/O ratio (initial ration of Zn/O with the value of 1.26 vs. final one with 1.10) due to evaporation of Zn^0 from XPS results, and also the observation of grey color of the vacuum annealed sample.

3.3 Reannealing in oxygen

In section 3.2 we have shown how vacuum annealing may affect both optical and paramagnetic properties of ZnO smoke. Based on the presence of an EPR signal specific of superoxide anions – while no molecular oxygen was admixed to the sample – we have suggested that O^{2-}_{latt} were desorbed upon such reducing treatment. Hence, for those spectroscopic features that appear in the course of such annealing (i.e. emission at 2.41 eV (515 nm) and EPR signal with g = 2.003) we have hypothesized them to be correlated to oxygen vacancies. To prove this hypothesis, the sample that was previously annealed (at 773K and $P < 10^{-5}$ mbar) was subjected to an O_2-re-annealing treatment – having in mind that such oxidizing treatment might compensate the loss of oxygen from the lattice and finally reduce the total amount of oxygen vacancies [96]. The role of O_2 is to re-oxidize the sample and induce the recovering of its properties to at least the stage of the as-synthesized sample – if even not to defect-less state. However, we have to keep in mind that such treatment involves two competing processes: the formation of oxygen vacancies (as due to the high $T_{ann.}$) and/or their passivation (as due to the presence of O_2). This was nicely evidenced by Drouilly et al. [96], who used two types of commercial ZnO and demonstrated the competitive process of creating and filling up oxygen vacancies. When $T_{ann.} > 473$ K, the generation of oxygen vacancies overcomes their passivation (or filling-up) even in an O_2-containing atmosphere, while for $T_{ann.} < 473$ K, only filling up of oxygen vacancies in such an atmosphere occurs.

The optical properties were checked at first and the Figure 3.16 displays the DR UV-vis spectra of the as-synthesized (violet curve), vacuum-annealed (green curve) and re-oxidized (brown curve) ZnO smoke. From Figure 3.16, it is found that the spectrum of the O_2-reannealed sample recovers to the initial form. Moreover, the sample also recovered its white color after being re-oxidized.

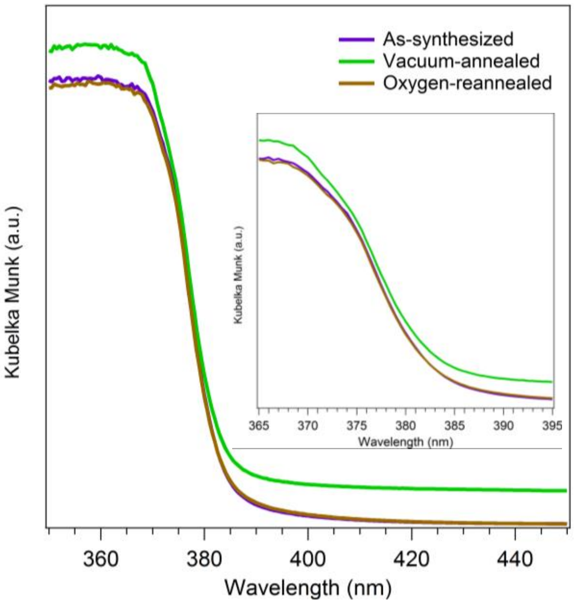

Figure 3.16 DR UV-Vis spectra of as-synthesized then vacuum-annealed then re-annealed in oxygen ZnO sample. The inset is the magnified UV-vis DR spectra corresponding to each sample compared.

PL spectra of the vacuum annealed sample and that of the re-annealed in oxygen one are compared in Figure 3.17. The PL spectrum obtained after O_2-re-anneling is very similar to the spectrum obtained on the as-synthesized sample (see Figure 3.4, section 3.1.2.). However, a slight red shift (10 nm, 0.07 eV) of the emission at 430 nm / 2.88 eV (in the as-synthesized one) in violet region is observed, implying that the defects responsible for the emission at ~ 440 nm (2.80 eV) are experiencing a different environment after annealing in O_2 than in the as-synthesized sample. A significant contribution of the emission at ~ 495 nm (2.50 eV) is observed in the spectrum of the re-oxidized sample. This can be the result of the competition between V_O-generation (high annealing temperature) and V_O-passivation (presence of O_2) –

as previously reported by Drouilly et al. [96]. As expected, sample previously annealed in vacuum recovers it crystallinity back once re-oxidized exhibiting again all spectroscopic features initially observed in as-synthesized sample.

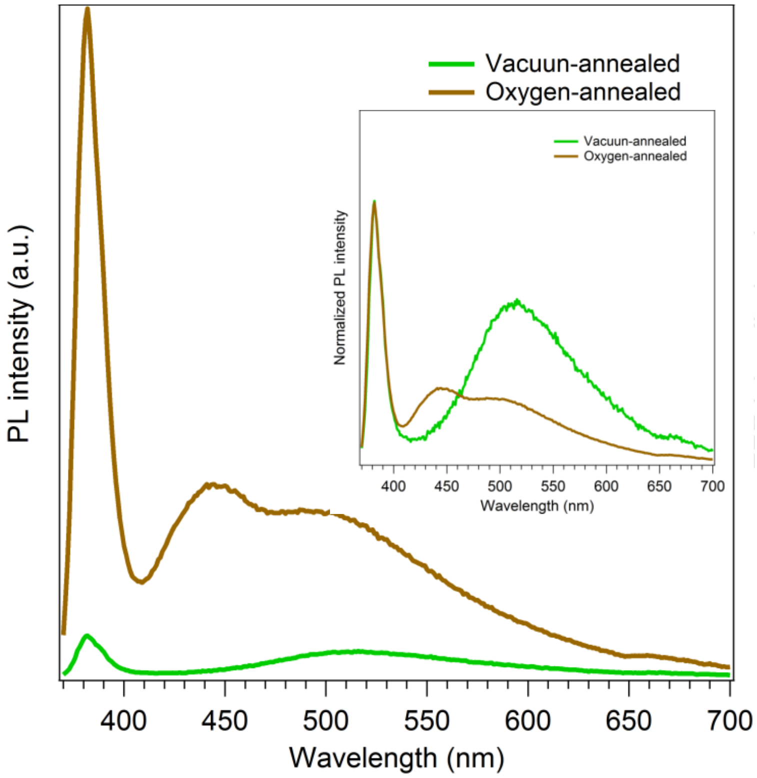

Figure 3.17 Comparison of PL spectra of vacuum-annealed (green curve) and oxygen re-annealed (brown curve) sample. The inset presents correspondingly normalized PL spectra for which the intensity of UV emissions has been normalized to 1.

This is also illustrated by the presence of the rhombic signals specific of superoxide anions (g_z = 2.047-2.043, g_y = 2.009 and g_x = 2.002) together with the isotropic one centered at g = 2.003 (Figure 3.18 (a), inset, brown curve) – the origin of which we once again suggest to be in correlation to V_O^+. The presence of signals of superoxide might be a consequence that the sample in contact with molecular oxygen was not efficiently extracted before the EPR spectrum was monitored. Overall, upon oxygen annealing, the intensity of EPR signal with g =1.960 decreased while g = 1.956 reappeared (see Figure 3.18 (b)). Having in mind that the signal with g = 1.96 is associated with bulk Zn_i^+, its oxidation, upon O_2-presence, results in the EPR silent Zn^{2+} explaining its intensity reduction. On the contrary, the oxidation of the

Zn^0_{surf} (that was produced out of $Zn_i^+{}_{surf}$ reduced upon vacuum annealing) to Zn_i^+ makes the signal at g = 1.956 to reappear. Finally, the recovery of signal resonating at g = 1.956 is in line with the recovery of the broad emission centered at 440 nm (2.80 eV) – for which the same explanation can be given. All the EPR signals detected after O_2-reannealing appear with much lower intensity whereas the lineshape remains the same as in as-synthesized sample (see Figure 3.7, EPR of as-synthesized sample, section 3.1.4).

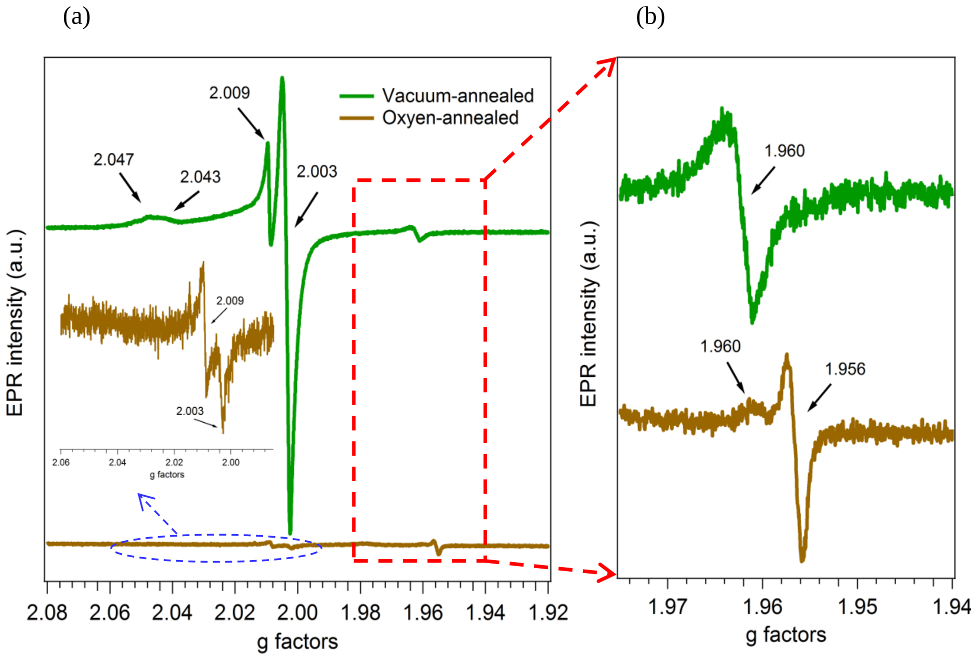

Figure 3.18 EPR (a) and magnified spectra of rectangular part in (b) of vacuum annealed (green curve) and oxygen re-annealed (brown curve) samples. Inset in (a) is the magnified spectrum of elliptical part.

As observed from the features that were collected after re-annealing treatment in oxygen, we summarized that this treatment can reduce the concentration of oxygen vacancies generated by vacuum annealing, but it is not efficient to fill in all at 773 K, since emission at 515 nm (2.41 eV) and weak EPR signal at g = 2.003 are still observed. In addition to this, it causes the transformation from Zn^0 to Zn_i^+ on the surface and/or from Zn_i^+ to Zn^{2+} in the bulk according to the detection of emission at 440 nm (2.80 eV) and EPR signals at g = 1.960 and g = 1.956.

3.4 Defects generated upon vacuum-annealing: interaction with H_2O

Adsorption of gases at the surface of ZnO has been explored since the 1960's [239-240]. It has been reported that surface defects are very sensitive to adsorption of gaseous molecules, resulting in surface adsorbates that can strongly influence the spectroscopic properties of semiconducting nanoparticles. For instance, Reish et al. [241] studied the influence of exposing the annealed sample to electron and hole scavengers on the PL emission spectra. They found that when the previously annealed sample was exposed to O_2 (electron scavengers) the quenching of visible emission was observed, while the exposure to methanol (hole scavengers) led to the recovering of the visible emission. Therefore, some molecules (H_2, O_2, CO, NH_3, H_2O) can act as probes since they can modify the electrical activity of defects which is then reflected in the changes of corresponding spectroscopic signatures [242-243].

Water has been used to investigate the reactivity of defects via its dissociation over ZnO surface. The surface of ZnO contains Zn^{2+}, Zn^{+}, O^{2-} and O^{-} ions and oxygen vacancies that may participate to the dissociation of water. The effects of water on electrical and other properties of zinc oxide depend on the adsorption site involved [244]. The dissociation of water taking place on oxygen vacancies has been proved by Noei and coworkers [245], and they concluded that the vibration at 3620 cm^{-1} correspond to OH group formed by the dissociation of water on oxygen vacancy sites located explicitly on the polar oxygen terminated ZnO surface (000-1). Similarly, Drouilly et al. also reported the same origin of a unique IR band but positioned at 3528 cm^{-1}.

Since, upon water adsorption, the oxygen vacancy is transformed into an OH group – the spectroscopic feature that is specific of oxygen vacancy must experience significant alterations if not even completely disappear. Due to the possible/facile dissociation of water on oxygen vacancies, water is very useful to probe these defects in metal oxides [246-247]. Before water adsorption measurements, the sample was annealed up to 773 K under dynamic vacuum, cooled down to 300 K and then exposed to water vapor (P = 10 mbar). It has to be emphasized that, for this experiment, we used the vacuum-annealed sample that was pumped for several days, which explains the absence of EPR signals specific of superoxide anions (green curve in Figure 3.14). Our purpose was to isolate the contribution of oxygen vacancies at g = 2.003 from those of superoxide anions. Sufficient time of pumping, allowed us to clearly point out that V_O^+ species were affected by the interaction with water.

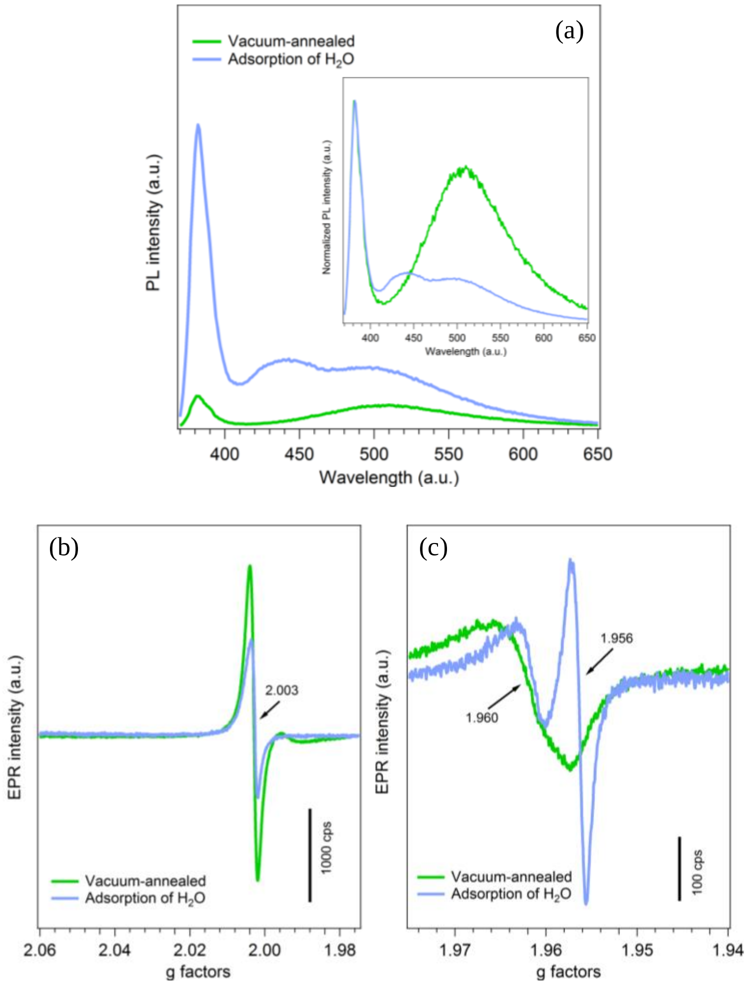

Figure 3.19 Spectroscopic characterization of ZnO after vacuum-annealing (green curve) and adsorption of water (P =10 mbar) (blue curve). (a) PL spectra. Inset presents PL spectra after normalizing the intensity of UV emissions to 1. (b) and (c) EPR spectra ranging from 2.060 to 1.985 and 1.975 to 1.940, respectively.

In Figure 3.19 (a) PL spectra of vacuum-annealed sample before (green curve) and after (blue curve) adsorption of H_2O are compared. The EPR spectrum of vacuum-annealed sample (Figure 3.19 (b) and (c), blue curve) only shows one signal in the range of $g > 2$. This further supports that $g = 2.003$ was overlapping with signals related to superoxides – the former one remains while the latter one is eliminated by pumping O_2 away. We can see that the intensity of UV emission increases strongly after H_2O adsorption – implying that surface crystallinity might be recovered due to incorporation of O^{2-} into the lattice of ZnO. At the same time, from the inset in Figure 3.19 (a) it is clear that the intensity of green emission is significantly reduced upon interaction with water. Following the previously mentioned rule in which oxygen vacancies can be passivated by water – the origin of the emission at 515 nm (2.41 eV) can be correlated to this specific defect. The reappearance of emission at 430 nm (2.88 eV) although slightly shifted to 440 nm (2.80 eV) upon water interaction is also not surprising. Indeed, it fits well to the previously proposed mechanism [248], in which Zn_{surf}^{2+} is, by accepting an electron from V_O^+, transformed into Zn_{surf}^+. This whole process can be simply described by Figure 3.20.

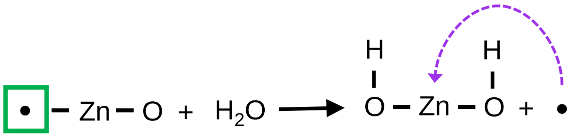

Figure 3.20 Scheme of PL and EPR active oxygen vacancy (V_O^+) filled by water. ⊡ and • here present V_O^+ and electron (e^-), respectively.

The newly formed Zn^+ serves for the interaction with photon – in a similar manner as Zn_i^+ does in the as-synthesized sample. It experiences, however, a different environment which explains the small shift in emission maximum. Matching results were also obtained by EPR spectroscopy upon water adsorption (Figure 3.19 (b) and (c)). When compared to the spectrum taken before adsorption i.e. on vacuum annealed sample (green curves in Figure 3.19), a decrease of the isotropic EPR signal at $g = 2.003$ (blue curve in Figure 3.19 (b)) can be observed along with an increase of $g = 1.956$ (blue curve in Figure 3.19 (c)). This strongly supports our assignment of $g = 2.003$ signal to oxygen vacancies (V_O^+) whereas the one with $g = 1.956$ can be attributed to Zn^+_{surf}, according to the same explanation as it was given for the reappearance of violet emission in the course of water-dissociation over ZnO surface. It is clearly seen that emission at 515 nm (2.41 eV) and EPR signal at $g = 2.003$ are reduced, which furthermore supports the assignments of the two features to V_O^+. Apparently, water molecule can act as an effective probe to identify oxygen vacancies.

3.5 Post-growth annealing in an excess of Zn or at high P_{O_2}

Inducing intrinsic defects into ZnO in a controlled way via certain post-treatments, like Zn- or O-ion implantation or annealing in proper atmosphere, may help discriminate the spectroscopic features and link them to defects – from which they originate. For example, in the work of Stavale and coworkers [249] the role of lattice defects in crystalline ZnO films was studied by combining photoluminescence spectroscopy and STM. They analyzed the PL features after either Zn- or O-ion implantation. They observed: (a) the reduction of the red emission (~730 nm) and the enhancement of the yellow emission (~ 595 nm) when O-ion implantation was applied; (b) the reduction of green emission (at ~535 nm) when Zn-ion was implanted. They, therefore, suggested that the green, yellow and red emissions were related to V_{Zn}, O_i, and V_O, respectively [249]. In an another study, by Børseth et al., annealing ZnO in O_2 and Zn atmosphere led to the assignment of PL emissions at ~ 528 and ~ 490 nm to V_{Zn} and V_O, respectively [124]. A variety of post-annealing treatments were also undertaken by many groups [134, 250-251] to control and identify the defects.

In this section, to intentionally affect the natural distribution of defects present in ZnO smoke, we adopted two annealing treatments which are based on the following trends: O_i and/ or V_{Zn} are favorably generated through annealing in O_2, while Zn_i and/ or V_O are formed preferably upon annealing in an excess of Zn [196].

3.5.1 Annealing in an excess of Zn

Figure 3.20 (a) compares the PL spectra of as-synthesized sample and the one subjected to annealing in Zn. As compared to as-synthesized sample (in Figure 3.20 (a)), annealing in Zn vapor causes an obvious intensity decrease of all the emissions. In addition to this, the emission at ~ 430 nm (2.88 eV) is strongly reduced, while the emission at 515 nm (2.41 eV) is generated upon such annealing according to the normalized PL spectra of these two samples shown in Figure 3.21 (a), inset. These observations after annealing in Zn are quite similar to that after annealing in vacuum. The reduction of the PL intensity, within the 370 nm to 700 nm range, implies that the surface of ZnO is somehow passivated in the course of this experiment. Most probably, when annealed together with ZnO sample, the metallic Zn firstly evaporates and adsorbs in the Zn^0 form at the surface where it acts as a non-radiative center that may quench luminescence. Interestingly, the effects of annealing in Zn on PL properties of as-synthesized ZnO smoke are similar to those observed after vacuum annealing (see Figure 3.13, Section 3.2.3). This supports our suggestion that the interstitial zinc, which is in the form of Zn_i^+ in the as-synthesized sample (as provided by PL emission at 430 nm (2.88 eV) and EPR signal at g = 1.956), becomes Zn^0 upon vacuum annealing, then diffuses to the surface to segregate there – leading to the loss of PL intensity. We know, however, from XPS (Section 3.2.2) that Zn^0 will not remain on the surface but most probably evaporates totally out of the sample. A more careful analysis of the intensity ratios of emission at 2.41 eV (515 nm) to that at 3.26 eV (380 nm) showing the value of 0.09 and 0.42 before and after annealing, respectively, demonstrates that the emission at 2.41 eV (515 nm) is favored when the sample is annealed in Zn vapor (Figure 3.21 (a), inset). Both the temperature at which Zn was evaporated as well as its presence during the annealing can be responsible for the presented green emission tendency. Similar results were also demonstrated by Cizek et al. [118], who showed green emission (2.47 eV / 502 nm) was generated after annealing hydrothermally as-grown ZnO single crystals, so they concluded that the green emission originates from oxygen vacancies. This interpretation is in good agreement with what we have observed, especially since it is further supported by the detection of the isotropic EPR signal with g = 2.003 (Figure 3.21 (b), light violet curve) – the signal that was also resulting from the vacuum-annealing treatment (section 3.2.4). In that case, however, this signal was only a part of the complex signal that was also containing components specific of superoxide anions. These components (g_z = 2.047, g_y = 2.009) cannot be detected in EPR spectrum obtained on the ZnO sample annealed in Zn although so that we propose that oxygen vacancies are created implying that oxygen must have been also removed from the ZnO lattice. Unlike the vacuum annealing case (excess of zinc is only present as Zn_i), we suggest that the presence of rather high amount of the initially added metallic Zn consumes any oxygen if desorbed from the ZnO lattice. In the spectrum of Zn-annealed sample, we note also an additional signal with g = 1.964. This signal is of a comparable intensity and overlaps with the signal previously detected for ZnO smoke under almost all examined conditions. A very small difference in the g-factor between these two signals implies on the similar / same type of paramagnetic species to be responsible for this signal but which are experiencing a different crystallographic environment. We should keep in mind that annealing in Zn not only favors formation of Vo^+ but also of Zn_i^0.

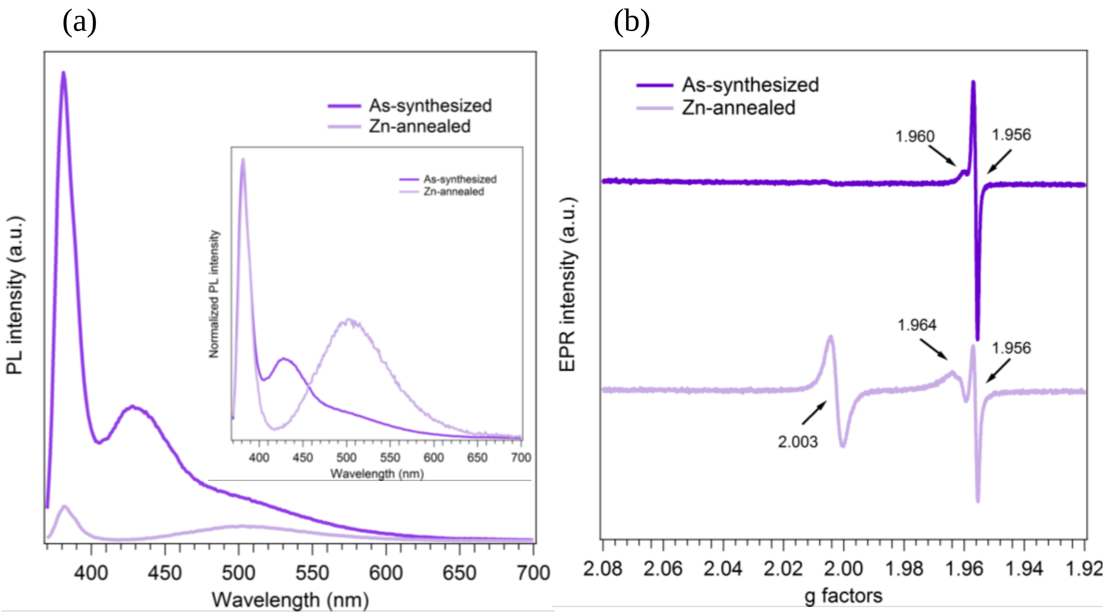

Figure 3.21 Normalized PL (a) and EPR (b) of ZnO smoke sample before (violet curve) and after (light violet curve) annealing in Zn. Inset is normalized PL spectra, and all the emissions have been to normalized to the UV emission in as-synthesized sample.

3.5.2 Annealing in high P_{O_2}.

In another set of experiments, ZnO smoke sample was systematically annealed at different P_{O_2}. Again, the effect of annealing on the defects naturally distributed in as-synthesized ZnO smoke was studied by PL. In Figure 3.22 we compare PL spectrum of as-synthesized sample with the spectra obtained on ZnO smoke annealed at different partial pressures of oxygen (100 ~ 300 mbar). For the lowest P_{O_2} (100 mbar, brown curve in Figure 3.22), we observe that both the intensity and shape of the spectrum resemble to that of the as-synthesized sample (violet curve) – except that the emission at 430 nm (2.88 eV) decreases on the benefit of a new broad photoluminescence developing in the 500 ~ 650 nm range. A slight intensity loss can be detected for the UV-emission as well. This becomes more and more visible and, finally, after multiple O_2-annealing – when P_{O_2} reaches 300 mbar (orange curve in Figure 3.22) – an intense and broad emission located at ~ 590 nm (2.10 eV) is clearly observed.

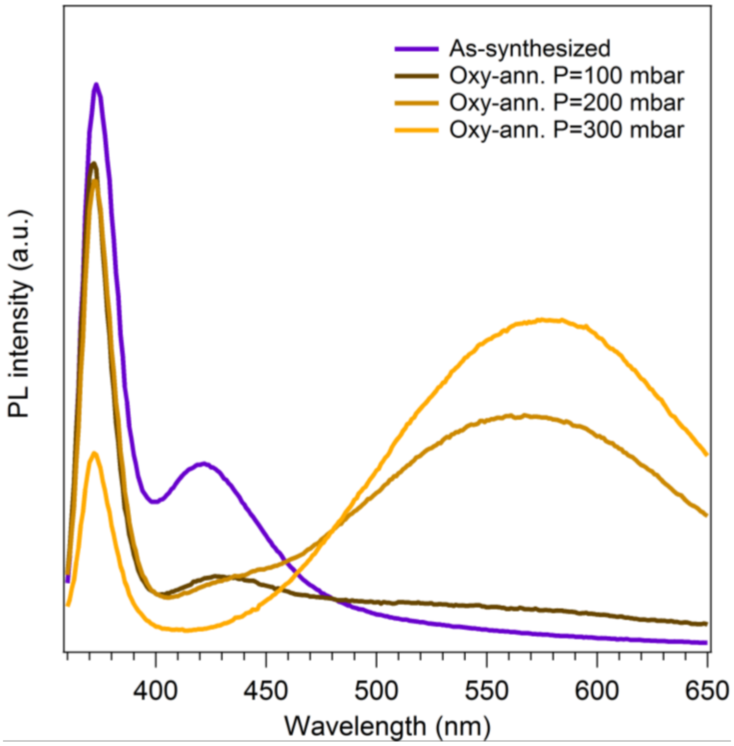

Figure 3.22 PL spectra of ZnO smoke systematically annealed at different oxygen pressures.

A strong intensity decrease of UV-emission indicates also that new defects are formed in the ZnO lattice. As for the yellow emission, according to the literature, it is almost systematically observed when the sample was either fabricated or intentionally post-annealed in oxygen-rich condition [139, 249, 252-253]. For instance, Gheisi et al. [126] not only observed the yellow emission in as-synthesized sample, as due to an excess of oxygen during the synthesis, but in addition they found that its intensity increases when annealing the sample in O_2. This strongly supports the origin of yellow emission to be related to oxygen interstitials. According to calculations by Janotti [65], the position of doubly charged oxygen interstitials is located at ~1.5 eV above the valence band – which is in line with the experimentally observed PL maximum. Both experimental and theoretical results demonstrate that yellow emission should result from oxygen interstitials. Multiple annealing in oxygen in this work seems to be in good agreement with that reported in the literature [125] and the correlation of an intensity increase of yellow-green emission under systematic increase of oxygen partial pressure supports well the origin of this emission to be related to O_i. Moreover, Stavale and coworkers [249] claim that oxygen interstitial results from an additional O^{2-} ion in an octahedral lattice site of ZnO. Being diamagnetic this species is obviously absent in our EPR spectra measured on O_2-annealed samples. As expected for the conditions applied, we also note the absence of emission at 430 nm (2.88 eV) after multiple annealing in oxygen. Certainly, high oxygen pressure and annealing at 773 K lead to the oxidation of Zn_i^+ transforming it into an optically non-active center / non-radiative site.

In short, two extreme thermal treatments, zinc-rich (zinc vapor) and oxygen-rich (high pressure of oxygen), are applied to as-synthesized samples to further identify the type of defects. We found that the emission at 515 nm (2.41 eV) appears after annealing in zinc vapor, the position and growth condition of which are quite similar to those of ZnO smoke annealed in vacuum. This further proves that this emission is due to V_O^+. The emission at 590 nm (2.10 eV) appears after annealing in high pressure of oxygen, and it is rationalized to assign it to O_i considering the O-rich atmosphere applied.

3.6 Catalysis as a probe of the surface state and reactivity

3.6.1 General features on the model MBOH reaction

In heterogeneous catalysis, the active sites are located at the extreme surface. Hence, catalytic model reactions can be used as a very sensitive tool to characterize the surface of solids and appreciate the influence of the some key synthesis parameters, pretreatment conditions, adsorbates or defects on the surface reactivity [254]. The 2-methyl-3-butyn-2-ol (MBOH) molecule was shown to react following different routes depending on the acid base properties of the surface (Figure 3.23). Upon acidic route, dehydration of MBOH leads to the formation of 3-methyl-3-butene-1-yne (Mbyne) and / or prenal. Basic route leads to the equimolar formation of acetone and acetylene. Being more sensitive to basicity, this reaction is commonly used to compare the basicity level of a series of catalysts and it was already used to evaluate the influence of oxygen vacancies on the basic reactivity of zinc oxide [25]. Upon ZnO, despite the presence of both acidic sites (Zn^{2+}) and basic sites (O^{2-}) respectively evidenced by adsorption of basic and acidic probe molecules in static conditions [255-256], only the basic reactivity is observed [25].

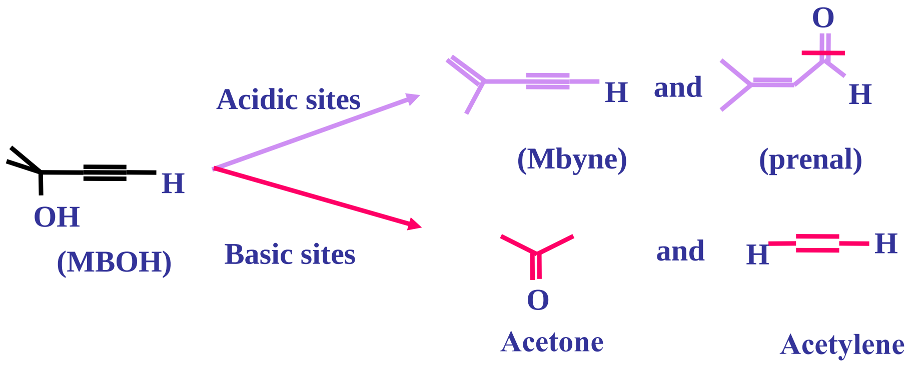

Figure 3.23 Reaction pathways of MBOH conversion depending on the acidic and basic routes

In fact, upon the basic route, an acid-base pair is involved (Figure 3.24): the basic site, usually an oxide anion, initiates the reaction by abstracting a proton from an organic molecule R–H and the resulting intermediate R^- anion transitorily adsorbs on a neighboring acid site to be further transformed in the adsorbed products, that finally desorb from the surface, regenerating the active site [257].

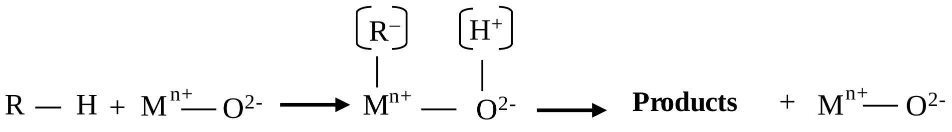

$$R - H + M^{n+}\!-\!O^{2-} \longrightarrow \overset{\overset{(R^-)}{|}}{M^{n+}} - \overset{\overset{(H^+)}{|}}{O^{2-}} \longrightarrow \textbf{Products} + M^{n+}\!-\!O^{2-}$$

Figure 3.24 Involvement of an acid-base pair in a basic catalytic reaction

Considering that acetone and acetylene are expected to be formed in equimolar ratio upon decomposition of MBOH molecule, it is very simple to discuss the basicity of a series of samples, simply comparing their conversion level.

However, in some cases, a deactivation upon reaction time is observed. It is usually ascribed to strong adsorption of reactant or products, possibly giving rise to secondary reaction of acetone [248, 258]. Depending on the relative strength of the basic and acid sites involved, acetone is likely to give rise to self-condensation (Figure 3.25). These secondary products are usually not detected in the gas phase, due to strong adsorption on the surface. This process is associated to a deficit of acetone in the gas phase resulting in a higher selectivity in acetylene compared to acetone. The carbon unbalance is also responsible for the discrepancy between the conversions calculated on the basis of MBOH consumption and of the detected products formed in the gas phase (see section 2.6 in the chapter 2). Other processes such as the influence of water present as a trace in the MBOH and also produced by secondary polymerization of acetone, and/or the modification of the surface upon reaction time may also participate to the deactivation.

Of course, one key parameter determining the basic reactivity of surfaces is the pretreatment conditions. Basic solids naturally adsorb water and CO_2, giving rise to the formation of hydroxyl and carbonates that will impact the acid-base properties of the related surface. To investigate at molecular level the role of the different active sites present on the surface, it is thus very important to adapt the pretreatment conditions.

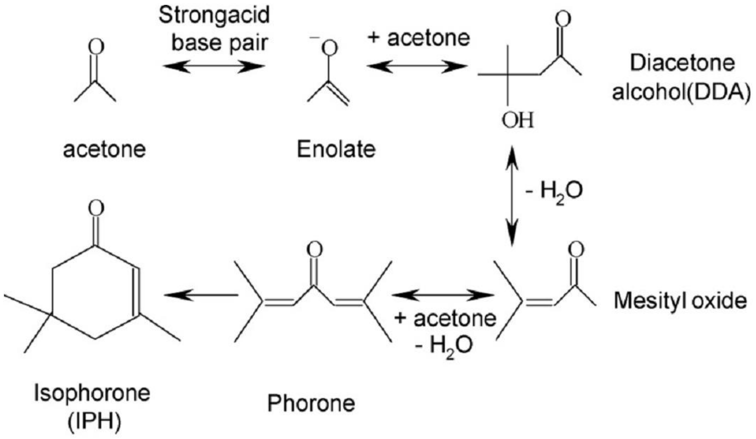

Figure 3.25 Chemical pathway involved in the self-polymerization of acetone

3.6.2 Influence of the pretreatment conditions applied

In the present study, the pretreatments are adapted to the conditions used for EPR and PL characterizations (Section 3.2 ~ 3.4). From the impact of the various pretreatments on the surface reactivity, we will discuss the influence of the various types of defects on the surface reactivity. Before discussing the results obtained with the related pretreatments, we will first examine the impact of different atmospheres, N_2 and O_2 applied during the pretreatment carried out in more conventional conditions, i.e. gaseous flow. These data will allow the comparison with previous data obtained over a commercial Kadox ZnO sample pretreated in these more conventional conditions.

3.6.2 (a) The reactivity of ZnO smoke after being treated in O_2 and N_2-flow

As expected from MBOH reactivity on basic surfaces of ZnO [259], the lone carbonated decomposition products detected in the gas phase are acetone and acetylene, in approximately equimolar ratio. This is consistent with the absence of carbon unbalance and thus with the good accordance of the two calculation methods to evaluate the conversion level (only the $Conv_{products}$ is thus provided) at reaction temperature of 403 K. The evolution of the conversions upon reaction time are plotted in Figure 3.26 after pre-treatments at 773 K of the as-synthesized ZnO smoke sample (100 mg) under N_2 (solid violet circle) or O_2 (hollow violet circle) flow. These two samples will be named Smoke-N_2 and Smoke-O_2, respectively.

Beside different conversion levels, the deactivation that takes place also exhibits quite different profiles. The Smoke-O_2 is globally less reactive than Smoke-N_2: the initial conversion (after 2 min of reaction) is only 31% *versus* 85 %. The deactivation is also significantly less pronounced for smoke-O_2. The steady state is reached after only 20 min, resulting in a conversion level of 14 %, whereas the conversion stabilizes around 23 % after 60 min for smoke-N_2. These data show that the modifications resulting from the different atmospheres of pretreatment significantly impact the surface state and its reactivity. These tendencies are in good agreement with previous work from Drouilly et al. [248] obtained on a kadox sample, involving a very similar specific surface area compared to the present smoke sample (9 m^2g^{-1}). In this previous study, it was shown that thermal treatment at 773 K under N_2 flow led to higher concentration of oxygen vacancies compared to O_2 treatment, no additional modifications of other defect types being identified. It was proposed that the electron release associated to oxygen formation participate to the increase of the electron density around the surface O^{2-} basic sites, increasing their basic strength.

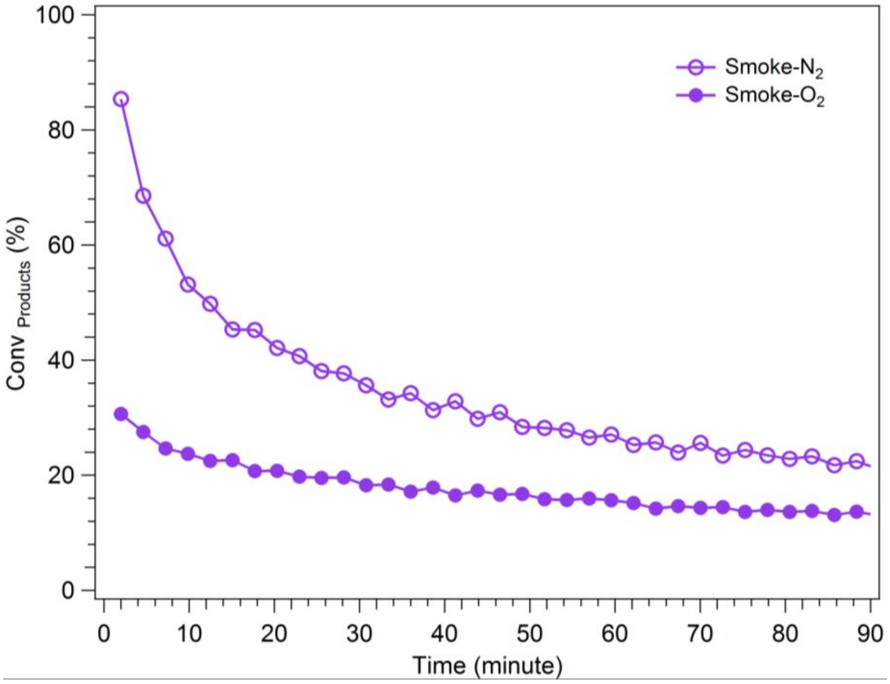

Figure 3.26 MBOH Conversion (Conv$_{products}$) at 403 K of ZnO smoke sample after pre-treatments under N_2 (solid violet circle), O_2 (hollow violet circle) flow at 773 K (w = 100 mg).

Given that the various annealing treatments as well as exposure of the surface to water considered in the previous section of this chapter do not only impact the concentration in oxygen vacancies, we will now investigate how these more complex situations affect the surface reactivity.

3.6.2 (b) The reactivity of ZnO smoke after being treated in vacuum and oxygen

To investigate this question, it is required to implement the pretreatment in conditions identical to those carried out in the previous sections of this chapter for EPR and PL characterizations.

After annealing under vacuum, a huge increase of the initial basic reactivity was observed, that made impossible the precise comparison with catalytic results obtained for smoke-O_2 and smoke-N_2 for experiments implemented in the same conditions (w = 100 mg) (results not shown).

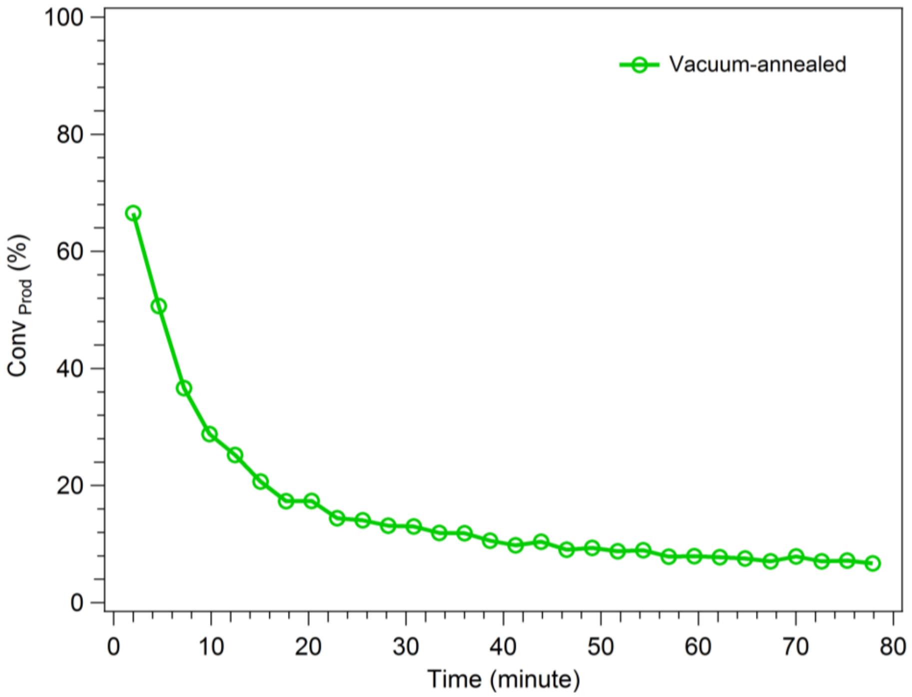

Figure 3.27 MBOH conversion (Conv$_{products}$) for ZnO smoke sample after annealing in vacuum at 773 K (w= 50 mg).

A new series of experiments was thus carried out, decreasing the contact time (same operating conditions but w = 50 mg). Figure 3.27 reports the conversion level of the vacuum annealed smoke. Despite half contact time, the initial conversion level remains very high, 70 % after 2 min of reaction, and the deactivation process is more pronounced than for smoke-N_2, being more rapid (stabilization reached after around 25 min) and more important, resulting in only 10 % of conversion after one hour. As in the case of smoke-N_2 or smoke-O_2, no carbon unbalance is observed, thus only the conversion calculated from conv$_{products}$ is reported.

For the next catalytic measurements, a fresh smoke sample was similarly vacuum annealed and further annealed at 773 K under oxygen (P_{O2} = 100 mbar). Then, two cooling ways in presence of oxygen were applied, either removing rapidly the furnace resulting in a rapid quenching of the temperature (hereafter referred to as “quenching”, this corresponds to the procedure achieved for EPR and PL measurements reported in the above section) or decreasing slowly the temperature for about 3 hours (hereafter referred to as “non-quenching”). Finally, once at room temperature, the sample was evacuated.

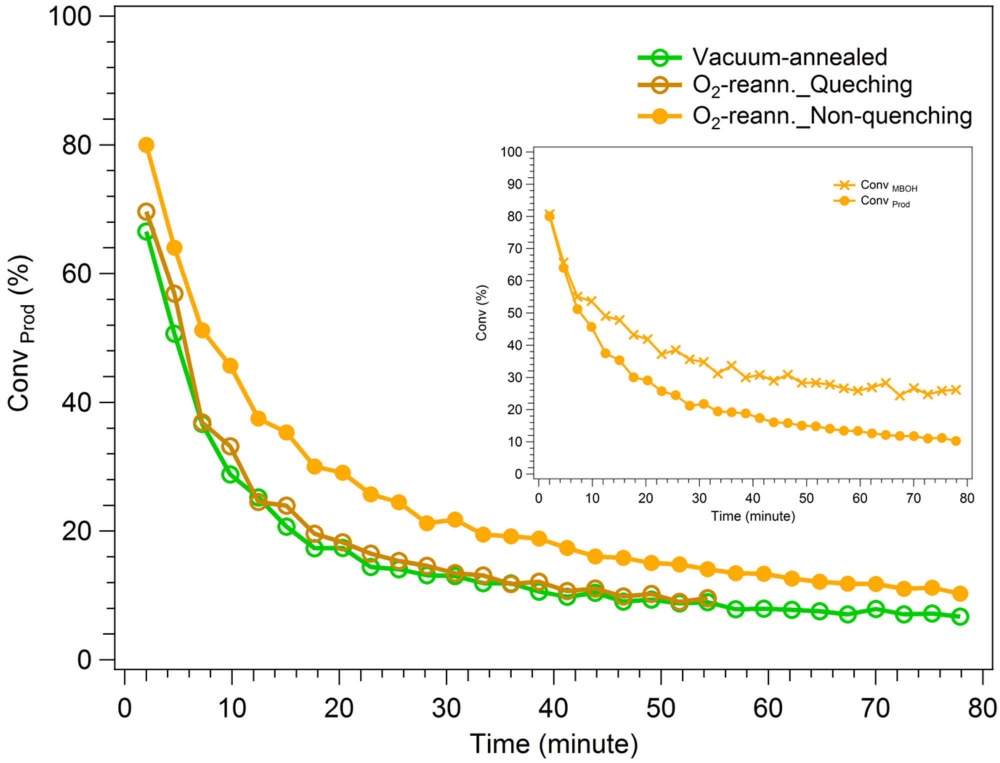

Figure 3.28 The MBOH conversion for ZnO smoke sample after different annealing pretreatments at 773 K: annealing in vacuum (hollow green circle), further annealing in oxygen and cooling down to RT by quenching (hollow brown circle) and without quenching (solid circle). Inset presents the comparison of conv$_{MBOH}$ (solid cross) and conv$_{products}$ (solid circle).

Opposite to the tendency observed when comparing smoke-N_2 and smoke-O_2, also considered as reducing and oxidative conditions, respectively, in the present case, annealing under oxygen with quenching or non-quenching procedures do not lead to any decrease of the conversion compared to vacuum annealing. In fact, annealing under oxygen with quenching surprisingly leads to very similar behavior to that reported for vacuum annealing as is shown in Figure 3.28. Annealing under oxygen without quenching even results in a both higher initial and final conversion levels (80 % after 2 min and 15 % after one hour). Note also that with the non-quenching procedure, we did observe for the first time a significant discrepancy between conversion calculated on the basis of consumption of the reactant and that calculated from the formation of the detected products (inset of Figure 3.28). This is significant of a carbon unbalance (15 % of carbon deficiency). The acetone selectivity slightly decreases upon reaction time, from 50 to 48 %. These results clearly show that the catalytic reaction is not only impacted by oxygen vacancies but is also sensitive to other defects which relative concentrations are modified upon these various pretreatments.

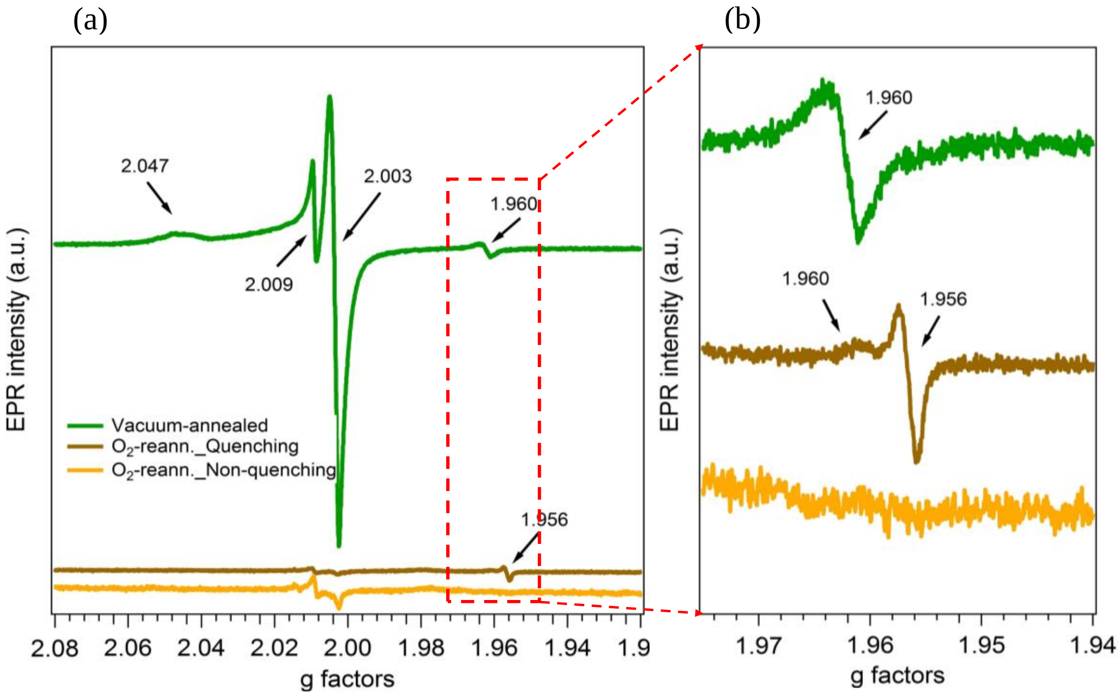

Figure 3.29 Comparison of different sample treated in various conditions. (a) EPR spectra of vacuum-annealed (green curve) and oxygen re-annealed sample differing from different cooling ways (brown curve is for quenching, while orange curve is for non-quenching), (b) Magnified spectra of rectangular part in (a).

In order to rationalize these data, let’s examine step by step how the defects are modified going from vacuum annealing to oxygen annealing, with or without quenching.

If the EPR features observed for vacuum annealing and oxygen annealing with quenching have already been compared in section 3.3 , we first have to discuss the processes occuring upon oxygen annealing with non quenching procedure. From Figure 3.29 gathering the EPR features obtained for the three pretreatment procedures, it is effecvtively shown that modifications occurring upon oxygen annealing lead to different defective states for the material depending on the implementation of quenching or non quenching cooling down procedure.

As summed up on the schema reported on Figure 3.30, considering EPR data, paramagnetic oxygen vacancies ($g = 2.003$) are formed after vacuum annealing treatment. It can not be excluded that other oxygen vacancies that are EPR silent are also formed. This contributes to the appearence of superoxide adsorbed species (anisotropic signal). Part of the electrons released by the formation of oxygen vacancies are thus consumed to reduce all the native surface Zn_i^+ (disappearance of $g = 1.956$ signal) into metallic zinc (as evidenced by XPS). The native bulk Zn_i^+ species ($g = 1.960$) are not modified. Hence, globally, the remaining electronic density (δ) will increase the electronic density of the remaining native surface O^{2-} basic sites to give $O^{(2+\delta)-}$ which is responsible for the huge increase of the basic reactivity.

Starting from this state, as illustrated by the decrease of $g = 2.003$ signal, annealing under oxygen with quenching leads to the filling of part of the oxygen vacancies previously formed. This filling consumes thus a fraction of the electrons previously released. It should thus contribute to the decrease of the basic reactivity. However, simultaneously, surface metallic zinc is oxidized into surface Zn_i^+ ($g = 1.956$), and potentially into surface Zn^{2+}, while native bulk Zn_i^+ ($g = 1.960$) is oxidized into bulk Zn^{2+}. These oxidation processes, together with the huge decrease of the amount of superoxide anions, release electrons. There are thus antagonistic effects from the point of view of electrons consumption and electrons release processes. Unfortunately, in the lack of available quantification of the various EPR signals (and of the process impacting the EPR silent oxygen vacancy), a precise balance between the electrons consumption or release processes is not easy to discuss. However, these counterbalancing effects in terms of electron density modulation that govern the basic reactivity may finally explain the comparable conversion levels obtained upon vacuum annealing and oxygen annealing with quenching treatments.

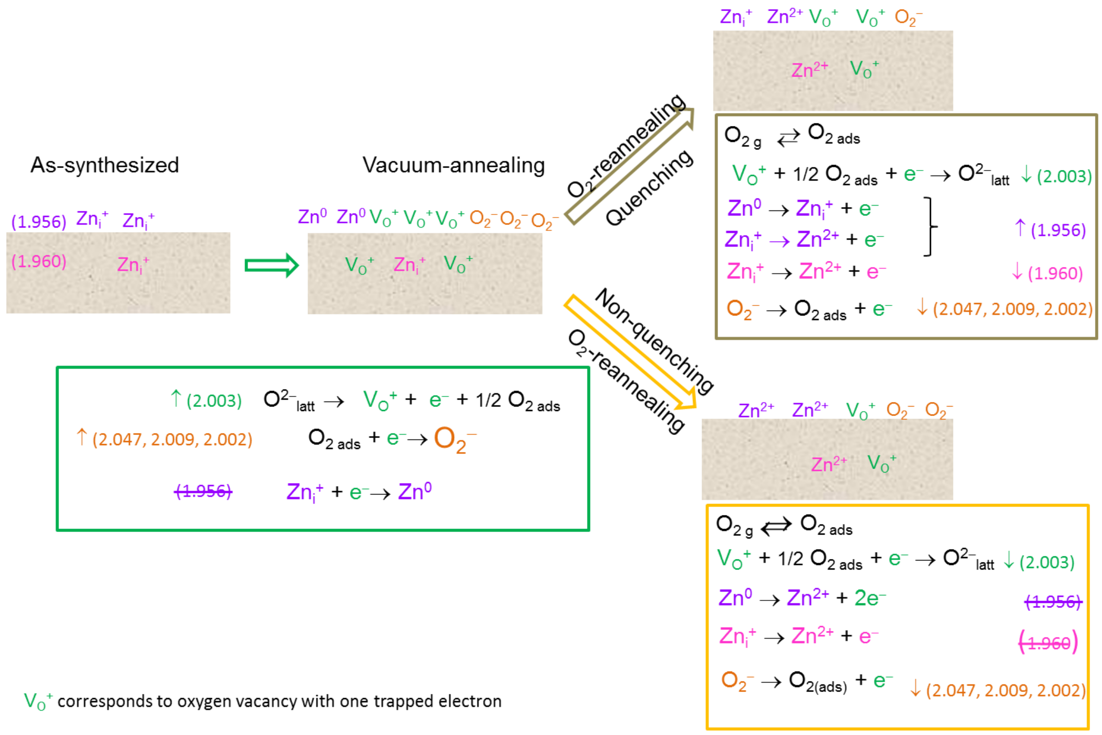

Figure 3.30 Schematic representation of the evolution of species and defects in/on ZnO deduced from defects characterization from the as-synthesized material to vacuum annealing and further reannealing under oxygen using either quenching or non quenching cooling procedures.

Oxygen annealing without quenching leads to a different state compared to quenching procedure (Figure 3.29). If oxygen vacancies formed upon vacuum annealing are filled up, compared to quenching procedure, the remaining ones (g = 2.003) are in larger amount compared with the quenching procedure. Superoxide species have also decreased but they still remain in higher amount than for the quenching procedure. The main difference between the two quenching / no quenching procedures concerns the modifications of the zinc species. Indeed, there is no more EPR evidence for Zn_i^+ neither in the bulk (g = 1.960) nor at the surface (g = 1.954). Probably due to longer contact time with oxygen, all bulk Zn_i^+ species (g = 1.960) are oxidized into Zn^{2+}. In a similar way, metallic zinc is also fully transformed into Zn^{2+} (no evidence for surface Zn_i^+ expected at g = 1.956). Hence, there are still some compensating processes impacting the electron consumption versus electron release processes. In fact, from the relative intensities of the remaining g = 2.003 signal, the electron consumption (oxygen vacancy filling) is less important compared to that of the quenching procedure. On the opposite, the oxidation reactions leading to electron release are comparatively more efficient. Hence, globally the remaining electron density available is increased ($O^{(2+\delta)-}$). This is in line with the enhanced conversion level compared with oxygen annealing with quenching.

In addition, it is also observed that, in absence of quenching, the disappearance of Zn_i^+ on the surface is observed at the benefit of the formation of Zn^{2+}. The associated strengthening of the surface acidity going from Zn^+ to Zn^{2+} modulates the relative acid-base balance of the active site involved in the transformation of MBOH. This feature may be responsible for a strong adsorption of reactant and/or products, leading to the carbon unbalance observed without quenching procedure.

3.6.3 The reactivity of ZnO smoke after exposure to water

Exposing the vacuum annealed sample to water (10 mbar) has a drastic effect on the MBOH conversion. The products desorbed in the gaseous phase ($Conv_{products}$ %) are strongly decreased from the beginning of the reaction (10 %) compared to vacuum annealing, and their formation only slightly decreases upon reaction time as shown in Figure 3.31. We can notice that the final conversion is very similar to that obtained upon deactivation for the vacuum annealed sample. However, more unusual is the progressive increase of the consumption of MBOH upon reaction time (inset in Figure 3.31). This finally results in a carbon deficiency in the gas phase of about 15%. This means that MBOH is increasingly adsorbed upon time. In fact, it was already reported that there are two adsorption modes of MBOH on ZnO surface, the first one allowing the decomposition of this molecule and further desorption of acetone and acetylene, while the second one corresponds to a spectator adsorption mode [248].

From EPR shown in Figure 3.19 (b) and (c), part of oxygen vacancies (g = 2.003) are filled up upon water adsorption and surface Zn^+ (g = 1.956) is formed. In fact, as already explained above, upon water dissociation, H^+ and OH^- formed interacts with O^{2-}_{latt} and Vo^+, respectively, resulting into two identical OH^- and a released electron. The latter is involved in the reduction of surface Zn^{2+} into surface Zn^+. Hence water dissociation contributed to the decrease of the basic strength of surface oxide anions since it decreases the available electronic density [248]. The progressively increasing adsorption of MBOH might originate from the displacement of adsorbed OH by MBOH molecule resulting in adsorbed alcoholate and water released. It may be proposed that this alcoholate adsorbed on the formed oxygen vacancy site (instead of on acid site in the reactive adsorption mode) finally leads to spectator adsorption mode.

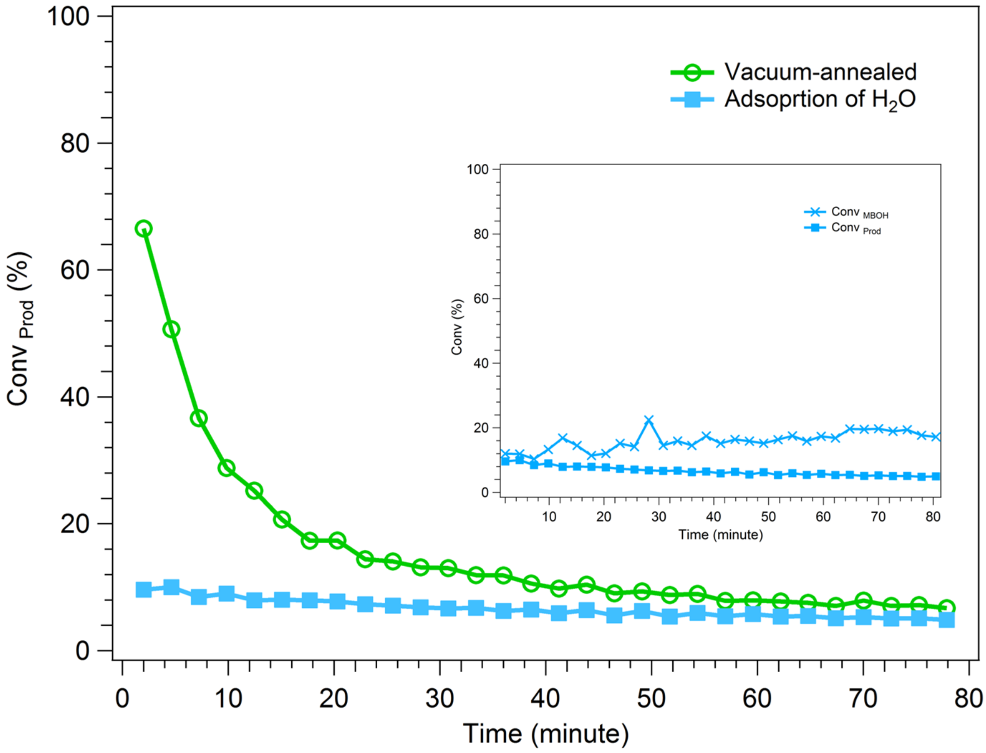

Figure 3.31 Influence of H_2O adsorption performed after vacuum annealing at 773 K on the MBOH conversion. The inset reports the discrepancy between Conv$_{products}$ (square) and Conv$_{MBOH}$ (cross).

Finally, it should be underlined that, except in the latter case, deactivation upon reaction time is always observed. Besides the modulation of the basic site strength mentioned above as well as the modulation of the acid-base balance, the water formed by the reaction (self-condensation of acetone), but even more, the water unavoidably present in the reactant flow due to the formation of an azeotrope with MBOH, may also play a key role in the deactivation process.

To conclude, the various pretreatments or pre-adsorption processes significantly affect the catalytic basic reactivity of the smoke ZnO sample. Thanks to implementations of identical pretreatments prior to EPR and catalytic measurements, structure-reactivity relationships could be established at a molecular level. It is shown that the basic conversion of MBOH into acetone and acetylene is not only sensitive to the concentration of oxygen vacancies, but also to other redox processes impacting the concentrations of other type of defects. In fact, processes responsible for electron release tend to increase the basic strength of active surface anions, ($O^{(2+\delta)-}$), whereas those associated to electron capture contribute to decrease it. The conversion level results thus of these antagonist processes. The modification impacting the acidic properties (Zn^{2+} versus Zn^{+}) also influence the acetone self-condensation reaction, which adsorbed products contribute to the carbon deficiency and deactivation. From pre-adsorption of water, it is shown that water also plays a key role in the deactivation process through the progressive filling up of oxygen vacancies upon water dissociation.

3.7 Conclusions

Defective ZnO smoke sample has been synthesized by burning metallic Zn in air. – Such a procedure that corresponds to a highly non-equilibrium process mostly leads to the formation of nanoparticles exhibiting tetrapod-like structure. By combining *in situ* PL and EPR measurements with other techniques, the presence of the native defects, Zn_i^+ located both on the surface (PL at 2.88 eV and g~1.956) and in the bulk (PL at 2.80 eV and g~1.960) in the as synthesized sample was evidenced. Besides, a PL contribution at 2.50 eV (495 nm) was detected, but its assignment still remains unclear. The relative concentrations of the defects as well as their nature can be modulated though annealing in various atmosphere or adsorption of oxygen, water or reactive molecule (MBOH).

Annealing in oxygen-poor conditions (such as annealing in vacuum and zinc vapor), Zn_i^+-related features of the surface are almost absent due to the huge reduction of surface Zn_i^+ which is also supported by the grey coloration and the XPS data. In addition, EPR signal characteristic of superoxide ions is formed. It is indicative departure of surface oxygen lattice. Hence, the simultaneous appearance PL emission at 2.41 eV (515 nm) together with EPR signal at g ~ 2.003 was assigned to Vo^+.

On the contrary, further annealing at 773 K in oxygen-rich condition (such as oxygen annealing / reannealing) leads to the partial filling up of these oxygen vacancies. In addition, the detection of surface Zn_i-related features is explained by the oxidation of Zn^0 transitory formed upon vacuum annealing from native Zn_i^+ whereas the decrease of bulk Zn_i-related features corresponds to the oxidation of native bulk Zn_i^+ into Zn^{2+}. Besides this, a new emission at 2.10 eV (590 nm) related to O_i is generated when increasing the partial pressure of oxygen during annealing.

Based on the fact that V_O^+ can be filled up by water, we later on used water molecules to probe the surface defects that are generated after vacuum annealing. By this, it is observed that the intensity of both emission at 2.41 eV (515 nm) and EPR signal at 2.003 is reduced. This further proves that these two features are caused by V_O^+. Once V_O^+ is filled up by water, the associated electron transfers to surface Zn^{2+} generating surface Zn^+ as supported related EPR signal and PL emission.

We also studied the catalytic basic reactivity of the smoke ZnO sample by applying the identical post-treatments and water pre-adsorption. The catalytic results show that the basic conversion of MBOH into acetone and acetylene is not only sensitive to the concentration of oxygen vacancies, but also to other redox processes impacting the concentrations of other type of defects, and thus, the electronic density available on surface Zn-O active sites.

Chapter 4: Influence of the synthesis conditions on the defects

In the Chapter 3, we have demonstrated how ZnO smoke nanoparticles could be used as a model system for studying native point defects, or those obtained by various post-growth treatments. We have shown that such highly non-equilibrium synthesis method results in Zn-rich samples and the corresponding PL (2.88 eV / 430 nm) and EPR (g ~ 1.956) fingerprints were identified to be in correlation with Zn^+ as the main defect. Moreover, we could show that strongly reducing post-growth treatment (T_{ann} = 773 K, $P \leq 10^{-5}$ mbar) results in ZnO smoke possessing singly positive oxygen vacancies (V_O^+), whereas the multiple annealing in relatively high P_{O2} generates oxygen interstitials. In this Chapter, we will show how the nature of defects can be modulated through varying the synthesis conditions.

It is well known that the nature of native defects in ZnO are strongly dependent on the O- and Zn chemical potentials set by the environment conditions during the crystal growth or, as we have shown in Chapter 3, through the post-growth treatments [260]. The relevance between defects concentration and oxygen and zinc chemical potentials in ZnO has been theoretically studied by many groups [74, 223, 260] (see also Chapter 1). The common statement is that tuning from oxygen-rich to zinc-rich condition, the formation energy of defects associated with oxygen excess (such as zinc vacancy and the oxygen interstitials) raises, whereas the formation energy of those associated with zinc excess (such as oxygen vacancy and the zinc interstitials) lowers. Later on, various experimental groups have supported this statement. For instance, Ma and coworkers [261] who studied the evolution of PL emissions in different ZnO films produced by metalorganic vapor phase epitaxy found that the intensity of UV emission was enhanced by increasing the partial pressure of oxygen during deposition, while the defect-related emission in visible range was, simultaneously, suppressed. Therefore, they deduced that the emission in the visible region resulted from oxygen vacancies. Likewise, Gao et al. [262] also reported the similar tendency of UV and defect-related emissions when increasing oxygen partial pressure, under which ZnO film was directly grown from Zn substrate. However, the relevant reports on ZnO nanoparticles are very few.

Given that the synthesis of ZnO smoke nanoparticles proceeds in rather control-less conditions (Zn-combustion in air), this Chapter is devoted to show how the control over oxygen / zinc chemical potentials – that is achieved by varying the oxygen partial pressure within the combustion of Zn – results in ZnO samples exhibiting desired type of defects. For that purpose, the synthesis of nanopowders took place in a home-made glove box, a set-up that allows for oxygen partial pressure to be varied and, above all, for the final product to be collected in an inert atmosphere i.e. without exposing the powders to the air. By applying this strategy, we have then synthesized ZnO nanopowders in oxygen-poor and oxygen-rich atmospheres. The nature of the defects in the selected samples was mainly investigated by combining EPR and PL spectroscopy. In addition to this, the reactivity of ZnO surface with water molecules was also studied by FTIR. Finally, given some limitations dealing with such combustion approach, preliminary results obtained from chemical vapor synthesis (CVS) are also included.

4.1 Morphological and structural characterization

Two ZnO samples were selected to study the influence of oxygen-pressure on their native defects: ZnO-5 was obtained by burning metallic Zn in the mixture Ar/O_2 = 95/5 while for ZnO-50 the ratio Ar/O_2 was 50/50. The total pressure in all cases was 1 bar.

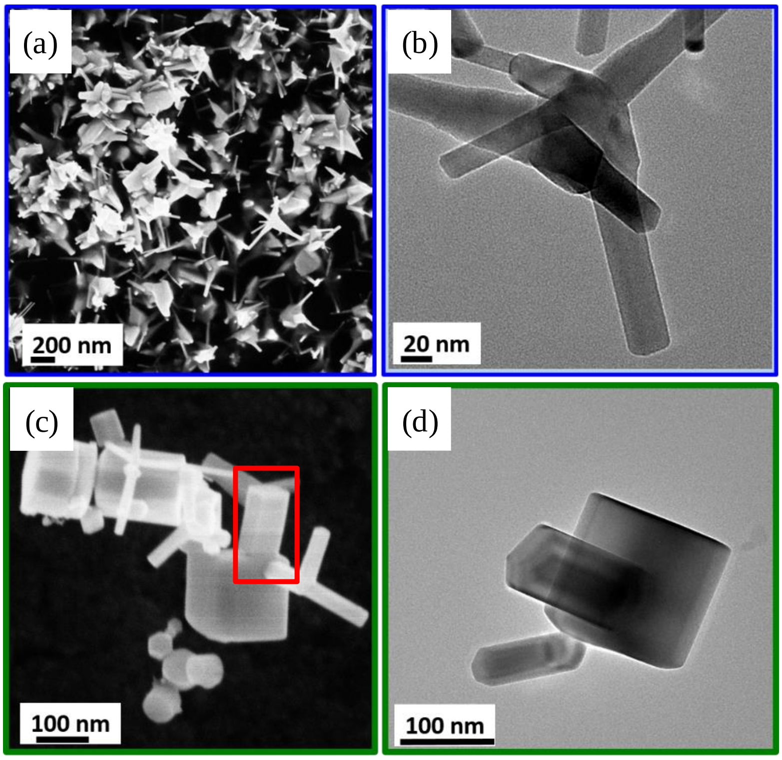

Figure 4.1 SEM (a) and TEM (b) images of ZnO-5. Corresponding images of ZnO-50 sample are respectively shown in (c) and (d).

The morphologies of ZnO-5 and ZnO-50 samples were characterized by SEM and TEM microscopies. The representative SEM and TEM images of ZnO-5 powder (observed to be yellowish in color) are shown in Figure 4.1 (a) and (b), respectively. As seen from SEM image in Figure 4.1 (a), ZnO-5 exhibits a strong degree of agglomeration with tetrapod-like structures of irregular sizes – a morphology rather similar to that of ZnO smoke. Closer inspection by TEM (Figure 4.1 (b)) confirms that the as-prepared nanoparticles of ZnO-5 sample are tetrapod nanowhiskers with four needle-like arms that originate from the center of the polyhedron. The length of the tetrapods arms exceeds 100 nm while the corresponding diameter of legs at the scale lower than 50 nm. Such morphology is typical of ZnO produced by combustion techniques and implies the presence of non-polar facets to be strongly favored over the two polar faces. In a recent study in our group [263], it has been demonstrated that ZnO smoke behaves as a multi-facet single crystal involving (10-10), (11-20), (0001), and (000-1) surfaces with the polar ones corresponding only to 25% of the total surface area. The representative illustration of each surface orientation is shown in Figure 4.2.

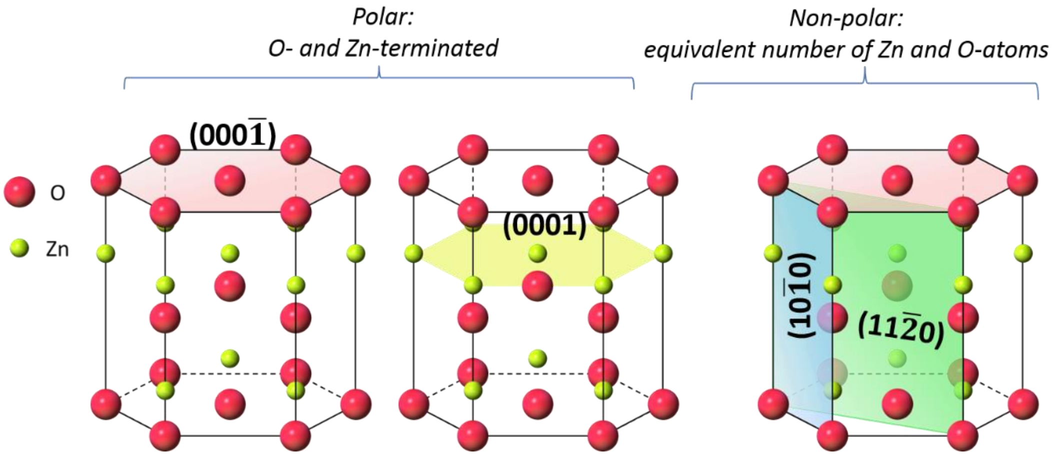

Figure 4.2 Illustration of four different surface orientations that can be present in ZnO nanocrystals. The polar faces correspond to 25% of the total ones in ZnO smoke [6].

As seen in SEM and TEM images in Figure 4.1 (c) and (d), respectively, the morphology of the as-prepared ZnO-50, that was purely white in color, strongly differs from that of ZnO-5 (i.e. ZnO smoke) while also being more regular. Although we cannot completely exclude the presence of tetrapods in ZnO-50 powder, only few of such shapes could be seen in SEM images, as presented in Figure 4.1 (c). Instead, the hexagonal prisms, shapes that are usually associated with the crystal growth along c-axes dominate in this sample. Such a shape is commonly obtained within more conventional synthesis approaches allowing thermodynamic equilibrium to be reached. A few particles that appear to look like a “cube” could be also observed in this sample (red frame in Figure 4.1 c). Cubic shape is in a strong contradiction with hexagonal crystal structure and may imply zinc-blende phase. Given that only one set of peaks – all of which are well indexed to the hexagonal ZnO – have been detected in X-ray diffractograms of both samples (Figure 4.3 (a)), no evidence of any additional crystalline phase is observed for ZnO-50 sample. In Debye-Scherrer formula (described in Chapter 3.1.1), the shape factor k = 0.9 assumes a spherical crystallite, which obviously does not fit to the shape of particles in our two samples. Nevertheless, k = 0.9 is used in this work in order to roughly estimate the crystalline size of ZnO-5 and ZnO-50 samples, giving the values of 37 nm and 73 nm, respectively.

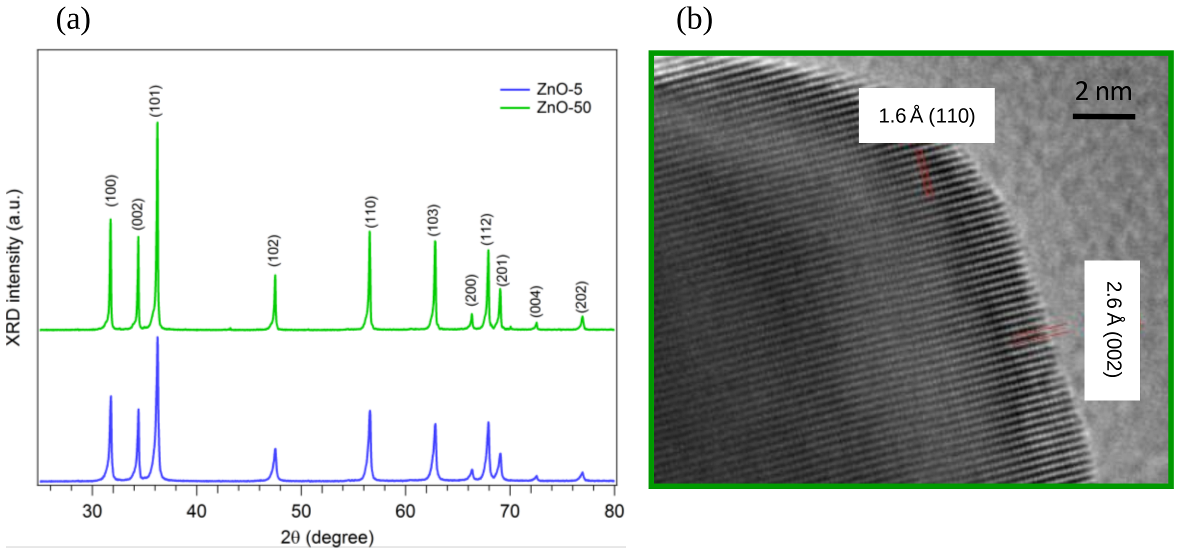

Figure 4.3 X-ray diffraction patterns of as-synthesized ZnO-5 (blue) and ZnO-50 (green) samples (a) and HRTEM image of ZnO-50 (b).

A closer inspection has been furthermore performed on HRTEM images (Figure 4.3 (b)) of ZnO-50 sample with a particular attention to such “cubically” shaped particles (such as the red-framed in Figure 4.1 (c)). One of the images, is shown in Figure 4.2 (b). Beside high crystal quality, it demonstrates the presence of two types of planes that are perpendicular to each other and with distances specific of wurtzite crystal structure (Figure 4.3 (b)) – which again excludes a possible presence of zinc-blende phase in ZnO-50. On the other hand, it is rather impossible to obtain a cubic shape through Wulff construction while taking into account the surface energy of the four above-mentioned surface orientations comprised in wurtzite ZnO. Based on these conditions (hexagonal phase + 4 surface orientations), the shape that can be constructed to approximate the "cubical" one implies strong reduction of the contribution of one of the non-polar faces. To illustrate this effect the corresponding shapes were obtained by Wulff construction and are shown in Figure 4.4. Apparently, the high O_2 content present during the synthesis of ZnO-50 provides conditions that favor one non-polar facet (10-10) over the other (11-20). The contribution of this face (11-20) is completely excluded in the representation of Wulff shape construction in Figure 4.4 (a) in order to underline the transformation from hexagonal shape to pseudo-cubic one. What we can say is that by increasing partial pressure of oxygen the contribution of this non-polar face is strongly reduced over the other (10-10) one – as demonstrated by corresponding SEM and TEM images in Figure 4.3 (c) and (d), respectively.

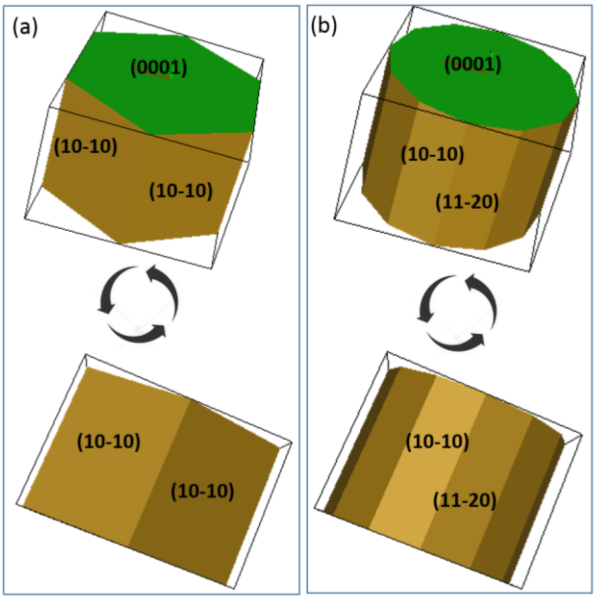

Figure 4.4 Wulff shape construction for ZnO representing different contributions of the non-polar faces: (a) (10-10) face is strongly dominating over the (11-20) (case: ZnO-50) (b) the contribution of the two non-polar faces is equal (Cases: ZnO-smoke and ZnO-5). The shapes were rotated in order to illustrate how the shape presented in (a) can appear as cubic.

The samples were furthermore characterized via Raman spectroscopy and the corresponding spectra are presented in Figure 4.5. The peaks centered at 329, 375, 434, 483 and 600 cm^{-1} are visibly present in the spectrum of ZnO-50 sample (Figure 4.5, green curve), while in the spectrum obtained on ZnO-5 sample (Figure 4.5, blue curve) these peaks are significantly weaker – illustrating an enhanced concentration of defects. The positions of these Raman peaks are consistent with those reported for wurtzite-ZnO in the literature [264-269]. Indeed, wurtzite structure of ZnO belongs to the space group C_{6v}^4 with two formula units per primitive cell. The Raman active zone-center optical phonons predicted by the group theory are $A_1 + 2E_2 + E_1$. The phonons of A_1 and E_1 symmetry are polar phonons and split into different frequencies for the transverse-optical (TO) and longitudinal-optical (LO) phonons. The E_2 modes are non-polar with low frequency mode (E_2^{low}) and high frequency mode (E_2^{high}).

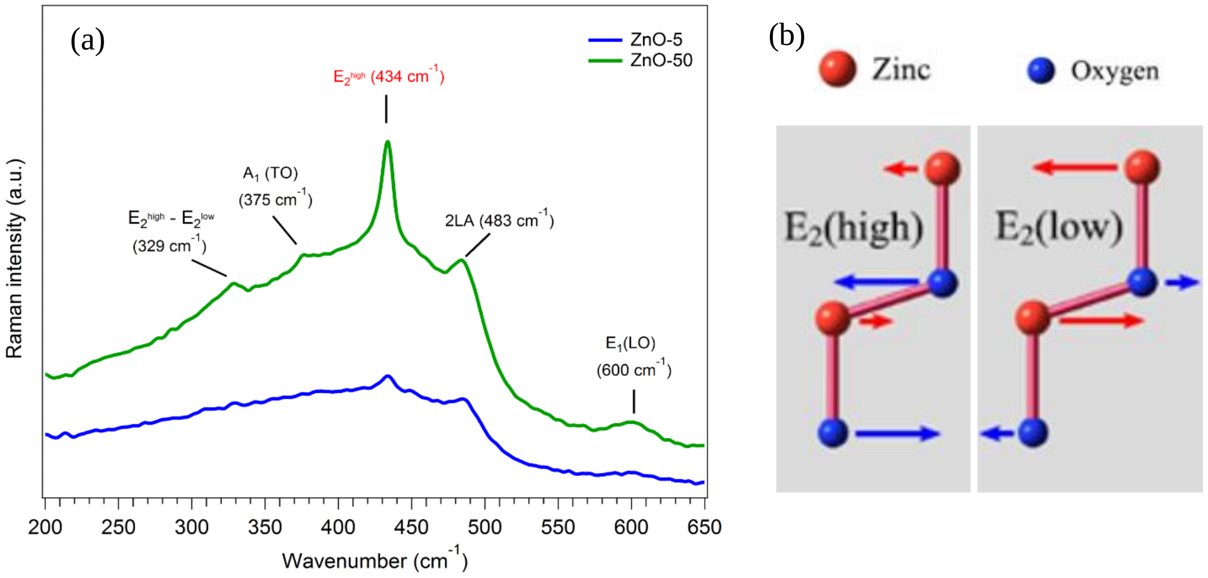

Figure 4.5 Raman spectra of ZnO-5 (blue curve) and ZnO-50 (green curve) samples (a) and the sketch of vibrations of E_2^{low} and E_2^{high} active modes in wurtzite ZnO structure (b).

A typical peak at 434 cm^{-1} is observed in the Raman spectra of both samples. This peak corresponds to E_2^{high} mode of ZnO that is particularly sensitive to the motion of oxygen sublattice of the wurzite structure [264-265]. The corresponding atomic displacement of this vibration mode is schematically shown in Figure 4.5 (b). In the same figure, the Raman mode specific of Zn-sublattice motion is shown for the sake of comparison, although it was impossible to be measured with our set-up since vibrating at ~100 cm^{-1}. Other peaks at 329, 375, 483 and 600 cm^{-1} detected in this work are related to the difference of $E_2^{high} - E_2^{low}$ [266, 270], A_1(TO) [267, 270], 2LA [266, 270] and E_1(LO) modes [270], respectively.

Since E_2^{high} mode is particularly sensitive to the oxygen sublattice, the changes of oxygen composition in ZnO can be indirectly evaluated by the variation of the intensity of this Raman mode [268]. From the comparison of Raman spectra in Figure 4.3, we see that this peak (at 434 cm^{-1}) is significantly weaker and broader in ZnO-5 sample than in ZnO-50. This is indicative of a lack of oxygen in the lattice of ZnO-5 that is in line with data reported in the literature [269].

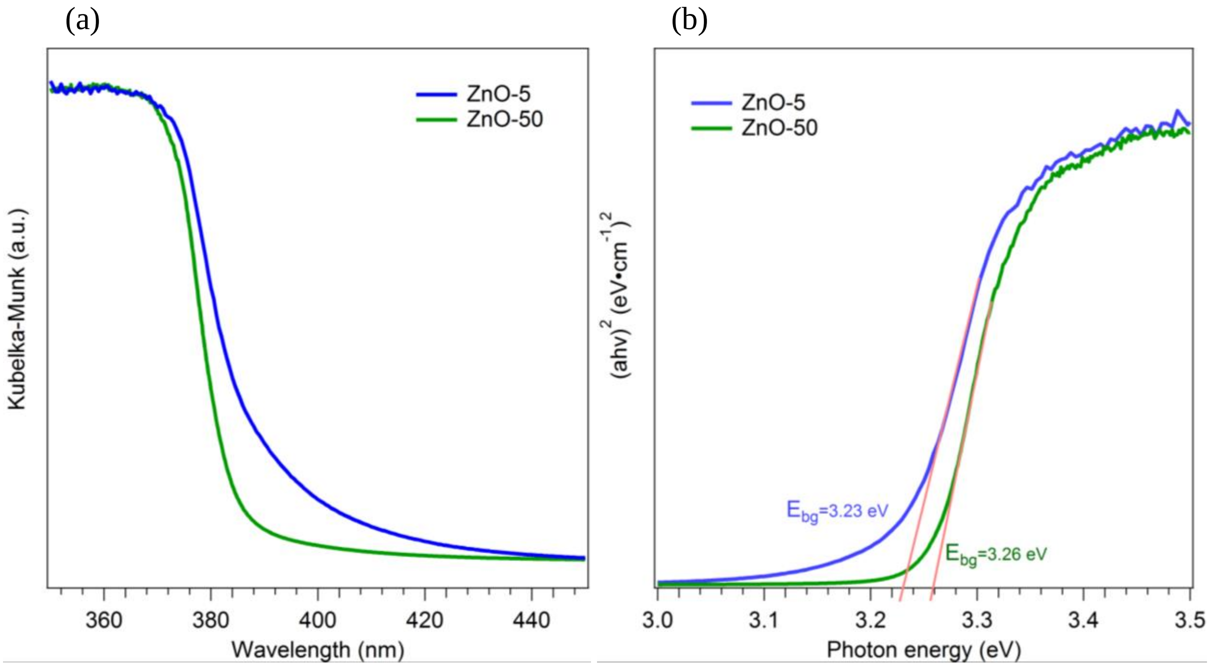

Figure 4.6 Diffuse Reflectance UV-vis spectra (a) and the corresponding Tauc-plots (b) of ZnO-5 (blue curve) and ZnO-50 (green curve).

The optical properties of the two samples are firstly investigated by UV-Vis diffuse reflectance spectroscopy and the corresponding spectra are compared in Figure 4.6 (a). The samples show nearly the same UV-absorption spectra except for a little tail in the case of

ZnO-5. This is in line with the slightly yellowish color of ZnO-5 when compared to the perfectly white powder of ZnO-50, implying that a certain type of defect causes the coloration present only in ZnO-5. Indeed, it was shown by both DFT studies [271] and experiments [272] that the presence of oxygen vacancies can effectively extend the visible light absorption of ZnO. Moreover, the same DFT studies have shown that oxygen vacancies in neutral form contribute the stronger in that respect. The band gap energies (E_{bg}) were calculated using the Tauc equation (described in Chapter 3.1.2) [273] and presented in Figure 4.6 (b). ZnO-5 and ZnO-50 samples show E_{bg} ~ 3.23 and 3.26 eV, respectively, which is comparable to ZnO smoke (3.26 eV) and slightly lower than the bandgap of bulk ZnO (3.37 eV). Indeed, some of the surface states, defects, and dangling bonds induce the formation of band tail and can cause a band gap narrowing [193, 274-275]. Taking into account that both ZnO-5 and ZnO-50 powders exhibit relatively large crystallites, the influence of defect structure on the band gap width could be the most important one.

4.2 Native defects identified by EPR and PL spectroscopies

4.2.1 EPR spectra

From Chapter 3, we have shown that the dominant defect in as-synthesized ZnO smoke is Zn_i^+ – as reflected by the presence of related EPR signals in the corresponding spectrum. Since ZnO-5 and ZnO-50 samples were synthesized by the same method, yet under different oxygen partial pressure, it is questionable if the same Zn_i^+ defects will still be favored, and if their relative concentrations are impacted. The synthesis of ZnO smoke taking place in air (the percentage of P_{O2} in 1 bar of air is 20 %), this sample might be considered as an intermediate case when compared with the two ZnO samples discussed here; ZnO-5 (the percentage of P_{O2} in 1 bar of mixed gases is 5 %) and ZnO-50 (the percentage of P_{O2} in 1 bar of mixed gases is 50 %). In this respect, EPR spectra of these three as synthesized samples were compared to evaluate how the partial pressure of oxygen impacts Zn_i-related defects.

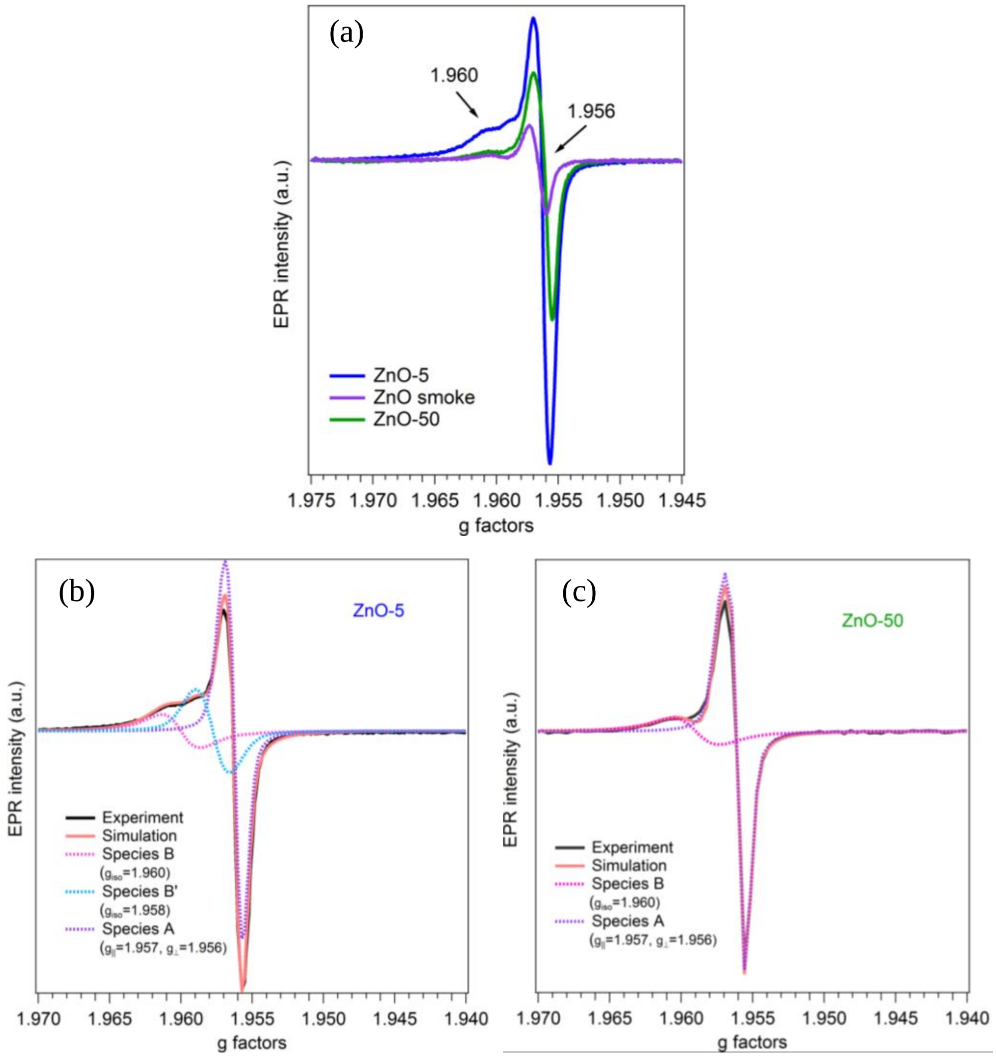

Figure 4.7 Comparison of EPR spectra of ZnO-5 (blue curve), ZnO smoke (violet curve) and ZnO-50 sample (green curve) (a), and corresponding simulated spectra of ZnO-5 and ZnO-50 samples in (b) and (c), respectively. The violet, bluish and magenta dotted curves show the contribution of each paramagnetic species.

EPR spectra of ZnO-5 and ZnO-50 samples compared to that of as-synthesized ZnO smoke are shown in Figure 4.7 (a). Overall, it is seen that the line shapes of EPR spectra for the two samples are quite similar to that detected in as-synthesized ZnO smoke: an intense EPR signals at g = 1.956 together with some weak signals that are very close to this value were detected in ZnO-5 and ZnO-50. In Chapter 3, EPR signals at g = 1.956 and 1.960 were attributed to Zn_i^+ located in the surface and bulk, respectively. Accordingly, both, ZnO-5 and ZnO-50 samples reveal a certain amount of Zn_i^+. Nevertheless, the intensity of Zn_i^+-related

EPR signals is different implying that the concentration of Zn_i^+ can be influenced by varying the partial pressure of oxygen. In order to quantitatively compare the concentration of Zn_i^+ species in ZnO-5 and ZnO-50 samples, EPR simulations were achieved and they are shown in Figure 4.7 (b) and (c), respectively. The results of these simulations are gathered in Table 4.1.

Table 4.1 Parameters for simulated EPR spectra of ZnO-5 and ZnO-50 samples.

Samples	g-factor	Contribution of each species	Double integrated area (a.u.)	Double integrated area of each signal (a.u.)
ZnO-5	g_{iso}= 1.960	6%	48	3
	g_{iso}=1.958	15%		7
	$g_{\|\|}$ = 1.957 $g_{\perp}$ = 1.956	79%		38
ZnO smoke	g_{iso}=1.960	91%	4	0.4
	$g_{\|\|}$= 1.957 $g_{\perp}$= 1.956	9%		3.6
ZnO-50	g_{iso}=1.959	6%	11	1
	$g_{\|\|}$ = 1.957 $g_{\perp}$ = 1.956	94%		10

The double integration areas of the two types of Zn_i^+ species, axial signal at $g_{||}$ =1.956, $g_{\perp}$ =1.957 (Species A, violet dotted curves in figure 4.7 (b) and (c)) and isotropic signal at g_{iso} =1.960 (Species B, magenta dotted curves in figure 4.7 (b) and (c)), are higher in the case of ZnO-5 than in samples produced in O_2-richer atmosphere, namely ZnO smoke and ZnO-50.

As expected, if higher oxygen partial pressure is used within the synthesis the concentration of Zn_i^+ related defects is lower, since under such conditions the metallic Zn is easily oxidized into Zn^{2+} (EPR silent). However, this sole explanation is not consistent with the higher concentration of Zn_i^+ in ZnO-50 compared to ZnO smoke sample. However, the unavoidable existence of water and other oxygen-consisting components in air (H_2O, CO, CO_2) may additionally influence the synthesis process in the case of ZnO-smoke. One may thus question the formation of Zn_i in an oxygen rich atmosphere as in the case of ZnO-50 sample. An excess of Zn in this sample is, however, well confirmed by XPS analysis (not shown here) revealing a Zn/O ratio of 1.26. This suggests that under strong non-equilibrium conditions, such as the metal combustion process, the partial pressure of oxygen / zinc is not the only parameter that modulates the type of defects – but the kinetics parameters are involved as well.

In addition, compared to other ZnO smoke and ZnO-50, ZnO-5 samples reveals another weak signal with g_{iso}=1.958 (Species B′, bluish dotted curve, Figure 4.7 (b)). Such signal being quite close to g=1.960 and g=1.956 signals, might also be related to Zn_i^+ species but which are located in crystallographic environments different than those for signals at g = 1.956 and 1.960 [276].

From EPR results, we can see that the concentration of Zn_i^+ is strongly dependent on the partial pressure of oxygen. In order to check how the partial pressure of oxygen impacts the nature of diamagnetic defects, PL measurements were then performed.

4.2.2 PL spectra

It is well established that, by increasing oxygen partial pressure, the concentration of Zn_i and / or V_O defects tends to decrease and above a certain P_{O2}, the concentration of V_{Zn} and / or O_i becomes more important. Similarly, as for EPR spectra, PL spectra of ZnO-5, ZnO-50 and ZnO smoke were compared and the correlation between P_{O2} and defect type was used to attribute accordingly the PL emissions. In addition, the variation in P_{O2} and the corresponding change in PL properties allowed to get more insights on the still unsolved assignment of PL emission at 2.50 eV (495 nm) that was previously detected in as-synthesized ZnO smoke sample.

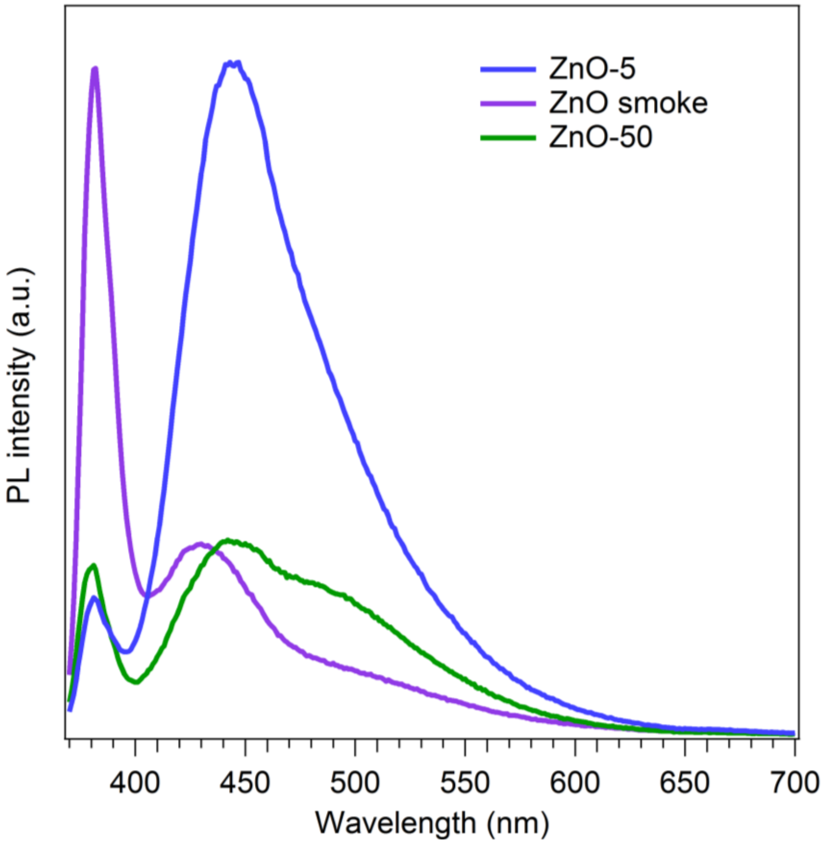

Figure 4.8 Comparison of PL spectra (a) of as-synthesized ZnO-5 (blue curve), ZnO smoke (violet curve) and ZnO-50 (green curve) samples (E_{exc} = 4.13 eV).

PL spectra of ZnO-5 (blue curve) and ZnO-50 (green curve) recorded under an excitation energy (E_{exc}) of 4.13 eV are presented in Figure 4.8 and compared to corresponding spectrum of ZnO smoke (violet curve). In contrast to ZnO-smoke, the domination of visible- over UV-emission is observable in PL spectra of both ZnO-5 and ZnO-50 samples. Obviously, extreme synthesis conditions – low or high P_{O2} – lead to lower crystal quality of samples and to an enhanced defects concentration, as reflected by the significantly stronger intensity of the visible (defect-related) emission over the UV emission. Among the three samples (Figure 4.8), ZnO smoke reveals the best crystal quality. We shall recall, that the synthesis of ZnO smoke takes place in the air where the percentage of P_{O2} (20%) is well between the one used in ZnO-5 and ZnO-50. Moreover, except pure oxygen, the air consists of other oxygen containing molecules (H_2O, CO, CO_2...). This, as well as the fact that the collection of this sample is also performed under air, can strongly affect the defects located on its surface which may be easily saturated by O_2-related molecules from the air, as well as interact with H_2O and so become passivated – leading finally to better crystal quality of ZnO smoke. From the comparison between ZnO-5 and ZnO-50 sample, we observed that the contribution of visible emission differs from one sample to another implying different concentrations of defects in the two samples. In order to quantitatively analyze how PL properties of ZnO are affected by changing oxygen partial pressure during the synthesis (and so by changing the nature of native defects), fitting analyses were performed on PL spectra of ZnO-5 and ZnO-50 samples and compared to the one previously shown for ZnO smoke.

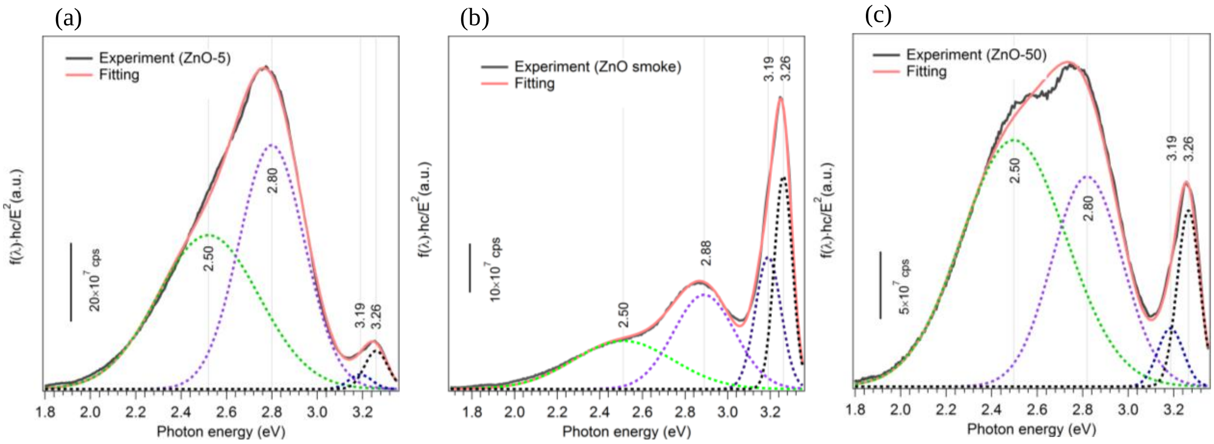

Figure 4.9 PL spectra of ZnO-5, ZnO smoke and ZnO-50 samples with their corresponding Gaussian fittings in (a), (b) and (c), respectively. Dashed curves indicate the component of each emission.

The results of the fitting analysis of the PL spectra of ZnO-5 and ZnO-50 samples are shown in Figure 4.9 and compared to that of ZnO smoke sample. The corresponding data are collected in Table 4.2. In both samples, the UV emission was fitted with two Gaussian bands at 3.26 and 3.19 eV that are similar to those used for the fitting of UV-emission in ZnO smoke sample (Chapter 3, section 3.1.2). In the case of ZnO-5 sample (Figure 4.9 (a)), the UV-emission is almost absent. In the case of ZnO-50 sample (Figure 4.9 (c)), the integration area of UV emission is stronger compared to ZnO-5 sample (see Table 4.2), implying a less defective structure for this sample. This result is in line with the results obtained by Raman spectroscopy (see Section 4.1).

Table 4.2 Position, FWHM and integrated area of emission peaks obtained from fitting results extracted from Figure 4.9.

Samples	Peak position (eV)	FWHM (eV)	Integrated area (a.u.)	Integrated area of each peak (a.u.)
ZnO-5	3.26	0.12	4.63×10^8	1.25×10^7
	3.19	0.12		4.80×10^6
	2.82	0.34		2.25×10^8
	2.50	0.53		2.21×10^8
ZnO smoke	3.26	0.10	2.15×10^8	4.64×10^7
	3.19	0.14		4.09×10^7
	2.88	0.34		7.01×10^7
	2.50	0.55		5.78×10^7
ZnO-50	3.26	0.12	1.87×10^8	1.61×10^7
	3.19	0.13		6.12×10^6
	2.82	0.36		5.98×10^7
	2.50	0.54		1.05×10^8

In both samples, the emission that is present in visible range of the spectrum can be fitted with two Gaussian bands at 2.80 eV (440 nm) and 2.50 eV (495 nm) with FWHM of ~ 0.3 and ~ 0.5 eV, respectively. The PL emission centered at ~2.80 eV experiences a slightly red shift compared to the one at 2.88 eV detected in ZnO smoke (Figure 4.9 (b)) and assigned to Zn_i^+ defects. Taking into account the presence of a strong EPR signal at 1.958 we assign the emission at 2.80 eV (440 nm) to Zn_i^+. As previously reported by Zeng et al. [90] Zn_i-related defects give rise for PL emissions at ~ 2.80 eV (440 nm). This interpretation is supported by the diagram of transition levels of Zn_i defects proposed by Gallino and coworkers [205]. In their work, they have calculated and shown that energy levels of Zn_i with different charge states are located very close to each other within the bandgap, which implies that the transitions from these states to valence band must be of similar emission energy. The shift of the PL maximum (2.80 eV / 440 nm) in ZnO-5 and ZnO-50, when compared to ZnO smoke (2.88 eV / 430 nm) is most probably due to different contributions of Zn_i defects in various oxidations states in these three samples. However, we shall not exclude also the possibility of different contributions of surface versus bulk Zn_i-related defects, when passing from one sample to the other in our work. In addition to this, different crystallographic environment of the Zn_i^+, whether it is located at the surface or in the bulk, might also shift the emission maximum to such small extent. Overall, the integration area of Zn_i^+-related PL emission (2.80 eV / 440 nm) in ZnO-5 sample is 4 times larger than that in ZnO-50 sample (Table 4.2). Such tendency is consistent to that obtained for Zn_i^+-related EPR signals (g ~ 1.956 and 1.960) in the two considered ZnO samples. Both PL and EPR results imply that Zn_i^+ related defects are in higher concentration in ZnO-5 sample compared with ZnO-50 sample (and / or ZnO smoke) – which appears logical according to different P_{O2} applied during synthesis. Moreover, XPS results (not shown here) reveal that in all three samples the Zn/O > 1 confirming an excess of zinc (or deficiency of oxygen) in all the samples. This strongly implies that in the course of combustion synthesis the partial pressure of Zn can be generally considered as fairly high – that is not an easy task to assess experimentally. Indeed, the combustion process is almost an instantaneous event in which the evaporation of Zn and the oxidation that follows are too rapid to allow us the determination of P_{Zn} as a function of temperature. Moreover, the highly exothermic oxidation reaction employs the self-released energy for the further Zn-evaporation complicating thus the evaluation of Zn-evaporation even more. In conclusion, the two extreme conditions for ZnO-5 and ZnO-50 can be analyzed such as, high P_{Zn} + low P_{O2} and high P_{Zn} + higher P_{O2}, respectively.

Taking into account Zn-rich condition, the PL emission at 2.50 eV (495 nm) – also detected in all the three samples – must be brought into the correlation with the second type of defects expected in such conditions, namely oxygen vacancies [68, 72, 222]. The possibility to obtain oxygen vacancies in ZnO can be easily questioned since many theoretical works claim that the formation energy for this type of defect is far too high. However, we must recall that all of the theoretical works are based on equilibrium conditions – which is not our case.

Moreover, we deal with nanosized ZnO and we know from the work by Pacchioni and coworkers [238] – who showed for ZrO_2 – how strongly the formation energy of oxygen vacancies is decreased by decreasing the particle size. Therefore, we can adopt the hypothesis that in nano-ZnO, which is obtained under non-equilibrium conditions, V_O-type of defects can be formed. The same reason was proposed in Chapter 3, in which a certain type of PL / EPR signals couple, that was detected in ZnO-smoke after annealing in high vacuum, was suggested to originate from V_O^+ defects.

If considering the emission at 2.50 eV (495 nm) to be in correlation with oxygen vacancies, its integration area in ZnO-5 and ZnO-50 samples should be correlated to the P_{O2} used during their synthesis. This is exactly what we demonstrate by the fitting analysis (see Table 4.2): the integration area of this emission is ~ 2 times higher in ZnO-5 sample than that in ZnO-50. We note that its maximum position (2.50 eV / 495 nm) differs slightly from that reported in Chapter 3, that was measured at 2.41 eV (515 nm) in ZnO smoke after annealing under high vacuum and assigned to singly charged oxygen vacancies (V_O^+). Moreover, there is no EPR signal that appear in parallel to PL at 2.50 eV (495 nm) suggesting that this emission must originate from charge states of oxygen vacancies different from +1, i.e. either V_O^{2+} or V_O^0. To determinate which of these two types of oxygen vacancies the PL at 2.50 eV (495 nm) can be correlated to, PL measurements in function of excitation energy were performed.

4.2.3 PL properties in function of excitation energy

In Figure 4.10, we compare PL spectra of ZnO-5, ZnO smoke and ZnO-50 samples obtained at: (1) $E_{exc} > E_{bg}$ (4.13 eV, black curves), (2) $E_{exc} = E_{bg}$ (3.26 eV, blue curves) and (3) $E_{exc} < E_{bg}$ (3.10 eV, red curves). Clearly, the PL spectra of all three samples exhibit an emission around 440 nm (2.80 eV) whatever the excitation energy. Interestingly, when $E_{exc} < E_{bg}$, the PL spectrum of ZnO-5 sample shows an additional emission band with the maximum at ~ 560 nm (2.22 eV) (Figure 4.10 (a)), while the PL spectrum of ZnO-5 (Figure 4.10 (c)) samples reveal only a decrease of the all emission bands. In particular, the behavior of emission ~ 2.50 eV (495 nm) in ZnO-50 sample (Figure 4.10 (c)) is similar to that observed in ZnO smoke sample (Figure 4.10 (b)) for PL spectra recorded at $E_{exc} < E_{bg}$. This implies again that the type of oxygen vacancies present in ZnO-5 is different from that in ZnO smoke and ZnO-50 samples.

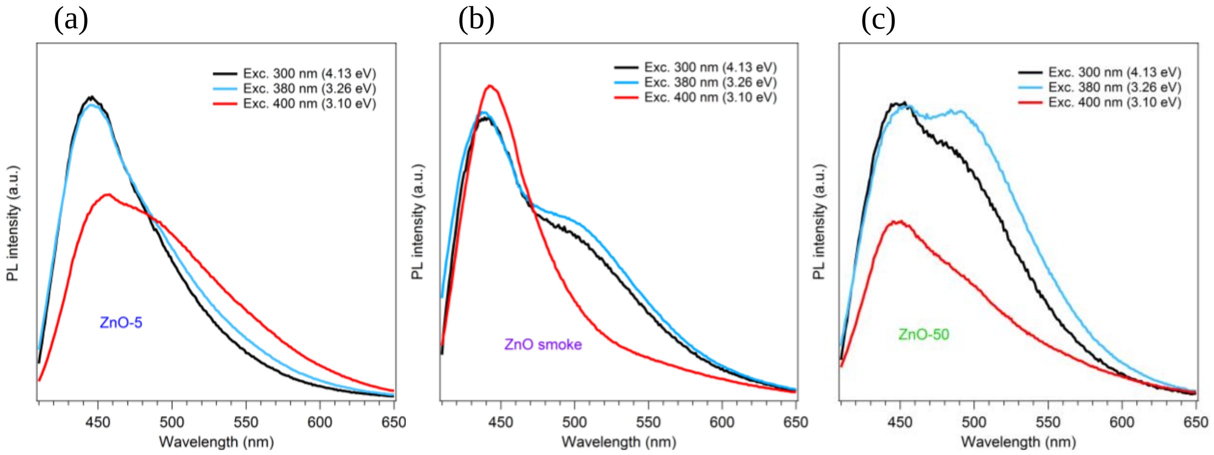

Figure 4.10 PL spectra recorded under the E_{exc} = 4.13 eV (300 nm, $E_{exc} > E_{bg}$), E_{exc} = 3.26 eV (380 nm, $E_{exc} = E_{bg}$) and E_{exc} = 3.10 eV (400 nm, $E_{exc} < E_{bg}$) for as-synthesized (a) ZnO-5, (b) ZnO smoke and (c) ZnO-50 samples.

Considering the new PL process appearing only in ZnO-5 sample and that is observable only under the excitation energy at 3.10 eV (400 nm), the band fitting analysis was performed for this particular case (Figure 4.11). Beside the two already discussed Gaussian bands (centered at 2.80 / 440 nm and 2.50 eV / 495 nm) the best fit was obtained by the use of an additional band centered at 2.22 eV (560 nm). We recall now, that both samples were obtained under Zn-rich conditions and only P_{O2} was varied during their synthesis from extremely low (ZnO-5) to relatively high (ZnO-50). High P_{Zn} combined with very low P_{O2} applied during the fabrication of ZnO-5 can only favor the type of defects which must be again brought into the correlation with oxygen vacancies. In conclusion, the two PL emissions, the one at 2.50 eV (495 nm) that is present in all samples and one at 2.20 eV (560 nm) present only in ZnO-5, are due to oxygen vacancies. None of them is paramagnetic (i.e. V_O^+) since no corresponding EPR signal was detected in any of these samples. To resolve the puzzle of V_O-oxidation state we considered the findings of many theoretical works [65, 197, 277] who demonstrate that under Zn-rich conditions the formation energy of V_O^{2+} is the lowest among the three possible Vo-charge states. Accordingly, the PL emission at 2.50 eV (495 nm) that is observable in all three samples can be assigned to this particular defect. The calculations performed by Alkauskas et al. [222], demonstrate furthermore that under extremely low P_{O2} the transition from V_O^{2+} to V_O^0 takes place. Consequently, we attribute the emission at 2.22 eV (560 nm) measured only in ZnO-5 to neutral oxygen vacancies (V_O^0).

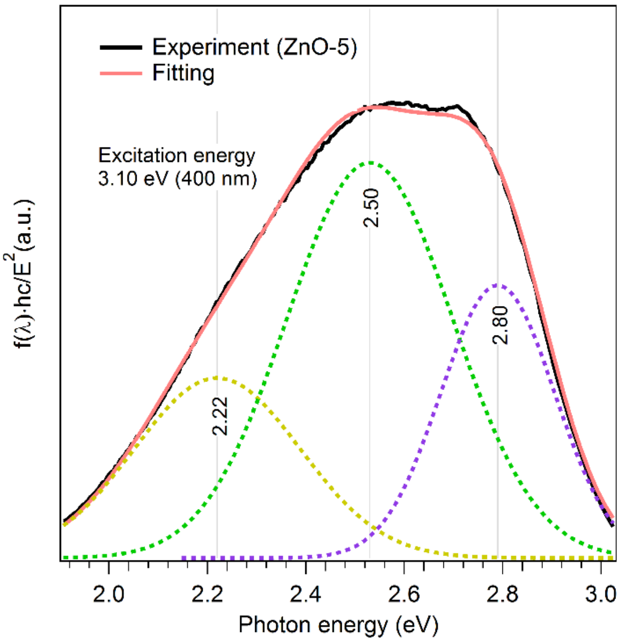

Figure 4.11 Band fitting analysis of PL spectrum of ZnO-5 obtained at E_{exc} = 3.10 eV (400 nm). Dashed curves indicate the component of each emission.

Among the three studied samples, ZnO-5 is the sample obtained under the lowest O_2-partial pressure. Therefore, in this sample neutral oxygen vacancies (V_O^0) may additionally occur and serve as the recombination center for the emission at 2.22 eV (560 nm) observed only in this sample. Interestingly, the optical transition that involves V_O^0 is favored under excitation energy lower than E_{bg}. The presence of neutral oxygen vacancies in ZnO-5 is strongly supported by the shape of its UV-absorption spectrum, shown in Figure 4.6 (a). Compared to the spectra of the other two samples, apart from the expected absorption edge around ~ 3.2 eV its spectrum shows an absorption tail that enters into the visible range. This can be explained by additional energy levels within the band gap from which the transitions of electrons can be provided with the energy lower than the E_{bg}, i.e. energy that corresponds to visible part of the emission spectrum ($\lambda > 400$ nm). Therefore, both, the yellowish color of the sample as well as the discussed PL-emission at 2.22 eV (560 nm), can only be explained by the presence of neutral oxygen vacancies that provide such electrons for the transitions (which would not be the case if considering the V_O^{2+}).

From this section, we conclude that the expected type of defects has been created by varying the partial pressure of oxygen. Furthermore, the concentration of zinc excess associated defects – Zn_i^+ and V_O^{2+} – can be reduced by increasing oxygen partial pressure (ZnO-50) while under extremely low P_{O2} also neutral oxygen vacancies can be additionally generated (ZnO-5).

4.3 ZnO-5 sample: PL properties in function of annealing temperature

ZnO-5 remains different from ZnO smoke and ZnO-50, mostly in terms of PL emission at 2.50 eV (495 nm) but also demonstrating the contribution of the emission at 2.80 eV (440 nm) (Zn_i^+) to be the highest among all. In order to reinforce the above assignments for the two existing emissions in this sample and also to get more insights into the defects behavior upon diverse experimental conditions, ZnO-5 was subjected to vacuum-annealing treatment ($P < 10^{-5}$ mbar) at different temperatures.

Figure 4.12 presents the PL spectra of ZnO-5 recorded after annealing in high-vacuum ($P < 10^{-5}$ mbar) at different temperatures. The intensity of UV emission falls down strongly after the annealing at $T_{ann} > 473$ K (magenta curve in Figure 4.12). Additionally, the intensity of the other emissions in the shown spectral range also decreases. Both of these observations are similar to the trend observed for ZnO smoke. The inset of Figure 4.13 compares the spectrum obtained at the last stage of annealing (673 K) with the one obtained on as-synthesized ZnO-5 sample. Both spectra were normalized to 1 regarding the intensity of the corresponding UV emission. Note that when annealing was performed at $T_{ann} = 773$ K PL emission was no longer detected in ZnO-5 (not shown here) which is not the case of ZnO-smoke (see Figure 3.13, section 3.1 in Chapter 3). As already demonstrated by EPR (the strongest EPR signal) and PL (almost no UV emission), ZnO-5 exhibits the highest concentration of defects among the three samples. This implies that its crystal structure is expected to be more easily damaged i.e. more drastically impacted in comparatively milder conditions. During the annealing, the color of ZnO-5 sample changes to gray: this was also observed in ZnO smoke sample upon vacuum-annealing and suggested to result from the formation of Zn^0 (out of Zn_i^+) which diffuse then to the surface and serve there as centers for non-radiative recombination (lowering the PL intensity). The loss of zinc, irrespectively of the oxidation state, is further demonstrated by XPS (not shown here). XPS results reveal that the ratio of integration area of Zn/O atoms decreases from 1.26 to 1.06 for the annealed ZnO-5 sample. All of these features indicate that the behavior of PL emission at 440 nm (2.80 eV) observed in ZnO-5 is similar to the one measured at 430 nm (2.88 eV) in as-synthesized ZnO smoke – implying Zn_i-related defects to lie in its origin.

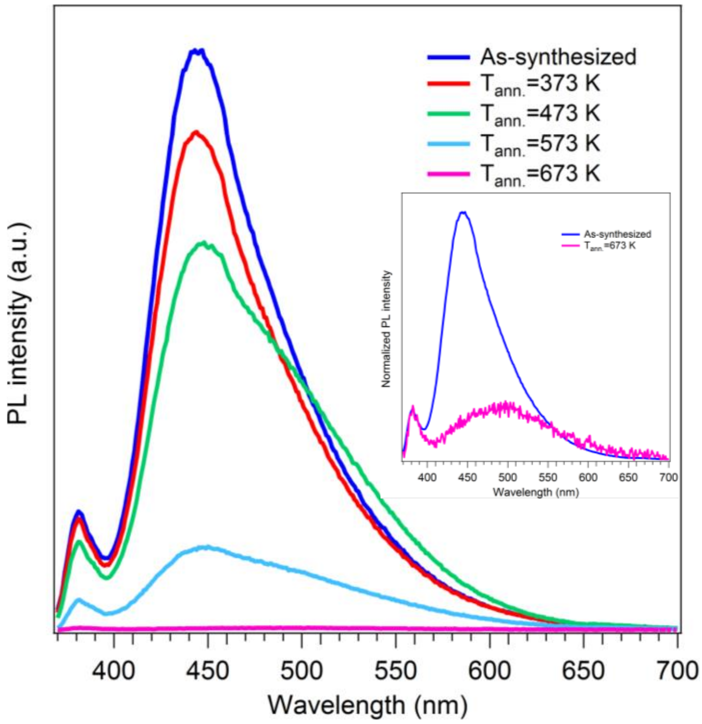

Figure 4.12 PL spectra of ZnO-5 sample in function of annealing temperature under high vacuum condition (P < 10^{-5} mbar). The inset presents normalized PL spectra corresponding to as-synthesized and the one after annealing in vacuum for 1 h at 673 K, and the UV emissions have been normalized to 1.

When T_{ann} reaches 473 K the emission at ~ 515 nm (2.41 eV) clearly shows up (green curve in Figure 4.12). According to analogue measurements performed on ZnO-smoke

(Chapter 3), this emission was associated with V_O^+. Considering now the presence of V_O^0 in ZnO-5 (suggested in previous section), the formation of V_O^+ can be proposed to occur via two simultaneous processes in this sample:

(1) $ZnO \rightarrow ZnO_{1-x} + x\, V_O^+ + x/2\, O_2 + x\, e^-$ (Equation 3.8)

This is the same as previously shown in ZnO-smoke i.e. via removal of lattice oxygen while an additional way may occur through the following reaction:

(2) $Zn_i^+ + V_O^0 \rightarrow Zn^0 + V_O^+$ (Equation 3.9)

Indeed, a complete loss of PL properties that was observed in ZnO-5 at earlier annealing stages ($T_{ann.}$ = 773 K) than in ZnO-smoke (T_{ann} >> 773 K) can be justified by such an additional process (Equation 3.9) occurring only in this sample.

In short, besides the native V_O^{2+} defects – that were also detected in ZnO smoke – V_O^0 is additionally and solely present in ZnO-5 sample. Upon vacuum annealing, this defect may transform into V_O^+ and hence reinforce the generation of Zn^0 – which as we know serve as a center for non-radiative recombination that is manifested in the loss of PL properties. Moreover, this occurs at annealing stages earlier than in ZnO smoke, since in ZnO-smoke the generation of Zn^0 goes only via oxygen desorption, i.e. process (1) (Equation 3.8).

4.4 FTIR: Adsorption of H_2O

Among other molecules (H_2, CO, CO_2 etc.) water is very commonly used to probe reactive surface sites on metal oxides. The OH-groups generated upon water dissociation at specific sites on metal oxide surfaces give rise to distinct vibration frequencies that can be easily tracked via infrared spectroscopy (IR). In that way, not only the reactivity of the given surface site is investigated but also its crystallographic environment, to which the corresponding vibrational frequency is strongly sensitive, can be distinguished. In a recent IR study in our group [263], ZnO smoke was used as a model system in interaction with water. Indirectly, by combining IR and DFT studies, its surface was identified to involve (10-10), (11-20), (0001), and (000-1) orientations with only 25% of the total surface area belonging to the polar orientations. In the same work, we were able to assign various OH-related frequencies to arise from the specific surface orientation. A unique OH whose band is measured at 3617 cm^{-1} and computed to stand up at the O-terminated (000-1) ZnO surface – in good agreement with previous studies obtained on single crystals by high-resolution electron energy loss spectroscopy (HREELS) [245]. We have furthermore assigned a bunch of OH-related IR bands, to come from (10-10) non-polar surface (these are located at 3690, 3673, 3555, 3240 3150 and 2530 cm^{-1}) and we also, for the first time, observed OH-bands related to (11-20) surface (peaks at 3240 and 2880 cm^{-1}) [6]. In another purely experimental study on ZnO nanopowders, the peak at 3617 cm^{-1} was more specifically assigned to OH groups formed by water dissociation on oxygen vacancy sites on O−ZnO(000-1) surfaces [245].

The electron microscopy study has shown that ZnO-5 and ZnO-50 present relatively different morphologies. More specifically, while ZnO-5 was found to expose surface orientations similar to those previously identified in ZnO smoke [6], ZnO-50 was shown to exhibit hexagonal prisms resulting in a quite different ratio between polar and non-polar contributions. In addition, in some of these hexagonal prisms, the contribution of one over another non-polar face was shown to be strongly reduced. Having in mind that the OH-stretching vibration at ~ 3617 cm^{-1} represents a fingerprint of the OH formed on oxygen vacancies sitting on O-terminated ZnO surface, the analysis of IR spectra, obtained after water adsorption on vacuum-annealed ZnO-5 and ZnO-50 samples can provide more insights into the type of defects existing in these two samples.

As we have proposed, oxygen vacancies in their neutral form are present in as-synthesized ZnO-5 sample, while specific spectroscopic signatures of V_O^+ were found after the sample was annealed in high-vacuum. Interestingly, such annealing treatment is anyway requested when IR-measurements are performed with using surface probes – such as OH-groups, since clean / adsorbate free surface is necessary before such an experiment. Therefore, annealing in ultra high vacuum (UHV) at 673 K was applied to ZnO-5 and ZnO-50 samples before water adsorption that was followed by IR-measurement.

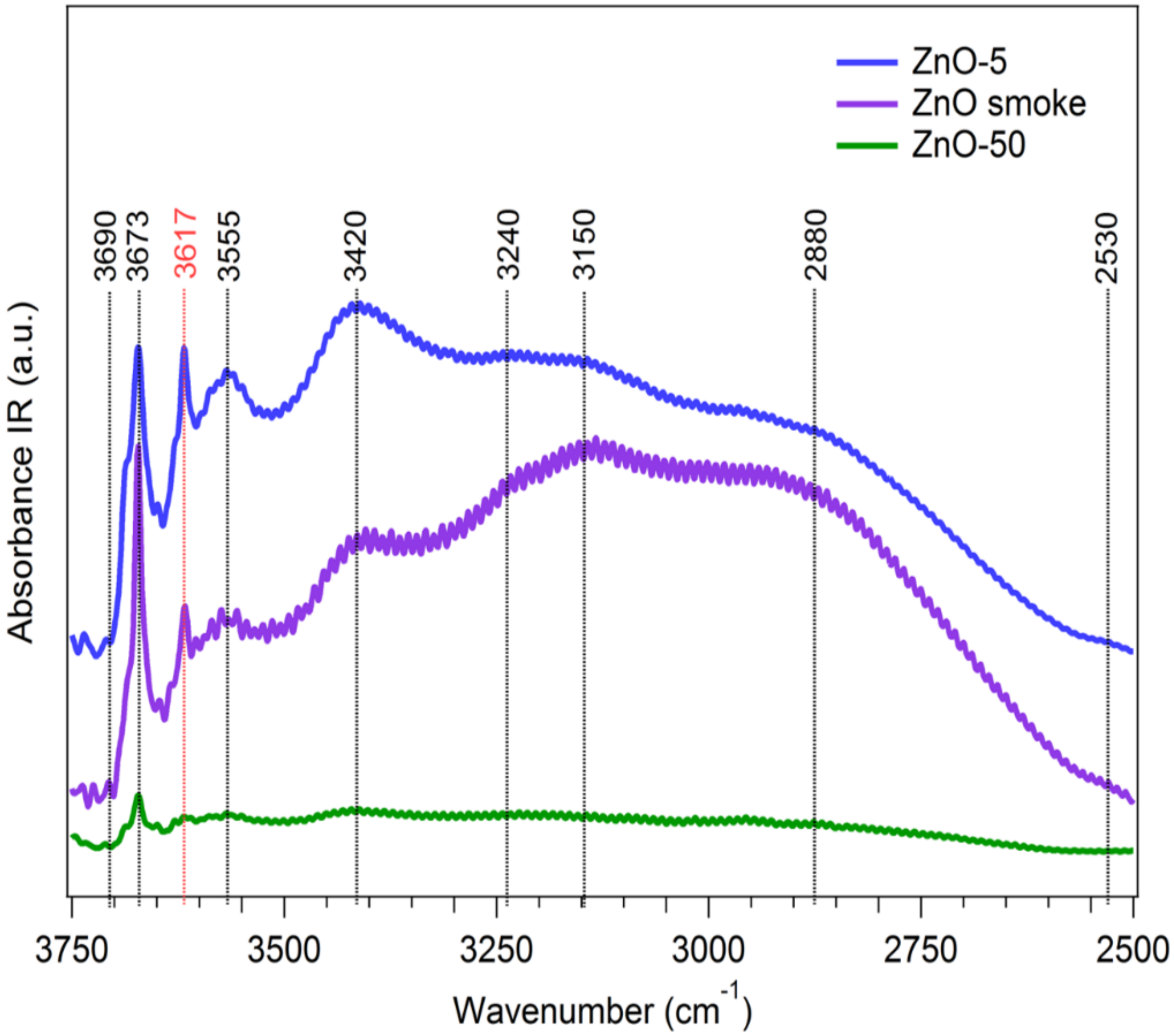

Figure 4.13 UHV-FTIR spectra obtained after exposing the clean ZnO-5 (blue curve) and ZnO-50 (green curve) to P_{H2O} *= 10 mbar at room temperature in an UHV chamber. Prior to* H_2O *adsorption the clean ZnO samples were thermally treated (*T_{ann} *= 773 K) in the UHV chamber in order to remove adsorbed species. All the spectra were recorded under* $P < 10^{-5}$ *mbar. IR spectrum obtained for ZnO smoke in the same conditions was taken from Reference 6 and presented for the sake of comparison (violet curve).*

The FTIR spectra – reported in Figure 4.13 – were recorded after the admission of water (P_{H2O} = 10 mbar) at 300 K onto cleaned surfaces of ZnO-5 and ZnO-50 samples. The IR spectrum obtained for ZnO-smoke under the same conditions is added for the sake of comparison. By comparing the IR spectra of the three ZnO samples, two important conclusions can be derived:

(1) The spectra obtained on ZnO-5 and ZnO-smoke appear to be very similar and to exhibit same structures – as also expected from their similar morphology. The most intense IR band is observed at 3673 cm^{-1} for these two samples (blue and violet curves in Figure 4.13) while for ZnO-50 (green curve) this band is significantly less intense. According to our previous findings, the peak at 3673 cm^{-1} can be attributed to OH-groups formed on (10-10) ZnO surface. The same is true for the band at 3690 cm^{-1} and a bunch of broad bands that additionally appear in the spectral range 3500-2500 cm^{-1} [245, 263]. Although with significantly lower intensity, the band at 3673 cm^{-1} is also observed for ZnO-50. This fits well to the illustration we have suggested in Figure 4.4 (section 4.1), represented by Wulff constructions, based on observed shapes from TEM images, and illustrate how the contribution of the two nonpolar ZnO surface orientations may be changed in this sample.

(2) The broad band centered ~ 3420 cm^{-1} was detected in the IR spectrum of ZnO-5. In our previous study this band was associated to water structures on (11-20) faces. This implies that, in the case of ZnO-5, the (11-20) non-polar orientation dominates over the (10-10) one – which is exactly opposite in ZnO-smoke. The band at 3417 cm^{-1} is hardly detectable for ZnO-50 – that is, again, in agreement with the morphology of this sample (shown by TEM to be quite different than that of ZnO-smoke and ZnO-5) and supports, again, our hypothesis of (10-10) surface orientation to be favorable over (11-20) in ZnO-50 (see Figure 4.4, section 4.1).

(3) The peak at 3617 cm^{-1} is of comparable intensity for ZnO-5 and ZnO smoke. It confirms our hypothesis that V_O^+ can be created in ZnO-5 upon vacuum-annealing treatment – and, obviously, interact with water. Indeed, the same is true for ZnO-smoke and the mentioned IR-feature (3617 cm^{-1}) can be put in correlation with PL emission (~ 515 nm / 2.41 eV) and EPR signal (g = 2.003). However, this peak is hardly detectable in ZnO-50 sample (green curve) implying that O-terminated surface is not favorable in this sample.

(4) All of the IR bands that are clearly visible on ZnO-5 and ZnO-smoke are strongly quenched in the spectrum of ZnO-50. Surely, when comparing the overall IR spectra of ZnO-5 and ZnO-50, the peak intensity or even the presence of a given peak can be questioned in terms of particle size. However, the difference in crystalline size measured for the two samples (ZnO-5 ~ 35 nm and ZnO-50 ~ 73 nm) cannot explain such differences in their IR spectra. Moreover, after the spectra were normalized with respect to the strongest peak,

namely the one at 3690 cm^{-1} (not shown here), trends in intensity were found to be comparable to those observed in the original spectra. An option to be considered is the presence of only zinc-terminated ZnO(0001) surface in ZnO-50, the hydroxylation of which is not expected to be observed in the IR spectra since the intensity of the related O–H stretching band is predicted to be too weak [263]. The stabilization of otherwise unstable, polar Zn-terminated face could be associated with the synthesis conditions. Although providing significantly less contaminations than the combustion of Zn in the air, the conditions used for the synthesis of ZnO-50 (and ZnO-5) are still far from UHV and may, therefore, contain some traces of residual water which at the end may contribute to the stabilization of Zn-terminated face. However, on the basis on our HRTEM results, we have no clear supports for this hypothesis and additional measurements have to be done.

4.5 Perspectives: ZnO nanoparticles produced by chemical vapor synthesis method

In ZnO samples prepared by combustion method we have shown the nature of point defects and that their relative concentrations can be modulated depending on the synthesis conditions going from O_2-poor to O_2-rich atmosphere. Indeed, we have concluded that in oxygen-poor conditions (oxidizing Zn in low P_{O2} or annealing in vacuum / zinc), oxygen vacancies (V_O^{2+}, V_O^{+} or V_O^{0}) are formed. Inversely, in oxygen-rich conditions (either annealing in oxygen) O_i-related spectroscopic signatures have been measured. Nevertheless, our home-made set-up used for the metal combustion, provides almost a sole synthesis parameter that can be varied, i.e. P_{O2}. Another disadvantage that was met by employing this fabrication method is a relative inhomogeneity of both, the size and shape of ZnO particles. Finally, ZnO material was obtained in most of the cases with an insufficient yield, preventing us to perform some experiments that request a significantly larger amount of powder.

In order to overcome the above-described drawbacks caused by technical limitations, we have introduced another fabrication method, chemical vapor synthesis (CVS), a technique fundamentally similar to metal combustion – since both are based on the oxidation reaction of zinc to occur in the gas-phase. CVS method is considered as an efficient way to produce ZnO nanoparticles with high purity, through which their particle size, shape and agglomeration are expected to be precisely controlled according to many studies [52-54]. In CVS synthesis, P_{O2}

and/or P_{Zn} can be varied adapting some experimental parameters such as the flow of oxygen and of the carrier gas (Ar or N_2), the evaporation temperature of Zn and the total pressure of the system.

In this section, we present some preliminary results obtained on one ZnO-CVS sample and the discussion and conclusion were made by comparison to ZnO-combustion samples.

4.5.1 Characterization of morphologies by TEM microscopy

The ZnO-CVS sample shown in this section was produced in an oxygen flow of 500 mL/min and an argon flow of 1000 mL/min. The evaporation temperature of Zn (923 K) corresponds to a Zn-vapor pressure of ~ 500 mbar and the total pressure of the system was kept constant ($P_{total} = 50$ mbar) during the synthesis.

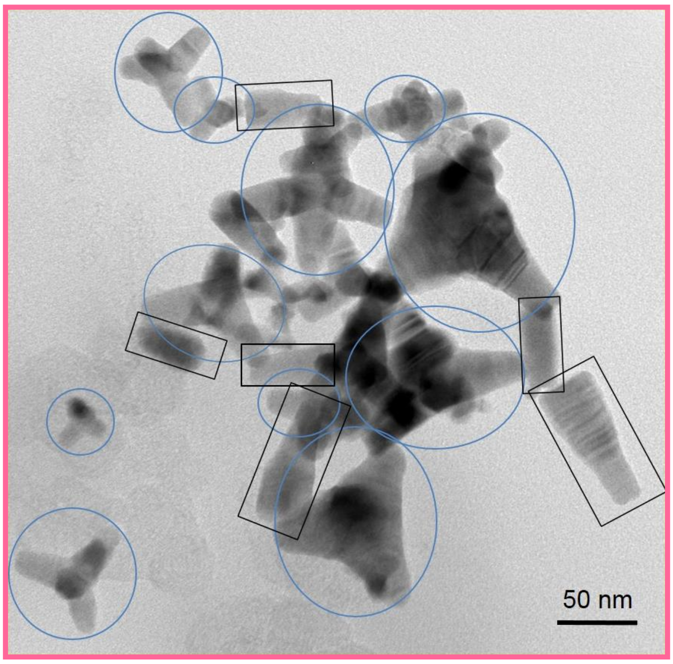

Figure 4.14 TEM images of ZnO-CVS sample

Figure 4.14 presents the TEM image of ZnO-CVS sample, from which the majority of shapes can be recognized as tetrapod-like (light-blue circles). However, those tetrapods are quite different to those typically observed in ZnO-smoke. Not only the diameter of the tetrapod legs (around 30 ~ 55 nm) or the length (around 15 ~ 40 nm) remain different from ZnO-smoke, but also the CVS particles do not provide well-defined surface facets such as observed in ZnO-smoke tetrapods. In addition, another irregular type of shapes can also be observed in TEM images of this material (black rectangles) – these look very like isolated fragments i.e. single legs of previously described tetrapods. Obviously, at this preliminary stage, we are still not mastering the synthesis parameters: though the particles size is rather homogeneous, the morphology of ZnO-CVS remains inhomogeneous. Moreover, the legs of ZnO-CVS tetrapods are almost two times shorter than in ZnO smoke and ZnO-5 samples. Finally, we note the presence of strongly stepped surfaces both in tetrapod-like or separated legs of ZnO-CVS sample. This implies surface orientations to be strongly different than those present in combustion samples. Additional HRTEM characterizations will be required to try to identify the indexation of the surface plane exposed.

4.5.2 DR UV-Vis spectroscopy

The UV-vis spectrum of ZnO-CVS (pink curve) is compared with those of ZnO smoke (violet curve) and ZnO-5 (blue curve) in Figure 4.15. Apart from the typical UV absorption gap, ZnO-CVS sample exhibits a tail state in the visible range of spectrum that is quite similar to that observed for ZnO-5 sample. This is also manifested by a strong coloration of the sample as dark yellow to almost orange. As already discussed in the previous sections such additional absorption tails in the UV-Vis spectrum implies on gap states populated with electrons, the transition of which occurs by absorbing energy lower than E_{bg} i.e. wavelengths larger than 400 nm. By analogy with conclusions drawn by similar features observed for ZnO-5, this might be indicative of the involvement of neutral oxygen vacancies V_O^0. The presence of states within the band gap in this sample can also be deduced from its E_{bg} value: Tauc-plot in Figure 4.15 (b), indicates the lowest E_{bg} value for ZnO-CVS sample is (~ 3.17 eV), when compared to that of ZnO-5 (3.23 eV) and ZnO smoke (3.26 eV) and especially to the value usually reported for bulk ZnO (3.33 eV). Also for other semiconducting metal oxides, such as TiO_2 [278] and CeO_2 [279], the presence of defects was reported to lead to intraband transitions and bandgap narrowing.

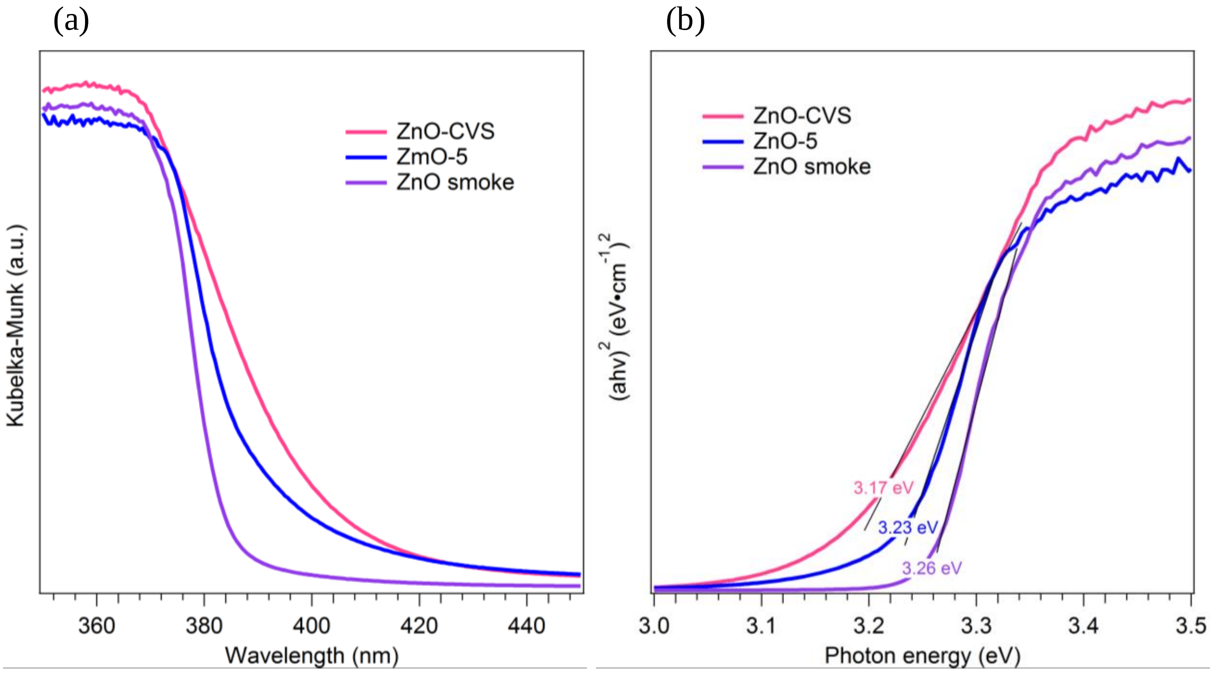

Figure 4.15 Comparison of UV-vis spectra of ZnO-CVS (pink curve), ZnO-5 (blue curve) and ZnO smoke (violet curve) samples (a) and corresponding Tauc-plots for determining their bandgap energies (b).

4.5.3 EPR spectroscopy

The native defects in ZnO-CVS sample were examined by EPR at 77 K and shown in Figure 4.16 together with corresponding EPR spectra obtained on ZnO-smoke (violet curve) and ZnO-5 (blue curve) samples. Seen from the compared EPR spectra of three samples in Figure 4.16, an intense signal with g~1.958 together with a weaker signal at 1.962 is observed. The line shape of these two signals is quite similar to those in as-synthesized ZnO smoke and ZnO-5 samples, however, with a shift of the g-values (+ 0.02) when compared to the other two samples. We propose that the signal with g~1.958 and g~1.962 may also originate from Zn_i^+-related defects, assuming that such shift of the g-values may be due to the different environments surrounding Zn_i^+ in ZnO-CVS sample from those in ZnO smoke and ZnO-5 samples. This might be related to more defective surfaces deduced from TEM characterizations. Consistently, the intensity of these EPR signals, related to Zn_i^+, is much stronger than that in the other two samples. Such a much increased amount of Zn_i^+ present in ZnO-CVS sample, even when compared to the case of ZnO-5 produced in extreme low partial pressure of oxygen, implies that the conditions used for producing this ZnO-CVS sample correspond to an even zinc-richer atmosphere. In ZnO-CVS sample, an isotropic and narrow signal was additionally detected at ~ 2.014 (inset, Figure 4.16). This signal implies that another paramagnetic defect is present in CVS sample the contribution of which is extremely weak (less than 0.2 %). Yet, due to the lack of complementary results at this stage, the origin of this signal cannot be assigned.

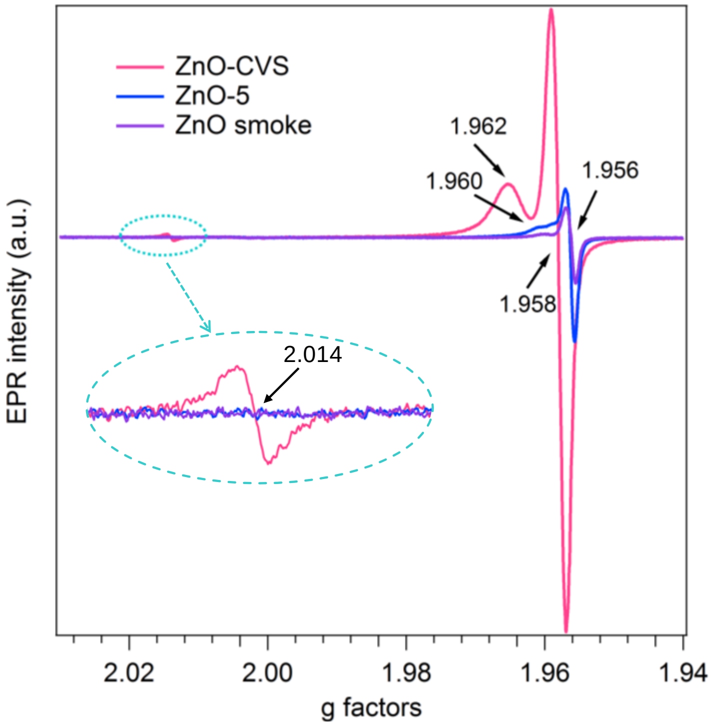

Figure 4.16 Comparison of EPR spectra of ZnO-CVS (pink curve), ZnO-5 (blue curve) and ZnO smoke (violet curve) samples, and the inset is the correspondingly zoomed EPR spectra in ellipsoid part.

4.5.4 PL properties

The defect-related properties of ZnO-CVS sample is further investigated by PL measurements performed under excitation energy at 300 nm (4.13 eV) at room temperature. Seen from the PL spectrum of ZnO-CVS (pink curve) in Figure 4.17, the typical UV emission related to band to band transition is weak, while an intense and broad emission in the visible region with a maximum at ~ 490 nm is detected. Comparing this to the PL spectra of ZnO smoke (violet curve) and ZnO-5 (blue curve) samples in Figure 4.17, we see that the contribution of visible emission in ZnO-CVS is the highest among the three samples, while the contribution of the UV emission is the lowest. This implies on the highest concentration of defects in this sample which is in line with the results obtained by UV-vis and EPR spectroscopy.

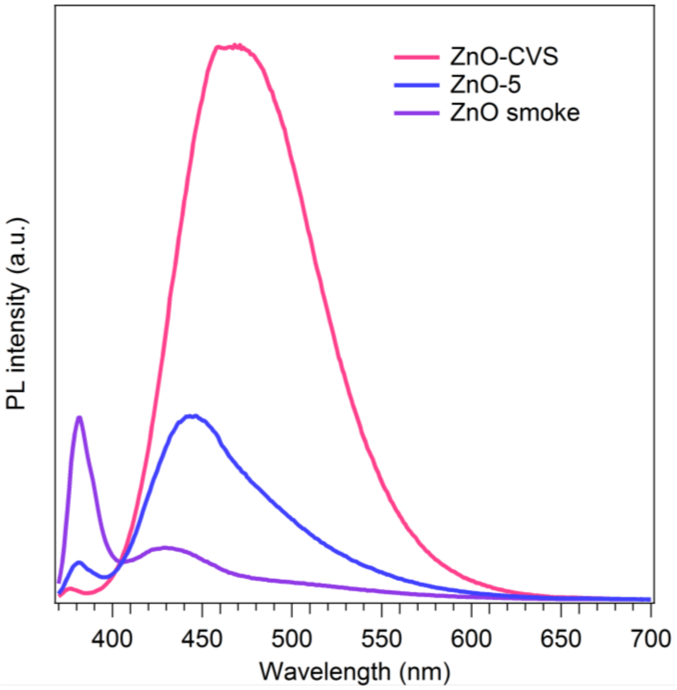

Figure 4.17 Comparison of PL spectra of ZnO-CVS (pink curve), ZnO-5 (blue curve) and ZnO smoke (violet curve) samples.

According to band fitting analysis, three peaks, at 2.78, 2.54 and 2.28 eV, must be used to achieve the best fitting result. The band at 2.78 eV / 445 nm can be related to above shown EPR signals with g factors at 1.958 and 1.962 and put in correlation with Zn_i^+ defects. When comparing to corresponding spectroscopic features previously discussed for ZnO-samples obtained by metal combustion, we note the shift in both, EPR and PL positions. This is not surprising having in mind the morphology of this sample, especially exhibiting stepped facets, which may lead to a quite different local environment of the defect in question when compared to previous samples. The same applies for the second band used for the fitting, here

2.54 eV / 490 nm against 2.5 eV / 495 nm in ZnO prepared by metal combustion, that, moreover, appears to dominate. Out of the preliminary results, obtained on this sample, but mostly based on our previous assignments – we attribute this PL peak (2.54 eV / 490 nm) to V_O^{2+} vacancies, which is not surprising since this defect was detected in our all as-synthesized samples (ZnO smoke, ZnO-5 and ZnO-50). Another fitting band, with maximum at 2.28 eV / 545 nm, seems also to be shifted if we correlate it to the band at 2.22 eV / 560 nm used for the fitting in case of ZnO-5 (section 4.2.3). In that case, this particular emission was attributed to neutral oxygen vacancies (V_O^0) in line with the absorption properties of this sample and its color. Interestingly, the same applies for the CVS sample. The powder exhibits strong yellow color and, as it was shown above in Figure 4.15 (b), it reveals the lowest E_{bg} as well as the most significant tail in visible absorption among all compared samples. Despite to some spectroscopic similarities with ZnO-5, we keep in mind the presence of an additional EPR peak in the spectrum of CVS-sample. This peak ($g \sim 2.014$), although weakly contributing (only by 0.2 %) implies that in CVS-ZnO some charged defect might be present additionally and the PL feature of which is most probably masked under the dominating and broad emission at 2.54 eV (490 nm). Therefore, additional sets of investigations are necessary to better assess the nature of native defects in CVS-samples. This includes the comparison of samples prepared by varying the synthesis parameters during CVS as well as to better control and understand their morphology.

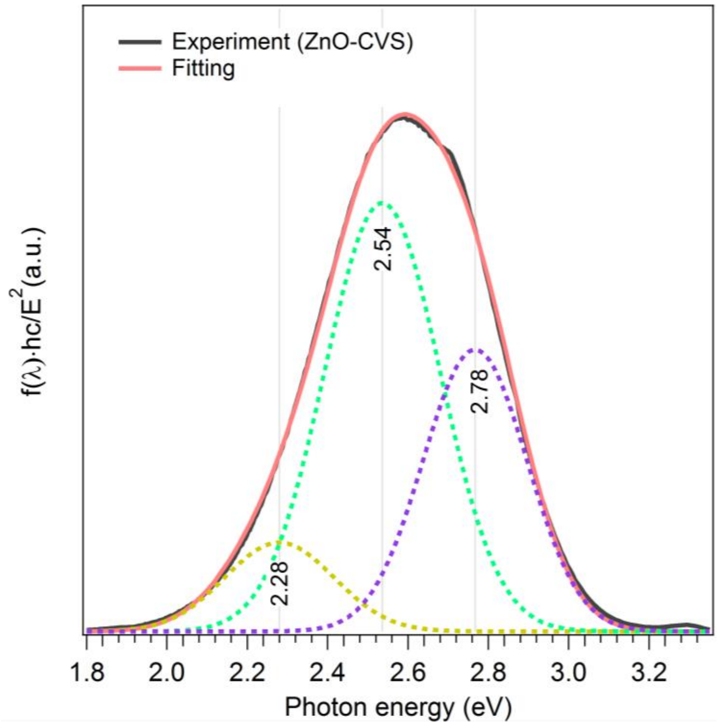

Figure 4.18 Fitting analysis of PL spectrum of ZnO-CVS sample.

Hence, via CVS method, less defined surface facets are induced in ZnO nanotetrapods compared to those produced by metal combustion method. In addition to this, the stepped surfaces observed in ZnO-CVS sample demonstrate that the surface orientations are strongly different from the synthesis methods.

Moreover, the comparison of spectroscopic properties of ZnO nanoparticles produced by two vapor-based methods indicates that the CVS sample is highly defective. The more intense EPR signals at g ~ 1.962 and g ~ 1.958 imply that ZnO-CVS sample contains the highest concentration of Zn_i^+. The crystallographic environments of these defects differ from those in ZnO samples produced by metal combustion method. The detection of Zn_i^+ and V_O^{2+} implies that the atmosphere for synthesizing ZnO-CVS sample is still oxygen poor / deficient. In addition, the existence of V_O^0, is deduced from the strongest shift of the tail state in UV-vis spectrum of ZnO-CVS samples and the dark yellow color of this sample itself. Moreover, the largest proportion of visible emission probably contributed by Zn_i^+, V_O^0, V_O^{2+} and other unidentified defect makes ZnO-CVS sample the most defective among all the obtained ZnO samples up to now.

To make out how the spectroscopic features are affected by the defects present in ZnO nanoparticles produced by vapor-based methods, further investigations are required to deal with unsolved problems, especially for the ZnO nanoparticles produced by CVS method, for instance, from the following aspects:

- Whether the morphology plays a role in the modification of nature defects and spectroscopic features. If yes, how it behaves?

- What is the origin of the EPR signal with g ~ 2.014?

- How synthesis parameters for CVS method will impact the nature of defect?

4.6 Conclusions

Two additional ZnO-5 and ZnO-50 samples were prepared by combustion of metallic Zn, using lower and higher partial oxygen pressures compared to that involved when producing ZnO smoke sample (air), respectively. As illustrated by the data gathered in Table 4.3, the oxygen partial pressure used during the combustion greatly impacts both the morphology properties and the spectroscopic features obtained for these two samples. In high oxygen partial pressure (ZnO-50), hexagonal prisms nanoparticles are obtained, but, in some cases, the growth of non-polar (10-10) planes prevails on that of (11-20) ones, resulting in quite unusual pseudo cubic shaped particles. Despite tetrapod-like nanoparticles obtained in ZnO-5, similar to those obtained for the smoke sample, the peculiar defectiveness of this sample is revealed by the lack of oxygen deduced from Raman and by the band tail observed by UV Vis diffuse reflectance spectroscopy.

Close examination of EPR and PL features allowed us to identify the nature of the native defects formed. The emission at ~ 2.80 eV (440 nm) together with EPR signals resonating at $g_{||} = 1.956$, $g_{\perp} = 1.957$ and $g = 1.960$ were observed in both samples, however contributing with significantly higher intensities in ZnO-5 sample. Moreover, a third EPR contributions was also detected in ZnO-5, with very close g value (1.958), rather directs to originate from defects of similar nature, but located in a different crystallographic environment. Given that the two sets of EPR signals was previously assigned to Zn_i^+ (Chapter 3), we can conclude that the partial pressure of oxygen used during the fabrication was still not sufficient to completely exclude this defect in ZnO-50.

Despite the absence of EPR signal characteristic of V_O^+, PL emission contributions at 2.50 eV (495 nm) are detected in ZnO-5 and ZnO-50 samples. Given that i) the relative concentration of this defect is enhanced in O-poor condition, ii) the correlated lack of oxygen was revealed by Raman and iii) the appearance of an additional PL emission at 2.22 eV (560 nm) upon excitation at lower energy than that of the band gap in the lone case of ZnO-5 was observed, we finally propose that PL signal at 2.50 (495 nm) eV is assigned to +2 charge state of oxygen vacancies (V_O^{2+}) whereas that at 2.22 eV (560 nm) would be related to neutral oxygen vacancies V_O^0. The presence of this latter defect in ZnO-5 would finally be responsible for its yellowish coloration.

Upon annealing the ZnO-5 sample up to 473 K, the PL emission at 2.41 eV (515 nm) grows up. Given that it was assigned to V_O^+ in chapter 3, the formation of Vo^+, in the present case, is not only associated to the desorption of oxygen lattice (as described in chapter 3), but also to the reduction of Zn_i^+ by V_O^0 to form metallic zinc and paramagnetic V_O^+ defect. Consistently, adsorption of water on the annealed ZnO-5 sample leads to the formation of OH groups with a characteristic IR band at 3617 cm^{-1} (resulting from water dissociation on V_O^+ defect) which supports the presence of oxygen vacancies.

Table 4.3 Comparison between as-synthesized ZnO-5 and ZnO-50 samples in terms of morphologies, structures and spectroscopic properties.

	Samples		Comments
	ZnO-5 (yellowish)	ZnO-50 (white)	
Morphology	Tetrapods (dominating)	hexagonal prisms (dominating), some cubic-like particles together with few tetrapods	

XRD	Intense Diffraction lines	Intense and thinner diffraction lines	Wurtzite
UV-Vis	3.23 eV Band tail	3.26 eV	Band gap energy
Raman	434 cm^{-1} (weak)	434 cm^{-1} (intense)	Oxygen sublattice
PL	~ 440 nm / 2.80 eV 22.5×10^{7} (a.u)	~ 440 nm / 2.80 eV 5.98×10^{7} (a.u.)	Zn_i^+
	~ 495 nm / 2.50 eV 22.1×10^{7} (a.u.)	~ 495 nm / 2.50 eV 10.5×10^{7} (a.u.)	V_O^{2+}
	560 nm / 2.22 eV	---	V_O^0
EPR	$g_{\|} = 1.956$, $g_{\perp} = 1.957$	$g_{\|} = 1.956$, $g_{\perp} = 1.957$	surface Zn_i^+
	$g_{iso} = 1.958$	---	Zn_i^+
	$g_{iso} = 1.960$ (bulk Zn_i^+)	$g_{iso} = 1.960$	bulk Zn_i^+
IR	3617 cm^{-1} (strong)	---	Dissociation of water on V_O^+

Alternative synthesis method (CVS method) was also preliminary investigated. It confirms how the synthesis conditions impacts both the particles morphology and the native defects. The EPR fingerprints of the paramagnetic ones, Zn_i^+ observed are slightly shifted compared to those observed for other samples, which raises the question of the influence of their local environment (may be due to peculiar facet of the tetrapods) on the spectroscopic features. In richer zinc conditions compared to ZnO samples prepared by direct combustion, the peculiar defectiveness of the ZnO obtained is illustrated by its dark yellow color and co-existence of different types of oxygen vacancies (V_O^{2+} and V_O^0), and of high relative concentration of Zn_i^+. The complexity of this system requires additional investigations to identify a new extremely weak EPR signal with g ~ 2.014 only detected in ZnO CVS sample.

Chapter 5: General conclusions and perspectives

Point defects play a key role in the applications of ZnO nanoparticles. The assignment of their corresponding spectroscopic fingerprints is, however, still questionable despite the numerous experimental and theoretical studies devoted to the identification of these defects. This is rather due to the variety of point defects (such as V_O, V_{Zn}, Zn_i, O_i, Zn_O and O_{Zn}) that also exhibit different charge states) and to the fact that the reported calculated formation energies and energy levels of each type of defect significantly differ from one calculation method to another. Moreover, measurement conditions are not always well controlled – neither described – which additionally complicates the observation and interpretation of the spectroscopic features. Finally, depending on the synthesis preparation methods, incorporation of extrinsic defects (impurities) may also be expected, except if using precursors in form of pure metallic zinc.

The aim of this thesis was to investigate the nature of defects in ZnO nanoparticles in relation with their condition of formation. Hence, two clean preparation routes were implemented to obtain nanostructured ZnO model systems. One is based on combustion of zinc in air (ZnO smoke, Chapter 3) or in an O_2/Ar mixture of variable molar ratios (5/95 for ZnO-5 and 50/50 for ZnO-50, Chapter 4). The second is a chemical vapor synthesis, and implies conditions in which flow of oxygen and argon is provided (preliminary results in chapter 4). Both synthesis methods led to the formation of wurzite ZnO nanoparticles whereas the morphology found to vary from tetrapod-like (ZnO smoke, ZnO-5, minor amount in ZnO-50, and with stepped surfaces in ZnO-CVS) to regular hexagonal prism or pseudo cubic shapes (ZnO-50).

Peculiar attention was paid to the discrimination of the native defects present in the as-synthesized ZnO samples and those detected after post-growth treatments in various atmospheres. In addition, the as-synthesized samples were transferred and stored in a cell dedicated to maintain the high vacuum to avoid any contaminations from air (except ZnO smoke which was exposed to the air during the fabrication itself). The evolution of defect-related spectroscopic features was monitored by a set of complementary techniques: photoluminescence (PL), electron paramagnetic resonance (EPR), diffuse reflectance UV-vis (DR UV-vis) spectroscopy, XPS (X-ray photoelectron spectroscopy), Raman and Fourier-transform infrared spectroscopy (FTIR). All these techniques were implemented under high vacuum conditions and a dedicated vacuum line was built up to allow measurements to be performed *in situ* (PL, EPR). Moreover, such set-up allowed for controlled post-growth treatments: annealing atmosphere from high-vacuum to P_{O2} = 100 mbar, adsorption of probe molecules (oxygen or water) P = 10^{-8} to 10 mbar. Various conditions were applied during the synthesis and the series of spectra were analyzed to provide reasonable assignments of the spectroscopic features.

This methodology enlightened how sensitive is the nature and concentration of the native defects to preparation conditions as well as to post synthesis treatments. By combining diverse spectroscopic features, it is concluded that all the as-synthesized ZnO samples obtained by combustion method contain Zn_i^+ species, located both in the bulk and on the surface. This was reflected in PL emission centered at ~ 2.8 eV (445 ~ 430 nm) and to close EPR signals with g factor around 1.96. The Zn_i^+-related EPR signal was found to be quite sensitive to the local crystallographic environment of these species, which allows us to assign the signal resonating at 1.956) to surface Zn_i^+ and the one at 1.960 to bulk. Out of the preliminary results obtained on ZnO-CVS, which exhibits quite particular morphology, we suggest the EPR signal with g ~ 1.958 to be related to Zn_i^+ located on stepped-surface. An enhancement of the oxygen partial pressure led to the decrease in the relative amount of the Zn_i^+ - as expected. The same tendency is observed for the second type of detected native defects, namely doubly charge positive oxygen vacancies (V_O^{2+}) associated to PL emission at ~ 2.5 eV (495 ~ 490 nm) present in all the samples. The spectroscopic properties of more defective sample, ZnO-5, indicate that neutral oxygen vacancies (Vo^0) are only present in this sample. This could be evidenced by additional absorption feature in DR UV-vis spectrum that allowed PL emission to be measured under excitation energy lower than the band gap. Consequently, yellowish color of ZnO-5 could be brought into the relationship with this specific defect – an assignment that is also often controversial in the literature. Even if still preliminary results, CVS method seems to lead to peculiar defects illustrated by the shift of EPR fingerprints (1.958 and 1.962) and all PL emissions revealed by band fitting analysis (2.78 eV/ 445 nm, 2.54 eV / 490 nm and 2.28 eV/ 545 nm proposed to be associated with Zn_i^+ and V_O^{2+}, and Vo^0, respectively). It is questioning if they are located on the stepped surface of the tetrapods. Higher concentration of Zn_i^+, V_O^{2+} and V_O^0, can be evidenced for this sample while the charge state of oxygen vacancies can also be tuned to some extent.

In the case of ZnO produced by combustion, the formation of V_O^+ is only observed upon annealing in oxygen-poor condition (such as high vacuum and zinc vapor). The generation of V_O^+ was reflected by the appearance of PL emission at 515 nm (2.41 eV) and EPR signals with g = 2.003 together with the detection of EPR fingerprints (2.043, 2.009, 2.002) specific of superoxide ions (O_2^-)- the creation of which occurred despite gaseous O_2 was not additionally added. Therefore, the creation of superoxide ions, and so the V_O^+, could be doubtless concluded to occur only through the removal of lattice oxygen. Upon V_O^+-formation, one electron is released and to reduce Zn_i^+ into Zn^0, explaining the significant decrease (ZnO-5) or complete disappearance (ZnO-smoke) of the related spectroscopic features. Such a reduction explains that the color of the powder changes from white to gray. On the contrary, annealing in presence of gaseous oxygen, oxygen vacancies become partially passivated whereas Zn^0, transitory formed on the surface, undergoes oxidation into Zn_i^+. This is magnified by the increase / reappearance of corresponding Zn_i^+ surface features (reappearance of 440 nm and 1.956). Finally, PL emission with the maximum at 2.10 eV (590 nm) was only detected upon annealing ZnO smoke in high partial pressure of oxygen and accordingly assigned to oxygen interstitials (O_i).

ZnO reactivity can be greatly affected by tuning its defects. Water interaction on the vacuum-annealing ZnO surface was investigated by *in situ* PL and EPR in the case of the ZnO-smoke and by IR in the case of the ZnO-5. It is found that V_O^+ are affected by water dissociation on Vo^+ and O^{2-} ion pair located on polar oxygen terminated (000-1) surface, resulting in the filling up of the related vacancy, the associated electron being then consumed to reduce Zn^{2+} in Zn^+. The expected two OH formed are structurally equivalent and give rise to a unique IR band at 3617 cm^{-1}. The adsorption of water on non-polar faces also leads to hydroxylation of the related surfaces. Besides adsorption experiments involving water vapor, the reactivity of the ZnO smoke surfaces was investigated by flowing a model alcohol molecule (2-methyl-3-butyn-2-ol (MBOH)) and following the gas phase catalytic reaction in which MBOH is converted into acetone and acetylene. We also shown that the basic behavior of ZnO smoke catalyst can be modulated after applying different controlled pretreatments. The related redox processes impact the relative concentrations of various defects and the associated electron release / consumption that are responsible for enhancement or lowering of the basic properties, respectively.

This PhD work opens up new perspectives in identifying the nature of defects natively present in ZnO nanopowders. In this context, ZnO nanoparticles synthesized by vapor-phase based techniques were shown as appropriate model systems. Defects of desired nature could be induced in ZnO powders by judicious choice of synthesis parameters. This requires a wider playground that can be achieved via CVS (only preliminary results shown here) which in contrast to metal combustion, provides a larger set of adjustable parameters. With this technique, not only partial pressure of Zn and/ or oxygen can be varied but also other factors, such as the total system pressure, the temperature in the reaction zone etc. Moreover, the morphology and the related ratios between polar/non-polar (or between two non-polar) facets were also shown to strongly affect the spectroscopic properties of the particles, both in samples produced by combustion (ZnO-50) and by CVS. It will be of great interest to study in detail the microscopic changes affected by synthesis parameters and asses at which particular surface orientation a given type of defects can be stabilized. For this purpose, a new low-temperature UHV-FTIR setup ($T < 10$ K) is under construction in the INSP group and the related results will be combined with HRTEM measurements.

References

[1] F. Xu, Y. Shen, L. Sun, H. Zeng and Y. Lu, Enhanced photocatalytic activity of hierarchical ZnO nanoplate-nanowire architecture as environmentally safe and facilely recyclable photocatalyst, *Nanoscale,* **2011,** *3,* 5020.

[2] H. Xu, X. Liu, D. Cui, M. Li and M. Jiang, A novel method for improving the performance of ZnO gas sensors, *Sensors and Actuators B: Chemical,* **2006,** *114,* 301.

[3] S. H. Ko, D. Lee, H. W. Kang, K. H. Nam, J. Y. Yeo, S. J. Hong, C. P. Grigoropoulos and H. J. Sung, Nanoforest of hydrothermally grown hierarchical ZnO nanowires for a high efficiency dye-sensitized solar cell, *Nano letters,* **2011,** *11,* 666.

[4] P. Duran, F. Capel, J. Tartaj and C. Moure, A strategic two-stage low-temperature thermal processing leading to fully dense and fine-grained doped-ZnO varistors, *Advanced Materials,* **2002,** *14,* 137.

[5] M. AbdElhady, Preparation and characterization of chitosan/zinc oxide nanoparticles for imparting antimicrobial and UV protection to cotton fabric, *International journal of carbohydrate chemistry,* **2012,** *2012,*

[6] B. Cao, X. Teng, S. H. Heo, Y. Li, S. O. Cho, G. Li and W. Cai, Different ZnO nanostructures fabricated by a seed-layer assisted electrochemical route and their photoluminescence and field emission properties, *The Journal of Physical Chemistry C,* **2007,** *111,* 2470.

[7] X. Ren, X. Zhang, N. Liu, L. Wen, L. Ding, Z. Ma, J. Su, L. Li, J. Han and Y. Gao, White Light‐Emitting Diode From Sb‐Doped p‐ZnO Nanowire Arrays/n‐GaN Film, *Advanced Functional Materials,* **2015,** *25,* 2182.

[8] A. Janotti and C. G. Van de Walle, Fundamentals of zinc oxide as a semiconductor, *Reports on Progress in Physics,* **2009,** *72,* 126501.

[9] J. H. Lim, C. K. Kang, K. K. Kim, I. K. Park, D. K. Hwang and S. J. Park, UV electroluminescence emission from ZnO light‐emitting diodes grown by high‐temperature radiofrequency sputtering, *Advanced Materials,* **2006,** *18,* 2720.

[10] C. Soci, A. Zhang, B. Xiang, S. A. Dayeh, D. Aplin, J. Park, X. Bao, Y.-H. Lo and D. Wang, ZnO nanowire UV photodetectors with high internal gain, *Nano letters,* **2007,** *7,* 1003.

[11] Z. Wang, Y. Lu, J. Liu, Z. Dang, L. Zhang and W. Wang, Preparation of nano‐zinc oxide/EPDM composites with both good thermal conductivity and mechanical properties, *Journal of Applied Polymer Science,* **2011,** *119,* 1144.

[12] M.-H. Zhao, Z.-L. Wang and S. X. Mao, Piezoelectric characterization of individual zinc oxide nanobelt probed by piezoresponse force microscope, *Nano Letters,* **2004,** *4,* 587.

[13] C. Wei, Y. Lin, Y. Hu, C. Wu, C. Shih, C. Huang and S. Chang, Partial-electroded ZnO pyroelectric sensors for responsivity improvement, *Sensors and Actuators A: Physical,* **2006,** *128,* 18.

[14] H. Tzou and C. Tseng, Distributed piezoelectric sensor/actuator design for dynamic measurement/control of distributed parameter systems: a piezoelectric finite element approach, *Journal of sound and vibration,* **1990,** *138,* 17.

[15] H. Gullapalli, V. S. Vemuru, A. Kumar, A. Botello‐Mendez, R. Vajtai, M. Terrones, S. Nagarajaiah and P. M. Ajayan, Flexible piezoelectric ZnO–paper nanocomposite strain sensor, *small,* **2010,** *6,* 1641.

[16] Y. Ito, K. Kushida, K. Sugawara and H. Takeuchi, A 100-MHz ultrasonic transducer array using ZnO thin films, *Ultrasonics, Ferroelectrics and Frequency Control, IEEE Transactions on,* **1995,** *42,* 316.

[17] R. Boppella, K. Anjaneyulu, P. Basak and S. V. Manorama, Facile synthesis of face oriented ZnO crystals: tunable polar facets and shape induced enhanced photocatalytic performance, *The Journal of Physical Chemistry C,* **2013,** *117,* 4597.

[18] A. Leelavathi, G. Madras and N. Ravishankar, Origin of enhanced photocatalytic activity and photoconduction in high aspect ratio ZnO nanorods, *Physical Chemistry Chemical Physics,* **2013,** *15,* 10795.

[19] M. Huang, Y. Yan, W. Feng, S. Weng, Z. Zheng, X. Fu and P. Liu, Controllable tuning various ratios of ZnO polar facets by crystal seed-assisted growth and their photocatalytic activity, *Crystal Growth & Design,* **2014,** *14,* 2179.

[20] E. S. Jang, J. H. Won, S. J. Hwang and J. H. Choy, Fine tuning of the face orientation of ZnO crystals to optimize their photocatalytic activity, *Advanced Materials,* **2006,** *18*, 3309.

[21] M. R. Alenezi, S. J. Henley, N. G. Emerson and S. R. P. Silva, From 1D and 2D ZnO nanostructures to 3D hierarchical structures with enhanced gas sensing properties, *Nanoscale,* **2014,** *6*, 235.

[22] X. Bai, L. Wang, R. Zong, Y. Lv, Y. Sun and Y. Zhu, Performance enhancement of ZnO photocatalyst via synergic effect of surface oxygen defect and graphene hybridization, *Langmuir,* **2013,** *29*, 3097.

[23] N. M. Flores, U. Pal, R. Galeazzi and A. Sandoval, Effects of morphology, surface area, and defect content on the photocatalytic dye degradation performance of ZnO nanostructures, *RSC Advances,* **2014,** *4,* 41099.

[24] H.-L. Guo, Q. Zhu, X.-L. Wu, Y.-F. Jiang, X. Xie and A.-W. Xu, Oxygen deficient ZnO 1− x nanosheets with high visible light photocatalytic activity, *Nanoscale,* **2015,** *7*, 7216.

[25] C. Drouilly, J.-M. Krafft, F. Averseng, H. Lauron-Pernot, D. Bazer-Bachi, C. Chizallet, V. Lecocq and G. Costentin, Role of oxygen vacancies in the basicity of ZnO: From the model methylbutynol conversion to the ethanol transformation application, *Applied Catalysis A: General,* **2013,** *453*, 121.

[26] P. Biswas, S.-D. Baek, S. H. Lee, J.-H. Park, S. J. Lee, T. I. Lee and J.-M. Myoung, Low temperature solution process-based defect-induced orange-red light emitting diode, *Scientific reports,* **2015,** *5*,

[27] S. Chen, Y. Liu, C. Shao, R. Mu, Y. Lu, J. Zhang, D. Shen and X. Fan, Structural and optical properties of uniform ZnO nanosheets, *Advanced Materials,* **2005,** *17*, 586.

[28] H. Zeng, W. Cai, Y. Li, J. Hu and P. Liu, Composition/structural evolution and optical properties of ZnO/Zn nanoparticles by laser ablation in liquid media, *The Journal of Physical Chemistry B,* **2005,** *109*, 18260.

[29] R. Chen, Q.-L. Ye, T. He, V. D. Ta, Y. Ying, Y. Y. Tay, T. Wu and H. Sun, Exciton localization and optical properties improvement in nanocrystal-embedded ZnO core–shell nanowires, *Nano letters,* **2013,** *13*, 734.

[30] S. H. K. Park, C. S. Hwang, M. Ryu, S. Yang, C. Byun, J. Shin, J. I. Lee, K. Lee, M. S. Oh and S. Im, Transparent and Photo‐stable ZnO Thin‐film Transistors to Drive an Active Matrix Organic‐Light‐Emitting‐Diode Display Panel, *Advanced Materials,* **2009,** *21*, 678.

[31] A. K. Chandiran, M. Abdi-Jalebi, A. Yella, M. I. Dar, C. Yi, S. A. Shivashankar, M. K. Nazeeruddin and M. Grätzel, Quantum-confined ZnO nanoshell photoanodes for mesoscopic solar cells, *Nano letters,* **2014,** *14*, 1190.

[32] B. Wei, K. Zheng, Y. Ji, Y. Zhang, Z. Zhang and X. Han, Size-dependent bandgap modulation of ZnO nanowires by tensile strain, *Nano letters,* **2012,** *12*, 4595.

[33] H. Wang, L. Jia, P. Bogdanoff, S. Fiechter, H. Möhwald and D. Shchukin, Size-related native defect engineering in high intensity ultrasonication of nanoparticles for photoelectrochemical water splitting, *Energy & Environmental Science,* **2013,** *6*, 799.

[34] Y. Lv, W. Xiao, W. Li, J. Xue and J. Ding, Controllable synthesis of ZnO nanoparticles with high intensity visible photoemission and investigation of its mechanism, *Nanotechnology,* **2013,** *24*, 175702.

[35] I. Shalish, H. Temkin and V. Narayanamurti, Size-dependent surface luminescence in ZnO nanowires, *Physical Review B,* **2004,** *69*, 245401.

[36] E. Erdem, Microwave power, temperature, atmospheric and light dependence of intrinsic defects in ZnO nanoparticles: A study of electron paramagnetic resonance (EPR) spectroscopy, *Journal of Alloys and Compounds,* **2014,** *605*, 34.

[37] L. Lazzarini, G. Salviati, F. Fabbri, M. Zha, D. Calestani, A. Zappettini, T. Sekiguchi and B. Dierre, Unpredicted nucleation of extended zinc blende phases in wurtzite ZnO nanotetrapod arms, *ACS nano,* **2009,** *3*, 3158.

[38] L. Shi, A. J. Naik, J. B. Goodall, C. Tighe, R. Gruar, R. Binions, I. Parkin and J. Darr, Highly sensitive ZnO nanorod-and nanoprism-based NO2 gas sensors: size and shape control using a continuous hydrothermal pilot plant, *Langmuir,* **2013,** *29*, 10603.

[39] N. T. Khoa, S. W. Kim, D. Van Thuan, D.-H. Yoo, E. J. Kim and S. H. Hahn, Hydrothermally controlled ZnO nanosheet self-assembled hollow spheres/hierarchical aggregates and their photocatalytic activities, *CrystEngComm,* **2014,** *16*, 1344.

[40] S. Cho, S.-H. Jung and K.-H. Lee, Morphology-controlled growth of ZnO nanostructures using microwave irradiation: from basic to complex structures, *The Journal of Physical Chemistry C,* **2008,** *112*, 12769.

[41] G.-S. Wang, Y.-Y. Wu, X.-J. Zhang, Y. Li, L. Guo and M.-S. Cao, Controllable synthesis of uniform ZnO nanorods and their enhanced dielectric and absorption properties, *Journal of Materials Chemistry A,* **2014,** *2*, 8644.

[42] P. Rai, W.-K. Kwak and Y.-T. Yu, Solvothermal synthesis of ZnO nanostructures and their morphology-dependent gas-sensing properties, *ACS applied materials & interfaces,* **2013,** *5*, 3026.

[43] S. Y. Sawant, S. Senthilkumar, R. S. Somani, M. H. Cho and H. C. Bajaj, Eco-friendly, catalyst-free synthesis of highly pure carbon spheres using vegetable oils as a renewable source and their application as a template for ZnO and MgO hollow spheres, *RSC Advances,* **2015,** *5*, 57114.

[44] E. Javon, M. Gaceur, W. Dachraoui, O. Margeat, J. r. Ackermann, M. I. Saba, P. Delugas, A. Mattoni, S. Bals and G. Van Tendeloo, Competing forces in the self-assembly of coupled ZnO nanopyramids, *ACS nano,* **2015,** *9*, 3685.

[45] Y. Yang, Y. Jin, H. He, Q. Wang, Y. Tu, H. Lu and Z. Ye, Dopant-induced shape evolution of colloidal nanocrystals: the case of zinc oxide, *Journal of the American Chemical Society,* **2010,** *132*, 13381.

[46] M. Fricke, A. Voigt, P. Veit and K. Sundmacher, Miniemulsion-based process for controlling the size and shape of zinc oxide nanoparticles, *Industrial & Engineering Chemistry Research,* **2015,** *54*, 10293.

[47] R. Q. Song, A. W. Xu, B. Deng, Q. Li and G. Y. Chen, From layered basic zinc acetate nanobelts to hierarchical zinc oxide nanostructures and porous zinc oxide nanobelts, *Advanced Functional Materials,* **2007,** *17*, 296.

[48] J.-J. Feng, Q.-C. Liao, A.-J. Wang and J.-R. Chen, Mannite supported hydrothermal synthesis of hollow flower-like ZnO structures for photocatalytic applications, *CrystEngComm,* **2011,** *13*, 4202.

[49] H. Zhang, D. Yang, X. Ma, Y. Ji, J. Xu and D. Que, Synthesis of flower-like ZnO nanostructures by an organic-free hydrothermal process, *Nanotechnology,* **2004,** *15*, 622.

[50] Z. Zhang, S. Liu, S. Chow and M.-Y. Han, Modulation of the morphology of ZnO nanostructures via aminolytic reaction: from nanorods to nanosquamas, *Langmuir,* **2006,** *22*, 6335.

[51] S. Stankic, M. Cottura, D. Demaille, C. Noguera and J. Jupille, Nucleation and growth concepts applied to the formation of a stoichiometric compound in a gas phase: the case of MgO smoke, *Journal of Crystal Growth,* **2011,** *329*, 52.

[52] S. Polarz, A. Roy, M. Merz, S. Halm, D. Schröder, L. Schneider, G. Bacher, F. E. Kruis and M. Driess, Chemical Vapor Synthesis of Size ‐ Selected Zinc Oxide Nanoparticles, *Small,* **2005,** *1*, 540.

[53] Y. Qiu and S. Yang, ZnO Nanotetrapods: Controlled Vapor ‐ Phase Synthesis and Application for Humidity Sensing, *Advanced Functional Materials,* **2007,** *17*, 1345.

[54] R. R. Bacsa, J. Dexpert ‐ Ghys, M. Verelst, A. Falqui, B. Machado, W. S. Bacsa, P. Chen, S. M. Zakeeruddin, M. Graetzel and P. Serp, Synthesis and Structure ‐ Property Correlation in Shape ‐ Controlled ZnO Nanoparticles Prepared by Chemical Vapor Synthesis and their Application in Dye ‐ Sensitized Solar Cells, *Advanced Functional Materials,* **2009,** *19*, 875.

[55] S.-M. Zhou, H.-C. Gong, B. Zhang, Z.-L. Du, X.-T. Zhang and S.-X. Wu, Synthesis and photoluminescence of a full zinc blende phase ZnO nanorod array, *Nanotechnology,* **2008,** *19*, 175303.

[56] F. Decremps, J. Pellicer-Porres, F. Datchi, J. Itié, A. Polian, F. Baudelet and J. Jiang, Trapping of cubic ZnO nanocrystallites at ambient conditions, *Applied physics letters,* **2002,** *81*, 4820.

[57] H. Morkoç and Ü. Özgür, *Zinc oxide: fundamentals, materials and device technology*. John Wiley & Sons: 2008.

[58] F. Viñes, A. Iglesias-Juez, F. Illas and M. Fernández-García, Hydroxyl identification on ZnO by infrared spectroscopies: theory and experiments, *The Journal of Physical Chemistry C,* **2014,** *118*, 1492.

[59] D. Scarano, G. Spoto, S. Bordiga, A. Zecchina and C. Lamberti, Lateral interactions in CO adlayers on prismatic ZnO faces: a FTIR and HRTEM study, *Surface science*, **1992,** *276*, 281.

[60] S. Kittaka, T. Sasaki and N. Fukuhara, Fourier transform infrared spectroscopy of water on the hydroxylated zinc oxide surface, *Langmuir*, **1992,** *8*, 2598.

[61] L. Schmidt-Mende and J. L. MacManus-Driscoll, ZnO–nanostructures, defects, and devices, *Materials today*, **2007,** *10*, 40.

[62] http://archive.cnx.org/contents/d2ad49b4-d12f-47f5-aeb1-4506f4909795@1/sspd-chapter-1-part-11-solid-state-of-matter-conclusin-defects-in-crystal-structures,

[63] http://chemistry.tutorcircle.com/inorganic-chemistry/crystal-defects.html,

[64] A. Russell and K. L. Lee, *Structure-property relations in nonferrous metals*. John Wiley & Sons: 2005.

[65] A. Janotti and C. G. Van de Walle, Native point defects in ZnO, *Physical Review B*, **2007,** *76*, 165202.

[66] L. Vlasenko, Magnetic resonance studies of intrinsic defects in ZnO: Oxygen vacancy, *Applied Magnetic Resonance*, **2010,** *39*, 103.

[67] S. B. Zhang, S. H. Wei and A. Zunger, Intrinsic n-type versus p-type doping asymmetry and the defect physics of ZnO, *Physical Review B*, **2001,** *63*, 075205.

[68] A. Janotti and C. G. Van de Walle, Oxygen vacancies in ZnO, *Applied Physics Letters*, **2005,** *87*, 122102.

[69] A. Janotti and C. G. Van de Walle, New insights into the role of native point defects in ZnO, *Journal of Crystal Growth*, **2006,** *287*, 58.

[70] S. Lany and A. Zunger, Dopability, intrinsic conductivity, and nonstoichiometry of transparent conducting oxides, *Physical Review Letters*, **2007,** *98*, 045501.

[71] C. Patterson, Role of defects in ferromagnetism in Zn 1− x Co x O: a hybrid density-functional study, *Physical Review B*, **2006,** *74*, 144432.

[72] F. Oba, A. Togo, I. Tanaka, J. Paier and G. Kresse, Defect energetics in ZnO: A hybrid Hartree-Fock density functional study, *Physical Review B*, **2008,** *77*, 245202.

[73] T. R. Paudel and W. R. Lambrecht, First-principles calculation of the O vacancy in ZnO: A self-consistent gap-corrected approach, *Physical Review B*, **2008,** *77*, 205202.

[74] F. Oba, S. R. Nishitani, S. Isotani, H. Adachi and I. Tanaka, Energetics of native defects in ZnO, *Journal of Applied Physics*, **2001,** *90*, 824.

[75] C. Kittel, *Introduction to solid state physics*. Wiley: 2005.

[76] P. Erhart and K. Albe, First-principles study of migration mechanisms and diffusion of oxygen in zinc oxide, *Physical Review B*, **2006,** *73*, 115207.

[77] F. Tuomisto, K. Saarinen, D. C. Look and G. C. Farlow, Introduction and recovery of point defects in electron-irradiated ZnO, *Physical Review B*, **2005,** *72*, 085206.

[78] G. H. Vineyard, Frequency factors and isotope effects in solid state rate processes, *Journal of Physics and Chemistry of Solids*, **1957,** *3*, 121.

[79] A. Janotti and C. G. Van de Walle, Hydrogen multicentre bonds, *Nature materials*, **2007,** *6*, 44.

[80] M. McCluskey and S. Jokela, Defects in zno, *Journal of Applied Physics*, **2009,** *106*, 071101.

[81] K. Vijayakumar, P. Ratheesh Kumar, C. Sudha Kartha, K. Wilson, F. Singh, K. Nair and Y. Kashiwaba, Effects of oxygen ion implantation in spray‐pyrolyzed ZnO thin films, *physica status solidi (a)*, **2006,** *203*, 860.

[82] Z. Wang, S. Su, F. C.-C. Ling, W. Anwand and A. Wagner, Thermal evolution of defects in undoped zinc oxide grown by pulsed laser deposition, *Journal of Applied Physics*, **2014,** *116*, 033508.

[83] Q. Zhu, C. Xie, H. Li, C. Yang, S. Zhang and D. Zeng, Selectively enhanced UV and NIR photoluminescence from a degenerate ZnO nanorod array film, *Journal of Materials Chemistry C*, **2014,** *2*, 4566.

[84] Y. Zang, X. He, J. Li, J. Yin, K. Li, C. Yue, Z. Wu, S. Wu and J. Kang, Band edge emission enhancement by quadrupole surface plasmon–exciton coupling using direct-contact Ag/ZnO nanospheres, *Nanoscale*, **2013,** *5*, 574.

[85] C. Chen, H. He, Y. Lu, K. Wu and Z. Ye, Surface passivation effect on the Photoluminescence of ZnO nanorods, *ACS applied materials & interfaces,* **2013,** *5*, 6354.
[86] Y. Lu, X. Li, P. Cao, S. Su, F. Jia, S. Han, W. Liu, D. Zhu and X. Ma, Study of ultraviolet emission spectra in ZnO thin films, *Journal of Spectroscopy,* **2012,** *2013,*
[87] Q. Zhao, M. Willander, R. Morjan, Q. Hu and E. Campbell, Optical recombination of ZnO nanowires grown on sapphire and Si substrates, *Applied Physics Letters,* **2003,** *83*, 165.
[88] A. B. Djurišić and Y. H. Leung, Optical properties of ZnO nanostructures, *small,* **2006,** *2*, 944.
[89] S.-H. Jeong, B.-S. Kim and B.-T. Lee, Photoluminescence dependence of ZnO films grown on Si (100) by radio-frequency magnetron sputtering on the growth ambient, *Applied Physics Letters,* **2003,** *82*, 2625.
[90] H. Zeng, G. Duan, Y. Li, S. Yang, X. Xu and W. Cai, Blue Luminescence of ZnO nanoparticles based on non ‐ equilibrium processes: defect origins and emission controls, *Advanced Functional Materials,* **2010,** *20*, 561.
[91] W. Wan, J. Huang, L. Zhu, L. Hu, Z. Wen, L. Sun and Z. Ye, Defects induced ferromagnetism in ZnO nanowire arrays doped with copper, *CrystEngComm,* **2013,** *15*, 7887.
[92] X. Fan, J. Lian, Z. Guo, L. Zhao and Q. Jiang, Influence of the annealing temperature on violet emission of ZnO films obtained by oxidation of Zn film on quartz glass, *Journal of materials science,* **2006,** *41*, 2237.
[93] L. Jia, W. Cai, H. Wang and H. Zeng, Polar-field-induced double-layer nanostructured ZnO and its strong violet photoluminescence, *Crystal Growth and Design,* **2008,** *8*, 4367.
[94] X. Xu, S. Lau, J. Chen, G. Chen and B. Tay, Polycrystalline ZnO thin films on Si (100) deposited by filtered cathodic vacuum arc, *Journal of Crystal Growth,* **2001,** *223*, 201.
[95] C. Chen, Y. Lu, H. He, M. Xiao, Z. Wang, L. Chen and Z. Ye, Violet emission in ZnO nanorods treated with high-energy hydrogen plasma, *ACS applied materials & interfaces,* **2013,** *5*, 10274.
[96] C. Drouilly, J.-M. Krafft, F. d. r. Averseng, S. Casale, D. Bazer-Bachi, C. l. Chizallet, V. Lecocq, H. Vezin, H. l. n. Lauron-Pernot and G. n. Costentin, ZnO oxygen vacancies formation and filling followed by in situ photoluminescence and in situ EPR, *The Journal of Physical Chemistry C,* **2012,** *116*, 21297.
[97] O. Mondal and M. Pal, Strong and unusual violet-blue emission in ring shaped ZnO nanocrystals, *Journal of Materials Chemistry,* **2011,** *21*, 18354.
[98] M. Kavitha, K. Jinesh, R. Philip, P. Gopinath and H. John, Defect engineering in ZnO nanocones for visible photoconductivity and nonlinear absorption, *Physical Chemistry Chemical Physics,* **2014,** *16*, 25093.
[99] D. Zhang, Z. Xue and Q. Wang, The mechanisms of blue emission from ZnO films deposited on glass substrate by rf magnetron sputtering, *Journal of Physics D: Applied Physics,* **2002,** *35*, 2837.
[100] N. Garces, L. Wang, L. Bai, N. Giles, L. Halliburton and G. Cantwell, Role of copper in the green luminescence from ZnO crystals, *Applied Physics Letters,* **2002,** *81*, 622.
[101] S. Muthukumaran and R. Gopalakrishnan, Structural, FTIR and photoluminescence studies of Cu doped ZnO nanopowders by co-precipitation method, *Optical Materials,* **2012,** *34*, 1946.
[102] C. Ton-That, L. Weston and M. Phillips, Characteristics of point defects in the green luminescence from Zn-and O-rich ZnO, *Physical Review B,* **2012,** *86*, 115205.
[103] S. Repp, S. Weber and E. Erdem, Defect Evolution of Nonstoichiometric ZnO Quantum Dots, *The Journal of Physical Chemistry C,* **2016,** *120*, 25124.
[104] Y. Y. Tay, T. Tan, F. Boey, M. H. Liang, J. Ye, Y. Zhao, T. Norby and S. Li, Correlation between the characteristic green emissions and specific defects of ZnO, *Physical Chemistry Chemical Physics,* **2010,** *12*, 2373.
[105] D. Wang, H. Seo, C.-C. Tin, M. Bozack, J. Williams, M. Park, N. Sathitsuksanoh, A.-j. Cheng and Y. Tzeng, Effects of postgrowth annealing treatment on the photoluminescence of zinc oxide nanorods, *Journal of Applied Physics,* **2006,** *99*, 113509.
[106] F. Liu, Y. H. Leung, A. B. Djurišić, A. M. C. Ng, W. K. Chan, K. L. Ng, K. S. Wong, C. Liao, K. Shih and C. Surya, Effect of plasma treatment on native defects and photocatalytic activities of zinc oxide tetrapods, *The Journal of Physical Chemistry C,* **2014,** *118*, 22760.

[107] Q. Zhao, P. Klason, M. Willander, H. Zhong, W. Lu and J. Yang, Deep-level emissions influenced by O and Zn implantations in ZnO, *Applied Physics Letters*, **2005,** *87*, 211912.

[108] Y. Heo, D. Norton and S. Pearton, Origin of green luminescence in ZnO thin film grown by molecular-beam epitaxy, *Journal of Applied Physics*, **2005,** *98*, 073502.

[109] B. Lin, Z. Fu and Y. Jia, Green luminescent center in undoped zinc oxide films deposited on silicon substrates, *Applied Physics Letters,* **2001,** *79*, 943.

[110] Z. Wang, X. Zu, S. Zhu and L. Wang, Green luminescence originates from surface defects in ZnO nanoparticles, *Physica E: Low-dimensional systems and nanostructures,* **2006,** *35*, 199.

[111] J. Lv and C. Li, Evidences of VO, VZn, and Oi defects as the green luminescence origins in ZnO, *Applied Physics Letters,* **2013,** *103*, 232114.

[112] N. Korsunska, L. Borkovska, B. Bulakh, L. Y. Khomenkova, V. Kushnirenko and I. Markevich, The influence of defect drift in external electric field on green luminescence of ZnO single crystals, *Journal of luminescence,* **2003,** *102,* 733.

[113] L. E. Greene, M. Law, J. Goldberger, F. Kim, J. C. Johnson, Y. Zhang, R. J. Saykally and P. Yang, Low‐temperature wafer‐scale production of ZnO nanowire arrays, *Angewandte Chemie International Edition,* **2003,** *42*, 3031.

[114] A. Djurišić, Y. Leung, K. Tam, Y. Hsu, L. Ding, W. Ge, Y. Zhong, K. Wong, W. Chan and H. Tam, Defect emissions in ZnO nanostructures, *Nanotechnology,* **2007,** *18*, 095702.

[115] F. Stavale, N. Nilius and H.-J. Freund, STM Luminescence Spectroscopy of Intrinsic Defects in ZnO $(000\bar{1})$ Thin Films, *The Journal of Physical Chemistry Letters,* **2013,** *4*, 3972.

[116] K. Knutsen, A. Galeckas, A. Zubiaga, F. Tuomisto, G. Farlow, B. Svensson and A. Y. Kuznetsov, Zinc vacancy and oxygen interstitial in ZnO revealed by sequential annealing and electron irradiation, *Physical Review B,* **2012,** *86*, 121203.

[117] O. Jayakumar, V. Sudarsan, C. Sudakar, R. Naik, R. Vatsa and A. Tyagi, Green emission from ZnO nanorods: Role of defects and morphology, *Scripta Materialia*, **2010,** *62,* 662.

[118] J. Čížek, J. Valenta, P. Hruška, O. Melikhova, I. Procházka, M. Novotný and J. Bulíř, Origin of green luminescence in hydrothermally grown ZnO single crystals, *Applied Physics Letters,* **2015,** *106,* 251902.

[119] Q. Zhao, X. Xu, X. Song, X. Zhang, D. Yu, C. Li and L. Guo, Enhanced field emission from ZnO nanorods via thermal annealing in oxygen, *Applied physics letters,* **2006,** *88*, 033102.

[120] H. S. Kang, J. S. Kang, J. W. Kim and S. Y. Lee, Annealing effect on the property of ultraviolet and green emissions of ZnO thin films, *Journal of Applied Physics,* **2004,** *95*, 1246.

[121] B. Panigrahy, M. Aslam, D. S. Misra, M. Ghosh and D. Bahadur, Defect‐related emissions and magnetization properties of ZnO nanorods, *Advanced Functional Materials*, **2010,** *20*, 1161.

[122] K. Vanheusden, C. Seager, W. t. Warren, D. Tallant and J. Voigt, Correlation between photoluminescence and oxygen vacancies in ZnO phosphors, *Applied Physics Letters,* **1996,** *68*, 403.

[123] N. Karak, P. K. Samanta and T. K. Kundu, Green photoluminescence from highly oriented ZnO thin film for photovoltaic application, *Optik-International Journal for Light and Electron Optics,* **2013,** *124*, 6227.

[124] T. M. Børseth, B. Svensson, A. Y. Kuznetsov, P. Klason, Q. Zhao and M. Willander, Identification of oxygen and zinc vacancy optical signals in ZnO, *Applied Physics Letters,* **2006,** *89*, 262112.

[125] B. Jin, S. Im and S. Y. Lee, Violet and UV luminescence emitted from ZnO thin films grown on sapphire by pulsed laser deposition, *Thin Solid Films,* **2000,** *366*, 107.

[126] A. R. Gheisi, C. Neygandhi, A. K. Sternig, E. Carrasco, H. Marbach, D. Thomele and O. Diwald, O 2 adsorption dependent photoluminescence emission from metal oxide nanoparticles, *Physical Chemistry Chemical Physics,* **2014,** *16*, 23922.

[127] Z. Wang, C. Lin, X. Liu, G. Li, Y. Luo, Z. Quan, H. Xiang and J. Lin, Tunable photoluminescent and cathodoluminescent properties of ZnO and ZnO: Zn phosphors, *The Journal of Physical Chemistry B,* **2006,** *110*, 9469.

[128] F. Morazzoni, R. Scotti and S. Volontè, Electron paramagnetic resonance investigation of paramagnetic point defects in ZnO and ZnO-supported ruthenium, *Journal of the Chemical Society, Faraday Transactions,* **1990,** *86*, 1587.

[129] J. Lv, C. Li and J. BelBruno, Defect evolution on the optical properties of H+-implanted ZnO whiskers, *CrystEngComm,* **2013,** *15*, 5620.

[130] K. Vanheusden, W. Warren, C. Seager, D. Tallant, J. Voigt and B. Gnade, Mechanisms behind green photoluminescence in ZnO phosphor powders, *Journal of Applied Physics*, **1996,** *79*, 7983.

[131] X. Xue, T. Wang, X. Jiang, J. Jiang, C. Pan and Y. Wu, Interaction of hydrogen with defects in ZnO nanoparticles–studied by positron annihilation, Raman and photoluminescence spectroscopy, *CrystEngComm,* **2014,** *16*, 1207.

[132] G. Neumann, On the Defect Structure of Zinc ‐ Doped Zinc Oxide, *physica status solidi (b),* **1981,** *105*, 605.

[133] W. K. Liu, K. M. Whitaker, A. L. Smith, K. R. Kittilstved, B. H. Robinson and D. R. Gamelin, Room-temperature electron spin dynamics in free-standing ZnO quantum dots, *Physical review letters,* **2007,** *98*, 186804.

[134] L. Halliburton, N. Giles, N. Garces, M. Luo, C. Xu, L. Bai and L. A. Boatner, Production of native donors in ZnO by annealing at high temperature in Zn vapor, *Applied Physics Letters,* **2005,** *87*, 172108.

[135] H. Kaftelen, K. Ocakoglu, R. Thomann, S. Tu, S. Weber and E. Erdem, EPR and photoluminescence spectroscopy studies on the defect structure of ZnO nanocrystals, *Physical Review B,* **2012,** *86*, 014113.

[136] J. Smith and W. Vehse, ESR of electron irradiated ZnO confirmation of the F+ center, *Physics Letters A,* **1970,** *31*, 147.

[137] V. Soriano and D. Galland, Photosensitivity of the EPR spectrum of the F+ center in ZnO, *physica status solidi (b),* **1976,** *77*, 739.

[138] V. Nikitenko, K. Tarkpea, I. Pykanov and S. Stoyukhin, EPR and thermoluminescence in ZnO single crystals with anionic vacancies, *Journal of Applied Spectroscopy,* **2001,** *68*, 502.

[139] D. Liu, Y. Lv, M. Zhang, Y. Liu, Y. Zhu, R. Zong and Y. Zhu, Defect-related photoluminescence and photocatalytic properties of porous ZnO nanosheets, *Journal of Materials Chemistry A,* **2014,** *2*, 15377.

[140] S. Choi, M. R. Phillips, I. Aharonovich, S. Pornsuwan, B. C. Cowie and C. Ton ‐ That, Photophysics of Point Defects in ZnO Nanoparticles, *Advanced Optical Materials,* **2015,** *3*, 821.

[141] A. J. Reddy, M. Kokila, H. Nagabhushana, J. Rao, C. Shivakumara, B. Nagabhushana and R. Chakradhar, EPR, thermo and photoluminescence properties of ZnO nanopowders, *Spectrochimica Acta Part A: Molecular and Biomolecular Spectroscopy,* **2011,** *81*, 59.

[142] A. Pöppl and G. Völkel, ESR and Photo ‐ ESR Investigations of Zinc Vacancies and Interstitial Oxygen Ions in Undoped ZnO Ceramics, *physica status solidi (a),* **1991,** *125*, 571.

[143] X. Xu, C. Xu, J. Dai, J. Pan and J. Hu, Evolutions of defects and blue–green emissions in ZnO microwhiskers fabricated by vapor-phase transport, *Journal of Physics and Chemistry of Solids,* **2012,** *73*, 858.

[144] X. Chen, Y. Li, X. Pan, D. Cortie, X. Huang and Z. Yi, Photocatalytic oxidation of methane over silver decorated zinc oxide nanocatalysts, *Nature Communications,* **2016,** *7*,

[145] S. Moribe, T. Ikoma, K. Akiyama, Q. Zhang, F. Saito and S. Tero-Kubota, EPR study on paramagnetic species in nitrogen-doped ZnO powders prepared by a mechanochemical method, *Chemical physics letters,* **2007,** *436*, 373.

[146] Z. Hao, L. Fen, G. Lu, J. Liu, L. An and H. Wang, In situ electron paramagnetic resonance (EPR) study of surface oxygen species on Au/ZnO catalyst for low-temperature carbon monoxide oxidation, *Applied Catalysis A: General,* **2001,** *213*, 173.

[147] J. O. Cope and I. D. Campbell, Electron spin resonance observations of oxygen chemisorption on zinc oxide, *Journal of the Chemical Society, Faraday Transactions 1: Physical Chemistry in Condensed Phases,* **1973,** *69*, 1.

[148] K. Senthilkumar, M. Subramanian, H. Ebisu, M. Tanemura and Y. Fujita, Trapping and Recombination Properties of the Acceptor-like VZn-H Complex Defect in ZnO, *The Journal of Physical Chemistry C,* **2013,** *117*, 4299.

[149] A. W. Cohn, N. Janßen, J. M. Mayer and D. R. Gamelin, Photocharging ZnO nanocrystals: picosecond hole capture, electron accumulation, and auger recombination, *The Journal of Physical Chemistry C*, **2012,** *116*, 20633.

[150] K. Tanabe, M. Misono, Y. Ono and H. Hattori, New solids acids and bases: their catalytic properties, **1989,** 365.

[151] J. A. Lercher, C. Grundling and G. Eder-Mirth, *CAtal Today*, **1996,** *27*, 353.

[152] A. Auroux and A. Gervasini, *J. Phys. Chem. C,* **1990,** *94*, 63.

[153] W. Mokwa, D. Kohl and G. Heiland, *Surface Science,* **1982,** *117*, 659.

[154] V. Bolis, B. Fubini, E. Giamello and A. Reller, *J. Chem. Soc. Faraday Trans. ,* **1989,** *85*, 855.

[155] D. Scarano, G. Spoto, S. Bordiga, A. Zecchnia and C. Lamberti, *Surface Sicence,* **1992,** *276*, 281.

[156] D. R. and H. Luth, Decomposition of ethanol on a ZnO supported Pdcatalyst,, *Surface Science,* **1997,** *68*, 385.

[157] W. An, X. Wu and X. C. Zeng, *Phys. Chem.*, **2008,** *112*, 5747.

[158] K. Fink, 2006, *Phys. Chem. Phys*, *8*, 1482.

[159] X. Xia, J. Strunk, W. Busser, W. Naumann DAlmoncourt and M. Muhler, *J. Phys. Chem. C,* **2008,** *112*, 10938.

[160] S. J., J. C. LAvalley and C. Bovet, *J. Chem. Soc. Faraday Trans.,* **1982,** *78*, 1457.

[161] M. Nagao and t. Morimoto, *J. Phys. Chem. C,* **1980,** *84*, 2054.

[162] H. Wilmer, M. Kurtz, K. V. Klementiev, O. P. Tkachenko, t. W. Gruner, O. Hinrichsen, A. Birkner, S. Rabe, K. Merz, M. Driess, C. Wall and r. M. Muhle, Methanol synthesis over ZnO: A structure-sensitive reaction, *Phys. Chem. Chem. Phys.*, **2003,** *5*, 4736.

[163] H. H. Kung, *Catalysis Reviews:Science and Engineering,* **1980,** *22*, 253.

[164] F. Boccuzzi , E. Borello, A. Zecchina, A. Bossi and M. Camia, IR detection of surface microscopic modes of microcrystalline ZnO, *J. Catal.*, **1978,** *51*, 150.

[165] S. Crook, H. Dhariwal and G. Thornton, HREELS study of the interaction of formic acid with ZnO, *Surface science*, **1997,** *382*, 19.

[166] C. Drouilly, J. M. Krafft, F. Averseng, H. Lauron-Pernot, D. Bazer-Bachi, C. Chizallet, V. Lecocq and G. Costentin, Role of oxygen vacancies in the basicity of ZnO: from the model methylbutynol conversion to the ethanol transformation application, *Appl. Catal. A. Gen* **2013,** 121.

[167] D. Calestani, S. C. Dhanabalan, M. Villani, L. Lazzarini and A. Zappettini, InZnO nanorods obtained via zinc vapour phase deposition on liquid indium seeded substrates, *CrystEngComm,* **2014,** *16*, 1696.

[168] S. Anantachaisilp. The effect of surface defects on the optical and electrical properties of ZnO nanorods. 2015.

[169] M. Grundmann, *The Physics of Semiconductors: An Introduction Including Nanophysics and Applications*. Springer: 2015.

[170] H. D. Cho, A. S. Zakirov, S. U. Yuldashev, C. W. Ahn, Y. K. Yeo and T. W. Kang, Photovoltaic device on a single ZnO nanowire p–n homojunction, *Nanotechnology,* **2012,** *23,* 115401.

[171] N. Xu, Y. Cui, Z. Hu, W. Yu, J. Sun, N. Xu and J. Wu, Photoluminescence and low-threshold lasing of ZnO nanorod arrays, *Optics express,* **2012,** *20*, 14857.

[172] M. Fukuda, *Optical semiconductor devices*. John Wiley & Sons: 1999; Vol. 46.

[173] J. R. Lackowicz, Principles of fluorescence spectroscopy, *Plenum Press,(New York, 1983) Chapter,* **1983,** *5*, 111.

[174] B. M. Weckhuysen, R. Heidler and R. A. Schoonheydt, Electron spin resonance spectroscopy. In *Characterization I*, Springer: 2004; pp 295.

[175] G. R. Eaton, S. S. Eaton, D. P. Barr and R. T. Weber, *Quantitative Epr*. Springer Science & Business Media: 2010.

[176] P. Kubelka and F. Munk, An article on optics of paint layers, *Z. Tech. Phys,* **1931,** *12*,

[177] J. Solé, L. Bausa and D. Jaque, *An introduction to the optical spectroscopy of inorganic solids*. John Wiley & Sons: 2005.

[178] F. Haque. Réactivité de nanoparticules d'oxydes d'orientations définies. Paris 6, 2015.

[179] R. Meija, S. Signetti, A. Schuchardt, K. Meurisch, D. Smazna, M. Mecklenburg, K. Schulte, D. Erts, O. Lupan and B. Fiedler, Nanomechanics of individual aerographite tetrapods, *NATURE,* **2017,** *8*, 1.

[180] D. Gedamu, I. Paulowicz, S. Kaps, O. Lupan, S. Wille, G. Haidarschin, Y. K. Mishra and R. Adelung, Rapid fabrication technique for interpenetrated ZnO nanotetrapod networks for fast UV sensors, *Advanced materials,* **2014,** *26*, 1541.

[181] S. Talam, S. R. Karumuri and N. Gunnam, Synthesis, characterization, and spectroscopic properties of ZnO nanoparticles, *ISRN Nanotechnology,* **2012,** *2012*,

[182] V. Mote, Y. Purushotham and B. Dole, Williamson-Hall analysis in estimation of lattice strain in nanometer-sized ZnO particles, *Journal of Theoretical and Applied Physics,* **2012,** *6*, 6.

[183] A. K. Zak, W. A. Majid, M. E. Abrishami and R. Yousefi, X-ray analysis of ZnO nanoparticles by Williamson–Hall and size–strain plot methods, *Solid State Sciences,* **2011,** *13*, 251.

[184] Y. K. Mishra, S. Kaps, A. Schuchardt, I. Paulowicz, X. Jin, D. Gedamu, S. Wille, O. Lupan and R. Adelung, Versatile fabrication of complex shaped metal oxide nano-microstructures and their interconnected networks for multifunctional applications, *KONA Powder and Particle Journal,* **2014,** *31*, 92.

[185] S. Stankic, M. Müller, O. Diwald, M. Sterrer, E. Knözinger and J. Bernardi, Size‐Dependent Optical Properties of MgO Nanocubes, *Angewandte Chemie International Edition,* **2005,** *44*, 4917.

[186] I. S. Altman, I. E. Agranovski and M. Choi, On nanoparticle surface growth: MgO nanoparticle formation during a Mg particle combustion, *Applied physics letters,* **2004,** *84*, 5130.

[187] M. Shiojiri and C. Kaito, Structure and growth of ZnO smoke particles prepared by gas evaporation technique, *Journal of Crystal Growth,* **1981,** *52*, 173.

[188] Q. Pang, L. Zhao, Y. Cai, D. P. Nguyen, N. Regnault, N. Wang, S. Yang, W. Ge, R. Ferreira and G. Bastard, CdSe nano-tetrapods: controllable synthesis, structure analysis, and electronic and optical properties, *Chemistry of materials,* **2005,** *17*, 5263.

[189] V. Roy, A. Djurišić, W. Chan, J. Gao, H. Lui and C. Surya, Luminescent and structural properties of ZnO nanorods prepared under different conditions, *Applied physics letters,* **2003,** *83*, 141.

[190] O. Lupan, L. Chow and G. Chai, A single ZnO tetrapod-based sensor, *Sensors and Actuators B: Chemical,* **2009,** *141,* 511.

[191] J. Huh, G.-T. Kim, J. S. Lee and S. Kim, A direct measurement of the local resistances in a ZnO tetrapod by means of impedance spectroscopy: the role of the junction in the overall resistance, *Applied Physics Letters,* **2008,** *93,* 042111.

[192] S. Khanchandani, P. K. Srivastava, S. Kumar, S. Ghosh and A. K. Ganguli, Band gap engineering of ZnO using core/shell morphology with environmentally benign Ag2S sensitizer for efficient light harvesting and enhanced visible-light photocatalysis, *Inorganic chemistry,* **2014,** *53*, 8902.

[193] S. A. Ansari, M. M. Khan, S. Kalathil, A. Nisar, J. Lee and M. H. Cho, Oxygen vacancy induced band gap narrowing of ZnO nanostructures by an electrochemically active biofilm, *Nanoscale,* **2013,** *5*, 9238.

[194] S. C. Rai, K. Wang, Y. Ding, J. K. Marmon, M. Bhatt, Y. Zhang, W. Zhou and Z. L. Wang, Piezo-phototronic effect enhanced UV/visible photodetector based on fully wide band gap type-II ZnO/ZnS core/shell nanowire array, *ACS nano,* **2015,** *9*, 6419.

[195] H. Lu, F. Zheng, M. Guo and M. Zhang, One-step electrodeposition of single-crystal ZnO nanotube arrays and their optical properties, *Journal of Alloys and Compounds,* **2014,** *588*, 217.

[196] E. H. Khan, M. H. Weber and M. D. McCluskey, Formation of isolated Zn vacancies in ZnO single crystals by absorption of ultraviolet radiation: A combined study using positron annihilation, photoluminescence, and mass spectroscopy, *Physical review letters,* **2013,** *111*, 017401.

[197] P. Erhart, K. Albe and A. Klein, First-principles study of intrinsic point defects in ZnO: Role of band structure, volume relaxation, and finite-size effects, *Physical Review B,* **2006,** *73*, 205203.

[198] S. Zhang, S.-H. Wei and A. Zunger, Intrinsic n-type versus p-type doping asymmetry and the defect physics of ZnO, *Physical Review B,* **2001,** *63*, 075205.

[199] D. C. Look, G. C. Farlow, P. Reunchan, S. Limpijumnong, S. Zhang and K. Nordlund, Evidence for native-defect donors in n-type ZnO, *Physical Review Letters,* **2005,** *95*, 225502.

[200] E. Epie and W. Chu, Ionoluminescence study of Zn− and O− implanted ZnO crystals: An additional perspective, *Applied Surface Science,* **2016,** *371,* 28.

[201] A. Djurišić, W. C. Choy, V. A. L. Roy, Y. H. Leung, C. Y. Kwong, K. W. Cheah, T. Gundu Rao, W. K. Chan, H. Fei Lui and C. Surya, Photoluminescence and electron paramagnetic resonance of ZnO tetrapod structures, *Advanced Functional Materials,* **2004,** *14,* 856.

[202] X. Wu, G. Siu, C. Fu and H. Ong, Photoluminescence and cathodoluminescence studies of stoichiometric and oxygen-deficient ZnO films, *Applied Physics Letters,* **2001,** *78,* 2285.

[203] V. Gurylev, C.-Y. Su and T.-P. Perng, Distribution pattern and allocation of defects in hydrogenated ZnO thin films, *Physical Chemistry Chemical Physics,* **2016,** *18,* 16033.

[204] X. Zhang, J. Qin, Y. Xue, P. Yu, B. Zhang, L. Wang and R. Liu, Effect of aspect ratio and surface defects on the photocatalytic activity of ZnO nanorods, *Scientific reports,* **2014,** *4,* 4596.

[205] F. Gallino, G. Pacchioni and C. Di Valentin, Transition levels of defect centers in ZnO by hybrid functionals and localized basis set approach, *The Journal of chemical physics,* **2010,** *133,* 144512.

[206] J. F. Cordaro, Y. Shim and J. May, Bulk electron traps in zinc oxide varistors, *Journal of applied physics,* **1986,** *60,* 4186.

[207] M. Abdullah, T. Morimoto and K. Okuyama, Generating Blue and Red Luminescence from ZnO/Poly (ethylene glycol) Nanocomposites Prepared Using an In‐Situ Method, *Advanced Functional Materials,* **2003,** *13,* 800.

[208] V. Ischenko, S. Polarz, D. Grote, V. Stavarache, K. Fink and M. Driess, Zinc oxide nanoparticles with defects, *Advanced functional materials,* **2005,** *15,* 1945.

[209] J. Qu, Y. Ge, B. Zu, Y. Li and X. Dou, Transition‐Metal‐Doped p‐Type ZnO Nanoparticle‐Based Sensory Array for Instant Discrimination of Explosive Vapors, *Small,* **2016,**

[210] C. G. Van de Walle, Hydrogen as a cause of doping in zinc oxide, *Physical review letters,* **2000,** *85,* 1012.

[211] S. Cox, E. Davis, S. Cottrell, P. King, J. Lord, J. Gil, H. Alberto, R. Vilao, J. P. Duarte and N. A. de Campos, Experimental confirmation of the predicted shallow donor hydrogen state in zinc oxide, *Physical Review Letters,* **2001,** *86,* 2601.

[212] D. M. Hofmann, A. Hofstaetter, F. Leiter, H. Zhou, F. Henecker, B. K. Meyer, S. B. Orlinskii, J. Schmidt and P. G. Baranov, Hydrogen: a relevant shallow donor in zinc oxide, *Physical Review Letters,* **2002,** *88,* 045504.

[213] B. Meyer, H. Alves, D. Hofmann, W. Kriegseis, D. Forster, F. Bertram, J. Christen, A. Hoffmann, M. Straßburg and M. Dworzak, Bound exciton and donor–acceptor pair recombinations in ZnO, *physica status solidi (b),* **2004,** *241,* 231.

[214] C. G. Van de Walle, Hydrogen as a shallow center in semiconductors and oxides, *physica status solidi (b),* **2003,** *235,* 89.

[215] N. Garces, L. Wang, N. Giles, L. E. Halliburton, D. C. Look and D. C. Reynolds, Thermal diffusion of lithium acceptors into ZnO crystals, *Journal of electronic materials,* **2003,** *32,* 766.

[216] Y. Li, F. Della Valle, M. Simonnet, I. Yamada and J.-J. Delaunay, Competitive surface effects of oxygen and water on UV photoresponse of ZnO nanowires, *Applied Physics Letters,* **2009,** *94,* 023110.

[217] Y. Seung Rim, W. Jeong, B. Du Ahn and H. Jae Kim, Defect reduction in photon-accelerated negative bias instability of InGaZnO thin-film transistors by high-pressure water vapor annealing, *Applied Physics Letters,* **2013,** *102,* 143503.

[218] V. Blagojevic, Y.-R. Chen, M. Steigerwald, L. Brus and R. A. Friesner, Quantum chemical investigation of cluster models for TiO2 nanoparticles with water-derived ligand passivation: studies of excess electron states and implications for charge transport in the Gratzel cell, *The Journal of Physical Chemistry C,* **2009,** *113,* 19806.

[219] B. Yao, L. Feng, C. Cheng, M. M. Loy and N. Wang, Tailoring the luminescence emission of ZnO nanostructures by hydrothermal post-treatment in water, *Applied physics letters,* **2010,** *96,* 223105.

[220] K. Kocsis, M. Niedermaier, J. Bernardi, T. Berger and O. Diwald, Changing interfaces: Photoluminescent ZnO nanoparticle powders in different aqueous environments, *Surface Science,* **2016,** *652*, 253.

[221] H. Noei, H. Qiu, Y. Wang, M. Muhler and C. Wöll, Hydrogen loading of oxide powder particles: A transmission IR study for the case of zinc oxide, *ChemPhysChem,* **2010,** *11*, 3604.

[222] A. Alkauskas and A. Pasquarello, Band-edge problem in the theoretical determination of defect energy levels: The O vacancy in ZnO as a benchmark case, *Physical Review B,* **2011,** *84*, 125206.

[223] P. Erhart, A. Klein and K. Albe, First-principles study of the structure and stability of oxygen defects in zinc oxide, *Physical Review B,* **2005,** *72*, 085213.

[224] S. Dutta, S. Chattopadhyay, M. Sutradhar, A. Sarkar, M. Chakrabarti, D. Sanyal and D. Jana, Defects and the optical absorption in nanocrystalline ZnO, *Journal of Physics: Condensed Matter,* **2007,** *19*, 236218.

[225] M. Puchert, P. Timbrell and R. Lamb, Postdeposition annealing of radio frequency magnetron sputtered ZnO films, *Journal of Vacuum Science & Technology A: Vacuum, Surfaces, and Films,* **1996,** *14*, 2220.

[226] J. Wang, Y. Xia, Y. Dong, R. Chen, L. Xiang and S. Komarneni, Defect-rich ZnO nanosheets of high surface area as an efficient visible-light photocatalyst, *Applied Catalysis B: Environmental,* **2016,** *192*, 8.

[227] F. Kayaci, S. Vempati, I. Donmez, N. Biyikli and T. Uyar, Role of zinc interstitials and oxygen vacancies of ZnO in photocatalysis: a bottom-up approach to control defect density, *Nanoscale,* **2014,** *6*, 10224.

[228] T. B. Hur, D. H. Yoo, G. S. Jeen, Y. H. Hwang, H. K. Kim, Y. H. Hwang and Y. H. Um, The effects of thermal annealing of ZnO ceramics, *Journal of the Korean Physical Society,* **2003,** *42*, 1283.

[229] F. Kayaci, S. Vempati, C. Ozgit-Akgun, I. Donmez, N. Biyikli and T. Uyar, Selective isolation of the electron or hole in photocatalysis: ZnO–TiO 2 and TiO 2–ZnO core–shell structured heterojunction nanofibers via electrospinning and atomic layer deposition, *Nanoscale,* **2014,** *6*, 5735.

[230] C. J. Powell, Surface and Microanalysis Science Division National Institute of Standards and Technology Gaithersburg, MD, USA,

[231] A. Jablonski, Institute of Physical Chemistry, Polish Academy of Sciences, Warsaw, Poland,

[232] J.-J. Yeh, *Atomic calculation of photoionization cross-sections and asymmetry parameters*. Gordon & Breach Science Publ.; AT&T Bell Laboratories: 1993.

[233] J. Yeh and I. Lindau, Atomic subshell photoionization cross sections and asymmetry parameters: $1 \leqslant Z \leqslant 103$, *Atomic data and nuclear data tables,* **1985,** *32*, 1.

[234] J. N. Zeng, J. K. Low, Z. M. Ren, T. Liew and Y. F. Lu, Effect of deposition conditions on optical and electrical properties of ZnO films prepared by pulsed laser deposition, *Applied surface science,* **2002,** *197*, 362.

[235] T. Mishra and D. K. Mahato, A comparative study on enhanced arsenic (V) and arsenic (III) removal by iron oxide and manganese oxide pillared clays from ground water, *Journal of Environmental Chemical Engineering,* **2016,** *4*, 1224.

[236] C. Gionco, M. C. Paganini, E. Giamello, R. Burgess, C. Di Valentin and G. Pacchioni, Paramagnetic defects in polycrystalline zirconia: an EPR and DFT study, *Chemistry of Materials,* **2013,** *25*, 2243.

[237] J. Cope and I. Campbell, Electron spin resonance observations of oxygen chemisorption on zinc oxide, *Journal of the Chemical Society, Faraday Transactions 1: Physical Chemistry in Condensed Phases,* **1973,** *69*, 1.

[238] A. R. Puigdollers, F. Illas and G. Pacchioni, Structure and properties of zirconia nanoparticles from density functional theory calculations, *The Journal of Physical Chemistry C,* **2016,** *120*, 4392.

[239] R. Eischens, W. Pliskin and M. Low, The infrared spectrum of hydrogen chemisorbed on zinc oxide, *Journal of Catalysis,* **1962,** *1*, 180.

[240] R. Kokes, The influence of chemisorption of oxygen on the electron spin resonance of zinc oxide, *The Journal of Physical Chemistry,* **1962,** *66*, 99.

[241] M. E. Reish, Z. Zhang, S. Ma, I. Harrison and H. Everitt, How Annealing and Charge Scavengers Affect Visible Emission from ZnO Nanocrystals, *JOURNAL OF PHYSICAL CHEMISTRY C,* **2016,**

[242] W. An, X. Wu and X. C. Zeng, Adsorption of O2, H2, CO, NH3, and NO2 on ZnO nanotube: a density functional theory study, *The Journal of Physical Chemistry C,* **2008,** *112*, 5747.

[243] H. Idriss and M. Barteau, Photoluminescence from zinc oxide powder to probe absorption and reaction of oxygen, carbon monoxide, hydrogen, formic acid, and methanol, *The Journal of Physical Chemistry,* **1992,** *96*, 3382.

[244] G. Sengupta, H. Ahluwalia, S. Banerjee and S. Sen, Chemisorption of water vapor on zinc oxide, *Journal of Colloid and Interface Science,* **1979,** *69*, 217.

[245] H. Noei, H. Qiu, Y. Wang, E. Löffler, C. Wöll and M. Muhler, The identification of hydroxyl groups on ZnO nanoparticles by infrared spectroscopy, *Physical Chemistry Chemical Physics,* **2008,** *10*, 7092.

[246] X. Pan, M.-Q. Yang, X. Fu, N. Zhang and Y.-J. Xu, Defective TiO 2 with oxygen vacancies: synthesis, properties and photocatalytic applications, *Nanoscale,* **2013,** *5*, 3601.

[247] N. G. Petrik and G. A. Kimmel, Reaction kinetics of water molecules with oxygen vacancies on rutile TiO2 (110), *The Journal of Physical Chemistry C,* **2015,** *119*, 23059.

[248] C. Drouilly, J.-M. Krafft, F. Averseng, H. Lauron-Pernot, D. Bazer-Bachi, C. Chizallet, V. Lecocq and G. Costentin, Origins of the deactivation process in the conversion of methylbutynol on zinc oxide monitored by operando DRIFTS, *Catalysis today,* **2013,** *205*, 67.

[249] F. Stavale, N. Nilius and H.-J. Freund, STM luminescence spectroscopy of intrinsic defects in ZnO (0001) thin films, *The Journal of Physical Chemistry Letters*, **2013,** *4*, 3972.

[250] C. J. Barnett, N. A. Smith, D. R. Jones, T. G. Maffeis and R. J. Cobley, Effects of Vacuum Annealing on the Conduction Characteristics of ZnO Nanosheets, *Nanoscale research letters,* **2015,** *10*, 368.

[251] T. M. Børseth, B. Svensson and A. Y. Kuznetsov, Annealing study of hydrothermally grown ZnO wafers, *Physica Scripta,* **2006,** *2006*, 10.

[252] D. Thapa, J. Huso, J. L. Morrison, C. D. Corolewski, M. D. McCluskey and L. Bergman, Achieving highly-enhanced UV photoluminescence and its origin in ZnO nanocrystalline films, *Optical Materials*, **2016,** *58*, 382.

[253] H.-M. Cheng, H.-C. Hsu, S.-L. Chen, W.-T. Wu, C.-C. Kao, L.-J. Lin and W.-F. Hsieh, Efficient UV photoluminescence from monodispersed secondary ZnO colloidal spheres synthesized by sol–gel method, *Journal of Crystal Growth,* **2005,** *277*, 192.

[254] H. Lauron‐Pernot, Evaluation of Surface Acido‐Basic Properties of Inorganic‐Based Solids by Model Catalytic Alcohol Reaction Networks, *Catalysis Reviews,* **2006,** *48*, 315.

[255] J. A. Lercher, C. Gründling and G. Eder-Mirth, Infrared studies of the surface acidity of oxides and zeolites using adsorbed probe molecules, *Catalysis Today,* **1996,** *27*, 353.

[256] A. Auroux and A. Gervasini, Microcalorimetric study of the acidity and basicity of metal oxide surfaces, *Journal of Physical Chemistry,* **1990,** *94*, 6371.

[257] M.-L. Bailly, C. Chizallet, G. Costentin, J.-M. Krafft, H. Lauron-Pernot and M. Che, A spectroscopy and catalysis study of the nature of active sites of MgO catalysts: Thermodynamic Brønsted basicity versus reactivity of basic sites, *Journal of Catalysis*, **2005,** *235*, 413.

[258] J. F. Groust, G. Costentin, J. M. Krafft and P. Massiani, Mechanism and deactivation process of the conversion of methylbutynol on basic faujasite monitored by operando DRIFTS, *Physical Chemistry Chemical Physics,* **2010,** *12*, 937.

[259] H. Lauron-Pernot, F. Luck and J. Popa, Methylbutynol: a new and simple diagnostic tool for acidic and basic sites of solids, *Applied catalysis,* **1991,** *78*, 213.

[260] A. Kohan, G. Ceder, D. Morgan and C. G. Van de Walle, First-principles study of native point defects in ZnO, *Physical Review B,* **2000,** *61*, 15019.

[261] Y. Ma, G. Du, T. Yang, D. Qiu, X. Zhang, H. Yang, Y. Zhang, B. Zhao, X. Yang and D. Liu, Effect of the oxygen partial pressure on the properties of ZnO thin films grown by metalorganic vapor phase epitaxy, *Journal of crystal growth,* **2003,** *255*, 303.

[262] W. Gao, Z. Li, R. Harikisun and S.-S. Chang, Zinc oxide films formed by oxidation of zinc under low partial pressure of oxygen, *Materials letters,* **2003,** *57*, 1435.

[263] F. Haque, S. Chenot, F. Viñes, F. Illas, S. Stankic and J. Jupille, ZnO powders as multi-facet single crystals, *Physical Chemistry Chemical Physics,* **2017,** *19*, 10622.

[264] R. S. Zeferino, M. B. Flores and U. Pal, Photoluminescence and Raman scattering in Ag-doped ZnO nanoparticles, *Journal of applied physics,* **2011,** *109*, 014308.

[265] C. Xu, X. Sun, X. Zhang, L. Ke and S. Chua, Photoluminescent properties of copper-doped zinc oxide nanowires, *Nanotechnology,* **2004,** *15*, 856.

[266] M. Šćepanović, M. Grujić‐Brojčin, K. Vojisavljević, S. Bernik and T. Srećković, Raman study of structural disorder in ZnO nanopowders, *Journal of Raman Spectroscopy,* **2010,** *41*, 914.

[267] K. Mahmood, S. B. Park and H. J. Sung, Enhanced photoluminescence, Raman spectra and field-emission behavior of indium-doped ZnO nanostructures, *Journal of Materials Chemistry C,* **2013,** *1*, 3138.

[268] J. Ye, S. Gu, S. Zhu, F. Qin, S. Liu, W. Liu, X. Zhou, L. Hu, R. Zhang and Y. Shi, Production of high-quality ZnO films by the two-step annealing method, *Journal of applied physics,* **2004,** *96*, 5308.

[269] F. Güell, P. R. Martínez‐Alanis, S. Khachadorian, J. Rubio‐García, A. Franke, A. Hoffmann and G. Santana, Raman and photoluminescence properties of ZnO nanowires grown by a catalyst‐free vapor‐transport process using ZnO nanoparticle seeds, *physica status solidi (b),* **2016,** *253*, 883.

[270] R. Cuscó, E. Alarcón-Lladó, J. Ibáñez, L. Artús, J. Jiménez, B. Wang and M. J. Callahan, Temperature dependence of Raman scattering in ZnO, *Physical Review B,* **2007,** *75*, 165202.

[271] R. M. Sheetz, I. Ponomareva, E. Richter, A. N. Andriotis and M. Menon, Defect-induced optical absorption in the visible range in ZnO nanowires, *Physical Review B,* **2009,** *80*, 195314.

[272] J. Wang, Z. Wang, B. Huang, Y. Ma, Y. Liu, X. Qin, X. Zhang and Y. Dai, Oxygen vacancy induced band-gap narrowing and enhanced visible light photocatalytic activity of ZnO, *ACS applied materials & interfaces,* **2012,** *4*, 4024.

[273] J. Tauc In *The optical properties of solids*, The Optical Properties of Solids, 1966.

[274] A. P. Roth, J. B. Webb and D. F. Williams, Band-gap narrowing in heavily defect-doped ZnO, *Physical Review B,* **1982,** *25*, 7836.

[275] F. De Angelis and L. Armelao, Optical properties of ZnO nanostructures: a hybrid DFT/TDDFT investigation, *Physical Chemistry Chemical Physics,* **2011,** *13*, 467.

[276] K. Sancier, ESR investigation of photodamage to zinc oxide powders, *Surface Science,* **1970,** *21*, 1.

[277] R. Vidya, P. Ravindran, H. Fjellvåg, B. Svensson, E. Monakhov, M. Ganchenkova and R. M. Nieminen, Energetics of intrinsic defects and their complexes in ZnO investigated by density functional calculations, *Physical Review B,* **2011,** *83*, 045206.

[278] X. Chen, L. Liu, Y. Y. Peter and S. S. Mao, Increasing solar absorption for photocatalysis with black hydrogenated titanium dioxide nanocrystals, *Science,* **2011,** *331*, 746.

[279] M. M. Khan, S. A. Ansari, D. Pradhan, D. H. Han, J. Lee and M. H. Cho, Defect-induced band gap narrowed CeO2 nanostructures for visible light activities, *Industrial & Engineering Chemistry Research,* **2014,** *53*, 9754.

List of Figures